Universitat d'Alacant
Universidad de Alicante

Catalizadores micro- y nanoestructurados para la oxidación de hidrocarburos y producción de hidrógeno

Javier Fernández Catalá

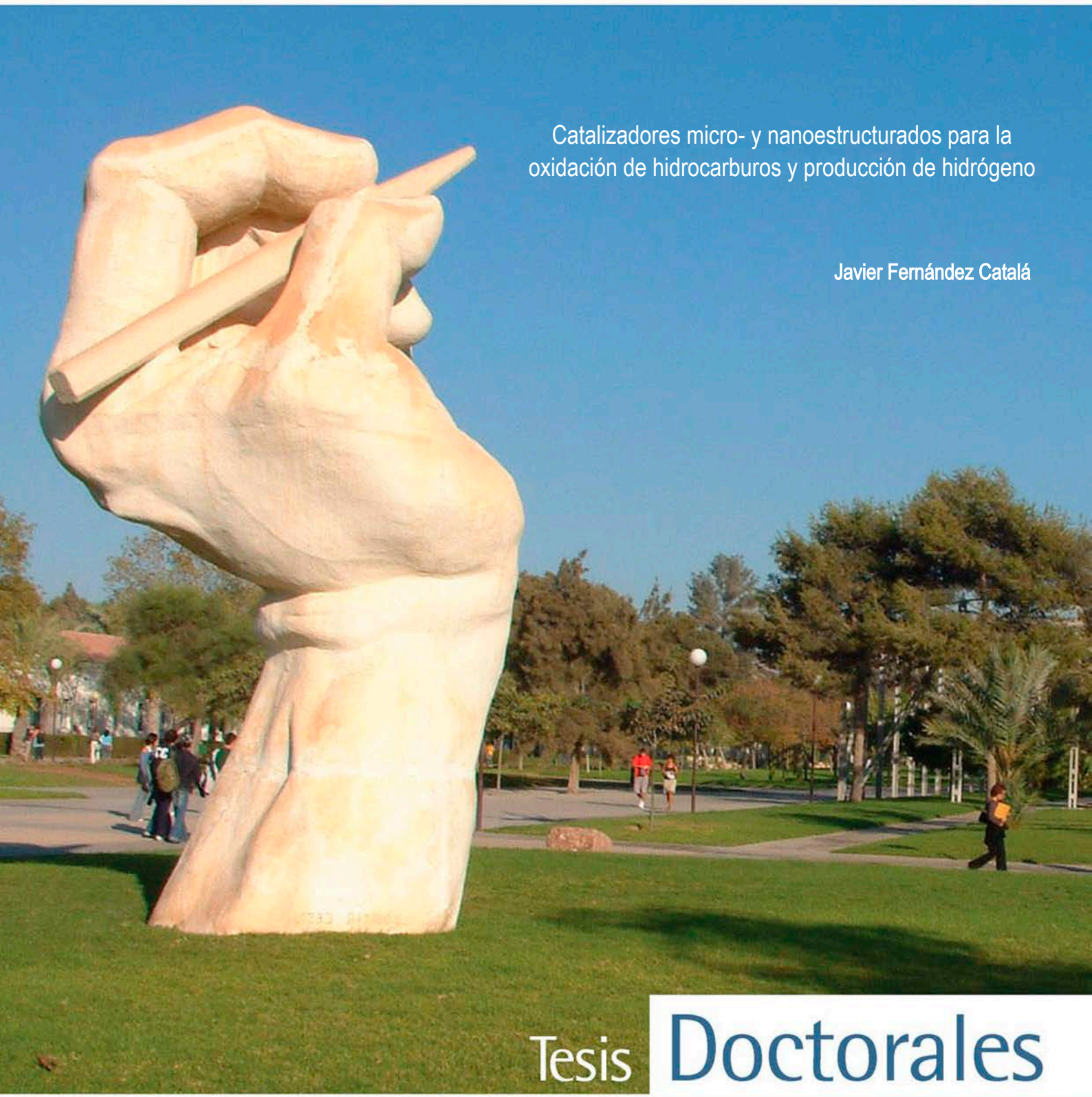

Tesis Doctorales
UNIVERSIDAD de ALICANTE

Unitat de Digitalització UA
Unidad de Digitalización UA

Grupo de Materiales Carbonosos y Medio Ambiente
Departamento de Química Inorgánica (Facultad de Ciencias)
Instituto Universitario de Materiales

Catalizadores micro- y nanoestructurados para la oxidación de hidrocarburos y producción de hidrógeno

Javier Fernández Catalá

Tesis presentada para aspirar al grado de
DOCTOR POR LA UNIVERSIDAD DE ALICANTE

MENCIÓN DE DOCTOR INTERNACIONAL

Doctorado en Ciencia de Materiales

Dirigida por:

Diego Cazorla Amorós
Catedrático de Química Inorgánica

Ángel Berenguer Murcia
Profesor Titular de Química Inorgánica

Alicante, Marzo de 2020

Diego Cazorla Amorós, Catedrático de Química Inorgánica, Ángel Berenguer Murcia, Profesor Titular de Química Inorgánica, ambos de la Universidad de Alicante.

CERTIFICAN QUE:

D. **Javier Fernández Catalá**, Graduado en Químicas, ha realizado en el Grupo de Materiales Carbonosos y Medio Ambiente (MCMA), del Departamento de Química Inorgánica e Instituto Universitario de Materiales, bajo nuestra dirección, el trabajo que lleva por título: "**Catalizadores micro- y nanoestructurados para la oxidación de hidrocarburos y producción de hidrógeno"** que constituye su Memoria para aspirar al grado de Doctor con mención Internacional por la Universidad de Alicante, reuniendo, a nuestro juicio, las condiciones necesarias para ser presentada y defendida ante el tribunal correspondiente.

Y para que conste a efectos oportunos, en cumplimiento de la legislación vigente, firmamos el presente certificado en Alicante a 23 de Enero del 2020.

Diego Cazorla Amorós
Catedrático de Química Inorgánica

Ángel Berenguer Murcia
Profesor Titular de Química Inorgánica

Agradecimientos

Antes de finalizar mi etapa predoctoral que termina con la defensa de esta Tesis Doctoral me gustaría dedicarles unas líneas de agradecimiento a todas aquellas personas que me habéis ayudado, apoyado y sois parte de la presente Tesis Doctoral. Y al gobierno de España por la financiación recibida para la realización de esta Tesis (BES-2016-078079).

En primer lugar, me gustaría agradecer a mis directores de Tesis, Diego y Ángel. A Diego decirle muchas gracias por haber confiado en mí para la realización de esta tesis, por la cual fui contratado. También agradecerle todas las discusiones que hemos tenido tanto científicas como no, además de ser un ejemplo de cómo llevar una trayectoria científica. A Ángel quería darle las gracias por su ayuda, visión y sus palabras tranquilizadoras cuando las cosas no han ido del todo bien.

I would like to thank Yamashita, Mori and Kuawahara senseis for letting me stay in your laboratory, your advice and kindness. Moreover, I would like to thank the laboratory partners and the friends in Osaka for doing my life more easy in Japan and made me feel at home.

Me gustaría agradecer también a todos mis compañeros por hacer que vaya al trabajo con una sonrisa, aunque a veces me cabreen. Mención especial merecen Jaime por su ayuda y darme su opinión siempre que lo he necesitado. A Laura por esas clases sobre fotocatálisis y lo más importante por ser una maravillosa persona. Miriam por su enorme ayuda en la estancia desde la distancia y por ser un ejemplo en lo que se refiere al esfuerzo. Al eje del mal, vaya nombre nos pusieron, por todas las cervezas y momentos que hemos vivido en esta etapa. A Vero por ser como eres, no cambies. Ana por su alegría y hippiadas. Juan Carlos y Juanjo por las partidas al pádel. María José y Atsushi por los cafés y las risas. Alessio y David por aconsejarme. Jessica, Zaira y Sergio por los nuevos momentos. Esther por esos congresos y charlas. Los compañeros del GEPE por su ayuda y compañerismo. A las secretarias y técnicos del departamento por su ayuda y consejos. A la secretaría del IUMA por resolverme todas las dudas que me han surgido. A Germán por su ayuda en todo momento, consejos y soportarme. Jero e Ion por su colaboración. A Ros y Llorenç por las discusiones de química orgánica, las risas y anécdotas. Yasuhiro because you are a nice friend in Osaka.

A los amigos de Muro “PATAPALOS” porque la mejor solución para cualquier problema son las risas y porque ya sabéis casi más de química que yo.

A mi padre, mi madre y hermano por soportar mi tontería, que no es poca, cuando las cosas se ponían complicadas en esta etapa y sobre todo por ser los pilares que sostienen mi vida.

Si buscas resultados distintos,

no hagas siempre lo mismo

Albert Einstein

Resumen

El estudio recogido en la presente Tesis Doctoral está motivado por los crecientes esfuerzos que la comunidad científica está dedicando a la búsqueda de soluciones para la problemática medioambiental existente en la sociedad actual, así como el interés en la síntesis de productos químicos de interés industrial. En este sentido, el estudio y el desarrollo de catalizadores y fotocatalizadores tanto en forma de polvo o como relleno en microrreactores está atrayendo una gran atención de los científicos debido a las numerosas aplicaciones que presentan estos sistemas.

Con esto en mente, el principal objetivo de la Tesis Doctoral es diseñar y preparar materiales basados en óxido de titanio y titanosilicatos para su aplicación en diversas reacciones catalíticas tanto desde un punto de vista medioambiental como para la síntesis de compuestos de interés industrial.

En la presente Tesis Doctoral se realiza una introducción general donde se describen los temas que se han abordado en la misma (preparación de materiales catalíticos y fotocatalíticos para aplicaciones medioambientales y síntesis de compuestos químicos de interés industrial). Con esta finalidad, se introduce muy brevemente la catálisis y su aporte a la sociedad. Además se centra en la catálisis heterogénea, más concretamente en la fotocatálisis heterogénea, abordando el diseño de materiales como los fototocalizadores, materiales compuestos, soportes de catalizadores y titanosilicatos, centrándose en el semiconductor óxido de titanio (TiO_2). También se describe el creciente interés de la comunidad científica en la inmovilización de los catalizadores en distintos soportes y en el diseño de nuevos reactores, haciendo hincapié en la inmovilización del fotocatalizador óxido de titanio en reactores y en microrreactores. Finalmente se describen brevemente las reacciones catalíticas de interés medioambiental y para la industria (oxidación fotocatalítica de propeno, oxidación selectiva de propileno y producción de H_2) que se han utilizado para realizar los ensayos la actividad de los catalizadores y fotocatalizadores diseñados en esta Tesis. En esta Tesis Doctoral también se presentan las diferentes técnicas usadas para llevar a cabo la caracterización físico-química de las muestras estudiadas. Las técnicas empleadas son las siguientes: Difracción de Rayos X, Espectrometría Ultravioleta-Visible, Adsorción Física de Gases, Microscopía Óptica, Microscopía Electrónica de Barrido, Microscopía Electrónica de Transmisión, Espectroscopia de Fluorescencia de Rayos X con análisis por Dispersión de Energía, Espectroscopia Fotoelectrónica de Rayos X, Espectroscopia Infrarroja por Transformada de Fourier, Fotoluminiscencia, Termogravimetría y Desorción a Temperatura Programada. Además, se describe la Cromatografía de Gases y la Espectrometría de Masas debido que en la presente Tesis estas técnicas se usan como técnicas de análisis durante los ensayos catalíticos. Por otro lado, también se incluyen las condiciones usadas para llevar a cabo los distintos ensayos catalíticos realizados en la presente Tesis (oxidación fotocatalítica de propeno en fase gas, oxidación

selectiva de propileno en fase gas y la descomposición fotocatalítica del amino borano en fase líquida).

En esta Tesis se han preparado diferentes materiales para diferentes aplicaciones (fotooxidación total de propeno, epoxidación de propileno y producción de hidrógeno) y en diferentes configuraciones (en polvo o incorporados en un microrreactor)

Inicialmente se desarrollan, sintetizan y estudian fotocatalizadores basados en óxido de titanio (óxido de titanio puro (TiO_2) y materiales compuestos (TiO_2/Material)), para su uso como fotocatalizadores en aplicaciones medioambientales (fotooxidacion total de propeno "COV"). Concretamente en esta Tesis se desarrolla una metodología para sintetizar un óxido de titanio que presenta una porosidad jerárquica (micro-, meso- y macroporosidad) y elevada estabilidad térmica para su aplicación como fotocatalizador en la eliminación de propeno en fase gas, obteniendo unos resultados de conversión ligeramente superiores al óxido de titanio comercial (P25). Además se describe y estudia la encapsulación de un óxido de titanio comercial (P25) en distintas sílices (sílice con porosidad jerárquica, sílice MCM-41 y una sílice precipitada) para su aplicación en la eliminación de propeno continuando con el trabajo realizado en el capítulo anterior. Se observa que la encapsulación del óxido de titanio comercial con una silice con porosidad jerárquica aumenta la actividad catalítica por mol de fotocatalizador respecto a los otros materiales compuestos y TiO_2 puros sintetizados. Finalizando este apartado de síntesis de materiales basados en óxido de titanio en forma de polvo para su aplicación en la fotooxidación de propeno en fase gas, se describe y estudia el efecto de incorporar nanotubos de carbono de pared múltiple (MWCNT) en el medio de reacción de la síntesis del óxido de titanio, así como el efecto de la dispersión de la especie fotoactiva y de los grupos superficiales oxigenados de los nanotubos de carbono de pared múltiple presentes en los materiales compuestos (TiO_2-MWCNT), en su actividad para la eliminación de propeno. El material compuesto (TiO_2-MWCNT) en todos los casos presenta una mayor conversión de propeno que el TiO_2 original. Además se observa en este estudio que una mejor dispersión de la fase fotoactiva y una mayor presencia de grupos superficiales oxigenados en los nanotubos de carbono de pared múltiple, favorecen la conversión de propeno.

En esta Tesis también se presenta y describe la síntesis de un titanosilicato, en el que los átomos de titanio están aislados en la estructura de la sílice, así como su impregnación con nanopartículas de níquel bien dispersas. Así, se ha obtenido un catalizador que presenta una propiedades catalíticas muy interesantes para la oxidación selectiva de propileno, siendo los valores de actividad y selectividad similares a los catalizadores basados en oro que son los más interesantes para esta aplicación, con la ventaja de usar un metal de transición más económico como el níquel.

Otro aspecto que se trata en esta Tesis es la producción de hidrógeno. Para ello se han preparado catalizadores con diferentes metales de transición soportados en el material TiO_2-MWCNT, para obtener el sistema catalítico Metal/TiO_2-MWCNT. Este sistema presenta unos resultados interesantes en la producción de hidrogeno mediante la descomposición de la molécula de amino borano, observándose que catalizadores con una baja carga de Cu presentan la mejor actividad catalítica.

Finalmente se desarrolla y estudia la incorporación y el relleno de óxido de titanio en diferentes microrreactores (microcapilares y reactores de chip para microfluídica) para aplicaciones medioambientales (fotooxidación total de propeno). Concretamente en esta Tesis se presenta una metodología sencilla de inmovilización de un fotocatalizador comercial (P25) en el interior de un microrreactor (microcapilar) para su aplicación en la fotooxidación de propeno. El sistema presenta una actividad catalítica superior por mol de P25 a la del mismo catalizador en polvo (reactor convencional); además, el sistema presenta una caída de presión baja, siendo este uno de los principales inconvenientes de usar esta tecnología en reacciones en fase gaseosa, en la actualidad. También se desarrolla y presenta otro fotomicrorreactor (reactores de chip para microfluídica) iluminado con luz LED de baja potencia como un sistema eficiente para la fotooxidación total de propeno. Este sistema consiste en inmovilizar un fotocatalizador comercial (óxido de titanio, P25) en el interior de los canales de reactores de chip para microfluídica. La P25 incorporada en este microrreactor da lugar a la oxidación total del propeno (100 % de conversión) en las condiciones experimentales estudiadas.

Summary

The study presented in this PhD Thesis has been motivated by the growing efforts that the scientific community is dedicating in the quest for solutions to the environmental problems existing nowadays in society, as well as the interest towards the synthesis of chemical products of industrial interest. In this sense, the study and development of catalysts and photocatalysts as powder or as fillings in microreactors is attracting a great attention from the scientific community due to the numerous applications of these systems.

With this in mind, the main objective of this PhD Thesis is to design and prepare materials based on titanium oxide and titanosilicates for their application in several catalytic reactions such as environmental reactions and synthesis of chemicals of industrial interest.

In this PhD Thesis a general introduction is made describing the topics that have been addressed in it (preparation of catalytic and photocatalytic materials for environmental applications and synthesis of chemical compounds of industrial interest). For this purpose, catalysis and its contribution to society are introduced briefly. This introduction is also focused on heterogeneous catalysis, more specifically in heterogeneous photocatalysis, addressing the design of materials such as phototocalysts, composite materials, catalysts supports and titanosilicates focusing on the semiconductor titanium oxide (TiO_2). The growing interest of the scientific community in the last years in immobilizing catalysts on different supports and in the design of novel reactors is also described, emphasizing the immobilization of the titanium oxide photocatalyst in reactors and microreactors. Finally, the catalytic reactions (photocatalytic oxidation of propene, selective oxidation of propylene and H_2 production) that have been used to perform the catalytic activity tests of catalysts and photocatalysts designed in this Thesis, are briefly described. Moreover, the different techniques used to carry out the physico-chemical characterization of the samples studied are also presented. The techniques used are the following: X-ray diffraction, Ultraviolet-Visible Spectrometry, Physical Adsorption of Gases, Optical Microscopy, Scanning Electron Microscopy, Transmission Electron Microscopy, X-Ray Fluorescence Spectroscopy with Energy Dispersion Analysis, X-ray Photoelectron Spectroscopy, Fourier Transform Infrared Spectroscopy, Photoluminescence, Thermogravimetry and Temperature Programmed Desorption. In addition, Gas Chromatography and Mass Spectrometry are described because these techniques are used as analysis techniques during catalytic tests performed in this PhD Thesis. Moreover, the conditions used to carry out the different catalytic tests studied in this PhD Thesis are described (photocatalytic oxidation of propene in gas phase, selective oxidation of propylene in gas phase and photocatalytic decomposition of ammonia-borane in liquid phase).

In this PhD Thesis different materials have been prepared for different applications (total propene photooxidation, propylene epoxidation and hydrogen production) and in different configurations (powder or incorporated in a microreactor)

First, photocatalysts based on titanium oxide (pure titanium oxide (TiO_2) and composite materials (TiO_2/Material)) are developed, synthesized and studied, for their application as photocatalysts in environmental applications (total propene photooxidation "VOC"). Specifically in this Thesis a methodology is developed to synthesize a titanium oxide presenting a hierarchical porosity (micro-, meso- and macroporosity) and high thermal stability for its application as a photocatalyst in the elimination of propene in gas phase, obtaining results of propene conversion slightly higher than a commercial titanium oxide (P25). These sections of the thesis also describe and study the encapsulation of a commercial titatanium oxide (P25) in different silicas (silica with hierarchical porosity, MCM-41 silica and precipitated silica) for its application in the elimination of propene continuing with the work done in the previous Chapter. It is observed that the encapsulation of commercial titanium oxide with a silica with hierarchical porosity favors an increase of the catalytic activity per mole of photocatalyst with respect to the other composites (MCM-41 silica and precipitated silica) and pure TiO_2 materials. The section of synthesis of materials based on titanium oxide in powder configuration for their application in gas phase propene photooxidation, is completed by studying the effect of incorporating multi-wall carbon nanotubes (MWCNT) in the reaction medium of the titanium oxide synthesis, as well as the effect of dispersion of the photoactive phase and of the surface oxygen groups of multi-wall carbon nanotubes, in the activity of TiO_2-MWCNT materials for the removal of propene. The composite material (TiO_2-MWCNT) in all cases presents a greater conversion of propene than the original TiO_2. It is also observed in this study that a better dispersion of the photoactive phase and a higher presence of surface oxygen groups in the multi-wall carbon nanotubes, favor the conversion of propene.

This PhD Thesis also presents and describes the synthesis of a titanosilicate, containing titanium single sites (i.e., isolated Ti atoms) in the structure of silica, as well as its impregnation with well dispersed nickel nanoparticles, obtaining a catalyst that has very interesting catalytic properties for the selective oxidation of propylene. The catalytic activity and selectivity values are similar to gold-based catalysts, which are the most interesting for the propylene epoxidation application, with the advantage of using an economic transition metal such as nickel.

Another aspect discussed in this PhD Thesis is the production of hydrogen. For this aim, different metals have been supported on TiO_2-MWCNT material, to obtain the Metal/TiO_2-MWCNT catalytic system. This system presents interesting results in the production of hydrogen through the decomposition of the ammonia borane molecule, observing that the photocatalysts with a low Cu loading have the best catalytic activity.

Finally, the incorporation and filling of titanium oxide in different microreactors (microcapillaries and microfluidic chip reactors) is developed and studied for environmental applications (propene photooxidation). More specifically, in this PhD Thesis a simple methodology of immobilization of a commercial photocatalyst (P25) inside a microreactor (microcapillary) for its application in the propene photooxidation is presented. The system has a catalytic activity per mole of photocatalyst superior that the same catalyst in powder form (P25 in a conventional reactor). In addition, the system has a low pressure drop, this being one of the main drawbacks of using this technology in gas phase reactions. Another photomicroreactor (microfluidic chip reactors) illuminated with low power LED light was also developed and presented as an efficient system for total propene photooxidation. This system consists of immobilizing a commercial photocatalyst (titanium oxide, P25) inside the chip reactor channels for microfluidics. The P25 incorporated in this microreactor produces the total photooxidation of propene at the experimental conditions used.

Índice

Capítulo 2. Técnicas Experimentales

Chapter 6. Propylene Epoxidation with Ni-$TiSiO_2$ Catalyst

Chapter 7. Ammonia-Borane Decomposition with Cu/TiO_2-MWCNT Photocatalyst

Chapter 9. Photooxidation of Propene Using Photo-Microfluidic Chip Reactors

Chapter 10. General Conclusions/Conclusiones Generales

Capítulo 0

Motivación, Objetivos y Estructura de la Tesis

En el presente Capítulo se han descrito las motivaciones y los objetivos para la realización de la Tesis Doctoral. Además se ha presentado la estructura que se ha seguido para una mejor comprensión de la Tesis.

0.1 Motivación

El estudio recogido en la presente Tesis Doctoral ha sido motivado por el creciente interés que existe en el grupo de investigación (Materiales Carbonosos y Medio Ambiente, del Instituto Universitario de Materiales y del Departamento de Química Inorgánica) en el cual se ha realizado este trabajo, hacia el estudio de la problemática medioambiental existente y la síntesis de productos químicos de interés para la sociedad. En este sentido, el estudio y el desarrollo de catalizadores y fotocatalizadores tanto en forma de polvo o como relleno en microrreactores está atrayendo una gran atención por parte de la comunidad científica debido a las numerosas aplicaciones que presentan estos sistemas.

0.2 Objetivos de la Tesis Doctoral

El objetivo principal de la presente Tesis Doctoral consiste en el diseño y preparación de materiales basados en óxido de titanio y titanosilicatos para su aplicación en diversas reacciones catalíticas tanto desde un aspecto medioambiental como para la síntesis de compuestos de interés industrial.

En este sentido los objetivos más relevantes de esta tesis son:

- Diseñar y modificar las propiedades de fotocatalizadores basados en óxido de titanio (óxido de titanio puro y materiales compuestos TiO_2/material) para su uso como fotocatalizadores en la fotooxidación total de propeno (un Compuesto Orgánico Volátil o "COV") así como en la reacción de descomposición del amino borano para la producción de H_2, debido al interés que presentan estas reacciónes para paliar los problemas medioambientales que existen en la sociedad actual.
- Sintetizar y estudiar titanosilicatos como soporte de metales de transición, principalmente níquel, para su aplicación en la reacción de epoxidación de propileno debido al gran interés industrial que esta presenta.
- Incorporar un fotocatalizador comercial (óxido de titanio, P25) en el interior de conducciones de tamaño micrométrico y así obtener microrreactores con los que se ha estudiado la reacción de fotooxidación total de propeno.

0.3 Estructura de la Tesis Doctoral

El contenido de esta Tesis Doctoral se ha divido en diferentes capítulos de acuerdo con su objetivo principal.

En el **Capítulo 1** se realiza una introducción general donde se describen los temas de investigación científica que se han abordado en la presente tesis. Con esta finalidad, se introduce muy brevemente la catálisis y su aporte a la sociedad. Además se comenta la catálisis heterogénea, más concretamente la fotocatálisis heterogénea, abordando el diseño de materiales como los fototocalizadores (centrándose en el semiconductor óxido de titanio o TiO_2), materiales compuestos, soporte de catalizadores y titanosilicatos. También se describe el creciente interés de la comunidad científica en la inmovilización de los catalizadores en distintos soportes y en reactores, centrándose en la inmovilización del fotocatalizador óxido de titanio en reactores, concretamente en microrreactores. Finalmente, se describen brevemente las reacciones catalíticas de interés medioambiental y para la industria (oxidación fotocatalítica de propeno, oxidación selectiva de propileno y producción de H_2) que se han utilizado para realizar los ensayos la actividad de los catalizadores y fotocatalizadores diseñados en esta tesis.

En el **Capítulo 2** se presentan las diferentes técnicas usadas para llevar a cabo la caracterización físico-química de las muestras estudiadas en la presente Tesis Doctoral. Las técnicas empleadas son las siguientes: Difracción de Rayos X, Espectrometría Ultravioleta-Visible, Adsorción Física de Gases, Microscopía Óptica, Microscopía Electrónica de Barrido, Microscopía Electrónica de Transmisión, Espectroscopia de Fluorescencia de Rayos X con análisis por Dispersión de Energía, Espectroscopia Fotoelectrónica de Rayos X, Espectroscopia Infrarroja por Transformada de Fourier, Fotoluminiscencia, Termogravimetría y Desorción a Temperatura Programada. Además, se describe la Cromatografía de Gases y la Espectrometría de Masas debido que en la presente Tesis se usan como técnicas de análisis durante los ensayos catalíticos. Por otro lado, también se incluyen las condiciones usadas para llevar a cabo los distintos ensayos catalíticos estudiados en la presente Tesis (oxidación fotocatalítica de propeno en fase gas, oxidación selectiva de propileno en fase gas y la descomposición fotocatalítica del amino borano en fase líquida).

En los **Capítulos 3, 4 y 5** se desarrollan, sintetizan y estudian fotocatalizadores basados en óxido de titanio, concretamente óxido de titanio puro (TiO_2) y materiales compuestos (TiO_2/material), para su uso como fotocatalizadores en aplicaciones medioambientales (fotooxidacion total de propeno como "COV" modelo).

Concretamente en el **Capítulo 3** se desarrolla una metodología para sintetizar un óxido de titanio que presenta una porosidad jerárquica (micro-, meso- y macroporosidad) y elevada estabilidad térmica para su aplicación como fotocatalizador en la eliminación de propeno en fase gas, obteniendo unos resultados

de conversión ligeramente superiores al óxido de titanio comercial (P25). Estos resultados han dado lugar a la siguiente publicación científica:

-J. Fernández-Catalá, L. Cano-Casanova, M.A. Lillo-Ródenas, A. Berenguer-Murcia, D. Cazorla-Amorós, Molecules 22 (2017) 2243.

En el **Capítulo 4** se describe y estudia la encapsulación de un óxido de titatanio comercial (P25) en distintas sílices (sílice con porosidad jerárquica, sílice MCM-41 y una sílice precipitada) para su aplicación en la eliminación de propeno continuando con el trabajo realizado en el capítulo anterior. Estos resultados han dado lugar a la siguiente publicación científica:

- J. Fernández-Catalá, A. Berenguer-Murcia, D. Cazorla-Amorós, Appl. Catal. A-Gen. 564 (2018) 123-132.

Continuando con los estudios descritos en los capítulos anteriores (3 y 4) en el **Capítulo 5** se describe y estudia el efecto de incorporar nanotubos de carbono de pared múltiple (MWCNT) en el medio de reacción de la síntesis del óxido de titanio que se describe en el Capítulo 3, mostrando el efecto de la dispersión, del área superficial activa ("active surface area", ASA) y de los grupos oxigenados superficiales de los MWCNT, en las propiedades de los materiales compuestos (TiO_2-MWCNT) para su aplicación en la eliminación de propeno

En el **Capítulo 6** se presenta y describe la impregnación con nanopartículas de níquel sobre un titanosilicato, descrito previamente por nuestro grupo de investigación, obteniendo un catalizador que presenta unas propiedades catalíticas muy interesantes para la oxidación selectiva de propileno. Estos valores son similares a los catalizadores basados en oro, siendo estos últimos los más interesantes para esta aplicación con la ventaja de usar un metal de transición como el níquel. Los resultados presentados en este capítulo han sido enviados a la revista ACS Catalysis y han dado lugar a una solicitud de patente.

- J. García-Aguilar, J. Fernández-Catalá, J. Juan-Juan, I. Such-Basáñez, L.E. Chinchilla, J.J. Calvino-Gámez, D. Cazorla-Amorós, Á. Berenguer-Murcia. ACS Catal. Envíado para publicación

- J. García-Aguilar, J. Fernández-Catalá, Á. Berenguer-Murcia, D. Cazorla-Amorós, Catalizadores basados en Ni sobre soportes inorgánicos y su uso en la oxidación selectiva de propileno en fase gas. Nº de solicitud: P201930310. País de prioridad: España

En el **Capítulo 7** se estudia el uso de diferentes metales para soportarlos en el material TiO_2-MWCNT, descrito en el Capítulo 5, para obtener el sistema catalítico Metal/TiO_2-MWCNT. Este sistema catalítico se estudia en la descomposición de amino borano para la producción de Hidrógeno. Los resultados presentados en este capítulo han sido enviados a la revista Catalysis Today:

- J. Fernández-Catalá, M. Navlani-García, P. Verma, Á. Berenguer-Murcia, K. Mori, Y. Kuwahara, H. Yamashita, D. Cazorla-Amorós, Catal. Today. Envíado para publicación.

En los **Capítulos 8 y 9** se desarrolla y estudia la incorporación y el relleno de óxido de titanio en diferentes microrreactores (microcapilares y reactores de chip para microfluídica) para aplicaciones medioambientales (fotooxidación total de propeno), siguiendo con los estudios de descontaminación medioambiental desarrollados en los Capítulos 3,4 y 5.

En el **Capítulo 8** se presenta una metodología sencilla de inmovilización de un fotocatalizador comercial (P25) en el interior de un microrreactor (microcapilar) para su aplicación en la fotooxidación de propeno. El sistema presenta una actividad catalítica por mol de fotocatalizador superior a la del mismo catalizador en polvo (reactor convencional); además, el sistema presenta una caída de presión baja, siendo este uno de los principales inconvenientes de usar esta tecnología en fase gaseosa. Estos resultados han dado lugar a la siguiente publicación científica:

- J. Fernández-Catalá, A. Berenguer-Murcia, D. Cazorla-Amorós, Materials 11 (2018) 1149.

En el **Capítulo 9** se presenta un fotomicrorreactor (reactores de chip para microfluídica) iluminado con luz LED de baja potencia como un sistema eficiente para la fotooxidación total de propeno. Este sistema consiste en inmovilizar un fotocatalizador comercial (óxido de titanio, P25) en el interior de los canales de un reactor de chip para microfluídica, utilizando la misma metodología descrita en el Capítulo 8. Además, se compara la actividad catalítica obtenida por este fotomicrorreactor (reactores de chip para microfluídica) con el fotomicrocapilar (Capítulo 8) y el catalizador en forma de polvo en un rector convencional (Capítulo 3). Estos resultados han dado lugar a la siguiente publicación científica:

- J. Fernández-Catalá, G. Garrigós-Pastor, Á. Berenguer-Murcia, D. Cazorla-Amorós, J. Environ. Chem. Eng. 7 (2019) 103408.

Finalmente, en el **Capítulo 10** se presentan las conclusiones más relevantes de la presente Tesis Doctoral.

Capítulo 1

Introducción

En el presente Capítulo se ha realizado una breve introducción de los temas que se han abordado y desarrollado en esta Tesis. En este aspecto, se ha introducido muy brevemente la catálisis y su aporte a la sociedad. Esta introducción se ha centrado en la catálisis heterogénea, más concretamente en la fotocatálisis heterogénea, ya que es un tema de interés para la sociedad y concretamente es un tema de interés en la presente Tesis, y en el estudio de distintos fotocatalizadores para distintas aplicaciones, principalmente medioambientales. Así, también se ha abordado el diseño de materiales como los fototocalizadores, materiales compuestos, soporte de catalizadores y titanosilicatos centrándose en el semiconductor óxido de titanio (TiO_2). En esta introducción también se ha tratado la inmovilización de catalizadores en distintos soportes y en reactores, concretamente en la inmovilización del fotocatalizador óxido de titanio en reactores y en microrreactores, además de estudiar el efecto de la configuración de los distintos reactores (reactor convencional y microrreactor) en la aplicación de los catalizadores. Para finalizar se han descrito brevemente las reacciones catalíticas de interés medioambiental y para la industria (oxidación fotocatalítica de propeno, oxidación selectiva de propileno y producción de H_2) que se han utilizado para realizar los ensayos la actividad catalítica de los catalizadores y fotocatalizadores diseñados en esta Tesis y así analizar su aplicabilidad.

1.1. Catálisis

Una de las primeras definiciones de la catálisis fue acuñada por Jons Jacob Berzelius a partir de sus numerosas experiencias y observaciones obtenidas de las transformaciones químicas. En la Edad Media los alquimistas se referían a las trasformaciones químicas, como "transformaciones mágicas". Fue en 1836 cuando Berzelius describió la catálisis como sigue: "Esta nueva fuerza, desconocida hasta ahora, es común en la naturaleza orgánica e inorgánica. No creo que esta sea una fuerza completamente independiente de las afinidades electroquímicas de la materia. Creo, por el contrario, que es solo una nueva manifestación, pero como no podemos ver su conexión y dependencia mutua, será más fácil designarla con un nombre diferente. Llamaré a esta fuerza como fuerza catalítica" [1,2].

En la actualidad la IUPAC ("International Union of Pure and Applied Chemistry") define la "catálisis" como la acción de un catalizador y a su vez define "catalizador" como una sustancia que aumenta la velocidad de una reacción sin modificar el cambio de energía estándar total de Gibbs en la reacción. Además, el catalizador no debe comportarse ni como un reactivo ni como un producto, por lo tanto no debe aparecer en la ecuación global de una reacción química [3,4]. Debido a esta definición los catalizadores presentan un gran interés para los procesos químicos actuales y de futuro, ya que estas sustancias, que no deberían sufrir ningún cambio tras su utilización en un proceso, aumentan la velocidad de reacción respecto a la misma reacción sin catalizador, afectando únicamente a la cinética de la reacción sin modificar la termodinámica [5,6]. El catalizador puede aumentar la velocidad de reacción de los procesos, debido que proporciona nuevas rutas o caminos que tienen una menor energía libre de Gibbs de activación. Además, por definición el catalizador no puede afectar a la energía libre Gibbs de la reacción global debido que esta es una función de estado (Fig .1.1) [7].

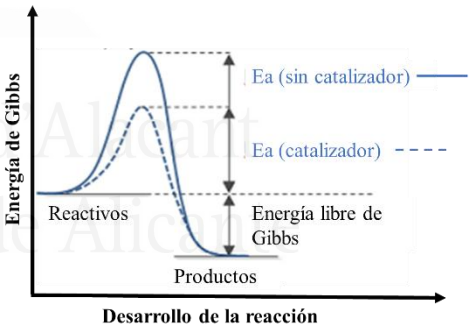

Figura 1.1. Representación esquemática de la energía de una reacción sin catalizar y catalizada [7].

En la actualidad la sociedad tiene muy presente el uso de catalizadores para diversas aplicaciones, por ejemplo, en la química industrial (proceso Haber-Bosch) [8] y en la química medioambiental (purificación de agua y aire) [9]. Sin embargo, la catálisis va mucho más allá de estas aplicaciones y usos ya que está presente en la propia naturaleza, debido a que los seres vivos sobreviven gracias al desarrollo de millones de reacciones químicas en las que intervienen catalizadores, denominados enzimas [10,11]. Además, hay que destacar que las enzimas son los catalizadores más selectivos y activos conocidos hasta la fecha. Por ello, la industria y la comunidad científica buscan diseñar catalizadores con una alta eficiencia catalítica, elevado

tiempo de vida, selectividad y bajo coste (material y energético) para que los catalizadores diseñados sean competitivos y útiles para diversas reacciones químicas con numerosas aplicaciones que mejoren el bienestar de la sociedad, como hacen las enzimas en la naturaleza [12-14].

En los distintos procesos catalíticos existentes, tanto a nivel natural, medioambiental o industrial, pueden existir distintos tipos de catálisis. La IUPAC establece que existen dos tipos principales de catálisis (catálisis homogénea y heterogénea) dependiendo de la fase en que ocurre la reacción y la fase en la que esté presente el catalizador. Se habla de catálisis homogénea cuando solo hay una fase involucrada en la reacción y de catálisis heterogénea cuando la reacción ocurre en o cerca de una interfase [4]. Debido a que en la presente Tesis nos centraremos en la catálisis heterogénea, a continuación se procede a describir brevemente su fundamento, así como la relevancia de esta en la sociedad actual.

La catálisis heterogénea presenta un gran interés industrial y en la comunidad científica, debido a sus ventajas, entre las cuales destacan la fácil separación del catalizador de los reactivos y de los productos, además de ser posible regenerar el catalizador sólido de una forma sencilla [15]. La investigación en catálisis heterogénea comenzó a principios de 1800, siendo Faraday el investigador pionero en esta área de investigación. Sus investigaciones se centraban en el estudio de las reacciones de oxidación catalizadas con platino [16]. Hoy en día, la catálisis heterogénea se ha estudiado y se aplica en diversos campos, por ejemplo en la eliminación de contaminantes en los automóviles o en diversas reacciones químicas de aplicación industrial, entre otras muchas más aplicaciones [14,17]. Con el objetivo de hacer los procesos catalíticos lo más adecuados posibles para su aplicación concreta, se requiere que los catalizadores presenten una elevada actividad catalítica y selectividad. Esto se puede lograr mediante el diseño de los catalizadores. Para este fin los catalizadores deben presentar de forma general las siguientes propiedades: elevada área superficial y porosidad, la fase activa debe estar en la superficie, capacidad de quimisorción/desorción y una buena capacidad de migración superficial [7,18].

Para poder entender la relevancia que presenta la catálisis heterogénea y su funcionamiento, hay que destacar que este proceso es un fenómeno superficial. También hay que mencionar que en el proceso de catálisis heterogénea hay involucrados procesos relacionados con la difusión de reactivos y productos en el medio de reacción y en el catalizador. Por lo tanto, en un ciclo catalítico ocurren diferentes etapas o procesos que suceden en el catalizador o en su periferia y afectan a la actividad catalítica [16,18]. Las etapas generales que existen en un ciclo catalítico se citan a continuación: (1) difusión externa de reactivos (2) difusión interna (dentro de los poros del catalizador) para acercarse a los sitios activos del catalizador, (3) adsorción de reactivos en los sitios activos, (4) reacción en la superficie del catalizador, (5) desorción de productos de los sitios activos del catalizador,

(6) difusión interna de los productos por la porosidad del catalizador y (7) difusión externa de los productos (Fig. 1.2).

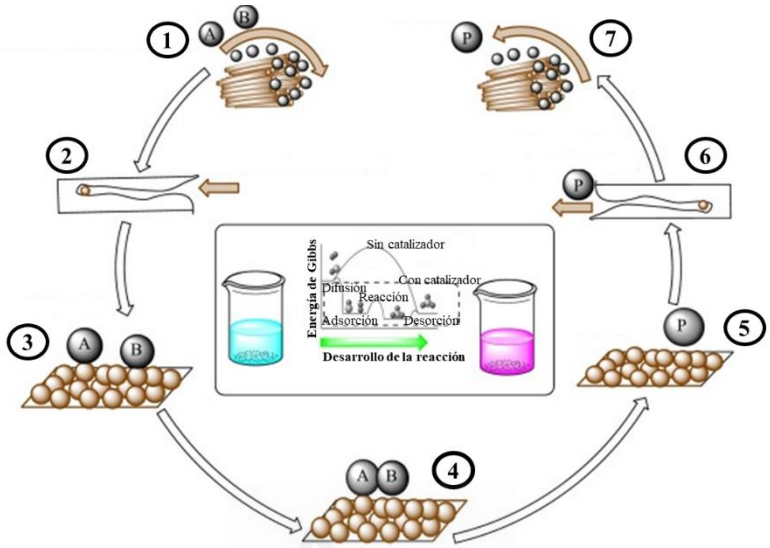

Figura 1.2. Esquema de un ciclo catalítico y la energía asociada al mismo. Figura adaptada del libro "Industrial Catalytic Processes for Fine and Specialty Chemicals" Capítulo 3 [16].

A lo largo de esta sección se ha comentado que generalmente el catalizador proporciona etapas o caminos de reacción alternativos a la reacción sin catalizador proporcionando menores energías de activación globales y, por lo tanto, aumentando la velocidad de reacción (Fig. 1.2). Sin embargo, un factor a tener en cuenta en la catálisis heterogénea es que el catalizador no debe presentar problemas difusionales, tanto en la difusión interna o externa ya que no se aprovecharía al máximo la eficiencia del catalizador [18,19].

Debido a los problemas asociados a la difusión de reactivos y a otros problemas asociados a los catalizadores (estabilidad, vida útil, y cambios en la actividad y selectividad, entre otros), en la preparación de catalizadores y la aplicación de estos materiales es muy interesante no solo estudiar y tener en cuenta las propiedades catalíticas de la fase activa, sino que es importante conocer todas las etapas del ciclo catalítico con la finalidad de aumentar la eficiencia del proceso (reactor, propiedades texturales del catalizador y soportes, entre otros aspectos) [19].

Con lo comentado en esta sección, en la presente Tesis se prepararán catalizadores y fotocatalizadores heterogéneos haciendo hincapié en el estudio de la fase activa basada principalmente en óxido de titanio (fotocatalizador), titanio presente como especies aisladas (titanosilicatos) y metales de transición (Ni, Cu y Co). Además, se estudiarán diversas propiedades de los catalizadores heterogéneos tales como la porosidad en los materiales y la interacción con distintos materiales (síntesis de materiales compuestos) y metales. También se estudiará el efecto del reactor centrándose en el estudio de microrreactores.

1.2. Fotocatálisis Heterogénea

La IUPAC en la actualidad define la fotocatálisis como el cambio en la velocidad de una reacción química o su inicio bajo la acción de la radiación ultravioleta, visible o infrarroja en presencia de una sustancia (fotocatalizador) que absorbe la luz y participa en la transformación química de los reactivos involucrados en la reacción [20]. Dicho en otras palabras, el proceso de fotocatálisis heterogénea se basa en la excitación de una sustancia (generalmente un semiconductor) mediante la absorción de luz que favorezca la generación de un par electrón-hueco (e^--h^+) y que, por tanto, presente un elevado potencial oxidante y reductor, de tal forma que a su vez produzca cambios en la estructura química de los reactivos y, por lo tanto, active su reacción [21,22]. En la actualidad, la fotocatálisis heterogénea está considerada como una alternativa viable a las tecnologías tradicionales de descontaminación biológica, química y física para el agua y el aire, debido a sus ventajas como la ausencia de selectividad y toxicidad, la posibilidad de eliminación total de contaminantes y subproductos, así como su rentabilidad [23].

Con la finalidad de entender las ventajas de la fotocatálisis hay que considerar el mecanismo de fotocatálisis que generalmente se puede explicar siguiendo el esquema de la Fig. 1.3 [24,25]. Inicialmente un fotón con energía igual o mayor que la de la banda de energía prohibida del semiconductor o "band gap" (E_g) es absorbido por el semiconductor. Entonces un electrón fotoexcitado (e^-) promociona de la banda de valencia (BV) llena a la banda de conducción (BC) vacía. Este efecto genera la formación de un hueco (h^+) en la BV de tal manera que se forma un par electrón-hueco (e^--h^+). El e^- y el h^+ generados pueden recombinarse en la superficie o en el seno del fotocatalizador rápidamente y así disminuir su actividad fotocatalítica o, por otro lado, pueden migrar a la superficie del semiconductor e iniciar la reacción redox con las especies adsorbidas en la superficie del fotocatalizador. Los huecos generados pueden inducir procesos de oxidación y los electrones procesos de reducción [26,27]. Estos procesos de reducción y oxidación transcurren generalmente mediante la formación de radicales.

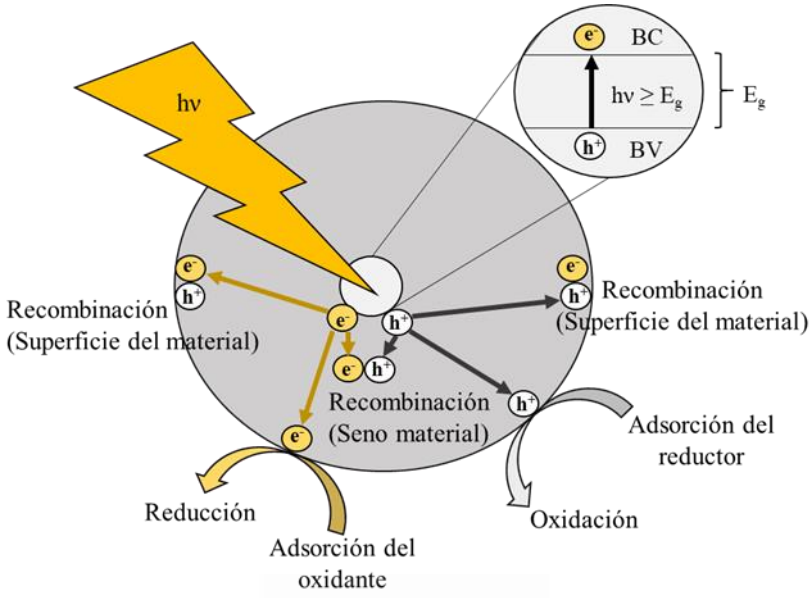

Figura 1.3. Esquema del proceso de la fotocatálisis que ocurre en un semiconductor [24].

En esta sección también se explicará la fotooxidación de compuestos orgánicos a través de la utilización de moléculas de oxígeno y la generación de radicales libres ($O_2^{\bullet-}$ y $OH^{\bullet}$) que participan en las reacciones de oxidación usando fotocatalizadores. Esta es una de las reacciones más estudiadas por la comunidad científica ya que estos compuestos orgánicos son perjudiciales para el medio ambiente y la salud humana [25,28]. El proceso de oxidación del compuesto orgánico que sucede en la superficie del fotocatalizador, se puede describir de la siguiente forma [29,30]: el e^- generado en el semiconductor debido a su iluminación reacciona con el O_2 adsorbido en la superficie del fotocatalizador y forma el anión superóxido (ec. 1.1), el h^+ también generado reacciona con los grupos -OH de la superficie del fotocatalizador generando el radical hidroxilo (ec. 1.2), además estos radicales hidroxilos se pueden formar por interacción de un h^+ con una molécula de agua (ec. 1.3) o por combinación del anión superóxido con un e^- y dos H^+ (ec. 1.4). Finalmente, el compuesto orgánico se oxidará directamente con los radicales hidroxilos (ec. 1.5) o por contacto indirecto con el catalizador, con lo que el reactivo adsorbido en forma radicalaria puede aceptar un hueco y descomponerse (ec. 1.6).

$$(O_2)_{ads} + e^- \rightarrow O_2^{\bullet -}{}_{ads} \quad (1.1)$$

$$OH_{superficial} + h^+ \rightarrow OH^{\bullet}{}_{superficial} \quad (1.2)$$

$$H_2O_{ads} + h^+ \rightarrow OH^{\bullet}{}_{ads} + H^+ \quad (1.3)$$

$$2H^+ + h^+ + O_2^{\bullet -}{}_{ads} \rightarrow H_2O_2 + 2OH^{\bullet}{}_{ads} \quad (1.4)$$

$$R\text{-}H_{ads} + OH^{\bullet}{}_{ads} \rightarrow R^{\bullet}{}_{ads} + H_2O \quad (1.5)$$

$$R^{\bullet}{}_{ads} + h^+ \rightarrow R^{\bullet +}{}_{ads} \rightarrow CO_2 + H_2O \quad (1.6)$$

A partir de las reacciones secundarías comentadas, la reacción global de la fotocatálisis heterogénea (ec. 1.7) usando un catalizador se indica a continuación:

$$\text{Contaminante orgánico} + O_2 \xrightarrow{\text{fotocatalízador + hv}} CO_2 + H_2O \quad (1.7)$$

Existen diversas propiedades del catalizador que se pueden modificar o mejorar con el objetivo de aumentar la eficiencia catalítica del fotocatalizador en sus distintas aplicaciones [31-33]. A continuación, se describen ciertas propiedades interesantes de los catalizadores para el proceso de fotocatálisis:

- Elevada área superficial del catalizador, debido a que el proceso de adsorción presenta una gran importancia en el proceso global porque las reacciones fotocatalíticas se originan en la interfase [34].

- Estructura cristalina apropiada, ya que las fases cristalinas, la presencia de defectos y el tamaño de cristal del catalizador influyen en la producción y el tiempo de vida de los pares e^--h^+, siendo estos fundamentales en el mecanismo de fotocatálisis (Fig. 1.3) [35,36].

- Química superficial adecuada, siendo interesante que los fotocatalizadores presenten grupos ácidos en superficie o grupos -OH ya que juegan un papel relevante en la eficiencia del proceso fotocatalítico [37,38].

- Una energía de banda prohibida del semiconductor y un potencial redox de los adsorbatos apropiados para que se lleve a cabo la reacción. Profundizando en esta propiedad, hay que entender que el nivel de energía inferior de la banda de conducción es el potencial de reducción de los electrones generados, mientras que el nivel de energía superior de la banda de valencia es la capacidad oxidante de los huecos generados. Por lo tanto, el semiconductor adecuado debe tener una energía de banda prohibida lo suficientemente grande como para proporcionar electrones y huecos con una energía grande para poder reaccionar con los reactivos, así como ser lo suficientemente pequeña (E_g) para que pueda presentar una eficiente absorción en el del espectro solar [39]. Con esta propiedad en mente, la Fig. 1.4 muestra la energía de banda prohibida de varios semiconductores y los potenciales redox estándar de distintas sustancias. En la Fig. 1.4 se observa que el dióxido de titanio es un semiconductor adecuado para ser utilizado como fotocatalizador ya que su E_g o "band

gap" es adecuado para generar los radicales superóxido e hidróxilo, siendo estos radicales fundamentales para el proceso de fotocatálisis [40].

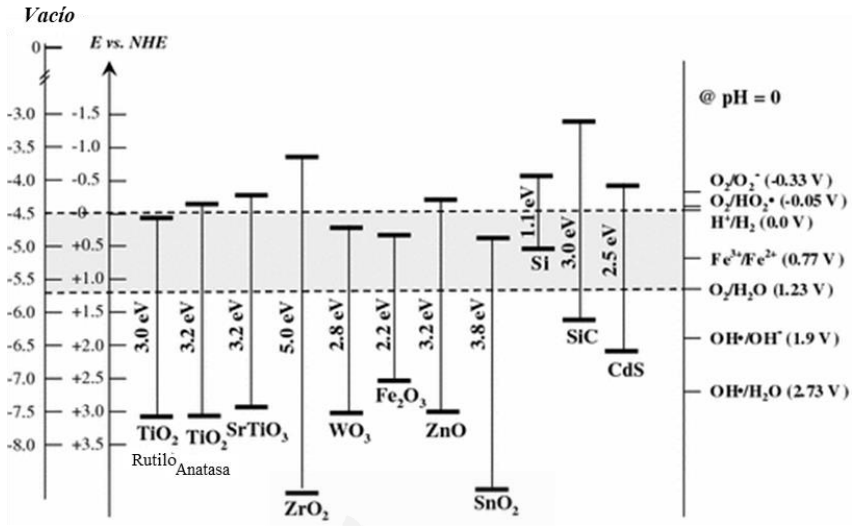

Figura 1.4. Energías de la banda prohibida y posición de las bandas de conducción y de valencia de diferentes semiconductores, juntos con los potenciales redox de algunas especies [40].

Otros factores a la hora de estudiar la actividad catalítica de los fotocalizadores, diferentes a las características y propiedades del semiconductor, son la longitud de onda e intensidad de la luz con la cual se ilumina el fotocatalizador, la cantidad de catalizador, la concentración inicial del contaminante, la temperatura y el diseño y tipo del reactor fotocatalítico con el objetivo de obtener una elevada eficiencia global del proceso [41,42].

Con lo comentado anteriormente y conociendo las características que necesita un material para ser aplicado como fotocatalizador, el estudio del óxido de titanio presenta un gran interés debido a las propiedades que presenta este semiconductor como se expondrá en la siguiente sección, además en la sección 1.4 se tratará la inmovilización e incorporación del óxido de titanio en sustratos y reactores.

1.3. Óxido de Titanio

El óxido de titanio (TiO_2) aunque se pudiera considerar un semiconductor intrínseco presenta comportamiento de semiconductor extrínseco tipo n, debido a que los defectos que existen en el material, en este caso vacantes de oxígeno (TiO_{2-x}), son compensadas por la adopción del estado de oxidación +3 por un número equivalente de átomos de titanio y estos iones Ti^{3+} actúan como dador de electrones. Además, este material es abundante en la naturaleza, barato, químicamente estable y altamente resistente a la corrosión foto-inducida. Estas características interesantes le permiten ser utilizado en multitud de aplicaciones como, por ejemplo, pigmento inorgánico, fotocatalizador, protector solar o en almacenamiento de energía, entre otras [43,44].

En la naturaleza el TiO_2 está presente en tres fases cristalinas, siendo estas fases la anatasa (estructura tetragonal centrada en el cuerpo), brookita (estructura ortorrómbica) y rutilo (estructura tetragonal). En las tres fases los átomos de titanio (Ti^{4+}) están coordinados con seis átomos de oxígeno (O^{2-}) formando octaedros de TiO_6 (Fig. 1.5) [45,46]. La fase rutilo es la más estable termodinámicamente, siendo las fases anatasa y brookita dos fases metaestables. Por lo tanto, el óxido de titanio con fase anatasa y brookita pueden transformarse a fase rutilo con el aumento de temperatura. Generalmente esta transición de fase ocurre en torno a los 600 ºC. La temperatura a la que se producen estas transformaciones varía en función del tamaño de partícula del TiO_2 [47].

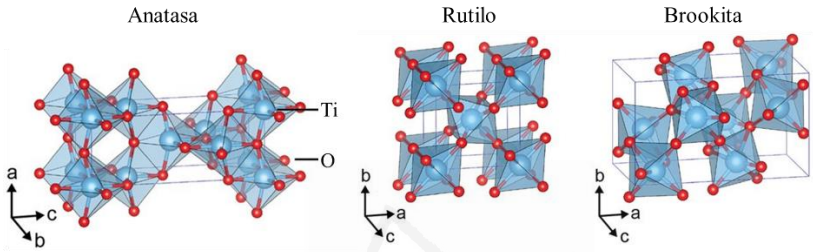

Figura 1.5. Estructuras de las fases cristalinas del TiO_2 (Anatasa, rutilo y brookita) [48].

Hoy en día existen diversas formas de sintetizar el óxido de titanio, aunque estos procedimientos de síntesis suelen utilizar temperaturas elevadas por lo que se obtiene principalmente TiO_2 con fase rutilo y tamaño de cristal grande. Debido a la relevancia de este compuesto se puede encontrar comercialmente. En este sentido, un TiO_2 comercial muy utilizado para diversas aplicaciones entre ellas la (foto)catálisis, es la llamada P25 (Degussa) debido a su alta elevada fotoactividad en la descomposición de compuestos orgánicos. Este material comercial se sintetiza mediante la hidrólisis del tetracloruro de titanio ($TiCl_4$) en presencia de hidrógeno y oxígeno a una temperatura superior a 1000 ºC (ec. 1.8) [49].

$$TiCl_4 + 2\ H_2 + O_2 \rightarrow TiO_2 + 4\ HCl \qquad (1.8)$$

Debido a las altas temperaturas de síntesis, el TiO_2 obtenido es una mezcla de fases entre anatasa (70 %) y rutilo (30 %). Sus propiedades más relevantes son que presenta un tamaño de cristal entre 20-50 nm, un área superficial de alrededor de 50 m^2/g y el ancho de banda prohibido (Eg) es de 3.1 eV [50]. Estas características hacen que el material comercial P25 sea muy interesante para su aplicación como fotocatalizador siendo este un material de referencia para comparar nuevos fotocatalizadores debido su alta actividad fotocatalítica [51,52]. Sin embargo, este material presenta una baja área superficial, una baja absorción de luz visible y una elevada recombinación de los pares electrón-hueco [44]. Estos inconvenientes hacen que la comunidad científica en la actualidad continúe estudiando la mejora de las propiedades del óxido de titanio mediante el desarrollo de nuevas metodologías de síntesis [53].

En la actualidad existen diversos métodos de síntesis de TiO_2, como por ejemplo depósito físico en fase vapor, síntesis hidrotermal, craqueo químico en fase vapor, métodos de precipitación y sol-gel, entre otros [54]. Entre estos métodos de síntesis, la metodología sol-gel presenta un gran interés debido a su simplicidad, bajo coste, bajas temperaturas, buen control sobre el tamaño de partícula obtenido, y la gran pureza y homogeneidad de los productos obtenidos [55]. El método sol-gel se fundamenta en reacciones de polimerización inorgánica incluyendo cuatro etapas, la hidrólisis, la policondensación, el secado y la descomposición térmica. La hidrólisis de los precursores (metálicos o no metálicos, generalmente alcóxidos) tiene lugar con agua o alcoholes, pudiéndose catalizar esta reacción usando un ácido o una base. Después de la formación del gel, se elimina el disolvente y luego se calcina el material para descomponer los restos del precursor orgánico. El esquema del proceso sol-gel para la síntesis de TiO_2 se muestra en la Fig. 1.6 [56,57].

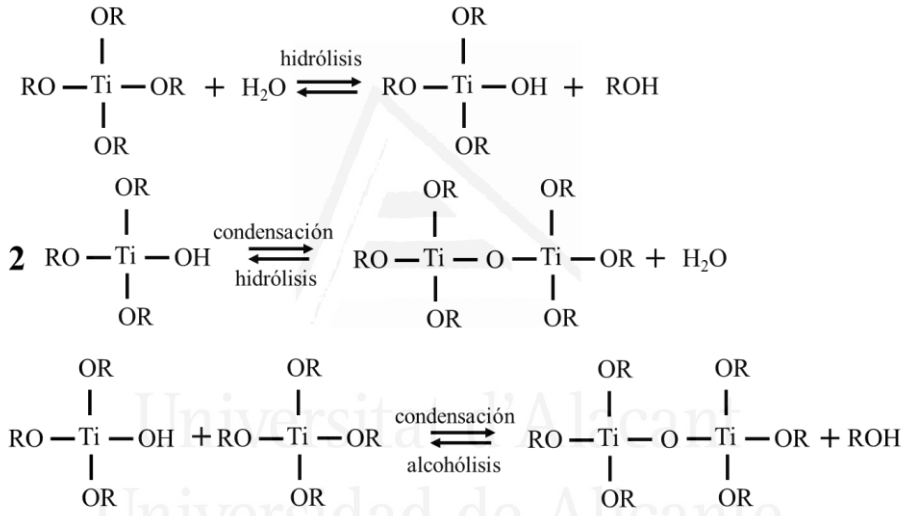

Figura 1.6. Reacciones presentes en la síntesis del óxido de titanio en el método sol-gel [56,57].

Con esta metodología (sol-gel) se puede obtener TiO_2 con fase anatasa de elevada área superficial (200 m^2/g) y tamaño de cristal pequeño que favorecen que el TiO_2 pueda ser utilizado en distintas aplicaciones y en especial como fotocatalizador o soporte de catalizadores [55].

Otra metodología interesante para la fabricación de TiO_2 es la síntesis solvotermal o hidrotermal [54], esta metodología se define como una síntesis donde suceden reacciones químicas de sustancias en una disolución acuosa o disolvente orgánico en un recipiente sellado y calentado a una temperatura entre 100 y 1000 ºC y a una presión entre 1 y 100 MPa. Estas reacciones generalmente se llevan a cabo en una autoclave en condiciones subcríticas o supercríticas del disolvente [58]. La síntesis hidrotermal presenta una serie de ventajas, entre las que destacan condiciones de funcionamiento relativamente suaves (temperaturas de reacción <300°C),

procedimiento sintético de un solo paso y buena dispersión en disolución. Además, la síntesis hidrotermal es económica en términos de instrumentación, energía y precursores de materiales en comparación con otros métodos de síntesis en disolución. Sin embargo, la síntesis hidrotermal o solvotermal en comparación con el método sol-gel, descrito anteriormente, es un método más complejo debido a que usa temperaturas y presiones más elevadas, además de usar disolventes orgánicos respecto a la síntesis sol-gel.

Otra forma muy interesante de sintetizar el óxido de titanio es unir las dos metodologías comentadas anteriormente (sol-gel e hidrotermal) [59]. Por este motivo, en la presente tesis se estudiará la síntesis de un óxido de titanio usando una síntesis sol-gel combinada con una síntesis hidrotermal.

1.3.1. Óxido de Titanio como Fotocatalizador

El óxido de titanio se puede utilizar en varias aplicaciones, como se explicó en la sección anterior, debido a sus propiedades interesantes. Una aplicación del óxido de titanio de relevancia en las últimas décadas es su uso como fotocatalizador en procesos medioambientales, producción y almacenamiento de energía, síntesis de productos químicos de interés industrial y en medicina (Fig.1.7) [60,61].

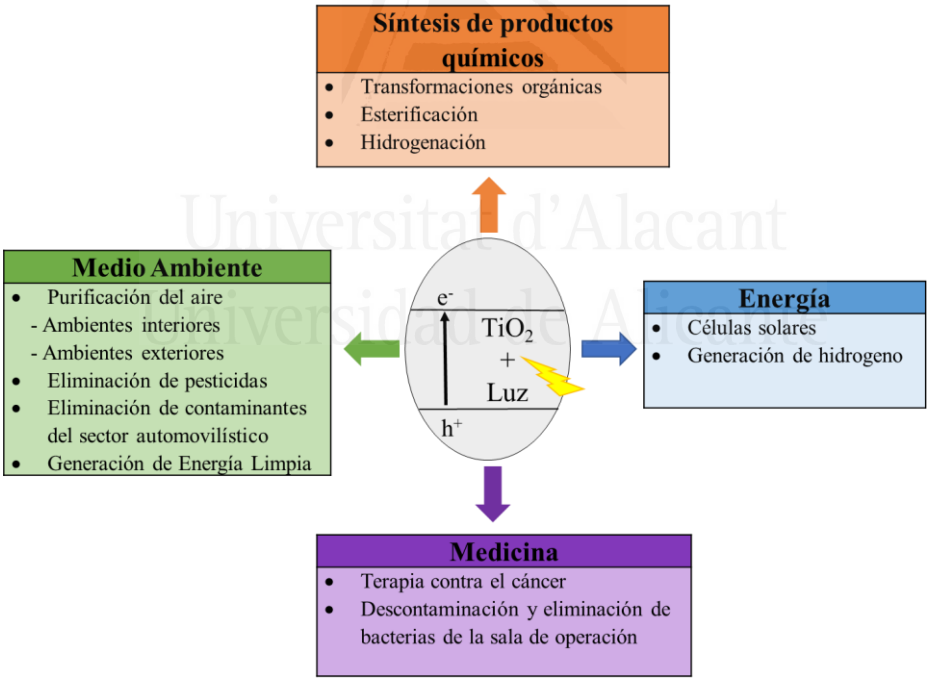

Figura 1.7. Aplicaciones del óxido de titanio como fotocatalizador.

En este sentido el TiO_2 ha sido ampliamente estudiado como fotocatalizador. En el año 1956 se publicaron una serie de artículos científicos realizados por Mashio y col. denominados "autooxidación mediante TiO_2 como fotocatalizador". Los autores dispersaron óxido de titanio en forma pulverulenta en varios disolventes orgánicos y estos fueron irradiados con luz ultravioleta (UV), observando la autooxidación de los disolventes a temperatura ambiente. Estos estudios se pueden considerar los primeros donde se publicó el efecto fotocatalítico del TiO_2 cuando se ilumina con luz UV [43,62]. Sin embargo, en esta época no hubo un gran interés hacia el uso del TiO_2 como fotocatalizador en la comunidad científica o en la industria. El auge en el estudio y, por lo tanto, de su interés dentro de la comunidad científica e industrial surgió en 1972 cuando Honda, Fujishima y col. descubrieron el efecto de la fotosensibilización de un electrodo de TiO_2 para la electrólisis del H_2O, estudio que fue publicado en la prestigiosa revista "Nature" [63]. En 1977 Bard y col. describieron por primera vez el uso del fotocatalizador TiO_2 como descontaminante medioambiental, concretamente estudiaron la eliminación de cianuro en presencia de una suspensión acuosa de óxido de titanio [64]. Este estudio favoreció que en los años 80 se realizarán varios estudios donde se demostró que el uso de TiO_2 en forma pulverulenta presentaba un gran interés como método de purificación fotocatalítica tanto en medio acuoso como para la purificación de aire [65]. Este interés por el uso del TiO_2 sigue estando presente en la actualidad, incluso a pesar de que este material presenta una serie de desventajas para su uso como fotocatalizador en aplicaciones reales, entre las que destacan una área superficial baja, baja absorción de la luz visible, agregación de las partículas, dificultad en la recuperación de las partículas y dificultad para distribuir las partículas uniformemente en el medio [61,66].

Teniendo en cuenta estos inconvenientes, la comunidad científica sigue centrándose en modificar el óxido de titanio con el objetivo de mejorar sus propiedades. Estas modificaciones se han realizado y se pueden realizar de diversas maneras, entre ellas destacan el dopaje metálico y no metálico, la sensibilización con moléculas orgánicas, la modificación de su superficie, fabricación de materiales compuestos e inmovilización y estabilización en soportes [43,67].

Concretamente en esta Tesis se estudia el efecto de modificar el TiO_2 mediante la incorporación de sustancias en la síntesis del TiO_2 puro que modifiquen sus propiedades o mediante la síntesis de materiales compuestos, por ejemplo, mediante la síntesis de materiales compuestos con TiO_2 y materiales adsorbentes.

1.3.2. Materiales Compuestos Basados en Óxido de Titanio

En los últimos años la comunidad científica ha dedicado importantes esfuerzos en mejorar las propiedades de los fotocatalizadores, como se ha comentado en la sección anterior. Una metodología interesante consiste en sintetizar materiales compuestos basados en TiO_2, con el propósito de obtener materiales que presenten un efecto sinérgico entre los distintos materiales presentes en el material compuesto y

así mejorar la actividad catalítica del óxido de titanio. Para este objetivo se pueden aplicar diferentes posibilidades: las más utilizadas son el dopado con heteroátomos (cationes metálicos o aniones no metálicos), la síntesis de materiales compuestos con otros semiconductores (ZnO, CdS, entre otros) y la síntesis de óxido de titanio con materiales adsorbentes o materiales que modifiquen sus propiedades (sílice, materiales de carbón, zeolitas, polímeros, entre otros) [68,69].

Entre los distintos métodos comentados anteriormente, en esta Tesis y por lo tanto en este apartado, nos centraremos en explicar los materiales compuestos basados en un material fotocatalizador (dióxido de titanio) y un material adsorbente, ya que el adsorbente favorece la adsorción de las moléculas a tratar, elevando la concentración superficial de estas moléculas y dirigiendo la difusión de estas hacia zonas cercanas a la fase activa (TiO_2), con lo que aumentará la actividad catalítica del dióxido de titanio (Fig. 1.8). Este concepto se denomina "Adsorb and Shuttle" [70]. Con este concepto en mente en esta sección nos centraremos en los materiales compuestos TiO_2/Ads donde los adsorbentes elegidos son la sílice o los materiales de carbón.

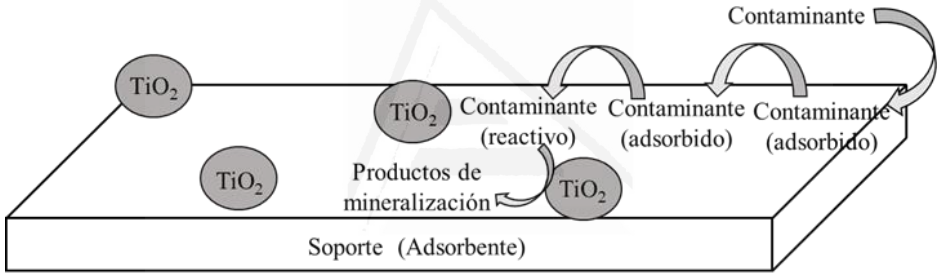

Figura 1.8. Concepto de Adsorción y transporte "Adsorb and Shuttle" [70].

- Materiales compuestos basados en óxido de titanio y sílice.

En la actualidad, los materiales compuestos TiO_2-SiO_2 presentan un gran interés, debido a las ventajas que la sílice puede aportar a las propiedades fotocatalíticas del TiO_2 en el material compuesto. Entre ellas destacan los tamaños de poro modulables (2–50 nm) y elevada área superficial, interconectividad de los poros (lo que facilita la transferencia de reactivos y productos), transparencia en un amplio intervalo de longitudes de onda del espectro UV/Vis y la presencia de una gran cantidad de grupos silanol para la modificación posterior que pueden usarse para anclar los fotocatalizadores [71-74]. Debido a las ventajas que presentan estos materiales compuestos respecto al TiO_2 original, en la presente Tesis se estudiará el efecto de la porosidad de distintas sílices en la actividad fotocatalítica de un dióxido de titanio comercial (P25).

- Materiales compuestos de óxido de titanio y materiales de carbón.

Entre los distintos materiales de carbón existentes, la presente Tesis se centrará en el uso de nanotubos de carbono para la síntesis de los materiales compuestos basados en óxido de titanio. Esta elección se debe a que los nanotubos de carbono

pueden reducir la velocidad de recombinación electrón-hueco que se produce en el óxido de titanio; además, presentan una elevada área superficial y favorecen la absorción de luz visible en los fotocatalizadores compuestos [75-78]. Por lo tanto, en esta Tesis se incorporarán nanotubos de carbono comerciales en la síntesis del óxido de titanio y se estudiará el efecto de los nanotubos de carbono en las propiedades del semiconductor y en la actividad fotocatalítica del material compuesto.

1.3.3. Óxido de Titanio como Soporte de Catalizadores

Entre los distintos usos del óxido de titanio, uno de interés para la presente Tesis es como soporte de catalizadores. El TiO_2 presenta unas excelentes propiedades para su uso como soporte de catalizadores, entre las que destacan su alta estabilidad química y térmica, además de la posibilidad de prepararse con áreas superficiales elevadas [79]. Además, se ha observado que puede existir una interacción fuerte entre la fase activa y el TiO_2, generando un incremento en la estabilidad y la actividad del catalizador.

En este sentido, la comunidad científica se está centrando en la síntesis y el estudio de catalizadores heterogéneos donde se soportan nanopartículas (NPs) metálicas (fase activa) sobre TiO_2. Como consecuencia de la interacción que existe entre las nanopartículas metálicas y el TiO_2, se produce una influencia positiva en la actividad catalítica y la selectividad del catalizador heterogéneo [43,80]. Otro factor a tener en cuenta es que el óxido de titanio puede actuar como fotocatalizador. Por lo tanto, bajo irradiación de luz el TiO_2 puede incrementar la actividad de la fase activa o actuar como fotocatalizador (Fig. 1.9).

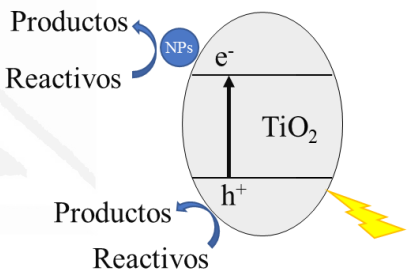

Figura 1.9. Uso del TiO_2 como soporte de catalizadores o fotocatalizador

Así, en esta Tesis se han soportado metales de transición, más económicos que los metales nobles, sobre TiO_2 y se ha estudiado su actividad catalítica teniendo en cuenta que este soporte también puede actuar en la reacción junto con el cocatalizador, debido a que el cocatalizador actúa generalmente como sitios activos para catalizar las reacciones, además de promover la separación de cargas entre el cocatalizador y el semiconductor.

1.3.4. Titanosilicatos, Ti en Sitios Aislados

En las últimas décadas los catalizadores heterogéneos donde la fase activa está diseñada en forma de sitios aislados (o en inglés “single sites”) han atraído mucho la atención tanto de la investigación académica como industrial. Este hecho se debe al descubrimiento de que la disminución del tamaño de partícula puede conducir a una

mejora significativa en la actividad catalítica [81]. Este descubrimiento dirigió a los investigadores al diseño de centros catalíticos a nivel molecular y atómico y, por lo tanto, al diseño estratégico de catalizadores con la fase activa bien dispersa en sitios aislados. Para que un catalizador pueda englobarse en esta categoría debe cumplir que cada centro activo esté aislado espacialmente sin interacciones laterales, que cada centro activo tenga la misma energía de interacción entre él y el reactivo, y que el centro activo, aunque pueda contener uno o más átomos, todos sean idénticos y con una estructura determinada [82].

Una forma interesante de obtener Ti en forma muy bien dispersa e incluso obtener Ti en sitios aislados, con la intención de que la fase activa (Ti) presente una gran actividad en la catálisis heterogénea, es mediante la síntesis de titanosilicatos (red de sílice donde se han intercambiado átomos de Si por Ti) (Fig. 1.10). Estos materiales presentan una serie de ventajas significativas sobre los catalizadores convencionales empleados en catálisis convencional y fotocatálisis, entre las que destacan elevada selectividad hacia el producto, condiciones de reacción moderadas, son hidrotermalmente estables y generan altos rendimientos del producto y conversiones del sustrato [83,84].

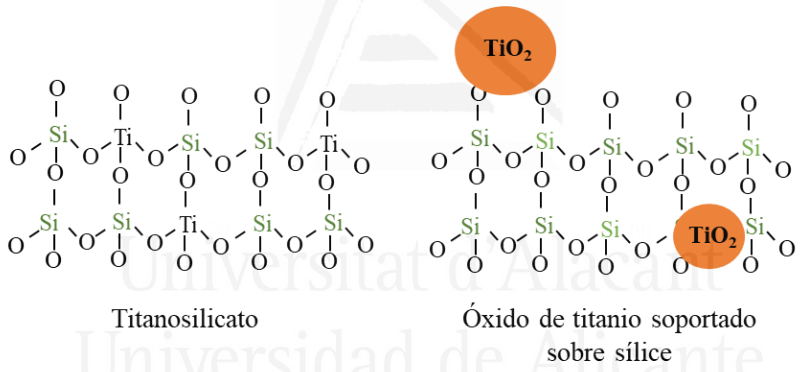

Figura 1.10. Esquema de la diferencia entre titanosilicato y óxido de titanio soportado sobre silice.

En este sentido, en la presente Tesis se usan titanosilicatos, donde el Ti está muy bien disperso, como soportes de nanoparticulas con el objetivo de disponer de dos centros activos (NPs de metal y Ti en forma de sitios activos) para favorecer la actividad catalítica de la reacción estudiada.

1.4. Inmovilización e Incorporación del Óxido de Titanio en Sustratos y Reactores

En el estudio de la fotocatálisis heterogénea, además de tener en cuenta y mejorar las propiedades del fotocatalizador, tal y como se ha ido explicando en esta introducción, hay que tener en cuenta el reactor de trabajo, la inmovilización del catalizador dentro del reactor, así como el efecto de la iluminación del catalizador presente en el reactor.

La mayoría de los estudios se centran en las propiedades de los fotocatalizadores en reactores convencionales de lecho empaquetado para fase gas y en suspensión con agitación para fase líquida, donde el TiO_2 presenta actividades catalíticas elevadas hasta el punto de que se ha llevado esta tecnología a plantas piloto. Sin embargo, esta metodología requiere de una etapa de separación de los líquidos y el sólido, que incrementa los costes del catalizador. Una alternativa sería la inmovilización del catalizador sobre un sustrato para que la etapa de separación fuera sencilla [85]. En este sentido la comunidad científica ha dedicado muchos esfuerzos para inmovilizar el catalizador en distintos sustratos como por ejemplo polímeros, cuarzo (en forma de films o recubriendo esferas), películas de carbón o en las paredes de los reactores, entre otros [86,87].

Otro factor a tener en cuenta en fotocatálisis, además de la inmovilización del catalizador en el reactor, es el efecto de la iluminación del fotocatalizador. En la actualidad la mayoría de los estudios fotoactalíticos con TiO_2 utiliza luz ultravioleta proveniente de lámparas convencionales (xenón o mercurio). Como norma general, estas lámparas presentan baja energía, poca eficiencia y poca penetración de luz, lo que provoca que la eficiencia del proceso catalítico disminuya [88]. Una alternativa a las lámparas convencionales es el uso de LED (diodos emisores de luz) como sistemas de iluminación del fotorreactor, debido a que son más eficientes [89,90].

Con lo comentado anteriormente respecto al efecto de la iluminación y el interés de incorporar e inmovilizar adecuadamente los fotocatalizadores en un reactor adecuado para mejorar la actividad catalítica del óxido de titanio, hay que destacar el uso de microreactores como una nueva tecnología interesante para su uso en fotocatalísis [91-93]. Se considera micrroreactor a un dispositivo en el que las reacciones químicas tienen lugar en un espacio reducido con dimensiones laterales inferiores a 1 mm. La forma más usual de que ocurra este confinamiento es dentro de los microcanales del reactor [94]. En este sentido, actualmente ya se encuentran numerosos estudios en la bibliografía donde se utilizan fotomicrorreactores para descontaminación ambiental en fase líquida y en síntesis orgánica. Este auge se debe a los beneficios que presentan los microrreactores respecto a los reactores convencionales de flujo continuo o discontinuo. Entre ellas destacan una elevada relación superficie-volumen, velocidades de transferencia de calor y masa optimizadas y una velocidad de reacción más alta, entre otras [95-97]. Con respecto

a la fotoquímica, otro factor importante a considerar y optimizar es la eficiencia y la homogeneidad de la irradiación de luz sobre el catalizador. En este aspecto, el uso de microrreactores es muy interesante debido a sus dimensiones pequeñas, lo que permite una mejor iluminación del catalizador respecto a reactores convencionales que presentan un mayor tamaño (Fig. 1.11).

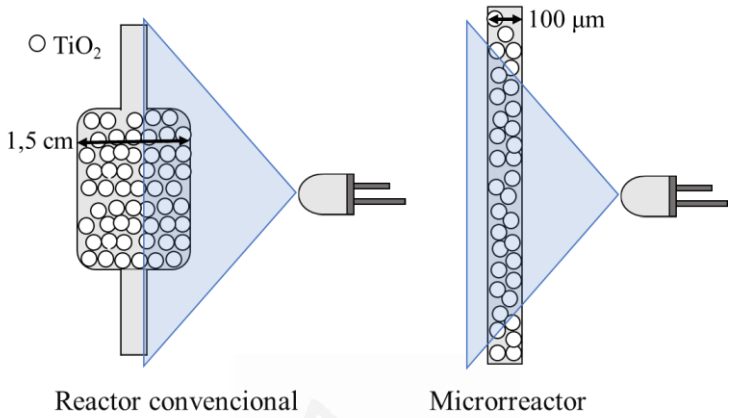

Figura 1.11. Comparación del efecto de la iluminación entre un reactor convencional y un microrreactor.

Debido al interés que presentan los microrreactores para ser usados en fotocatálisis, en esta Tesis se estudia la incorporación de la P25 (óxido de titanio comercial) en dos microrreactores (microcapilares y reactores de chip para microfluídica) en forma de lecho empaquetado y se compararán con el mismo catalizador incorporado en un reactor convencional.

1.5. Procesos Catalíticos de Interés

Esta sección se centrará en describir ciertas reacciones catalíticas de interés para la sociedad, tanto desde un punto de vista industrial como medioambiental, en las cuales se han probado los catalizadores desarrollados en la presente Tesis. Los catalizadores desarrollados han sido analizados en distintas áreas de la catálisis y la fotocatálisis, concretamente en tres áreas: descontaminación ambiental (oxidación fotocatalítica de propeno), síntesis de compuesto químicos (epoxidación del propileno) y producción de H_2 (hidrólisis del aminoborano mediante fotocatálisis).

1.5.1. Oxidación Fotocatalítica de Propeno

La eliminación de compuestos orgánicos volátiles (COVs, un grupo de compuestos químicos orgánicos con un punto de ebullición bajo a temperatura ambiente), todavía es un tema de gran interés debido a que en la actualidad se produce una gran emisión de estos contaminantes a la atmósfera. Estos compuestos se acumulan en la atmosfera, presentan alta inflamabilidad, alta toxicidad y baja biodegrabilidad, entre otros efectos, por lo que generan importantes problemas medioambientales [98]. Además, hay que tener en cuenta que la mayor concentración de COVs en la actividad human se encuentra en sistemas cerrados, por ejemplo en industrias o en hogares, debido a los productos usados en los procesos industriales, así como al uso de productos de limpieza y pinturas, entre otros [99,100].

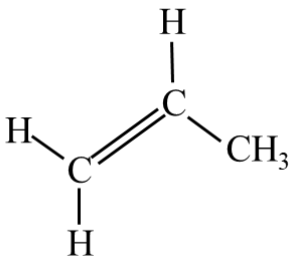

Figura 1.12. Molécula de propeno.

Entre los distintos COVs existentes, la eliminación de propeno, también denominado propileno (Fig. 1.12), presenta un gran interés porque este contaminante está involucrado en la formación del "smog" fotoquímico y está presente en el humo del tabaco. Además, este contaminante se considera una molécula prueba de COVs con bajo peso molecular [101-103].

En las últimas décadas la fotocatálisis ha surgido como una metodología alternativa para eliminar este tipo de contaminantes (COVs) debido a que puede actuar a temperatura ambiente, presión atmosférica y a concentraciones bajas, siendo esta la concentración en la cual se encuentran normalmente estos contaminantes [104]. Por estas razones, la comunidad científica ha dedicado y continúa dedicando muchos esfuerzos en desarrollar catalizadores basados en distintos semiconductores (TiO_2, ZnO, CdS…) que presenten una alta actividad en la eliminación de COVs [30,105,106]. En este sentido, el óxido de titanio (TiO_2) presenta una elevada actividad fotocatalítica para esta finalidad debido a las propiedades que se han ido comentando a lo largo de este Capítulo. Otro punto a tener en cuenta es que el óxido de titanio se puede modificar desde un punto de vista químico y del centro activo (dopando con metales o mediante la síntesis de materiales compuestos) para que presente una mejor actividad para esta reacción. Sin embargo, otro enfoque es preparar el fotocatalizador en distintas conformaciones (polvo, películas delgadas, monolitos…) o incorporar el catalizador en distintos reactores (reactores de lecho fijo, microrreactores, reactores fluidizados...) con el objetivo de mejorar la velocidad de reacción del fotocatalizador (Sección 1.3.2 y 1.4).

En esta Tesis Doctoral se han desarrollado fotocatalizadores de TiO_2 con diferentes propiedades, centrándose en su porosidad, para su uso en la fotooxidación de propeno. También se han desarrollado materiales compuestos basados en TiO_2 con

diferentes materiales (sílices y materiales de carbón) con el objetivo de mejorar las propiedades del catalizador y así aumentar la velocidad de reacción en la eliminación de propeno. Además, se comparó la actividad catalítica de la reacción de estudio, incorporando el mismo óxido de titanio comercial (P25, Degussa) en un reactor convencional de lecho fijo y en distintos microrreactores comerciales (microcapilares y reactores de chip para microfluídica).

1.5.2. Oxidación Selectiva de Propileno

En los últimos años la industria química y la comunidad científica han mostrado un interés creciente en la síntesis del epóxido de propileno (Fig. 1.13), (líquido incoloro, volátil e inflamable), debido a su alta reactividad y versatilidad para la formación de una gran variedad de productos, entre los que destacan determinados polímeros y propilenglicol [107,108]. Estas propiedades permiten su uso como prepolímero de poliuretanos y poliésteres, entre otros. Esto ha provocado un incremento continuo en la producción global del epóxido de propileno en los últimos años en las principales industrias químicas (DOW, Lyondell o BASF) estimándose que en 2020 su producción puede llegar a 13 millones de toneladas (Fig. 1.14) [109-111].

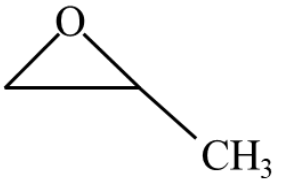

Figura 1.13. Molécula del epóxido de propileno

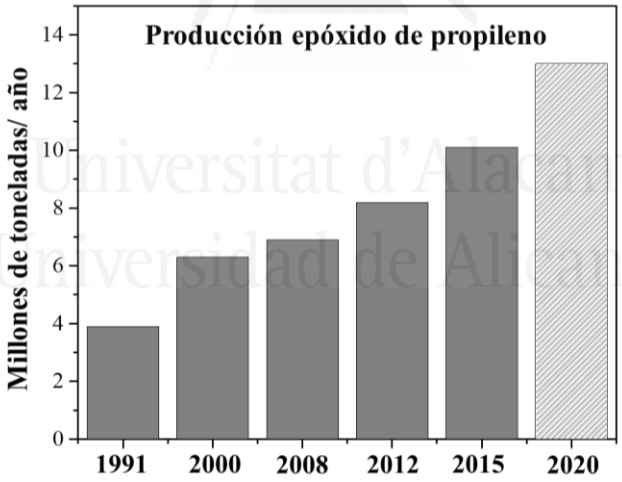

Figure 1.14. Evolución de la producción del epóxido de propileno [109].

En la actualidad, el epóxido de propileno es sintetizado industrialmente por procesos no catalíticos, los cuales destacan el proceso de clorhidrina (40% de la producción) y el proceso con hidroperóxidos orgánicos. Sin embargo, estos procesos usan reactivos peligrosos o altamente oxidantes como el Cl_2 o los peróxidos orgánicos (R-OOH), además de generar una gran cantidad de subproductos difíciles de separar [112-113]. Una alternativa al uso de los procesos mencionados anteriormente es la

oxidación selectiva de propileno usando mezclas de H_2/O_2 o O_2 y catalizadores heterogéneos, con la que solo se obtendría H_2O como subproducto [110-112].

En este sentido, la comunidad científica se ha centrado en las últimas décadas en el estudio de la producción del epóxido de propileno mediante la catálisis heterogenea en fase gaseosa y líquida. [111,114,115]. Desde que Haruta y col. demostraron que los catalizadores Au/TiO_2 (nanopartículas de oro dispersadas en TiO_2) podían realizar la reacción de epoxidación de propileno utilizando mezclas de H_2/O_2 en fase gaseosa con una selectividad hacia el epóxido elevada (95%), aunque presenten unas conversiones bajas (1%), los catalizadores basados en oro con diferentes soportes (principalmente titanosilicatos) han atraído una gran atención para este propósito debido a la producción casi insignificante de subproductos no deseados como la acroleína (Acr) o los óxidos de carbono (CO_x) [116]. Estos catalizadores basados en oro han sido desarrollados hasta alcanzar una selectividad hacía el epóxido de aproximadamente el 90% con una conversión de propeno de alrededor del 10% a temperaturas suaves utilizando una mezcla H_2/O_2 como reactivo. Estos resultados muestran que los catalizadores de titanosilicato basados en Au ($Ti\text{-}SiO_2$) son muy interesantes para la epoxidación de propileno [117,120]. Sin embargo, el uso de un metal noble (Au) presenta algunos inconvenientes, como el alto precio del catalizador, la baja eficiencia de H_2 y también la conversión relativamente baja de propileno.

Por estas razones, es crucial desarrollar nuevos catalizadores basados en metales de transición más económicos que presenten eficiencias similares a los catalizadores existentes. En este sentido la comunidad científica se ha centrado en diversos metales de transición (Cu, Fe, Co entre otros) usando diferentes oxidantes como O_2 o N_2O (de elevado poder oxidante) [121-124]. Sin embargo, ningún catalizador encontrado en la bibliografía presenta selectividades tan elevadas como los catalizadores basados en Au, aunque sí presentan valores de conversión de propileno más elevadas consiguiendo alcanzar valores de rendimiento o de generación de epóxido similares.

En esta Tesis Doctoral se han desarrollado catalizadores basados en metales de transición, principalmente níquel (Ni), soportado en un titanosilicato para la reacción de epoxidación empleando una atmósfera de H_2/O_2. También se ha estudiado y se ha profundizado en el mecanismo de reacción en los catalizadores desarrollados.

1.5.3. Producción de H_2

Otro tema de gran relevancia para la sociedad actual que se estudiará en esta Tesis, es la producción de hidrógeno. Este interés se debe a que es una etapa fundamental para afrontar el cambio hacia el uso de hidrógeno como vector energético en la transición energética basada actualmente en la economía del carbono [125]. Este hecho se debe a las ventajas del H_2 como son alta densidad de energía y la formación de H_2O como producto de su oxidación para generar energía. Sin embargo, el H_2 es difícil de almacenar de una manera segura, de manipular y de distribuir. Otro inconveniente es que en la actualidad la producción de hidrógeno se

basa en el reformado de hidrocarburos con vapor de agua, es decir, empleando combustible fósiles [126].

Con esta problemática, una alternativa al almacenamiento de hidrógeno es el uso de moléculas pequeñas que contengan un alto contenido de hidrógeno en su estructura, como por ejemplo ácido fórmico y el amino borano, para almacenar el hidrógeno y poderlo obtener mediante la descomposición de estas moléculas [127].

En las últimas décadas, la comunidad científica se ha centrado en el estudio de la descomposición del amino borano (Fig. 1.15) debido a su alto contenido en hidrógeno (19.6 % de H_2), alta densidad volumétrica y gravimétrica, bajo peso molecular y alta estabilidad, entre otras [128,129]. En la actualidad, los catalizadores que presentan una mayor actividad catalítica para esta reacción son los catalizadores basados en metales nobles (Pt, Au, Pd, Ru) o sus aleaciones con metales de transición (Ni, Co…) soportados en diferentes materiales (TiO_2, materiales de carbón, zeolitas…) [130-133]. Sin embargo, el alto precio de los metales nobles hace que la comunidad científica se esté centrando en el desarrollo de catalizadores basados en metales de transición (Ni, Co, Cu…) aunque estos presenten una serie de inconvenientes tales como su fácil oxidación, sinterización y largos periodos de inducción [134-137].

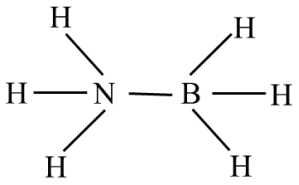

Figura 1.15. Molécula de amino borano

En esta Tesis doctoral se han desarrollado fotocatalizadores basados en metales de transición, principalmente nanopartículas de cobre soportadas en dióxido de titanio modificado con nanotubos de carbono, con el objetivo de que el fotocatalizador sea activo bajo luz visible y presente una baja velocidad de recombinación de pares electro-hueco.

1.6. Referencias

[1] J.A. Moulijn, P.W.N.M. van Leeuwen, R.A. van Santen, Catalysis: An Integrated Approach to Homogeneous, Heterogeneous and Industrial Catalysis, Elservier Science, 1993, pp. 3-21.

[2] J. Wisniak, Educ. Quím. 21 (2010) 60-69.

[3] P. Muller, Pure Appl. Chem. 66 (1994) 1077-1184.

[4] K.J. Laidler, Pure Appl. Chem. 68 (1996) 149-192.

[5] E. Roduner, Chem. Soc. Rev. 43 (2014) 8226-8239.

[6] G.J. Hutchings, C.R.A. Catlow, C. Hardacre, M.G. Davidson, Phil. Trans. R. Soc. A. 374, (2016) 1-8.

[7] P. Atkins, T. Overton, J. Rourke, M. Weller, F. Armstrong, Química Inorgánica, 4a ed. Mc Graw Hill, México, 2006.

[8] T. Kandemir, M.E. Schuster, A. Senyshyn, M. Behrens, R. Schlögl, Angew. Chemie - Int. Ed. 52 (2013) 12723-12726.

[9] G. Ertl, H. Knozinger, J. Weitkamp, Handbook of Heterogeneous Catalysis, 2nd Ed. Wiley-VCH, Weinheim, Germany, 2008, pp. 2265-2274.

[10] G.M. Cooper, The Cell, A Molecular Approach, 2nd Ed. Oxford, 2000.

[11] W. Aehle, Enzymes in Industry: Production and Applications, 3rd Ed. Wiley-VCH, Weinheim, Germany, 2007.

[12] G.W. Parshall, J. Mol. Catal. A Chem. 4 (978) 243-270.

[13] A. Corma, H. García, Chem. Rev. 103 (2003) 4307-4365.

[14] S. Wacławek, V.V.T. Padil, M. Černík, Ecol. Chem. Eng. S. 25 (2018) 9-34.

[15] P.B. Weisz, Annu. Rev. Phys. Chem. 21 (1970) 175-196.

[16] S. S. Joshi, V.V. Ranade, Industrial Catalytic Processes for Fine and Specialty Chemicals, Elservier Science, 2016, pp. 41-111.

[17] K. Ralphs, C. Hardacre, S.L. James, Chem. Soc. Rev. 42 (2013) 7701-7718

[18] J. M. Thomas, W. J. Thomas, Principles and Practice of Heterogeneous Catalysis, 2nd Ed. Wiley-VCH, Weinheim, Germany, 2007.

[19] G. Ertl, H. Knozinger, J. Weitkamp, Handbook of Heterogeneous Catalysis, Wiley-VCH, Weinheim, Germany, 1997.

[20] S.E. Braslavsky, Pure Appl. Chem. 79 (2007) 293-465.

[21] A.O. Ibhadon, P. Fitzpatrick, Catalysts. 3 (2013) 189-218.

[22] U. Gaya, Heterogeneous Photocatalysis Using Inorganic Semiconductor Solids, Springer, Netherlands, 2014.

[23] V.H. Grassian, Environmental catalysis, CRC Pres, United States, 2005.

[24] D. Zhu, Q. Zhou, Environ. Nanotechnology, Monit. Manag. 12 (2019) 100255.

[25] U.I. Gaya, A.H. Abdullah, J. Photochem. Photobiol. C Photochem. Rev. 9 (2008) 1-12.

[26] S. Zhu, D. Wang, Adv. Energy Mater. 7 (2017) 1-24.

[27] M.A. Fox, M.T. Dulay, Chem. Rev. 93 (1993) 341-357.

[28] I.S. Kang, J. Xi, H.Y. Hu, Front. Environ. Sci. Eng. 12 (2018) 8.

[29] H. Gerischer, A. Heller, J. Phys. Chem. 95 (1991) 5261-5267.

[30] Y. Huang, S.S.H. Ho, R. Niu, L. Xu, Y. Lu, J. Cao, S. Lee, Molecules. 21 (2016) 56.

[31] H. Cheng, J. Wang, Y. Zhao, X. Han, RSC Adv. 4 (2014) 47031-47038.

[32] S. Weon, F. He, W. Choi, Environ. Sci. Nano. (2019) 3185-3214.

[33] N. Serpone, J. Photochem. Photobiol. A Chem. 104 (1997) 1-12.

[34] A. V. Vorontsov, E.N. Kabachkov, I.L. Balikhin, E.N. Kurkin, V.N. Troitskii, P.G.

Smirniotis, J. Adv. Oxid. Technol. 21 (2018) 127-137.
[35] K. Tanaka, M.F.V. Capule, T Chem. Phys. Lett. 187 (1991) 73-76.
[36] W. Cen, T. Xiong, C. Tang, S. Yuan, Ind. Eng. Chem. Res. 53 (2014) 15002-15011.
[37] P. V. Kamat, Acc. Chem. Res. 50 (2017) 527-531.
[38] S. Liu, D. Li, H. Sun, H.M. Ang, M.O. Tadé, S. Wang, J. Colloid Interface Sci. 468 (2016) 176-182.
[39] Ș. Neațu, J.A. Maciá-Agulló, H. Garcia, Int. J. Mol. Sci. 15 (2014) 5246-5262.
[40] W. Choi, Catal. Surv. Asia. 10 (2006) 16-28.
[41] A. Kumar, Mater. Sci. Eng. Int. J. 1 (2017) 106-114.
[42] C. McCullagh, N. Skillen, M. Adams, P.K.J. Robertson, J. Chem. Technol. Biotechnol. 86 (2011) 1002-1017.
[43] J. Schneider, M. Matsuoka, M. Takeuchi, J. Zhang, Y. Horiuchi, M. Anpo, D.W. Bahnemann, Chem. Rev. 114 (2014) 9919-9986.
[44] S.M. Gupta, M. Tripathi, Chinese Sci. Bull. 56 (2011) 1639-1657.
[45] S.J. Tsai, S. Cheng, Catal. Today. 33 (1997) 227-237.
[46] J. Buckeridge, K.T. Butler, C.R.A. Catlow, A.J. Logsdail, D.O. Scanlon, S.A. Shevlin, S.M. Woodley, A.A. Sokol, A. Walsh, Chem. Mater. 27 (2015) 3844-3851.
[47] H. Zhang, J.F. Banfield, J. Phys. Chem. B. 104 (2000) 3481-3487.
[48] J.E.S. Haggerty, L.T. Schelhas, D.A. Kitchaev, J.S. Mangum, L.M. Garten, W. Sun, K.H. Stone, J.D. Perkins, M.F. Toney, G. Ceder, D.S. Ginley, B.P. Gorman, J. Tate, Sci. Rep. 7 (2017) 1-11.
[49] A. Mills, S. Le Hunte, J. Photochem. Photobiol. A Chem. 108 (1997) 1-35.
[50] B. Ohtani, O.O. Prieto-Mahaney, D. Li, R. Abe, J. Photochem. Photobiol. A Chem. 216 (2010) 179-182.
[51] R. Trejo-Tzab, J.J. Alvarado-Gil, P. Quintana, T. López, J. Mol. Catal. A Chem. 281 (2008) 113-118.
[52] J. Ryu, W. Choi, Environ. Sci. Technol. 42 (2008) 294-300.
[53] B. Zhang, S. Cao, M. Du, X. Ye, Y. Wang, J. Ye, Catalysts. 9 (2019) 91.
[54] X. Chen, S.S. Mao, Chem. Rev. 107 (2007) 2891-2959.
[55] U. Chandra, Recent Aplications in Sol-Gel Synthesis, Intech Open, 2017
[56] M.A. Behnajady, H. Eskandarloo, N. Modirshahla, M. Shokri, Desalination. 278 (2011) 10-17.
[57] I. Sopyan, N. Hafizah, Int. J. Photoenergy. 2009 (2009) 8-10.
[58] R. Xu, Y. Xu, Modern Inorganic Synthetic Chemistry, 2nd Ed. Elservier Science, 2017, pp. 733-104.
[59] V. Guzmán-Velderrain, Y. Ortega López, J. Salinas Gutiérrez, A. López Ortiz, V.H. Collins-Martínez, Green Sustain. Chem. 4 (2014) 120-132.
[60] Y. Nam, J.H. Lim, K.C. Ko, J.Y. Lee, J. Mater. Chem. A. 7 (2019) 13833-13859.
[61] X. Kang, S. Liu, Z. Dai, Y. He, X. Song, Z. Tan, Catalyst, 9 (2019) 191.
[62] B. Ohtani, Chem. Lett. 37 (2008) 216-229.
[63] A. Fujishima, K. Honda, Nature. 238 (1972) 37-38.
[64] S.N. Frank, A.J. Bard, J. Am. Chem. Soc. 99 (1977) 303-304.
[65] K. Hashimoto, H. Irie, A. Fujishima, JJAP, 44 (2005) 8269-8285.
[66] H. Dong, G. Zeng, L. Tang, C. Fan, C. Zhang, X. He, Y. He, Water Res. 79 (2015) 128-146.
[67] Z. Xiong, Z. Lei, Y. Li, L. Dong, Y. Zhao, J. Zhang, J. Photochem. Photobiol. C Photochem. Rev. 36 (2018) 24-47.

[68] D. Sudha, P. Sivakumar, Chem. Eng. Process. Process Intensif. 97 (2015) 112-133.
[69] J. Ge, Y. Zhang, Y.J. Heo, S.J. Park, Catalyst 9 (2019) 122.
[70] Y. Paz, Solid State Phenom. 162 (2010) 135-162.
[71] C. Anderson, A.J. Bard, J. Phys. Chem. 99 (1995) 9882-9885.
[72] X. Qian, K. Fuku, Y. Kuwahara, T. Kamegawa, K. Mori, H. Yamashita, ChemSusChem. 7 (2014) 1528-1536.
[73] Š. Paušová, J. Krýsa, J. Jirkovský, V. Prevot, G. Mailhot, J. Chem. Technol. Biotechnol. 89 (2014) 1129-1135.
[74] S.N. Kane, A. Mishra, A.K. Dutta, J. Phys. Conf. Ser. 755 (2016) 1-8.
[75] R. Leary, A. Westwood, Carbon, 49 (2011) 741-772.
[76] J. Ge, Y. Zhang, S.J. Park, Materials, 12 (2019) 1916.
[77] P. Vincent, A. Brioude, C. Journet, S. Rabaste, S.T. Purcell, J. Le Brusq, J.C. Plenet, J. Non. Cryst. Solids. 311 (2002) 130-137.
[78] K. Woan, G. Pyrgiotakis, W. Sigmund, Adv. Mater. 21 (2009) 2233-2239.
[79] S. Bagheri, N.M. Julkapli, S.B.A. Hamid, Sci. World J. 2014 (2014) 21.
[80] K. Wenderich, G. Mul, Chem. Rev. 116 (2016) 14587-14619.
[81] R. Clift, N. Grobert, D. Hutton, R. Oliver, O. Oneill, J. Pethica, N. Pidgeon, J. Porritt, J. Ryan, R. Soc. R. Acad. Eng. Rep. 46 (2004) 618-618.
[82] J.M. Thomas, R. Raja, D.W. Lewis, Angew. Chemie - Int. Ed. 44 (2005) 6456-6482.
[83] H. Xu, P. Wu, Chinese J. Chem. 35 (2017) 836-844.
[84] J. Přech, Catal. Rev. - Sci. Eng. 60 (2018) 71-131.
[85] A.Y. Shan, T.I.M. Ghazi, S.A. Rashid, Appl. Catal. A Gen. 389 (2010) 1-8.
[86] M. Delnavaz, B. Ayati, H. Ganjidoust, S. Sanjabi, J. Environ. Heal. Sci. Eng. 13 (2015) 1-10.
[87] T. Kamegawa, N. Suzuki, H. Yamashita, Energy Environ. Sci. 4 (2011) 1411-1416.
[88] C.J. Bueno-Alejo, J.L. Hueso, R. Mallada, I. Julian, J. Santamaria, Chem. Eng. J. 358 (2019) 1363-1370.
[89] M. Khademalrasool, M. Farbod, M.D. Talebzadeh, J. Sci. Adv. Mater. Devices. 1 (2016) 382-387.
[90] F. Khodadadian, M.W. de Boer, A. Poursaeidesfahani, J.R. van Ommen, A.I. Stankiewicz, R. Lakerveld, Chem. Eng. J. 333 (2018) 456-466.
[91] M. Oelgemöller, O. Shvydkiv, Molecules. 16 (2011) 7522-7550.
[92] A. Šalić, A. Tušek, B. Zelić, J. Appl. Biomed. 10 (2012) 137-153.
[93] K.S. Elvira, X.C. Solvas, R.C.R. Wootton, A.J. de Mello, Nat. Chem. 5 (2013) 905-915.
[94] T. Wirth, Microreactors in Organic Chemistry and Catalysis, 2 nd Ed. Wiley-VCH, Germany, 2013, pp. 1-33.
[95] Y. Matsushita, N. Ohba, S. Kumada, K. Sakeda, T. Suzuki, T. Ichimura, Chem. Eng. J. 135 (2007) 303-308.
[96] X. Yao, Y. Zhang, L. Du, J. Liu, J. Yao, Renew. Sustain. Energy Rev. 47 (2015) 519-539.
[97] A. Tanimu, S. Jaenicke, K. Alhooshani, Chem. Eng. J. 327 (2017) 792-821.
[98] E. Olsen, F. Nielsen, Molecules. 6 (2001) 370-389.
[99] M.S. Kamal, S.A. Razzak, M.M. Hossain, Atmos. Environ. 140 (2016) 117-134.
[100] H. Rodhe, Science. 248 (1990) 1217-1219.
[101] G. Barrefors, G. Petersson, J. Chromatogr. A. 643 (1993) 71-76.
[102] C.F. Murphy, D.T. Allen, Atmos. Environ. 39 (2005) 3785-3798.

[103] F. Mühlberger, T. Streibel, J. Wieser, A. Ulrich, R. Zimmermann, Anal. Chem. 77 (2005) 7408-7414.

[104] Kaneko, M.; Okura, I. Photocatalysis: Science and Technology, Springer, Berlin, Germany, 2002.

[105] J. Das, E.R. Rene, J. Krishnan, J. Environ. Chem. Toxicol. 2 (2018) 57-59.

[106] Z. Shayegan, C.S. Lee, F. Haghighat, Chem. Eng. J. 334 (2018) 2408-2439.

[107] D. Trent, Kirk-Othmer Encyclopedia of Chemical Technology. 2001, pp. 1-26.

[108] Ullmans, Propylene Oxide, Rep. Carcinog. 12, (2011) 367-9.

[109] M. Hoeven, Y. Kobayashi and R. Diercks, Technology roadmap energy and GHG reductions in the chemical industry via catalytic processes, International Energy Agency, 2013, pp. 1-60.

[110] J. Huang, M. Haruta, Res. Chem. Intermed. 38 (2012) 1-24.

[111] S.J. Khatib, S.T. Oyama, Catal. Rev. 57 (2015) 306-344.

[112] T.A. Nijhuis, M. Makkee, J. A. Moulijn, B.M. Weckhuysen, Ind. Eng. Chem. Res. 45 (2006) 3447-3459.

[113] V. Russo, R. Tesser, E. Santacesaria, M. Di Serio, Ind. Eng. Chem. Res. 52 (2013) 1168-1178.

[114] Y. Wang, W. Yang, L. Yang, X. Wang, Q. Zhang, Catal. Today. 117 (2006) 156-162.

[115] V. Duma, D. Hönicke, J. Catal. 191 (2000) 93-104.

[116] T. Hayashi, K. Tanaka, M. Haruta, J. Catal. 178 (1998) 566-575.

[117] S.T. Oyama, Mechanisms in Homogeneous and Heterogeneous Epoxidation Catalysis, Elservier Science, 2008, pp. 297-354.

[118] A.K. Sinha, S. Seelan, S. Tsubota, M. Haruta, Angew. Chemie - Int. Ed. 43 (2004) 1546-1548.

[119] B. Chowdhury, J.J. Bravo-Suárez, M. Daté, S. Tsubota, M. Haruta, Angew. Chemie - Int. Ed. 45 (2006) 412-415.

[120] J. Lu, X. Zhang, J.J. Bravo-Suárez, T. Fujitani, S.T. Oyama, Catal. Today. 147 (2009) 186-195.

[121] J. García-Aguilar, I. Miguel-García, J. Juan-Juan, I. Such-Basáñez, E. San Fabián, D. Cazorla-Amorós, A. Berenguer-Murcia, J. Catal. 338 (2016) 154-167.

[122] B. Horváth, M. Hronec, I. Vávra, M. Šustek, Z. Križanová, J. Dérer, E. Dobročka, Catal. Commun. 34 (2013) 16-21.

[123] X. Yang, S. Kattel, K. Xiong, K. Mudiyanselage, S. Rykov, S.D. Senanayake, J.A. Rodriguez, P. Liu, D.J. Stacchiola, J.G. Chen, Angew. Chemie - Int. Ed. 54 (2015) 11946-11951.

[124] Y. Wang, H. Chu, W. Zhu, Q. Zhang, Catal. Today. 131 (2008) 496-504.

[125] I.P. Jain, Int. J. Hydrogen Energy. 34 (2009) 7368-7378.

[126] N. Armaroli, V. Balzani, ChemSusChem. 4 (2011) 21-36.

[127] M. Navlani-García, K. Mori, Y. Kuwahara, H. Yamashita, NPG Asia Mater. 10 (2018) 277-292.

[128] Z. Huang, T. Autrey, Energy Environ. Sci. 5 (2012) 9257-9268.

[129] U.B. Demirci, Int. J. Hydrogen Energy. 42 (2017) 9978-10013.

[130] T. Kamegawa, T. Nakaue, Chem. Commun. 51 (2015) 16802-16805.

[131] K. Mori, K. Miyawaki, H. Yamashita, ACS Catal. 6 (2016) 3128-3135.

[132] S. Jo, P. Verma, Y. Kuwahara, K. Mori, W. Choi, H. Yamashita, J. Mater. Chem. A. 5 (2017) 21883-21892.

[133] M. Chandra, Q. Xu, J. Power Sources. 168 (2007) 135-142.

[134] M. Wen, Y. Cui, Y. Kuwahara, K. Mori, H. Yamashita, ACS Appl. Mater. Interfaces. 8 (2016) 21278-21284.

[135] C. Wang, D. Sun, X. Yu, X. Zhang, Z. Lu, X. Wang, J. Zhao, L. Li, X. Yang, Inorg. Chem. Front. 5 (2018) 2038-2044.

[136] A. Yousef, N.A.M. Barakat, M.H. EL-Newehy, M.M. Ahmed, H.Y. Kim, Colloid Surfac A. 470 (2015) 194-201.

[137] J. Li, Q.L. Zhu, Q. Xu, Catal. Sci. Technol. 5 (2015) 525-530.

Capítulo 2

Técnicas Experimentales

En el presente Capítulo se han presentado y descrito las distintas técnicas de caracterización utilizadas a lo largo de esta Tesis para estudiar las propiedades físico-químicas de los diferentes materiales desarrollados. Entre las distintitas técnicas se incluyen técnicas espectroscópicas, microscópicas y técnicas de caracterización estructural. Además, se han citado y descrito los distintos sistemas experimentales utilizados para la realización de los ensayos catalíticos (fotooxidación de propeno, oxidación selectiva de propileno y descomposición de amino borano) así como las condiciones utilizadas.

2.1. Introducción

En este capítulo se presentarán y describirán los fundamentos y características más relevantes de las técnicas de caracterización usadas en esta Tesis que permiten obtener información sobre las propiedades físico-químicas y estructurales de los materiales desarrollados. En este capítulo también se describirán los montajes y procedimientos experimentales usados para evaluar la actividad o fotoactividad catalítica de los materiales en las distintas reacciones que se estudian en esta Tesis (oxidación fotocatalítica de propeno, oxidación selectiva de propileno al epóxido de propileno y producción de hidrógeno a partir de la descomposición del amino borano). Sin embargo, no se describirán los reactivos, materiales, métodos de preparación de las muestras y condiciones específicas de las técnicas de caracterización y de análisis ya que se describirán en la sección experimental de los respectivos Capítulos para una mejor claridad.

2.2. Técnicas de Caracterización y Análisis

A continuación, se describirán las técnicas de caracterización empleadas en la presente Tesis entre las que se encuentran la difracción de rayos X (DRX), la espectrometría ultravioleta-visible (UV-Vis), la adsorción física de gases, la microscopía óptica, la microscopía electrónica de barrido (SEM), la microscopía electrónica de transmisión (TEM), la espectroscopia de fluorescencia de rayos X con un detector de dispersión de energía (EDX), la espectroscopia fotoelectrónica de rayos X (XPS), la espectrometría de emisión óptica por plasma de acoplamiento inductivo (ICP-OES), la espectroscopia infrarroja por transformada de Fourier (FTIR), la fotoluminiscencia (PL), termogravimetría (TG) y la desorción a temperatura programada (DTP). La información obtenida con estas técnicas permite interpretar y comprender mejor los resultados catalíticos de las muestras, por lo que en este apartado también se incluirán las técnicas de análisis (cromatografía de gases (GC) y/o espectrómetría de masas (EM)) empleadas para la detección y seguimiento de los reactivos y productos que están presentes o aparecen en las reacciones químicas estudiadas en la presente Tesis.

2.2.1. Difracción de Rayos X

El fenómeno de la difracción de rayos X se basa en la interacción de un haz de rayos X con la nube electrónica de los átomos de un sólido cristalino cuyos parámetros de celda son del orden de magnitud de la longitud de onda de la radiación de los rayos X incidentes. Parte de esta radiación es absorbida por el material de estudio y devuelta en forma de radiación dispersa en todas las direcciones del espacio. La radiación dispersada por la muestra que se quieren analizar sufre fenómenos de interferencia que, debido a la simetría del cristal, únicamente es constructiva en direcciones concretas, dando lugar a la figura de difracción o difractograma del cristal de estudio [1].

La ley de Bragg determina las condiciones necesarias para que se produzca la difracción de rayos X en un material. Según esta ley, una sustancia cristalina se puede describir mediante familias de planos paralelos y equidistantes entre sí. Además cada familia de planos presenta unos índices de Miller (hkl) y un espaciado d_{hkl} característicos de cada sustancia. Cuando un haz de rayos X monocromático incide sobre los planos cristalinos con una longitud de onda λ, en una dirección que forma un ángulo θ con la superficie de los planos solo ocurrirá la difracción si el ángulo de incidencia, la longitud de onda de incidencia, y el espaciado de la familia de planos cumplen con la relación de la ley de Bragg (ec. 2.1) [2].

$$\lambda = 2d_{hkl}\text{sen}\theta \qquad (2.1)$$

donde λ es la longitud de onda del haz incidente y θ el ángulo al que aparece el máximo de difracción.

En la práctica, los difractogramas no están formados por líneas, sino que estas presentan un cierto ensanchamiento. Este efecto es debido a factores instrumentales (equipo de análisis) o al grado de imperfección cristalina de la muestra o al tamaño de partícula. Debido a estos inconvenientes Scherrer formuló una ecuación (ec. 2.2) que relaciona el tamaño medio de los cristales (B) con la anchura a mitad de altura del pico de intensidad principal (β).

$$B = \frac{K\lambda}{\beta \cos\theta} \qquad (2.2)$$

donde β es la anchura a mitad de altura del pico de intensidad principal, λ es la longitud de onda del haz incidente, θ el ángulo al que aparece el máximo de difracción y K es una constante cuyo valor es de 0.9 para las condiciones de operación utilizadas [3].

Las intensidades de los rayos difractados están íntimamente relacionadas con la naturaleza de los átomos y con las posiciones que estos ocupan en la red cristalina, este hecho hace que el análisis mediante DRX sea muy efectivo para obtener información de la estructura cristalina.

En la presente Tesis la técnica de DRX se ha utilizado para identificar las diferentes fases cristalinas y determinar el tamaño de cristal de las muestras desarrolladas a lo largo de esta Tesis (TiO_2, materiales compuestos basados en óxido de titanio y nanopartículas metálicas). Para esta finalidad se han empleado dos equipos distintos dependiendo de la temperatura utilizada para el análisis de las muestras. Para las muestras analizadas a temperatura ambiente se utilizó un difractómetro Miniflex II Rigaku (Fig. 2.1 a)), 30 kV/15 mA que se encuentra en los laboratorios del Departamento de Química Inorgánica de la Universidad de Alicante. Para la caracterización a temperaturas elevadas hasta 900ºC se utilizó un difractómetro Bruker D8-Advance (Fig. 2.1 b)), este equipo presenta un espejo

Göebel (muestras no planas), una cámara de alta temperatura (hasta 900ºC) y un generador de rayos-X KRISTALLOFLEX K 760-80F (Potencia: 3000W, Tensión: 20-60kV y Corriente: 5-80mA) provisto de un tubo de RX con ánodo de cobre. Se encuentra en los Servicios Técnicos de Investigación de la Universidad de Alicante. Para ambos equipos el análisis de las muestras se ha empleado una velocidad de escaneo de 2º/min en un ángulo comprendido entre 5-80º.

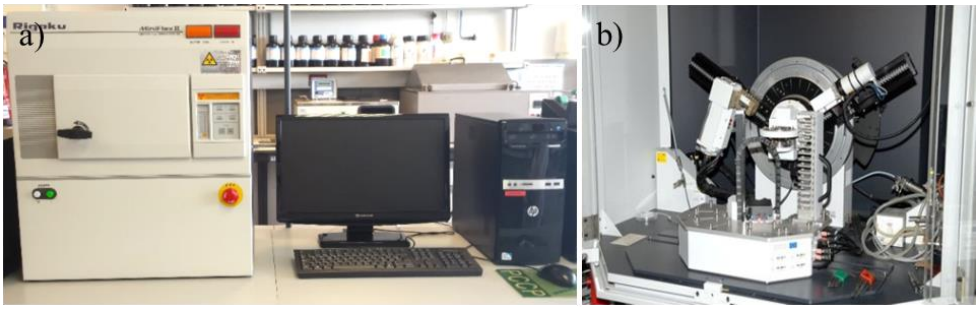

Figura 2.1. Equipos de difracción de Rayos X usados en la presente Tesis: a) Miniflex II Rigaku y b) Bruker D8-Advance.

2.2.2. Espectrometría Ultravioleta-Visible

La espectrometría UV-Vis está basada en el proceso de absorción de la radiación ultravioleta-visible (entre 160 y 780 nm) por una molécula o por un sólido, aunque en esta técnica también se utiliza luz en el intervalo adyacente (infrarrojo cercano). Esta absorción de radiación de la molécula o sólido provoca la promoción de un electrón del estado fundamental a un estado excitado. Como consecuencia de que los electrones excitados al absorber radiación con esta frecuencia son electrones de enlace, las bandas de absorción del espectro se pueden relacionar con los distintos tipos de enlace de las moléculas o de los sólidos [4].

Está técnica es muy interesante también para el estudio de catalizadores o fotocatalizadores sólidos (concretamente los semiconductores) ya que permite observar la transición de electrones desde la banda de valencia a la banda de conducción. Como consecuencia, esta técnica permite el cálculo de la energía de la banda prohibida (Eg).

El cálculo del valor de la Eg se ha realizado usando el método de la absorbancia [5] que consiste en obtener la longitud de onda del borde de absorción mediante la intersección de la recta con mayor pendiente a absorbancia cero para cada uno de los espectros obtenidos individualmente entre 200 y 800 nm. La energía de banda prohibida se obtiene a partir de la ecuación (ec. 2.3):

$$E_g = \frac{1239,8}{\lambda} \qquad (2.3)$$

donde Eg es la energía de banda prohibida (eV), 1239,8 (eV·nm) es el producto resultante de la constante de Planck (eV·s) y la velocidad de la luz (nm·s^{-1}) y λ (nm) es la longitud de onda del borde de absorción.

Las muestras se analizaron en un espectrofotómetro UV-Vis (V-670, JASCO) (Fig. 2.2), que dispone de un monocromador único con doble red, una para la región UV-Vis y otra para la región NIR. El detector utilizado consiste en tubos fotomultiplicadores y las fuentes utilizadas son una lámpara de deuterio (de 190 a 350 nm) y una lámpara halógena (de 330 a 2700 nm), además este instrumento puede incorporar una esfera de integración (ISN-723-UV-Visible-NIR, JASCO) que permite la medida de la reflectancia o transmisión difusa de muestras sólidas en polvo. Este equipo se encuentra en el Grupo de Electrocatálisis y Electroquímica de Polímeros del Instituto de Materiales de la Universidad de Alicante. También se utilizó otro equipo, en este caso fue el UV-2600 (SHIMADZU) que también permite el análisis de muestras sólidas. Este equipo se encuentra en el grupo de investigación del profesor Hiromi Yamashita en la Universidad de Osaka (Japón).

Para el análisis de las muestras en ambos equipos se ha empleado un intervalo de longitudes de onda entre 200-1200 nm y se ha usado $BaSO_4$ como referencia.

Figura 2.2. Espectrofotómetro UV-vis (V-670, JASCO) usado para el estudio de catalizadores solidos.

2.2.3. Adsorción Física de Gases

La adsorción física de gases se mide generalmente determinando la cantidad de gas adsorbido por el material adsorbente (sólido poroso) mediante medidas de diferencias de presión en un volumen constante calibrado, a una temperatura constante conocida. Las isotermas de adsorción se definen como la variación de la cantidad adsorbida de gas, expresada como mmoles/g o cm^3/g respecto a la presión relativa del adsorbato, a temperatura constante. Las formas de las isotermas dan una aproximación del mecanismo de adsorción que está ocurriendo. A partir de las isotermas se pueden calcular parámetros relativos a la muestra (superficie específica, volumen de poros del sólido y distribución de tamaños de poros del material). Este

hecho hace que la adsorción física de gases sea una de las técnicas más utilizadas en la caracterización textural de los materiales porosos [6,7].

Según la normativa de la IUPAC [8] (Fig. 2.3), las isotermas se pueden clasificar según su forma en:

- Tipo I: característica de sólidos microporosos que presentan superficie externa pequeña. Dentro de este tipo se pueden diferenciar dos subtipos, el tipo I a) característica de materiales microporosos que presentan principalmente microporos estrechos (anchura de poro < 1 nm aproximadamente) y el tipo I b) característica de materiales que presentan distribuciones de tamaño de poro más amplia, incluyendo microporos amplios y posiblemente mesoporosidad estrecha (anchura de poro < 2,5 nm aproximadamente).

- Tipo II: característica de procesos de adsorción en sólidos no porosos o macroporos, representa el caso de adsorción en multicapa. El punto B indica el final de la adsorción en monocapa.

- Tipo III: característica de procesos de adsorción en los que la interacción adsorbente-adsorbato es débil.

- Tipo IV: característica de sólidos mesoporos, estos sólidos se caracterizan por presentar condensación capilar. Dentro de este tipo se pueden diferencias dos subtipos, el Tipo IV a) ocurre condensación capilar de N_2 en los poros del adsorbente y presenta histéresis. Este proceso ocurre cuando la anchura de poro excede una cierta anchura de poro crítica, que es dependiente del sistema de adsorción y de la temperatura. La isoterma Tipo IV b) se observa cuando la anchura de los mesoporos es estrecha, siendo el proceso de condensación capilar reversible.

- Tipo V: Se observa cuando hay baja afinidad entre el adsorbente y el adsorbato y además presenta histéresis, esta isoterma es poco común. Concretamente es característica de la adsorción de agua en adsorbentes microporosos y mesoporosos hidrofóbicos.

- Tipo VI: es característica de materiales no porosos que presenten una superficie muy uniforme y una adsorción capa a capa.

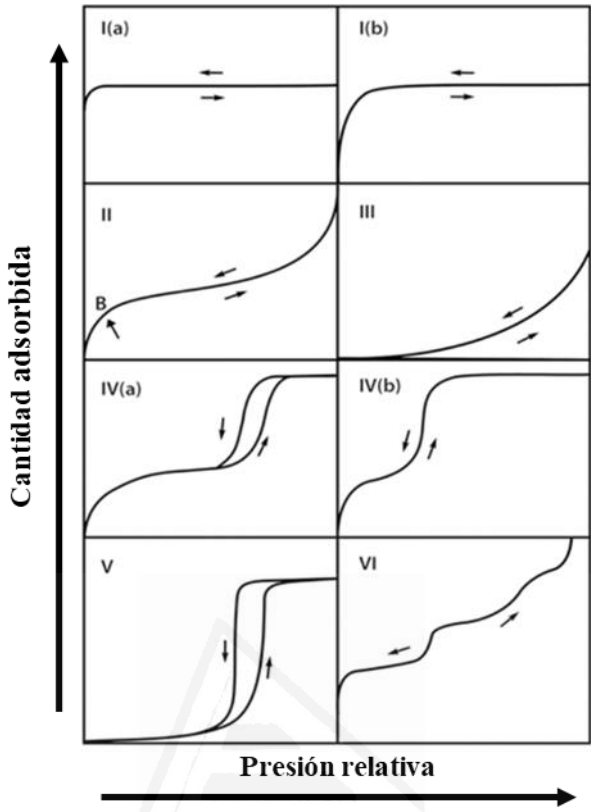

Figura 2.3. Clasificación de las isotermas de adsorción de gas, según normativa de la IUPAC [8].

En este trabajo se utiliza la ecuación de BET así como la de Dubinin-Radushkevich (D-R) para la interpretación de las isotermas de N_2 de los materiales sintetizados. Por lo que a continuación se citarán y explicarán brevemente estas ecuaciones.

El modelo de adsorción descrito por Brunauer, Emmett y Teller (BET) se desarrolló para tener en cuenta la adsorción en multicapa [9], ya que el modelo de Langmuir (monocapa) no lo considera [6]. Esta ecuación supone: i) la superficie de adsorbente está constituida por sitios localizados de adsorción que son equivalentes e independientes entre sí, ii) durante el proceso de adsorción, se alcanza un equilibrio dinámico en el cual la velocidad con que las moléculas de adsorbato se condensan en los sitios vacíos es igual con la que se evaporan de los sitios ocupados y iii) sólo se forma una capa de moléculas adsorbida sobre la superficie del sólido. A continuación, se presenta la ecuación linealizada (ec. 2.4).

$$\frac{P/P_0}{n\cdot(1-P/P_0)}=\frac{1}{n_m\cdot C}+\frac{C-1}{n_m\cdot C}\cdot P/P_0 \qquad (2.4)$$

donde P/P_0 es la presión relativa a la presión de saturación del adsorbato en el equilibrio, n es la cantidad adsorbida, n_m es la cantidad de moles adsorbidas en la monocapa y C es un parámetro adimensional.

La ecuación BET se utiliza ampliamente para calcular el área superficial de los adsorbentes mediante las isotermas de adsorción de N_2 a -196 ºC tanto en sólidos no porosos como porosos. A partir de la ec. 2.5 y sabiendo n_m de la ec. 2.4 se puede estimar el área superficial BET S_{BET} (m^2/g).

$$S_{BET}=n_m\cdot A_m\cdot N_A\cdot 10^{-21} \qquad (2.5)$$

donde A_m es el área ocupada por una molécula de nitrógeno (0,162 nm^2/molécula), N_A es el número de Avogadro ($6{,}023\cdot 10^{23}$ moléculas/mol).

Para caracterizar la textura porosa de un sólido, además de determinar su superficie específica o área superficial, es necesario conocer el volumen y distribución del tamaño de poros. Por esta razón se utiliza la ecuación de Dubinin-Radushkevich (D-R) [10]. La ecuación de D-R considera la existencia de superficies equipotenciales que delimitan diversos espacios de adsorción.

Dubinin y colaboradores [11] encontraron que los carbones activados presentan una curva muy similar a la rama positiva de una distribución gaussiana, lo que implicaba que los espacios de adsorción podrían expresarse como una función gaussiana de los potenciales de adsorción correspondientes, resultando, después de algunas operaciones, la ecuación conocida como ecuación de DR (ec. 2.6):

$$\log V=\log V_0-D\cdot\log^2(P_0/P) \qquad (2.6)$$

donde V es el volumen de nitrógeno adsorbido (cm^3/g), V_0 es el volumen total de microporos (cm^3/g) y D es una constante que está relacionada con el tamaño del poro y la energía de interacción.

Si se representa la ec. 2.6 se obtiene una línea recta cuya ordenada en el origen es log V_0, es decir, el logaritmo del volumen de microporos y, por lo tanto, se puede obtener el volumen de microporos.

Después de citar brevemente las ecuaciones para la interpretación de las isotermas de adsorción de nitrógeno, se explicará el equipo utilizado.

La porosidad en esta Tesis se evalúa a partir de las isotermas de adsorción de N_2 a -196 ºC hasta una presión de 1 bar, aunque es importante destacar que se pueden utilizar diversos adsorbatos como por ejemplo CO_2, Ar y H_2 entre otros [8]. En la presente Tesis, para la evaluación de las muestras se utiliza un equipo volumétrico

automático Autosorb 6B (Quantachrome) (Fig. 2.4) que se encuentra en el grupo de investigación Materiales Carbonosos y Medio Ambiente del Instituto de Materiales y del Departamento de Química Inorgánica de la Universidad de Alicante. Antes de llevar a cabo el experimento de adsorción se debe desgasificar la muestra para eliminar la humedad y/o especies adsorbidas que contenga el material poroso y puedan bloquear la porosidad del mismo. En esta Tesis, de forma general las muestras se desgasifican a 250 ºC durante 4 horas en vacío. Durante la adsorción del gas las muestras deben estar sumergidas en un baño de nitrógeno líquido (-196ºC). Para el análisis de los datos se asume una densidad de 0,808 g/cm^3 para el nitrógeno líquido. Además, otro factor a tener en cuenta es que hay que asegurarse que las isotermas de adsorción se realizan en condiciones de equilibrio.

Figura 2.4. Equipos utilizados para obtener las isotermas de adsorción-desorción de N_2 a -196 ºC en la presente Tesis: a) Equipo de desgasificación, Autosorb Degasser (Quantachrome) y b) Equipo de adsorción y desorción, Autosorb-6B Quantachrome.

A partir de las isotermas de nitrógeno se pueden calcular los siguientes parámetros [6,8].

- Volumen total de poros, V_t (cm^3/g): es el volumen de N_2 adsorbido a P/P_0=0.95.

- Volumen de microporos, $V_{N_2,DR}$ (cm^3/g).

- Volumen de mesoporos, V_{meso} (cm^3/g): Se calcula mediante la diferencia entre el V_t y el $V_{N_2,DR}$ (ec. 2.7).

$$V_{meso} = V_t - V_{N_2,DR} \quad (2.7)$$

- Superficie especifica de BET, S_{BET} (m^2/g).

2.2.4. Microscopía Óptica

El funcionamiento de un microscopio óptico se basa en la propiedad de algunos materiales que permite cambiar la dirección de los rayos de luz visible (400-780 nm). Este efecto permite fabricar lentes capaces de hacer converger o divergir los rayos de luz visible y mediante la combinación de estas lentes se puede generar una imagen aumentada del objeto a estudio [12]. El ejemplo más sencillo sería utilizar una sola lente para formar una imagen aumentada de una muestra, siendo este el caso de la lupa.

En el caso de un microscopio óptico se genera la imagen aumentada a partir de distintas lentes. Algunas de ellas montadas en el objetivo del microscopio y otras en el ocular. En primer lugar, las lentes del objetivo generan una imagen real aumentada de la muestra. Esta imagen real es a continuación ampliada mediante las lentes del ocular dando lugar a una imagen virtual de tamaño superior a la muestra original.

El microscopio óptico común está formado, de forma general, por tres sistemas: El sistema mecánico que permiten el movimiento de las lentes para poder realizar el enfoque de la muestra a estudio y una pletina donde se coloca la muestra. El sistema óptico comprende un conjunto de lentes, dispuestas de tal manera que producen el aumento de las imágenes que se observan a través de ellas. El sistema de iluminación comprende las partes del microscopio que reflejan, transmiten y regulan la cantidad de luz necesaria para efectuar la observación a través del microscopio.

En esta Tesis se ha utilizado la microscopía óptica como técnica de caracterización, concretamente una lupa EZ4 HD (Leica) (Fig. 2.5), que se encuentra en los laboratorios del Departamento de Química Inorgánica de la Universidad de Alicante. Este sistema se ha empleado para el estudio de los microrreactores rellenados con TiO_2, haciendo posible la caracterización de los materiales incorporados y así observar si existe una incorporación adecuada del catalizador en el interior de microrreactor

Figura 2.5. Lupa utilizada para la caracterización del relleno de catalizador en los mecrorreactores.

2.2.5. Microscopía Electrónica de Barrido

La microscopia electrónica de barrido o SEM utiliza un haz de electrones para generar la imagen. Con este objetivo, el equipo tiene incorporado un filamento que genera un haz de electrones, al someterlo a una diferencia de potencial muy elevada (entre 10 y 30 kV), para iluminar la muestra y diferentes detectores para crear una imagen que refleje las características superficiales de la muestra, pudiendo proporcionar información morfológica y topográfica de la superficie de la muestra sólida [13].

En microscopía SEM la imagen se forma mediante la interacción de los electrones emitidos por una fuente de electrones (filamento) y la superficie de la muestra, ya que ocurren diversos fenómenos, como que los electrones pueden atravesar la muestra, pueden ser reflejados o absorbidos por la muestra. Cuando la muestra absorbe los electrones esta puede emitir luz, emitir electrones secundarios de baja energía, electrones retrodispersados, electrones Auger o rayos X. En este caso, la microscopía electrónica de barrido utiliza los electrones secundarios desprendidos por la muestra, que se encuentran generalmente a una distancia pequeña de la superficie (entre 50 y 100 Å) y son emitidos al recibir una transferencia de energía procedente de algún proceso de dispersión inelástica, para formar la imagen de la superficie analizada [14].

En esta técnica hay que tener en cuenta que las muestras analizadas deben ser conductoras para que no se carguen o en su defecto se debe llevar a cabo un recubrimiento de las muestras aislantes con una película delgada de un material conductor (oro o carbono). Además, se debe considerar que la emisión de los electrones dispersados depende del número atómico de la muestra. Este hecho implica que dos zonas de la misma muestra con distinta composición se observan con distinta intensidad.

Las muestras de estudio de la presente Tesis se analizaron con un equipo Hitachi modelo S3000N (Fig. 2.6 a). Este microscopio cuenta con un detector de rayos X marca Bruker modelo XFlash 3001 para microanálisis (EDX) y mapping. En este equipo se estudió la morfología de las partículas de TiO_2 que forman el relleno de los microrreactores, concretamente en los microcapilares. Para las muestras en forma de polvo desarrolladas en esta Tesis se utilizó un Microscopio electrónico de barrido de emisión de campo (FE-SEM) marca ZEISS modelo Merlin VP Compact equipado con un sistema de microanálisis por EDX marca BRUKER modelo Quantax 400 (Fig. 2.6 b)). La resolución que alcanza es 0,8 nm a 15 kV y 1,6 nm a 1 kV. La principal diferencia entre un FE-SEM y un SEM reside en el sistema generación de electrones. El FE-SEM utiliza como fuente de electrones un cañón de emisión de campo que proporciona haces de electrones de alta y baja energía muy focalizados, lo que mejora notablemente la resolución espacial y permite trabajar a potenciales más bajos, (0.02

- 5 kV). Ambos equipos se encuentran en los Servicios Técnicos de Investigación de la Universidad de Alicante.

Figura 2.6. Microscopios electrónicos de barrido utilizados en esta Tesis: a) SEM Hitachi S3000N y b) FE-SEM ZEISS Merlin VP Compact.

2.2.6. Microscopía Electónica de Transmisión

La microscopía electrónica de transmisión consiste en irradiar una película fina de muestra con un haz de electrones, con una energía muy elevada (potencial de emisión >100 kV). En esta técnica, a diferencia del SEM, el análisis de la muestra se realiza a partir de los electrones que atraviesan la muestra de estudio (y que por tanto son transmitidos por la muestra). Estos electrones forman una imagen en 2 dimensiones de la muestra. Por lo tanto, la muestra de estudio en esta técnica debe ser delgada (grosor inferior a 100 nm) con el objetivo de que los electrones pasen a través de la muestra y poder obtener una imagen con buena calidad [14,15].

En esta técnica hay que considerar que los electrones que atraviesan la muestra pueden sufrir dispersión cuando interaccionan con la muestra (elástica o inelástica) o no experimentar ningún cambio en su trayectoria. De entre estos tres fenómenos hay que destacar que los electrones dispersados elásticamente son los responsables de la formación de las imágenes de difracción, los electrones no dispersados forman imágenes directas del material y los dispersados de forma inelástica son los responsables del ruido de fondo.

Un microscopio electrónico de transmisión proporciona dos tipos de información complementaria: por un lado, la obtención de la imagen directa del material mediante el análisis de los electrones transmitidos no dispersados y por otro la obtención del diagrama de difracción, a partir del análisis de la distribución espacial de los electrones dispersados elásticamente pudiendo deducir la disposición de los átomos en el sólido.

Las muestras preparadas en esta Tesis se han caracterizado mediante el equipo JEOL modelo JEM-2010 (Fig. 2.7). Este microscopio cuenta con un detector de rayos X marca OXFORD modelo INCA Energy TEM 100 para microanálisis (EDX). La cámara de adquisición de imágenes es de la marca GATAN modelo ORIUS SC600.

Este equipo se encuentra en los Servicios Técnicos de Investigación de la Universidad de Alicante.

Figura 2.7. Microscopio electrónico de transmisión JEM-2010 (JEOL) utilizado en la presente Tesis.

2.2.7. Espectroscopia de Fluorescencia de Rayos X con análisis por Dispersión de Energía

La espectroscopia de fluorescencia de rayos X con un analizador por dispersión de energía (EDX) se basa en el proceso que ocurre cuando se irradia con un haz de electrones una muestra, concretamente cuando la radiación es absorbida por parte de la muestra y por tanto se produce la ionización de esta. Esta pérdida de un electrón (ionización) de una capa interna del átomo provoca que otro electrón de una capa más externa del átomo salte a la capa deficitaria rellenando el hueco producido. Este hecho produce una liberación de energía cuyo valor es igual a la diferencia entre las energías que tenía cada electrón en su orbital correspondiente. Esta energía es característica de cada elemento y su intensidad es directamente proporcional a la proporción del mismo en el conjunto de la muestra. Estos rayos X se detectan y ordenan en función de sus energías. Por lo tanto, con la intensidad de los picos característicos de los elementos presentes en el espectro se puede determinar la relación atómica y la composición de la muestra [16].

Generalmente esta técnica se encuentra asociada a las técnicas de microscopía (SEM y TEM). En la presente Tesis la realización de microanálisis composicional y/o "mapping" se ha llevado a cabo mediante EDX acoplado a la técnica SEM y/o TEM (Fig. 2.8) que están disponibles en los Servicios Técnicos de Investigación de la Universidad de Alicante.

Figura 2.8. Microscopio electrónico de transmisión JEM-2010 con un EDX acoplado.

2.2.8. Espectroscopia Fotoelectrónica de Rayos X

La espectroscopia fotoelectrónica de rayos X (XPS) se basa en la medición de la energía cinética de los electrones emitidos desde niveles internos de los átomos que han sido excitados mediante la irradiación de un haz de rayos X sobre la superficie del material estudiado. Cuando se irradia la muestra con un haz de rayos X, parte de la energía aportada se invierte en liberar electrones de los niveles atómicos internos, quedando los átomos superficiales parcialmente ionizados. A este efecto se le conoce como efecto fotoeléctrico [17]. El átomo excitado recuperará su estado fundamental cuando los electrones de las capas superiores pasen a ocupar los huecos generados en las capas internas. Cuando la muestra se irradie con un haz de rayos X de una energía determinada, esta liberará fotoelectrones con una energía cinética determinada y característica de los elementos que los componen. Por lo tanto, conociendo el valor de esta energía cinética se puede determinar la composición elemental y la concentración de cada elemento del material, haciendo que esta técnica sea muy empleada en la caracterización superficial de materiales [18]. La velocidad de los electrones emitidos se puede cuantificar mediante un espectrómetro y el espectro de XPS generalmente representa el número de electrones detectados frente a la energía de ligadura de estos electrones emitidos.

Un factor que se debe tener en cuenta en esta técnica es que tiene una sensibilidad que se limita a la superficie de los materiales (1-2 nm de profundidad) debido que solo los electrones procedentes de las regiones más próximas a la superficie son capaces de escapar del sólido manteniendo su energía característica [19].

En esta Tesis se han caracterizado mediante esta técnica distintos materiales (TiO_2) y materiales compuestos (TiO_2/CNT) así como los diferentes metales de transición soportados. Para ello se ha utilizado un equipo K-Alpha (Thermo-Scientific) (Fig. 2.9) totalmente automatizado. Este equipo está disponible en los Servicios Técnicos de la Universidad de Alicante.

Figura 2.9. Espectrómetro K-Alpha (Thermo-Scientific) utilizado para el análisis XPS en la presente Tesis.

2.2.9. Espectrometría de Emisión Óptica por Plasma de Acoplamiento Inductivo

La técnica de espectrometría de emisión óptica por plasma de acoplamiento inductivo se basa en el análisis de la radiación ultravioleta/visible emitida por un elemento al ser excitado en un plasma [20], que es una mezcla gaseosa conductora de la electricidad que contiene una concentración significativa de cationes y electrones y con una carga neta próxima a cero, siendo generalmente el plasma de argón el más utilizado para esta aplicación [21]. La fuente de ICP donde se genera el plasma consta de tres tubos concéntricos de cuarzo a través de los cuales fluye una corriente de argón. Rodeando la parte externa del tubo más ancho se encuentra una bobina de inducción refrigerada que está alimentada por un generador de radiofrecuencias. La ionización del argón que fluye se inicia por medio de una chispa que proviene de una bobina Tesla. Los iones resultantes interaccionan con el campo magnético oscilante que se produce por la bobina de inducción. Los iones de argón, una vez formados en el plasma, pueden absorber suficiente potencia de una fuente externa como para mantener un nivel de temperatura que puede llegar a los 10000 ºC. Cuando la muestra llega al plasma, tiene lugar el proceso de ionización y cuando la energía cesa la muestra tiende a alcanzar su estado fundamental, de forma que hay una emisión de radiación en la región UV-Vis del espectro, cuya longitud de onda es característica de cada elemento que la compone. Dicha radiación emitida se separa según su longitud de onda y se registra la intensidad en los detectores del sistema. De esta

manera, a partir de la longitud de onda se pueden identificar los elementos presentes en la muestra y a partir de la intensidad de la radiación se puede cuantificar la concentración de éstos mediante el empleo de una curva de calibrado de cada elemento.

En la presente Tesis Doctoral la técnica de ICP-OES ha sido realizada en el equipo Perkin Elmer 4300 (Fig 2.10), el cual está ubicado en los Servicios Técnicos de Investigación de la Universidad de Alicante. Esta técnica se ha empleado para determinar el contenido metálico de las diferentes muestras preparadas y la proporción de TiO_2 en los materiales compuestos.

Figura 2.10. Equipo Perkin Elmer 4300 utilizado para el análisis de ICP-OES en esta Tesis.

2.2.10. Espectroscopia Infrarroja por Transformada de Fourier

La espectroscopia infrarroja se basa en la interacción de un haz de luz infrarroja con una muestra. El intervalo de números de onda del espectro infrarrojo de trabajo (4000 y 100 cm^{-1}) coincide con las energías de vibración de los enlaces de las moléculas. En los espectros de infrarrojo se observa que a determinadas longitudes de onda aparecen picos que corresponden a la absorción de parte de la radiación, debido a un fenómeno de resonancia, por parte de la muestra y que ocurre para las longitudes de onda correspondientes a las energías de vibración de los enlaces de las moléculas presentes en la misma [22].

Los espectrómetros de infrarrojo se suelen distinguir en dos tipos, dispersivos y no dispersivos. En los dispersivos se emplea un prisma o una red de difracción como elemento dispersivo, para separar espacialmente la luz en sus diferentes longitudes de onda, y una rendija para seleccionar la longitud de onda que queremos hacer pasar por la muestra. En el caso de los sistemas no dispersivos, estos elementos son sustituidos por un Interferómetro de Michelson, que consta de tres partes fundamentales: un espejo móvil, un espejo fijo y un semiespejo (beamsplitter). Este último permite separar el haz que llega de la fuente en dos, uno de ellos se dirige hacia

el espejo fijo y el otro hacia el móvil. El movimiento de este último provoca una diferencia entre la distancia que debe recorrer cada uno de los haces (diferencia de caminos). Así, cuando éstos vuelven a coincidir en el semiespejo, se produce un fenómeno de interferencia, que puede ser constructiva (si la diferencia de caminos es "n" veces la longitud de onda de la radiación), o destructiva (si es "n" veces la mitad de la longitud de onda). Si se añaden infinitas fuentes, es decir, un continuo de frecuencia, tendríamos un haz policromático y al detector le llegaría la intensidad total de la suma de todas las componentes. El siguiente paso consiste en transformar el interferograma, es decir, la intensidad del haz en función del desplazamiento del espejo, en un espectro, en el que se represente, la intensidad en función de la frecuencia del haz de irradiación. Para ello, se emplea una técnica matemática conocida como Transformada de Fourier. Dependiendo del modo de obtención de los espectros se pueden distinguir distintas técnicas, entre las que cabe destacar la reflectancia difusa (DR), reflectancia total atenuada (ATR) o el método de transmisión.

Los materiales desarrollados en la presente Tesis se han analizado en el modo de reflectancia difusa, que consiste en que el haz de infrarrojo incide sobre la superficie de la muestra de estudio, analizando solo las partículas externas de la superficie. La muestra se mezcla con KBr (proporción muestra/KBr de 1/100). El equipo utilizado para el análisis de las muestras fue un equipo JASCO FT/IR-410 (Fig 2.11) disponible en el grupo de investigación Materiales Carbonosos y Medio Ambiente del Instituto de Materiales y del Departamento de Química Inorgánica de la Universidad de Alicante. Este equipo también dispone de un sistema de reacción para poder trabajar bajo diferentes atmosferas y calentar la muestra de forma simultánea a la medida de IR.

Figura 2.11. Espectrofotómetro JASCO FT/IR-410 utilizado en esta Tesis.

2.2.11. Fotoluminiscencia

La fotoluminiscencia (PL) se basa en analizar la radiación emitida por un material que se origina de la transición de un electrón de un estado excitado al estado fundamental. En el caso de la fotoluminiscencia, la excitación es inducida ópticamente por la absorción de fotones [23].

En la espectroscopia de fotoluminiscencia en un semiconductor, los electrones se excitan a un nivel electrónico superior. Posteriormente, los electrones se relajan al mínimo de la banda y emiten radiación de luminiscencia. La composición espectral de esta luz puede proporcionar información sobre el tipo de estados de la banda de valencia, las probabilidades de transición o vacantes e impurezas. Para obtener este análisis, un láser sintonizado a una longitud de onda cercana a la energía de banda prohibida de la muestra se hace incidir sobre la muestra. Cuando el rayo láser incide en la muestra, se produce la fotoluminiscencia y la muestra emite luz a longitudes de onda que dependen de la composición de la muestra. La muestra está orientada de tal manera que el rayo láser reflejado y la emisión de radiación fotoluminiscente se propagan en diferentes direcciones. La radiación emitida se dirige a un espectrómetro. Dentro del espectrómetro, una rejilla de difracción separa las diferentes longitudes de onda en diferentes direcciones hacia un conjunto de fotodetectores que miden la intensidad de cada componente de longitud de onda. La información obtenida se trata con un ordenador para obtener el espectro de fotoluminiscencia. El espectro indica las intensidades relativas de la luz a diferentes longitudes de onda que llegan al detector.

En la presente Tesis los materiales compuestos de TiO_2/CNT se caracterizaron mediante un espectrofluorímetro Fluorolog-3 (HORIBA) (Fig 2.12), la longitud de onda de la radiación fue 380 nm y se hizo un barrido de 400 a 700 nm. Estos análisis se realizaron en el grupo de investigación del profesor Hiromi Yamashita en la Universidad de Osaka (Japón).

Figura 2.12. Equipo de fotoluminiscencia Fluorolog-3 (HORIBA).

2.2.12. Termogravimetría

La técnica de termogravimetría se basa en registrar la variación de masa de la muestra de estudio cuando esta se somete a un programa de temperatura bajo una atmósfera determinada. Generalmente un equipo de análisis térmico se compone de un sistema de control de gases (controla la atmósfera de análisis), una balanza, un horno, un controlador de temperatura y un sistema de adquisición de datos. El análisis térmico se puede realizar usando un programa de temperatura constante (isotermo), calentando a velocidad constante, enfriando o cualquier combinación de ellos. La atmósfera también se puede controlar pudiendo ser estática o dinámica y este control de la atmósfera de análisis permite descomponer sustancias bajo atmósfera inerte o llevar a cabo reacciones químicas [24,25].

En esta técnica hay que considerar que la velocidad de calentamiento, el tamaño de partícula de la muestra, la cantidad de la muestra y la atmósfera y el caudal del gas empleado son factores que influyen en los resultados obtenidos. Además, una característica fundamental de la técnica es que únicamente permite detectar procesos que lleven asociados una variación de masa, como por ejemplo descomposición, sublimación, reducción, desorción, adsorción o absorción, entre otros. Por lo tanto, esta técnica de análisis térmico es una de las más utilizadas, debido a que presenta innumerables aplicaciones tanto para análisis cualitativos como cuantitativos.

En esta Tesis la termogravimetría se ha utilizado para determinar de forma cuantitativa la masa perdida o temperatura óptima de calcinación/descomposición de los materiales preparados en la presente Tesis. También se ha empleado para determinar la cantidad de material carbonoso presente en los materiales compuestos desarrollados. Con este objetivo, se calentaron 10 mg de muestra en una termobalanza a una velocidad 5 ºC/min en aire (100 mL/min) desde temperatura ambiente hasta 900 ºC. Los experimentos se realizaron mediante una termobalanza TG SDT 2960 (TA instrument) (Fig. 2.13), que se encuentra disponible en el grupo de investigación Materiales Carbonosos y Medio Ambiente del Insituto de Materiales y del Departamento de Química Inorgánica de la Universidad de Alicante.

Figura 2.13. Termobalanza TG SDT 2960 (TA instrument) utilizada en la presente Tesis.

En esta Tesis también se ha realizado el análisis termogravimétrico en condiciones isotermas, con el objetivo de calcular el área superficial activa de los materiales carbonosos (ASA), debido que este parámetro es muy útil para entender la reactividad de estos [26,27]. El procedimiento se realizó con una termobalanza TG SDT 2960 (TA instrument), que se encuentra disponible en el grupo de investigación Materiales Carbonosos y Medio Ambiente del Instituto de Materiales y del Departamento de Química Inorgánica de la Universidad de Alicante. Este análisis consiste en calentar 10 mg de muestra a 920 ºC con una velocidad de calentamiento de 5 ºC/min, con un flujo de 100 mL/min y se mantiene a temperatura constante (920 ºC) durante 30 min en atmósfera de nitrógeno. Seguidamente se enfría a 250 ºC y se mantiene 1 h a temperatura constante en atmósfera de N_2. Finalmente se permuta la atmósfera de nitrógeno a una atmósfera de aire sintético y se mantiene a temperatura constante (250 ºC) durante 7 h, para favorecer la quimisorción de oxígeno en el material de carbón (Fig. 2.14).

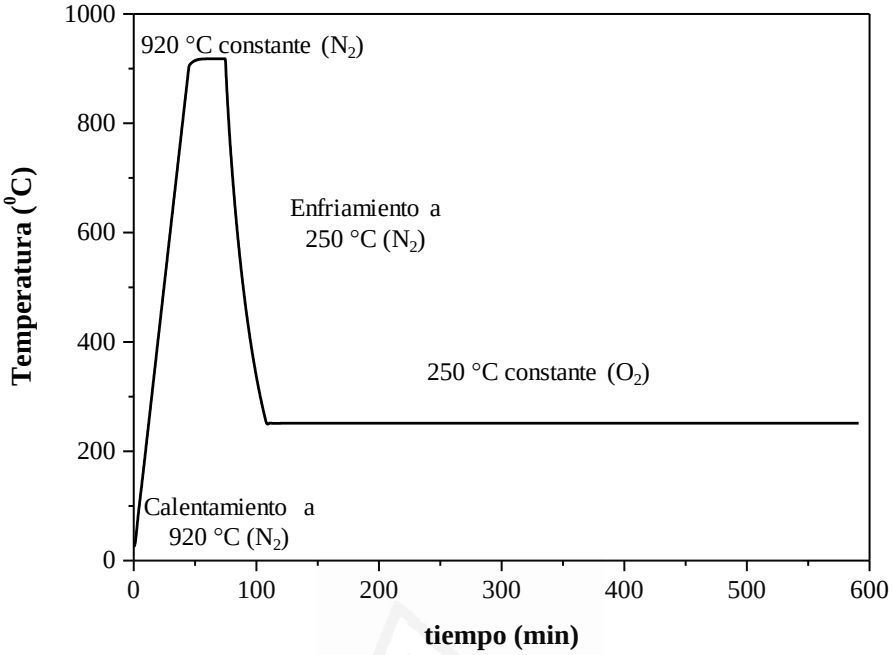

Figura 2.14. Programa de temperaturas usado para el análisis del ASA de los materiales carbonosos analizados en la presente Tesis.

A partir de la siguiente ecuación se obtiene el área superficial activa del material carbonoso (ASA) (ec. 2.8):

$$\mathrm{ASA}\ (m^2/g) = \frac{1}{w_0} \cdot \frac{A \cdot N_A \cdot (w_c - w_0)}{N_O} \qquad (2.8)$$

donde ASA es el área superficial activa del material, w_0 es la masa inicial en la etapa de la quimisorción, A es el área de un átomo de oxígeno (0.083 nm^2), N_A es el número de Avogadro, N_O es el peso molecular del oxígeno atómico.

2.2.13. Desorción a Temperatura Programada

La técnica de desorción a temperatura programada (DTP) se basa en someter la muestra de estudio, a un programa de temperaturas controlado bajo una atmósfera controlada (gas inerte). Los gases emitidos por la muestra generalmente proceden de la descomposición de los grupos superficiales presentes en la superficie del material y se analizan en un detector que se encuentra a la salida de la termobalanza, como por ejemplo un espectrómetro de masas. El análisis de los gases a través del espectrómetro de masas permite obtener información acerca de la composición química y la estabilidad de los grupos funcionales superficiales presente en los materiales. Este hecho hace que esta técnica presente una gran relevancia en el estudio de materiales, entre los que destacan los materiales carbonosos, debido a que permite caracterizar su química superficial [28].

En el proceso de calentamiento de un material carbonoso bajo una atmosfera inerte, este generalmente desorbe CO, CO_2 y H_2O que pueden proceder de la descomposición de los grupos funcionales oxigenados superficiales o descomposición de compuestos inorgánicos presentes y/o de la desorción del agua adsorbida en el material. Estos gases se desorben a distintas temperaturas dependiendo de la estabilidad de cada especie. Los grupos carboxílicos, lactonas y anhidridos descomponen como CO_2 a distintas temperaturas (300-500 ºC), mientras los grupos carbonilos, quinonas, fenoles o éter descomponen como CO a temperaturas más elevadas (600-1200 ºC) debido que estas especies son más estables (Fig. 2.15) [29-31].

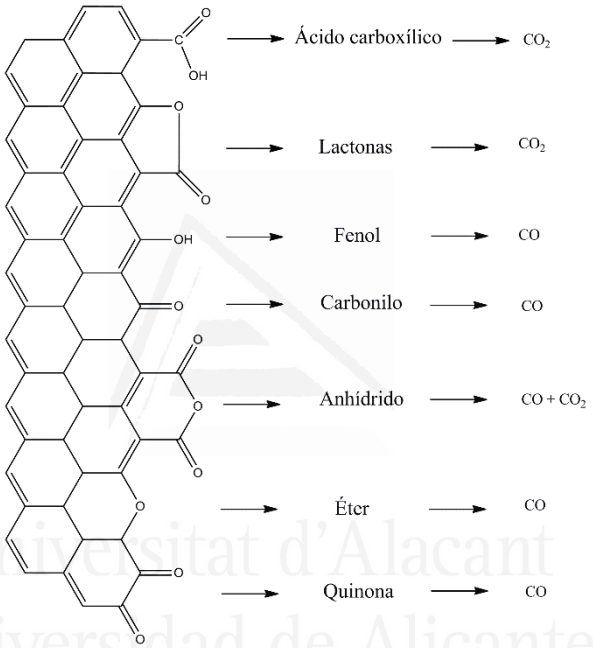

Figura 2.15. Grupos funcionales presentes en los materiales de carbón y los gases emitidos debido a su descomposición.

En esta Tesis se han estudiado mediante análisis a temperatura programada los grupos superficiales presentes en los nanotubos de carbón (CNT) usados para la síntesis de materiales compuestos TiO_2-CNT. Con este propósito se utilizó un equipo DSC-TGA SDT 2960 Simultenaous (TA instruments) acoplado a un espectrómetro de masas Thermostar GSD 300 T3 (Balzers) (Fig. 2.16), este equipo se encuentra en el grupo de investigación Materiales Carbonosos y Medio Ambiente del Insituto de Materiales y del Departamento de Química Inorgánica de la Universidad de Alicante. Para la realización de estos análisis se utilizaron 10 mg de muestra y se realizó utilizando un flujo de Helio como gas portador (100 mL/min) y atmosfera, desde temperatura ambiente hasta 950 ºC con una velocidad de calentamiento de 20 ºC/min.

Figura 2.16. Sistema experimental empleado para llevar a cabo los ensayos de DTP.

2.2.14. Espectrometría de Masas

La espectrometría de masas (EM) es una técnica de análisis que permite identificar los componentes de una mezcla ya que convierte las especies de análisis en iones gaseosos y los acelera para que se separen en función de su relación masa/carga. El fundamento de la técnica se basa en detectar iones que se generan debido al bombardeo electrónico de los analitos [32]. A consecuencia de este bombardeo se generan iones debido a la eliminación de electrones o por la ruptura de moléculas del analito, de manera que se obtiene un espectro característico de cada molécula. El haz de iones generado se acelera hacia el interior del analizador, donde se separan los iones en función de la relación masa/carga (m/z) de cada ion generado y estos llegan al detector donde se registra una corriente eléctrica en función del tiempo. De esta manera es posible seguir la evolución de las especies de estudio en función del tiempo. Una condición relevante a tener en cuenta es que los espectrómetros de masa deben trabajar en alto vacío (10^{-10} a 10^{-6} atm) para mantener bajas presiones en el equipo, con el objetivo de que ni los electrones generados por la fuente ni los iones generados por el bombardeo de la muestra se vean afectados en su trayectoria y velocidad por las moléculas de gas que estén presentes en el equipo.

En la presente Tesis se han utilizado dos equipos de espectrometría de masas quadrupolar, el modelo Thermostar (Fig. 2.17) y el Ommistar (ambos de Pfeiffer Vacuum). Estos equipos están disponibles en el grupo de investigación Materiales Carbonosos y Medio Ambiente del Insituto de Materiales y del Departamento de Química Inorgánica de la Universidad de Alicante. Estos espectrometros se han utilizado como detector en la técnica de caracterización DTP y para los ensayos catalíticos de fotoxidación total de propeno y oxidación selectiva de propileno con el objetivo de monitorizar la presencia y cuantificación de los componentes de las mezclas de gases.

Figura 2.17. Espectrofotómetro de masas ThermoStar (Pfeiffer Vacuum) usado en esta Tesis.

2.2.15. Cromatografía de Gases

La cromatografía es un método físico de separación empleado para la caracterización de mezclas complejas. Es un conjunto de técnicas que se basan en el principio de retención selectiva, cuyo objetivo es separar los distintos componentes de una mezcla, permitiéndo su identificación y cuantificación [33].

En cromatografía de gases la muestra se volatiliza y se inyecta en una columna cromatográfica. La elución se produce por el flujo de una fase móvil de gas inerte (generalmente He), que no interactúa con las moléculas de analito y que tiene como función transportar el analito a través de la columna cromatográfica, donde las especies que forman parte de la muestra son separadas en función de su naturaleza física y/o química para después poder analizarlas en un detector. La columna cromatográfica consiste en una conducción tubular de longitud variable (entre 2 y 60 m) en cuyo interior se encuentra una fase estacionaria con la que interacciona la corriente de gas portador y gas de análisis (fase móvil). En cromatografía de gases, la fase estacionaria está constituida por un sólido activo con elevado grado de porosidad. Dichas columnas pueden ser de dos tipos, columnas capilares o empaquetadas. Las columnas capilares son generalmente tubos de vidrio o sílice fundida que tienen un diámetro pequeño, de unos cientos de micras. En ellas, la fase estacionaria se puede distribuir de diferentes maneras, bien directamente en forma de recubrimiento sobre las paredes del tubo, o bien distribuyendo un soporte inerte sobre las paredes del tubo y depositando la fase estacionaria sobre éste. En las columnas empaquetadas, que tienen un diámetro de mayor tamaño (2-5 mm), la fase estacionaria se distribuye en forma de relleno a lo largo de toda la columna, que generalmente es de vidrio o acero inoxidable. La separación de los distintos componentes de la mezcla de gases se basa en que cada molécula de la mezcla de gases interacciona con la fase estacionaria de la columna, dependiendo de su tamaño y de su polaridad. Por este motivo, las moléculas se separan en función de su naturaleza química, de manera que los tiempos de retención (tiempo al que sale cada especie de la columna) de cada especie son

diferentes y su elución ocurre a tiempos diferentes. Los distintos compuestos de análisis separados pasan al detector, donde se obtiene una señal que es proporcional a la cantidad de analito. Por lo tanto, de esta forma se pueden identificar y cuantificar los componentes de la mezcla. Generalmente los detectores usados en cromatografía son el detector de conductividad térmica (TCD) y el detector de ionización en llama (FID). El detector TCD responde a la diferencia de conductividad térmica existente entre una corriente del gas portador puro y el gas portador mezclado con alguna otra sustancia. Sin embargo, el FID se basa en la detección de iones formados durante la combustión de compuestos orgánicos en una llama de oxígeno/hidrógeno.

En el desarrollo experimental de la presente Tesis Doctoral se ha empleado la cromatografía de gases para estudiar la actividad catalítica de los materiales desarrollados para las distintas aplicaciones, como son las reacciones de fotooxidación total de propeno, en la oxidación selectiva de propileno y en la producción de H_2 a partir de la descomposición de amino borano utilizando el catalizador en forma de polvo.

En el caso de ensayos catalíticos de las reacciones de fotooxidación total de propeno en fase gas se ha utilizado un cromatógrafo de gases 6890N (Agilent) (Fig. 2.18) equipado con un detector de TCD y FID para la detección del propeno y los productos generados en la reacción. La temperatura del inyector es de 185 ºC. La columna utilizada para los análisis es una columna empaquetada de 182 cm de longitud, que contiene dos rellenos distintos concéntricos (Alltech, CTR-I). El relleno interno de la columna tiene un diámetro de 1/8" y el externo tiene un diámetro de 1/4". La temperatura de operación de la columna es de 75 ºC y el caudal de muestra es 60 mL/min. La temperatura de trabajo del detector es de 250 ºC. En estas condiciones, el tiempo empleado para cada análisis es de 5 minutos. Este cromatógrafo está disponible en el grupo de investigación Materiales Carbonosos y Medio Ambiente del Insituto de Materiales y del Departamento de Química Inorgánica de la Universidad de Alicante.

Figura 2.18. Cromatógrafo de gases 6890N (Agilent) usado en esta Tesis.

En el caso de los ensayos catalíticos de las reacciones de oxidación selectiva de propileno en fase gas, se ha utilizado un cromatógrafo de gases 7820A (Agilent) equipado con dos columnas, una empaquetada CTR-I (Alltech) conectada al detector TCD y la otra en forma de capilar de 25 cm Porabond-Q (Agilent) conectada al detector FID. Para poder determinar cuantitativamente la composición deseada de la reacción de estudio (epóxido de propileno) se deben calibrar previamente los posibles productos de reacción, entre los que destacan el epóxido de propileno, acetaldehído, acroleína, propanal, y/o isopropanol entre otros. El método utilizado para poder medir los compuestos se describe brevemente y consta de una inyección de la muestra gaseosa a 130 ºC. A continuación, el cromatógrafo se calienta hasta 180 ºC y se mantiene a esta temperatura en condiciones isotermas durante aproximadamente 6 min desde la inyección. Este cromatógrafo se encuentra disponible en el grupo de investigación Materiales Carbonosos y Medio Ambiente del Insituto de Materiales y del Departamento de Química Inorgánica de la Universidad de Alicante.

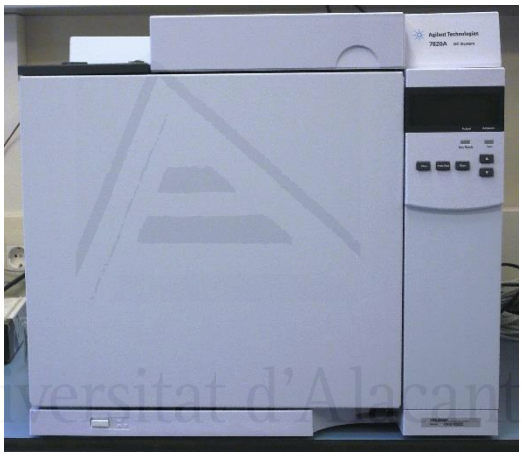

Figura 2.19. Cromatógrafo de gases 7820A (Agilent) usado en esta Tesis.

En el caso de los ensayos de descomposición del amino borano en fase líquida, se ha utilizado un cromatógrafo GC8A (Shimadzu) para analizar el H_2 producido por el catalizador. El cromatógrafo GC8A está equipado con una columna Molecular Sieve 5A de 4 m. La temperatura de la columna es de 110 ºC y la del detector y el inyector es de 120 ºC. Este cromatógrafo se encuentra en el grupo de investigación del profesor Hiromi Yamashita en la Universidad de Osaka (Japón).

Figura 2.19. Cromatógrafo de gases GC8A (Shimadzu).

2.3. Ensayos Catalíticos

A continuación, se presentarán y describirán lo ensayos catalíticos que se han utilizado en la presente Tesis para estudiar y probar los catalizadores desarrollados con distintas conformaciones (catalizador en polvo o como relleno en microrreactores) en distintas aplicaciones (oxidación fotocatalítica de propeno en fase gas, oxidación selectiva de propileno en fase gas y la descomposición fotocatalítica del amino borano en fase líquida).

2.3.1. Oxidación Fotocatalítica de Propeno en Fase Gas con el Fotocatalizador en Polvo o Como Relleno en Microrreactores

En esta Tesis se han llevado a cabo ensayos de actividad catalítica en la reacción de fotooxidación total de propeno en dos conformaciones diferentes del catalizador. Se han probado los catalizadores en polvo y conformados en dos tipos de microrreactores diferentes (microrreactores capilares y reactores de chip para microfluídica).

- Procedimiento para el análisis del ensayo de fotooxidación de propeno utilizando catalizadores en polvo.

El procedimiento para llevar a cabo el experimento de oxidación fotocatalítica de propeno [34] se ha realizado introduciendo 0.11 g de fotocatalizador en polvo sobre un lecho de lana de cuarzo en el interior de un reactor de cuarzo lineal. Seguidamente, el reactor se conecta al sistema de forma paralela a la lámpara. Tras purgar el sistema con He, se hace pasar una corriente de propeno de 100 ppmv en aire con un flujo de 30 mL/min. Una vez se alcanza una concentración de propeno estable (aproximadamente 2 h), se enciende la lámpara UV y la iluminación se mantiene durante 2 h más aproximadamente, hasta que la señal de propeno alcanza un valor estable (se considera que se ha alcanzado el estado estacionario). Los gases de salida fueron analizados por espectrometría de masas en un equipo Ommistar (Pfeiffer

Vacuum) (Fig. 2.20 a) o por cromatografía de gases en un equipo 6890N (Agilent) (Fig. 2.20 b) dependiendo del sistema utilizado. Ambos sistemas se encuentran en el grupo de investigación Materiales Carbonosos y Medio Ambiente del Insituto de Materiales y del Departamento de Química Inorgánica de la Universidad de Alicante.

Figura 2.20. Sistemas experimentales utilizados en la oxidación fotocatalítica de propeno: a) sistema con un espectrofotómetro de masas como detector y b) sistema con un cromatógrafo de gases como como detector

El parámetro utilizado para evaluar la actividad de los catalizadores en la reacción de fotooxidación total de propeno ha sido la conversión de propeno, que se ha calculado de acuerdo de la siguiente expresión (ec. 2.9), a partir del calibrado de los distintos gases de forma previa.

$$\text{Conversión de Propeno (\%)} = \frac{C_{\text{inicial } C_3H_6} - C_{\text{estado estacionario}_{C_3H_6}}}{C_{\text{inicial } C_3H_6}} \times 100 \qquad (2.9)$$

El procedimiento utilizado para evaluar la actividad de los catalizadores se describirá más específicamente para cada fotocatalizador (TiO_2 y materiales compuestos basados en TiO_2) en los Capítulos 3, 4 y 5, indicando qué detector se ha utilizado (espectrometro de masas o cromatógrafo de masas) para el análisis, ya que pueden haber pequeñas discrepancias en la actividad catalítica dependiendo del detector utilizado.

- Procedimiento para el análisis del ensayo de fotooxidación de propeno utilizando catalizadores conformados en microrreactores.

El procedimiento para llevar a cabo los experimentos de oxidación fotocatalítica de propeno en los fotocatalizadores incorporados en los microrreactores es similar al procedimiento usado para los catalizadores en polvo. Para el ensayo, los microrreactores (microrreactores capilares y reactores de chip para microfluídica) se conectan como si fueran una columna de cromatografía al cromatógrafo GC2020 (Shimadzu) para poder introducir los gases de reacción en el interior del microrreactor

y así poder realizar la reacción catalítica (Fig. 2.21). El caudal habitual empleado en estos experimentos es de aproximadamente 5 mL/min, aunque en determinadas ocasiones se han realizado ensayos a distinto caudal para estudiar el efecto de la velocidad espacial sobre la actividad de estos catalizadores. El sistema experimental consta de un medidor de presión, que es de especial importancia cuando se trabaja con los microrreactores, puesto que en alguno de estos casos la caída de presión en el sistema es significativamente superior a la observada al trabajar con los catalizadores en polvo. Los gases de salida se han evaluado con un cromatógrafo de gases 6890N (Agilent). El sistema de reacción se encuentra en el grupo de investigación Materiales Carbonosos y Medio Ambiente del Insituto de Materiales y del Departamento de Química Inorgánica de la Universidad de Alicante.

Figura 2.21. Sistema experimental utilizado en la oxidación fotocatalítica de propeno utilizando catalizadores conformados en microrreactores.

El procedimiento utilizado para evaluar la actividad de los catalizadores conformados en microrreactores se describirá más específicamente para esta aplicación en los Capítulos 8 y 9, indicando qué tipo de microrreactor se ha utilizado para los análisis (microrreactores capilares y reactores de chip para microfluídica).

2.3.2. Oxidación Selectiva de Propileno en Fase Gas con el Catalizador en Polvo.

El procedimiento utilizado para la evaluación de la actividad catalítica de los catalizadores en polvo desarrollados en esta Tesis en la oxidación selectiva de propileno a óxido de propileno en fase gas se explicará brevemente a continuación [35]. Previamente a los ensayos catalíticos, los catalizadores se pretratan mediante un tratamiento térmico a 500 ºC con una rampa de calentamiento de 10 ºC/min, pasando

una corriente de gas (30 mL/min) compuesta por 5% en volumen de H_2 en He con la finalidad de reducir las nanopartículas de metal. Después de este pretratamiento, se analiza la actividad de los catalizadores en la reacción de oxidación de propileno durante al menos 4 h en condiciones de estado estacionario a una temperatura constante de 200 ºC. Para este análisis se utilizaron unas condiciones estándar donde la velocidad espacial fue 10.000 $mL \cdot g^{-1} \cdot h^{-1}$ y la composición de la fase gas fue de un 10 % de C_3H_6, un 10% H_2, un 10% O_2 y un 70% He en volumen. La composición de los gases de salida fue analizada por un espectrómetro de masas (Pfeiffer Vacuum, Thermostar) y un cromatógrafo de gases (Agilent 7820A) equipado con dos columnas, PoraBond Q (Agilent) y CTR-I (Alltech), la primera separa compuestos orgánicos (propileno, propano, oxido de propileno, acetaldehído y acetona) y la segunda separa compuestos inorgánicos (principalmente, O_2 y CO_2) (Fig. 2.22).

Figura 2.22. Sistema experimental utilizado para los ensayos de actividad catalítica en la reacción de oxidación selectiva de propileno.

Los parámetros utilizados para evaluar la actividad de los catalizadores en la reacción de oxidación selectiva de propileno han sido la conversión de propileno, el rendimiento de OP, la selectividad a OP y la eficiencia del H_2 que se han calculado de acuerdo a las siguientes expresiones (ec. 2.10, 2.11, 2.12 y 2.13) a partir del calibrado de los distintos gases de forma previa.

$$\text{Conversión de Propileno } (\%) = \frac{C_{\text{inicial } C_3H_6} - C_{\text{estado estacionario}_{C_3H_6}}}{C_{\text{inicial } C_3H_6}} \times 100 \qquad (2.10)$$

$$\text{Rendimiento de PO } (\%) = \frac{C_{\text{salida}_{PO}}}{C_{\text{inicial } C_3H_6}} \times 100 \qquad (2.11)$$

$$\text{Selectividad PO } (\%) = \frac{C_{\text{salida}_{PO}}}{C_{\text{inicial } C_3H_6} - C_{\text{estado estacionario } C_3H_6}} \times 100 \qquad (2.12)$$

$$\text{Eficiencia de } H_2 \ (\%) = \frac{C_{\text{salida}_{PO}}}{C_{\text{estado estacionario } H_2O}} \times 100 \qquad (2.13)$$

El procedimiento descrito en este apartado (Oxidación selectiva de propileno en fase gas con el catalizador en polvo) y los parámetros utilizados para evaluar la actividad de los catalizadores se describirán más específicamente para los catalizadores (Ni/Ti-SiO_2) utilizados para esta aplicación en el Capítulo 6.

2.3.3. Descomposición Fotocatalítica de Amino Borano en Fase Líquida con el Fotocatalizador en Polvo

El procedimiento utilizado para la evaluación de la actividad catalítica de los catalizadores desarrollados en esta Tesis (Me/TiO_2-MWCNT) para su aplicación en la producción de H_2 en fase líquida con el fotocatalizador en polvo se explicará brevemente a continuación [36]. La cantidad requerida de catalizador se introduce en un vial de cuarzo, seguidamente se añade agua destilada y se sella el vial mediante un septum y parafilm. Se burbujea Ar en el interior del vial durante 30 min para purgar el aire (Fig. 2.23 a)). Para dar comienzo a la reacción (temperatura ambiente), se ilumina el vial con una lámpara de luz UV-Vis y se introduce el amino borano que se va a descomponer. Cada 5 min se retiran 0.2 mL del gas generado en el interior del vial (Fig. 2.23 b)) y se inyectan en el cromatógrafo GC8A (Shimadzu) equipado con una columna Molecular Sieve 5A de 4 m, con el objetivo de obtener la concentración de H_2 producido en la reacción.

Figura 2.23. Sistema experimental utilizado para los ensayos de actividad catalítica en la descomposición del amino borano: a) Sistema del purgado del catalizador y b) Sistema de reacción.

El procedimiento descrito en este apartado (descomposición fotocatalítica de amino borano en fase líquida con el fotocatalizador en polvo) se describirá más específicamente para los catalizadores (Metal/TiO_2-MWCNT) utilizados para esta aplicación en el Capítulo 7.

2.4. Referencias

[1] W.H. Zachariasen, Theory of X-Ray Diffraction in Crystals, Dover Publications, United States, 2004.

[2] W.H. Bragg, X Rays and Crystal Structure, G. Bell and Sons, England, 1915.

[3] H. Zhang, J.F. Banfield, J. Phys. Chem. B. 104 (2000) 3481-3487.

[4] T.R. Dulski, Trace Elemental Analysis of Metals Methods and Techniques, CRC Press, United States, 1999, pp. 177-252.

[5] B.O. Regan, M. Grätzel, Nature. 353 (1991) 737-740.

[6] F. Rouquerol, J. Rouquerol, K. Sing, Adsorption by Powders and Porous Solids: Principles, Methodology and Applications, Academic Press, London, 1999

[7] J.B. Condon, Surface Area and Porosity Determinations by Physisorption, Measurements and Theory, Elsevier Science, 2006.

[8] M. Thommes, K. Kaneko, A. V. Neimark, J.P. Olivier, F. Rodriguez-Reinoso, J. Rouquerol, K.S.W. Sing, Pure Appl. Chem. 87 (2015) 1051-1069.

[9] S. Brunauer, P.H. Emmett, E. Teller, J. Am. Chem. Soc. 60 (1938) 309-319.

[10] J.M, Martín-Martínez, Adsorción Física de Gases y Vapores por Carbones, University of Alicante, Spain, 1990.

[11] M.M. Dubinin, Chem. Rev. 60 (1960) 235-241.

[12] A.D. Gianfrancesco, Materials for Ultra-Supercritical and Advanced Ultra-Supercritical Power Plants, Elsevier Science, 2006, p. 197-245.

[13] R. Marassi, F. Nobili, Measurament Methods, Structural and Chemical Properties: Scanning Electron Microscopy, in: Encycl. Electrochem. Power Sources, Elsevier Science 2009, pp. 758-768.

[14] R.F. Egerton, Physical Principles of Electron Microscopy. An Introduction to TEM, SEM and AEM, Springer, United States, 2005.

[15] D.B. Williams, C.B. Carter, Transmission Electron Microscopy, 2nd Ed. Springer-Verlag, United States, 2009.

[16] D.B. Williams, C.B. Carter, Transmission Electron Microscopy, 2nd Ed. Springer-Verlag, United States, 2009, pp. 581-603.

[17] E.P. Bertin, Introduction to X-Ray Spectrometric Analysis, Springer, United States, 1978.

[18] V.B. Crist, Handbook of Monochromatic XPS Spectra: Semiconductors, Wiley, United States, 2000.

[19] J.M. Albella-Martín, A.M. Cintas, T. Miranda, J.M. Serratosa, Introducción a la Ciencia de Materiales. Técnicas de Preparación y Caracterización, Consejo Superior de Investigaciones Científicas, España, 1946

[20] D.A. Skoog, J. Leary, Análisis Instrumental, McGraw-Hill, 1993.

[21] A. Montaser, D.W. Golightly, Inductively Coupled Plasmas in Analytical Atomic Spectrometry, 2nd Ed. Wiley, United Sates, 1992.

[22] B.C. Smith, Fundamentals of Fourier Transform Infrared Spectroscopy, 2nd Ed., CRC Press, United States 2011.

[23] M. Anpo, M. Kondo, C. Louis, M. Che, S. Coluccia, J. Am. Chem. Soc. 111 (1989) 8791-8799.

[24] M.E. Brown, Introduction to Thermal Analysis. Thecniques and Applications, Springer, London, 1988. [25]D.A. Skoog, F.J. Holler, S.R. Crouch, Principles of Instrumental Analysis, 6th Ed., Cengage Learning, 2006.

[26] N. R. Laine, F. J. Vastola, P. L. Walker J. Phys. Chem. 67 (1963) 2030-2034.

[27] A. Gabe, R. Ruiz-Rosas, E. Morallón, D. Cazorla-Amorós, Carbon, 148 (2019) 430-440.
[28] P. Serp, J.L. Figueiredo, Carbon Materials for Catalysis, Wiley, 2008, pp. 45-92.
[29] M.C. Román-Martínez, D. Cazorla-Amorós, A. Linares-Solano, C. Salinas-Martínez de Lecea, Carbon, 31 (1993) 895-902.
[30] J.L. Figueiredo, M.F.R. Pereira, M.M.A. Freitas, J.J.M. Órfão, Carbon 37 (1999) 1379-1389.
[31] H.P. Boehm, Carbon, 40 (2002) 145-149.
[32] D.A. Skoog, F. Holler, T. Nieman, Principios de Análisis Instrumental, 5a ed, McGraw-Hill, 2001.
[33] P. Kusch, Gas Chromatography: Derivatization, Sample Preparation, Application, IntechOpen, 2019.
[34] M.A. Lillo-Ródenas, N. Bouazza, A. Berenguer-Murcia, J.J. Linares-Salinas, P. Soto, A. Linares-Solano, Appl. Catal. B Environ. 71 (2007) 298-309.
[35] J. García-Aguilar, I. Miguel-García, J. Juan-Juan, I. Such-Basáñez, E. San Fabián, D. Cazorla-Amorós, Á. Berenguer-Murcia, J. Catal. 338 (2016) 154-167.
[36] J. García-Aguilar, M. Navlani-García, Á. Berenguer-Murcia, K. Mori, Y. Kuwahara, H. Yamashita, D. Cazorla-Amorós, RSC Adv. 6 (2016) 91768-91772.

Chapter 3

Photooxidation of Propene with TiO_2 Photocatalyst

In this Chapter, we have developed a methodology to synthesize TiO_2 that allows obtaining meso-macroporous materials with hierarchical porosity and high thermal stability for their application as photocatalysts in the removal of VOCs, in this specific case propene. The materials synthesized in this work were characterized by SEM, TEM, XRD, TG and nitrogen adsorption. It is observed that the samples calcined at 250 °C and 500 °C present a high photoactivity for the photooxidation of propene, which is similar to the benchmark material P25 (commercial TiO_2 sample). Moreover, the textural properties are better than those for P25, indicating that the samples are interesting for the preparation of photocatalysts with different conformations, such as in the form of coatings and fillings in different size scales.

3.1. Introduction

Nowadays, the removal of volatile organic compounds (VOCs) at low concentrations is still a hot topic, as it was mentioned in Chapter 1, because these compounds are very harmful to the environment and human health. These pollutants cause carcinogenic effects, problems in the central nervous system and climate change, among several other adverse effects [1,2].

Among the different VOCs, the removal of propene is interesting because this contaminant is considered a highly reactive volatile organic compound (HRVOC) which is involved in the formation of ground-level and tropospheric ozone and, therefore, in photochemical smog [3,4]. This contaminant appears in vehicle emissions and in many industrial applications, such as petrochemical plants, cigarette smoke, and others [5,6]. There are several ways to eliminate propene, for example, incineration, adsorption, absorption, condensation, among others. However, heterogeneous photocatalytic oxidation (PCO) is a novel way to eliminate this pollutant because it can be performed at room temperature and at atmospheric pressure [7]. A wide variety of semiconductors has been studied as photocatalysts, such as ZnO [8], CdS [9] and, most noticeably, TiO_2 [10-12].

Titania (TiO_2) has received significant attention in the last decades for its unique properties, including photocatalytic activity, photo- and chemical stability, nontoxicity, and relatively low production cost [13-15]. Moreover, TiO_2 is an important industrial product in many applications such as inorganic pigment, photocatalyst, sunscreen, or in energy storage and electrochromism [16-20]. From a structural point of view, titanium dioxide has three crystalline polymorphs: anatase, rutile, and brookite. Among the three crystalline phases, anatase shows a better photocatalytic behavior [21]. An interesting commercial TiO_2 powder is P25 (EVONIK), which consists of 70% of the anatase phase and 30% of the rutile phase of titanium dioxide. This commercial titania nanomaterial is widely used as photocatalyst in photochemical reactions due to their very high photocatalytic activity [22] and is used as benchmark material to assess the potential of different photocatalysts.

Many factors influence the photocatalytic properties of TiO_2, such as the particle size, morphology, exposed lattice planes, and crystalline phase [23,24]. P25 has already been optimized in many of these factors. Nevertheless, this material presents comparatively low surface area and this factor may be important to improve the photo-oxidation of propene. For this reason, it is interesting to synthesize new TiO_2 materials that improve on factors such as the surface area and the capacity to photo-oxidize propene with respect to P25 [25-27]. Despite the fact that propene is a reasonably small molecule, if its mineralization is not complete, deposition of carbon on the catalyst surface cannot be ruled out and, thus, diffusional limitations and deactivation may arise. Furthermore, the way TiO_2 powders are usually produced is

in the form of nanoparticles, as we have already reported [26]. Thus, the use of the catalyst in a bed configuration will likely result in compacting which will ultimately give rise to diffusional limitations. In order to ensure a proper mass transfer, a hierarchical catalyst architecture with linked macro-mesoporosity could be an interesting option.

In this Chapter, we have synthesized several TiO_2 samples with hierarchical porosity to obtain materials with large accessible surface area to improve the results obtained using P25, commercial TiO_2. These materials have been synthesized through modifications on the report by Zhu et al [25] by incorporating urea in the sol synthesis in order to develop a material with pores large enough to warrant the absence of any diffusional limitations [28,29]. If this larger porosity can be enhanced by producing an interconnected network of meso- and macropores (which would give to a so-called hierarchical porosity) it would be of interest for the preparation of photocatalysts. It is of course also promising if such materials could be prepared with different conformations, such as in the form of coatings and fillings in different size scales for applications that need a robust continuous material and a good mass transfer for a good photooxidation performance [28]. Moreover, removal of the templates used during synthesis has been carried out by washing or calcination in order to check the effect of these treatments. The prepared materials were studied in photooxidation of propene at low concentrations under UV irradiation at room temperatures, yielding promising results in terms of photocatalytic performance.

3.2. Materials and Methods

3.2.1. Materials

Titanium (IV) butoxide (TTB, 97%, Sigma-Aldrich), glacial acetic acid (HAc, 99%, Sigma-Aldrich), Pluronic F-127 (F-127, Sigma-Aldrich), absolute ethanol (EtOH, 99.8%, Fisher Scientific), formamide (FA, 99.5%, Sigma-Aldrich), urea (99%, Merck), and deionized water were used in the present work. All reactants were used as received, without further purification.

3.2.2. Sample Preparation

The TiO_2 samples were prepared adapting a previously reported synthesis performed by Zhu et al [25]. The main difference was the incorporation of urea in order to induce the desired formation of mesoporosity, through the gradual decomposition of urea giving rise to a controlled and homogeneous pH variation as reported by our research group, which has successfully given rise to robust hierarchical silica monoliths [28].

The synthesis of TiO_2 samples was performed as follows: 5 g of the titanium precursor (titanium tetrabutoxide, TTB) were weighed and dissolved in 7.9 g of EtOH. This solution ("solution A") was stirred vigorously for 10 min. Then, in this order 1.6 g of HAc, 0.3 g of F-127, 1.6 g of deionized water, 7.9 g EtOH, 0.4 g of FA, and 0.4

g of urea were weighed and added in a separate vessel. The mixture was stirred for 10 min ("solution B"). Solution B was added dropwise on "solution A" under vigorous stirring. The resulting solution was rapidly transferred to an autoclave and heated at 60 °C for 24 h to promote gel formation and the temperature was later increased to 120 °C with a dwelling time of 24 h to promote the decomposition of urea. The samples obtained were washed or calcined at different temperatures. The nomenclature of the samples used in this work were TiO_2_AS for sample without treatment (as-synthesized), TiO_2_W for sample washed with ethanol for 9 h under reflux conditions and TiO_2_250, TiO_2_500, TiO_2_700, and TiO_2_900 for samples calcined at 250 °C, 500 °C, 700 °C, and 900 °C, respectively, for 6 h with a heating ramp rate of 1 °C/min.

3.2.3. Sample Characterization

Several techniques were employed for the characterization of the samples. The crystal phase composition and crystallinity of TiO_2 were determined by X-ray diffraction (XRD) analysis using a Bruker D8-Advance equipment. Cu Kα (1.54056 Å) radiation was used. The scanning velocity was 2º/min, and diffraction patterns were recorded in the angular 2θ range of 6-80º. The crystallite size was estimated by applying the Scherrer equation (eq. 3.1) [30] using the full width at half-maximum (FWHM) data of the major diffraction peak and a K factor of 0.9:

$$B = \frac{K \cdot \lambda}{\beta \cdot \cos\theta} \qquad (3.1)$$

where B is the crystalline size (nm); K is the dimensionless shape factor whose value is 0.9; λ is the wavelength of the radiation source used, which is 1.54056 Å for Cu Kα radiation; β is the full width at half maximum intensity (FWHM) (radians), and θ is the Bragg angle at the position of the peak maximum. We used an internal standard (Silicium carbide, SiC) to correct the effect of both the equipment and the analysis temperature on peak width.

The organic residue contained in the TiO_2 samples (due to any template leftovers) was determined by thermogravimetric analysis using a thermobalance (SDT 2960 instrument). In these analyses, the sample was heated up at 900 °C in air (heating rate of 5 °C min^{-1}).

The surface chemistry of the TiO_2 materials was analyzed by Fourier transform infrared (FTIR) spectroscopy (FTIR JASCO 4100) in transmission mode from 400 cm^{-1} to 4000 cm^{-1}. KBr was used as reference standard.

The optical absorption properties were studied by UV-Vis/DR spectroscopy (Jasco V-670). $BaSO_4$ was used as the reference standard and the reflectance signal was calibrated with a Spectralon standard (Labsphere SRS-99-010, 99% reflectance). The absorption edge wavelength was estimated from the intercept at zero absorbance

of the high slope portion of each individual spectrum in the range 200–800 nm (absorbance method). Then, the band gap (eq. 3.2) can be calculated [31] as:

$$Eg = \frac{1239.8}{\lambda} \tag{3.2}$$

where Eg is the band gap energy (eV) and λ is the edge wavelength (nm).

Textural properties were determined by applying the Brunauer-Emmett-Teller (BET) equation, and the Dubinin-Raduskevich equation to the N_2 adsorption data obtained at -196 °C using an Autosorb-6B apparatus from Quantachrome [32], obtaining the BET surface area (S_{BET}) and total micropore volume (V_{N_2}), respectively. The as-synthesized and washed TiO_2 samples were degassed at 110 °C for 11 h and the calcined TiO_2 samples were degassed at 250 °C for 4 h prior to adsorption experiments. Pore volume was determined from the nitrogen adsorption volume at a relative pressure of 0.95. Mesopore size distributions for all the samples were obtained applying the Barrett-Joyner-Halenda (BJH) formula to the N_2 desorption branch data from the adsorption isotherms at -196 °C, using the software provided by Quantachrome.

The morphology of the samples was analyzed by transmission electron microscopy (TEM, JEOL JEM 2010) and field emission scanning electron microscope (FESEM, ZEISS Merlin VP Compact). Average nanoparticle size was carried out by counting 100 particles (except for samples TiO_2_700, TiO_2_900, for which 50 and 30 particles were counted, respectively) for each sample.

The evolution of crystal phase composition and crystallinity of TiO_2 was determined by X-ray diffraction (XRD) in situ by changing the temperature using a Bruker D8-Advance equipment. Cu Kα (1.54056 Å) radiation was used. The scanning velocity was 2 °/min, and diffraction patterns were recorded in the angular 2θ range of 6-60 °. SiC was used to correct the effect of temperature. The ramp used in this experiment was the following, the sample was heated from 25 to 900 °C (heating rate of 5 °C min^{-1}) measuring the XRD pattern at 25, 250, 500, 700, and 900 °C for dwelling times of 0, 30, and 60 min in these temperatures. The crystallite size was estimated by applying the Scherrer Equation (eq. 3.1). The content of anatase was calculated by applying the Spurr-Myers equation, as shown in Equation (eq. 3.3) [33].

$$W_A = \frac{100}{1+1.26 I_R/I_A} \tag{3.3}$$

$$W_R(\%) + W_A(\%) = 100 \tag{3.4}$$

where W_A is the weight fraction of anatase in the mixture; W_R is the weight fraction of rutile in the mixture; I_R is the intensity of the diffraction peak of rutile; and I_A is the intensity of the diffraction peak of anatase.

3.2.4. Catalytic Test

The photocatalytic performance of the different photocatalysts was studied using an experimental system designed in our laboratory [34]. The system consists of a vertical quartz reactor where the photocatalyst bed is placed on a quartz wool bed. The reactor is 50 mm in height, its diameter is 20 mm, and the quartz wool support height is around 10 mm. A UV lamp is placed parallel to the quartz reactor, at a distance around 1 cm. The UV lamp radiation peak appears at 365 nm. The commercial reference of this lamp is a TL 8W/05 FAM (1W). Finally, the coupled quartz reactor lamp is surrounded by a cylinder covered with aluminum foil (Fig. 3.1).

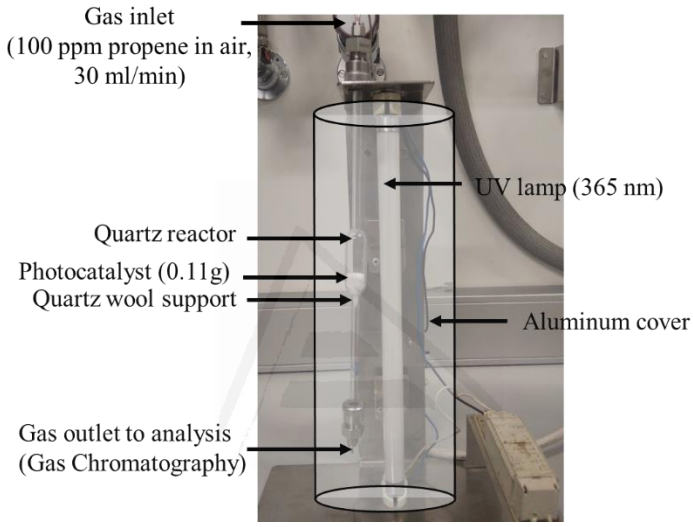

Figure 3.1. Experimental system used in the photooxidation of propene.

The weight of photocatalyst used in these experiments was 0.11 g for all the samples. The photocatalysts were used for the oxidation of propene at 100 ppmv in air at room temperature, 25 °C. The calibrated gas cylinder was supplied by Carburos Metálicos, S.A. The flow rate of the propene-containing stream was 30 (STP) mL/min in all experiments.

The propene-containing stream was passed through the photocatalyst bed and, afterwards it was injected in a GC chromatograph (Agilent 6890N) operating with a CTR-I column (Alltech) at 75 °C. GC chromatograph permits to follow the evolution of the concentration of propene in the outlet gas. Propene conversion was calculated using the flowing expression (eq. 3.5):

$$\text{Propene conversion (\%)} = \frac{C_{\text{initial}_{C_3H_6}} - C_{\text{steady state}_{C_3H_6}}}{C_{\text{initial}_{C_3H_6}}} \times 100 \qquad (3.5)$$

where $C_{\text{initial}C_3H_6}$ is the initial propene concentration, 100 ppmv and $C_{\text{steady state}C_3H_6}$ is the propene concentration at steady state conditions in the photocatalyst bed outlet gas when the UV light is switched on.

Additionally, blank tests were performed under the same experimental conditions as the catalytic tests, but in the absence of the TiO_2 photocatalysts, and no catalytic activity was detected.

3.3. Results and Discussion

3.3.1. Materials Characterization

The changes in crystal phase and crystallite size of all the samples were studied by ex situ powder X-ray diffraction (XRD), and the corresponding patterns of the samples calcined at different temperatures for 6 h are presented in Fig. 3.2. The corresponding results regarding crystallite size and phase composition are listed in Table 3.1. In the XRD patterns it is observed that the as-synthesized TiO_2 (without treatment) is composed of anatase phase with very low crystallinity. Upon increasing the calcination temperature in the 250-700 °C range, the crystallinity of the samples increases (as evidenced from the sharper, narrower characteristic peaks of anatase TiO_2) while maintaining the same anatase phase. As some authors have reported in the literature, the temperature up to which the anatase phase is stable is around 500 °C [35]. Treating the sample at higher temperatures results in the formation of the more stable rutile phase. In our case, the anatase-to-rutile transformation occurs in a significantly higher temperature range, between 700 °C and 900 °C, which indicates a very high thermal stability for the TiO_2 samples prepared in this work. Given our modification of the reported protocol (see Sample Preparation (Section 3.2.2) for full details), it appears that urea favors the thermal stabilization of the anatase phase [29].

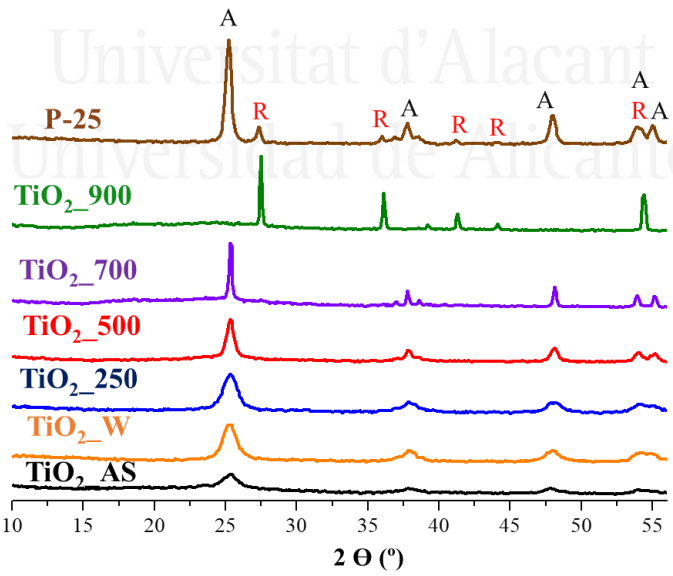

Figure 3.2. XRD patterns of TiO_2 samples. Key: A = anatase; R = rutile.

With respect to the crystallite size of the samples shown in Table 3.1, the washing and low-temperature calcination treatments did not affect the crystallite size, being 7 nm in three cases (as-synthesized, washed, and calcined at 250 °C). Nevertheless, increasing the calcination temperature results in the sintering and growth of larger crystals [36].

Table 3.1. Crystallite size and phase composition of the TiO_2 samples prepared in this study (see Sample Characterization (Section 3.2.3) for full details).

Samples	Crystal Phase Composition	Crystallite Size (nm)
TiO_2_AS	100% Anatase	6
TiO_2_W	100% Anatase	7
TiO_2_250	100% Anatase	7
TiO_2_500	100% Anatase	13
TiO_2_700	100% Anatase	26
TiO_2_900	100% Rutile	48

In order to quantify the amount of organic matter present in the prepared samples, thermogravimetric analysis (TG) was done in all samples. The results of the performed TG experiments are showed in Fig. 3.3. The as-synthesized TiO_2 samples had a weight loss of about 25.8%, but samples TiO_2_W and TiO_2_250 already presented weight losses of around 9.0% and 6.0%, respectively, which are indicative of the removal of a substantial part of the organic matter used during the synthesis. The complete removal of the template requires higher temperatures, and this is necessary since it may block the porosity, affecting the photocatalytic performance. At calcination temperatures of 500 °C, 700 °C, and 900 °C these values were 2.5%, 0.58%, and 0.25%. The weight loss detected for the sample calcined at 500 °C could be due to the removal of traces of organic matter and weakly-adsorbed water at lower temperatures [37]. In order to corroborate this observation, FTIR experiments were conducted for the prepared TiO_2 samples (vide infra).

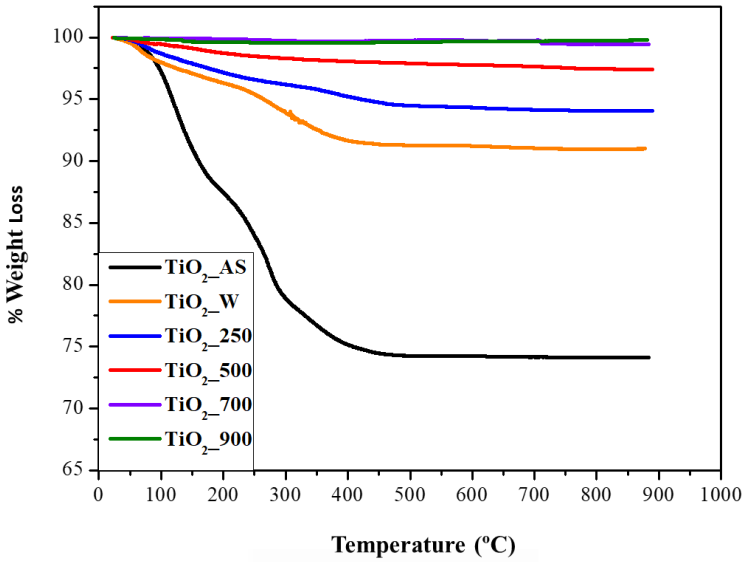

Figure 3.3. TG curves of the TiO_2 samples prepared in this study.

The analysis of the surface chemistry and the removal of reagents/templates (organic matter) after heat treatment were analyzed by FTIR. The results are presented in Fig. 3.4. The broad band at about 3000–3500 cm^{-1} and 1600 is attributed to the OH stretching of physisorbed water on the TiO_2 surfaces and hydrogen-bonded hydroxyl groups [38]. The as-synthesized sample and the washed sample show this broad band. After calcination at 250 °C the bands at 3000-3500 and 1600 cm^{-1} decreased in intensity, indicating the loss of physisorbed water on the TiO_2 surface. Moreover, when the calcination temperature is further increased this adsorbed water is eliminated and the bands appearing at 3000-3500 and 1600 cm^{-1} disappear. The remaining bands appearing at 3130 and 3220 cm^{-1} are indicative of the presence of OH groups on the surface of the TiO_2 [39]. This result agrees with the TG analyses in which the samples washed and calcined at 250 °C presented noticeable weight losses up to 500 °C, probably due to the removal of water and organic residues at lower temperature and adsorbed water at higher temperatures. In this respect, as the FTIR results show, increasing the calcination temperature not only removes the template molecules along with any remaining organic reagents used (lower wavenumber region), but also removes the physisorbed water (both weakly and strongly adsorbed water [37], higher wavenumber region) which might be detrimental towards photocatalytic applications.

The bands at 1110 cm^{-1} and 1420 cm^{-1} in the as-synthesized sample are assigned to the stretching vibration of C-N and the presence of the deformation mode of ammonium ions formed by the decomposition of excess urea [29], respectively. Moreover, this sample also presents bands at 1420, 1330, and 1110 cm^{-1} corresponding to C–H [11] vibrations of surfactants and complexing agents. In the sample washed with ethanol the band at 1110 cm^{-1} is not present because this step

removed a significant amount of organic reagents but, as indicated in the TG experiments (Fig. 3.3), not all organic matter was removed in the washing step. When the sample was calcined at low temperature (TiO_2_250) the bands corresponding to templates (organic matter) decreased. For this reason, and following up on the FTIR and TG results, it is necessary to calcine at 500 °C or higher temperatures in order to eliminate all reagents. Washing or calcination at lower temperatures may result in porosity blocking and/or adverse effects in the surface chemistry of the final material. These results are consistent with TG experiments (Fig. 3.3), because the as-synthesized TiO_2 has the higher loss of organic matter and presents the relevant characteristic bands for the corresponding compounds, as discussed above.

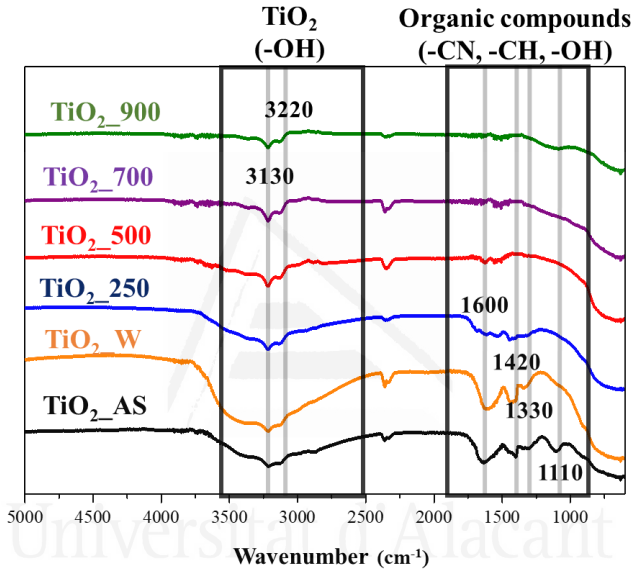

Figure 3.4. FTIR spectra of the TiO_2 samples prepared in this study.

The UV-Vis absorption properties of the TiO_2 materials prepared in this work was evaluated. The results are presented in Fig. 3.5 and in Table 3.2. The samples with the anatase crystal phase present a similar absorption edge and band gap, which is typical for anatase. However, the as-synthesized TiO_2 sample shows a slightly smaller band gap. This might be attributed to the very low crystallinity of the anatase phase and the presence of the templating agents used during the synthesis as shown in the XRD analysis, TG experiments, and FTIR spectra. Sample TiO_2_900 (the pure rutile phase from our XRD results) presents a different absorption edge and band gap (414 nm and 2.99 eV, respectively) with respect to the other samples, which is characteristic for the rutile phase.

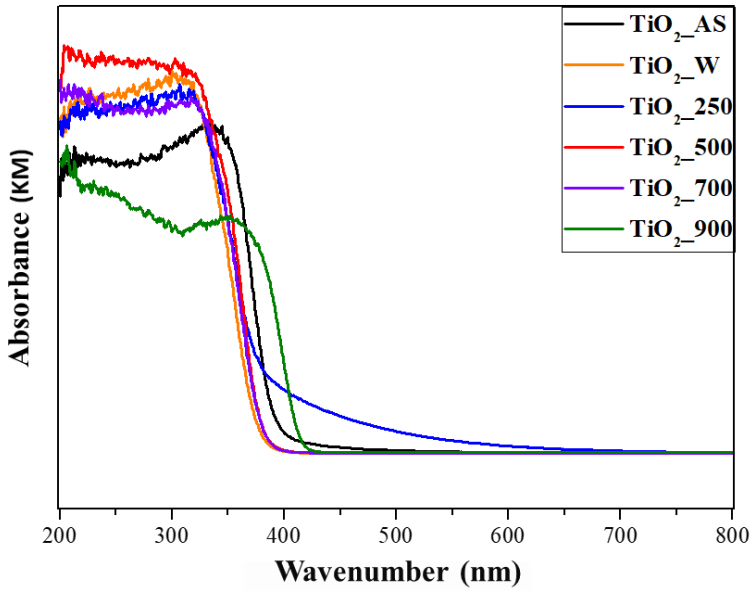

Figure 3.5. UV–Vis absorption spectra of the TiO_2 prepared samples.

Table 3.2. Absorption edge wavelengths (nm), band gap (Eg) and crystal phase composition values of the TiO_2 samples prepared in this study. The data for benchmark material P25 are shown for comparison purposes. Key: A = anatase; R = rutile.

Samples	λ (nm)	Eg (eV)	Crystal Phase Composition
TiO_2_AS	391	3.17	100% A
TiO_2_W	377	3.29	100% A
TiO_2_250	390	3.17	100% A
TiO_2_500	383	3.23	100% A
TiO_2_700	381	3.25	100% A
TiO_2_900	414	2.99	100% R
P25	409	3.03	70% A + 30% R

Nitrogen adsorption–desorption measurements were performed to determine the textural properties of the TiO_2 samples. As revealed in Fig. 3.6, the isotherms are of type IV with a hysteresis which is typical of mesoporous materials. The N_2 uptake and the size of the hysteresis loop is dependent on the treatment applied. In this sense, samples TiO_2_W and TiO_2_250 exhibit the highest uptakes, although present a small uptake at low relative pressures, which is indicative of a small amount of microporosity. Thus, both washing and calcination at a low temperature are able to activate the samples almost to a full extent, even if some organic moieties are still present (vide supra). Samples TiO_2_700 and TiO_2_900 show a significant interparticle sintering and collapse of the porous structure, as evidenced from their small surface areas. However, sample TiO_2_500 presents an isotherm close to that of sample

TiO_2_AS, but, as shown in the TG experiments (Fig. 3.3), the presence of leftover template/chemicals is very low.

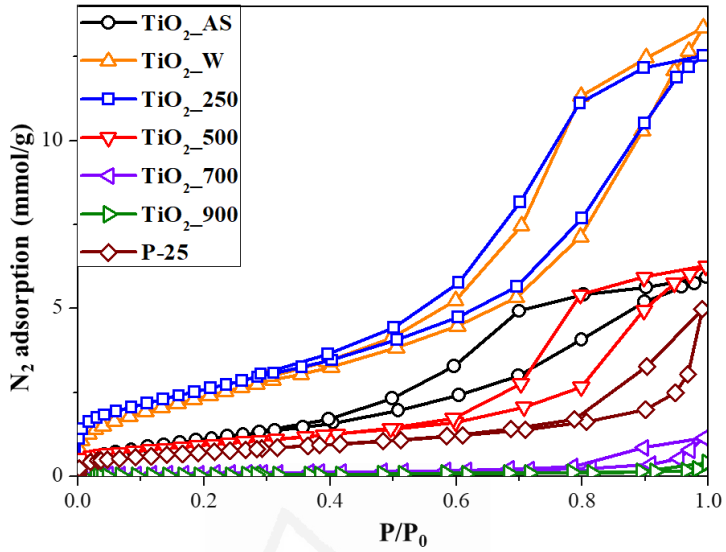

Figure 3.6. Isotherms of N_2 at 77 K for the different TiO_2 samples prepared in this study. The adsorption isotherm of the benchmark material P25 is also shown for comparison purposes.

Concerning the textural properties shown in Table 3.3, as the calcination temperature is increased, the BET surface area decreases from ~200 m^2/g (samples TiO_2_W and TiO_2_250) to 4 m^2/g (sample TiO_2_900). It, thus, appears that while sufficiently high calcination temperatures are needed in order to completely remove the organic matter, the very small TiO_2 crystallites have a strong tendency to sinter (even at relatively low temperatures) given their high surface energy and the TiO_2 structure collapses at temperatures ≥700 °C. This, however does not compromise the thermal stability of the anatase phase, which might be due to the synthesized samples being constituted by very small crystallites (see below, TEM analysis) with a large population of defects (probably as a consequence of the urea synthesis method employed) which block the anatase-to-rutile transition [35]. A similar trend is also observed for the total pore volume and the total micropore volume calculated applying the DR equation to the N_2 adsorption data, which indicates the collapse of the structure as the sample is heated to higher temperatures.

Table 3.3. Textural properties of the TiO_2 samples prepared in this study derived from the analysis of the N_2 adsorption isotherms. The data for benchmark material P25 are shown for comparison purposes.

Samples	S_{BET} (m^2/g)	$V_{total,0.95}$ (cm^3/g)	V_{N2DR} (cm^3/g)	Mean Pore Size (nm)
TiO_2_AS	96	0.20	0.04	6.2
TiO_2_W	201	0.43	0.07	8.8
TiO_2_250	212	0.42	0.08	6.2
TiO_2_500	85	0.20	0.03	8.7
TiO_2_700	7	0.02	0.00	-
TiO_2_900	4	0.01	0.00	-
P25	55	0.18	0.02	7.6

The morphology of the TiO_2 samples prepared in this study is shown in Fig. 3.7 (SEM images) and 3.8 (TEM images). As shown in Fig. 3.7, all samples present a heterogeneous morphology. The rougher surface observed for the as-synthesized sample, as well as those for samples calcined at temperatures below 500 °C, seems to become smoother upon calcination at higher temperatures, which might be indicative of the sintering of the crystallites and the collapse of the structure. Upon observation under TEM the samples consist of the aggregation of nanoparticles synthesized during the sol-gel process. Samples TiO_2_AS, TiO_2_W, and TiO_2_250 have similar mean particle sizes, which agrees very well with the crystallite sizes determined from XRD analyses. At higher calcination temperatures, the mean particle size noticeably increases (Fig. 3.8 and Table 3.4) in agreement with the literature [26]. The insets images in Fig. 3.8 show higher magnification pictures taken for the samples prepared in this study, in which a small surface amorphous layer is visible. This layer becomes less noticeable as the calcination temperature is increased. Given our observations, this amorphous layer might be similar to that previously reported [40] for inorganic-organic core-shell TiO_2 materials prepared by the combustion sol-gel method. It must be emphasized that, from the SEM and N_2 adsorption results, the samples prepared in this work present a hierarchical structure, as it can be evidenced by the large difference between the total pore volumes with respect to the values reported in the literature for similar solids [26]. It must be noted that, differently from our previous studies, the reported synthetic strategy did not rely on the precipitation of TiO_2 nanoparticles based on a sol-gel route, but on the transformation of a TiO_2 hydrogel into a TiO_2 hierarchical monolithic structure as a continuation of our previous efforts in which we have prepared continuous SiO_2 monoliths and coatings following a very similar approach [28] for applications needing a robust continuous material. In this respect, the materials prepared in this study are comprised of nanoparticles which have formed from a gel and which are organized in two different levels: one around a nonionic surfactant, and the other arising from the decomposition of urea during the

second step of the hydrothermal treatment. Comparing the particle size in TEM with the crystallite size obtained by XRD (Table 3.1), it is observed that at high temperatures there are significant discrepancies between the observed crystallite size and that determined by XRD. This is ascribed to the fact that the particles observed in TEM are not TiO_2 single crystals, but aggregates comprised of several TiO_2 smaller crystals which preserve their domains upon sintering.

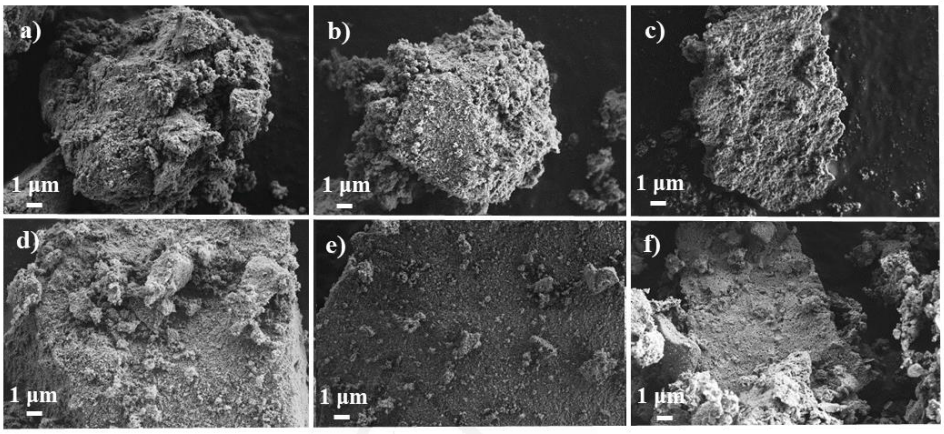

Figure 3.7. SEM of the different TiO_2 samples prepared in this study: a) TiO_2_AS, b) TiO_2_W, c) TiO_2_250, c) TiO_2_500, e) TiO_2_700 y f) TiO_2_900.

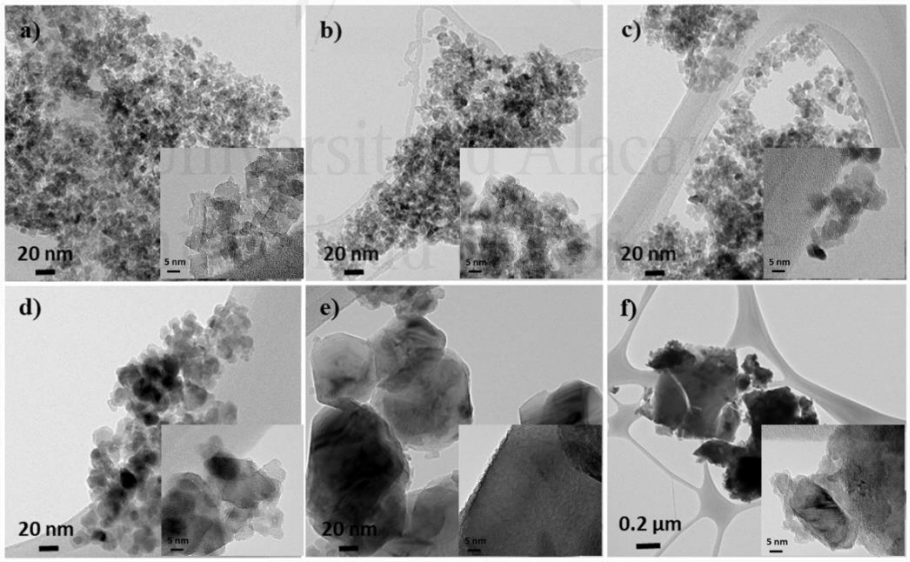

Figure 3.8. TEM of the different TiO_2 samples prepared in this study: a) TiO_2_AS, b) TiO_2_W, c) TiO_2_250, d) TiO_2_500, e) TiO_2_700 y f) TiO_2_900. Insets: higher magnification images for all samples. Scale bars for insets images: 5 nm.

Table 3.4. Crystal size obtained with TEM and XRD of TiO_2 samples. The mean crystallite size from TEM analysis was performed by counting 100 separate particles (unless stated otherwise) and averaging the results.

Samples	Crystallite Size (nm) "TEM"	Crystallite Size (nm) "XRD"
TiO_2_AS	6.4 ± 1.0	6
TiO_2_W	7.1 ± 0.9	7
TiO_2_250	7.2 ± 0.9	7
TiO_2_500	12.9 ± 1.5	13
TiO_2_700	80 ± 20 (50 part.)	26
TiO_2_900	270 ± 90 (30 part.)	48

In order to gain a better insight on the thermal stability of the prepared TiO_2 samples, in situ XRD measurements were carried out. Sample TiO_2_AS (as-synthesized) was mounted in the holder and a first scan was obtained at room temperature. The sample was then treated as described in the Experimental Section, collecting XRD spectra at the indicated temperatures and times. The results corresponding to the regions where the two characteristic peaks for anatase and rutile appear are presented in Fig. 3.9. Table 3.5 shows the phase composition of the samples after each respective treatment and the corresponding crystallite size. In Fig. 3.9 it is observed that the only phase for the starting sample TiO_2_AS is pure anatase, whose crystallinity increases with increasing temperature. The anatase to rutile transition takes place between 700 °C and 900 °C, which is a high temperature compared with the literature [35,41]. Moreover, when heating at temperatures >500 °C the size of the crystallites grows over time, as it can be seen comparing the results from the spectra obtained at 0 and 60 min of dwelling time. In this respect, the calcination time is an important tool to control the final crystallite size, as shown in Table 3.5.

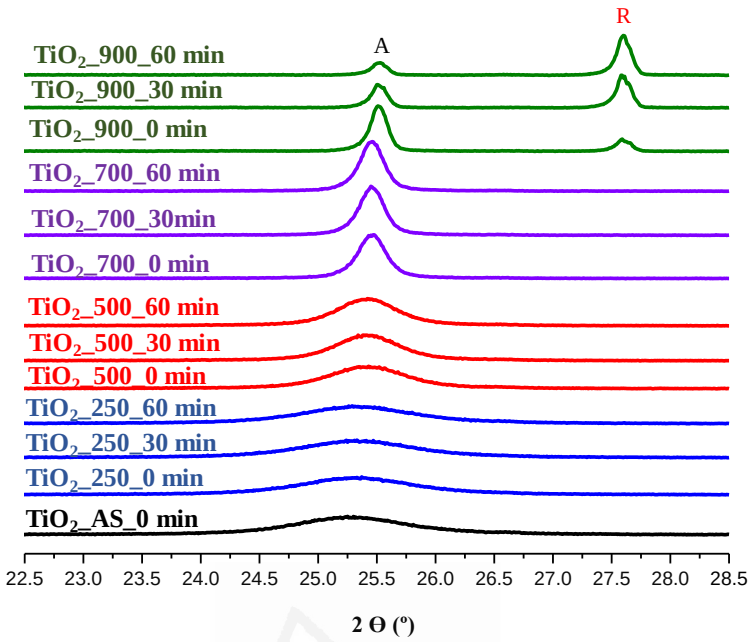

Figure 3.9. In situ XRD patterns at different temperatures of TiO2 samples. Key: A = anatase; R = rutile.

With respect to the phase composition, up to 700 °C all samples with different dwelling time present only the anatase phase. However, upon reaching 900 °C the phase composition of the sample changes over time. Initially (no dwelling time) sample TiO_2_900 is composed of 75% anatase and 25% rutile (similar to P25, that presents 70% anatase and 30% rutile). Moreover, if one compares this XRD in-situ at 900 °C with the XRD at 900 °C shown in Fig. 3.2 it is clear that the same sample calcined at 900 °C for 6 h has completely undergone the anatase-to-rutile transition, indicating once again how calcination time is an important parameter for the preparation of the samples in terms of both phase composition and crystal size.

Table 3.5. Phase composition and crystallite size of TiO_2 samples obtained in XRD in situ at different temperatures and dwelling times. A = anatase; R = rutile.

Samples	Phase Composition	Anatase Crystallite Size (nm)
TiO_2_AS_0 min	A (100%)	7
TiO_2_250_0 min	A (100%)	7
TiO_2_250_30 min	A (100%)	7
TiO_2_250_60 min	A (100%)	7
TiO_2_500_0 min	A (100%)	11
TiO_2_500_30 min	A (100%)	13
TiO_2_500_60 min	A (100%)	14
TiO_2_700_0 min	A (100%)	31
TiO_2_700_30 min	A (100%)	33
TiO_2_700_60 min	A (100%)	34
TiO_2_900_0 min	A (75%) + R (25%)	48
TiO_2_900_30 min	A (35%) + R (65%)	49
TiO_2_900_60 min	A (3%) + R (97%)	51

3.3.2. Photocatalytic Activity

The photocatalytic activity of TiO_2 materials prepared in this work was evaluated by studying the mineralization of propene in the gas phase (100 ppmv in air) to CO_2 at room temperature, following the reaction shown in eq. 3.6 [34]. Given that the photocatalyst used is no different from both a chemical and structural point of view, the mechanism responsible for the photooxidation process is the one already reported in literature [15,42]. Additionally, P25 was also used as a reference material. The results are summarized in Fig. 3.10.

$$2C_3H_6 + 9O_2 \leftrightarrow 6CO_2 + 6H_2O \quad (3.6)$$

The as-synthesized TiO_2 sample did not show photooxidation of propene because the TiO_2 active sites were blocked to reactants due to the presence of urea and the templating agent and/or the fact that the TiO_2 structure was not consolidated. When the sample was washed with EtOH under reflux the photoactivity increases noticeably, but the conversion is still below the performance of the benchmark P25 catalyst. This might be due to the fact that the washing does not remove all the organic matter (as evidenced by TG analysis) and does not increase the crystallinity (as shown by XRD). The porosity of the sample is more accessible (BET surface area over 200 m^2/g) but the structure is still not sufficiently consolidated and the remaining organic matter may be affecting the catalytic activity. The sample calcined at lower temperature (250 °C) presents a good conversion of propene (around 50%) which

surpasses the conversion of propene observed for sample P25. However, this sample has some residues from the template and a similar crystallinity to the washed sample. The main difference between these two samples is ascribed to the presence of water in the washed sample, which is detrimental in the photocatalytic activity of the resulting TiO_2. The sample calcined at 500 °C presents the best photocatalytic activity reported in this study. This sample present lower porosity compared to the samples washed or calcined at 250 °C, and a noticeable sintering of particles with respect to sample TiO_2_250 (from the TEM analysis). However, sample TiO_2_500 presents an improved crystallinity over these two samples and the absence of any organic impurities and adsorbed water (FTIR). These factors can improve the photocatalytic activity. For the samples calcined at 700 °C and 900 °C, the propene conversion decreases sharply because of the sintering of the particles and the collapse of the porous structure.

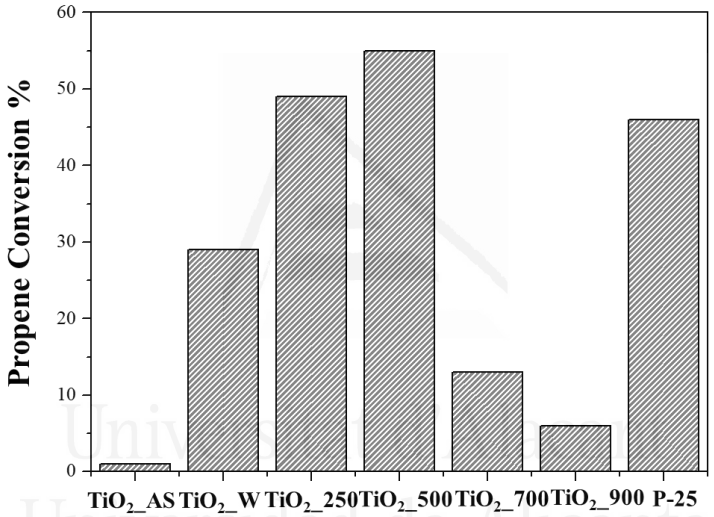

Figure 3.10. Propene conversion for TiO_2 samples and P25.

Considering the results obtained in this study in terms of crystal size, porous texture, and surface chemistry, it would appear that a compromise solution is mandatory in order to come up with the sample displaying the best performance. The most promising outlook seems to be the following: (1) large surface areas are beneficial for an enhanced access of reagents to the active sites of the photoactive material; (2) water adsorbed on the surface of the TiO_2 impoverishes the photocatalytic activity since it may enhance the recombination rate of electron-hole pairs [43]; (3) high crystallinities translate into improved photocatalytic activity. In this respect, the samples which show the highest surface area values do not present adequate surface chemistry (i.e., large bands in the 3000-3300 cm^{-1} region evidence a large amount of adsorbed water), have some organic matter or do not have a sufficiently crystalline structure. Thus, the obtained results are below those expected for a high surface area TiO_2 sample. On the other hand, the samples calcined at higher

temperatures present a significantly more crystalline structure, but their surface area is greatly diminished, which undermines their photocatalytic performance to a very large extent. In this respect, the sample calcined at 500 °C presents the best interplay because it still possesses a BET surface area of around 85 m^2/g together with a structure showing sufficient crystallinity and appropriate surface chemistry without organic matter, as shown by XRD, TG, and FTIR. This, in turn, results in a material which can be prepared by a simple, reproducible, and cost-effective sol-gel method which displays a remarkable photocatalytic activity.

3.4. Conclusions

In this study, a strategy of synthesis of TiO_2 of hierarchical porosity has been developed through modification of a reported synthesis. The protocol allows obtaining meso-macroporous materials which may be applied in the photocatalytic elimination of propene. Samples TiO_2_250 and TiO_2_500 prepared in this study have a high photocatalytic activity for propene photooxidation. Their performance is similar, and even slightly higher, to P25 (commercial TiO_2), indicating that the TiO_2_250 and TiO_2_500 samples are interesting for the preparation of photocatalysts with different conformations, such as in the form of coatings and fillings in different size scales furthermore show a good photooxidation performance at low concentrations. Interestingly, the nanostructure generated by this methodology delays the conversion of anatase to rutile to temperatures higher than 700 °C. Probably, the mesoporosity induced by the presence of urea generates a large concentration of defects that slows down the phase transition rate.

3.5. References

[1] H.J. Rafson Odor, VOC Control Handbook, 1st ed.; McGraw Hill: New York, NY, USA, 1998.
[2] S.E. Manahan, Environmental Chemistry, 8th ed.; CRC Press: Boca Raton, FL, USA, 2004.
[3] G. Barrefors, G. Petersson, J. Chromatogr. A. 643 (1993) 71-76.
[4] C.F. Murphy, D.T. Allen, Atmos. Environ. 39 (2005) 3785-3798.
[5] A. Petit, X. Montagne, SAE Tech. Paper 1993.
[6] F. Mühlberger, T. Streibel, J. Wieser, A. Ulrich, R. Zimmermann. Anal. Chem., 77 (2005) 7408-7414.
[7] M. Kaneko, I. Okura, Photocatalysis: Science and Technology, 1st ed.; Springer: Berlin, Germany, 2002.
[8] Y.H. Jang, S.T. Kochuveedu, M.A. Cha, Y.J. Jang, J.Y. Lee, J. Lee, J. Kim, D.Y. Ryu, D.H. Kim, J. Colloid Interface Sci. 345 (2010) 125-130.
[9] B.J. Liu, T. Torimoto, H. Yoneyama, J. Photochem. Photobiol. A Chem. 113 (1998) 93-97.
[10] M. Wei, X.L. Peng, Q.S. Liu, F. Li, M.M. Yao, Molecules. 22 (2017) 950.
[11] N. Arconada, Y. Castro, A. Durán, Appl. Catal. A Gen. 385 (2010) 101-107.
[12] C. Yu, X. Li, Z. Liu, X. Yang, Y. Huang, J. Lin, J. Zhang, C. Tang, Mater. Res. Bull. 83 (2016) 609-614.
[13] A. Hagfeldtt, M.A. Gratzel, Systems. Chem. Rev. 95 (1995) 49-68.
[14] A. Mills, S.K. Lee, J. Photochem. Photobiol. A Chem. 152 (2002) 233-247.
[15] J. Schneider, M. Matsuoka, M. Takeuchi, J. Zhang, Y. Horiuchi, M. Anpo, D.W. Bahnemann, Chem. Rev. 114 (2014) 9919-9986.
[16] J. Winkler, Titanium Dioxide: Production, Properties and Effective Usage, 2nd ed.; Vincentz Network: Hanover, Germany, 2013.
[17] X. Chen, S.S. Mao, Chem. Rev. 107 (2007) 2891-2959.
[18] A. Fujishima, X. Zhang, D.A. Tryk, Surf. Sci. Rep. 63 (2008) 515-582,
[19] A. Fujishima, K. Honda, Nature. 238 (1972) 37-38.
[20] M. Grätzel, Nature. 414 (2001) 338-344.
[21] J. Zhang, P. Zhou, J. Liu, J. Yu, Phys. Chem. Chem. Phys. 16 (2014) 20382-20386.
[22] J. Ryu, W. Choi, Environ. Sci. Technol. 42 (2008) 294-300.
[23] M. Yasmina, K. Mourad, S.H. Mohammed, C. Khaoula, Energy Procedia. 50 (2014) 559-566.
[24] H. Xu, J. Liao, S. Yuan, Y. Zhao, M. Zhang, Z. Wang, L. Shi, Mater. Res. Bull. 51 (2014) 326-331.
[25] W. Zhu, H. Yang, Y. Xie, S. Sun, X. Guo. Mater. Res. Bull. 73 (2016) 48-55.
[26] M. Ouzzine, M.A. Lillo-Ródenas, A. Linares-Solano, Appl. Catal. B Environ. 134 (2013) 333-343.
[27] M. Ouzzine, J.A. Maciá-Agulló, M.A. Lillo-Ródenas, C. Quijada, A. Linares-Solano, Appl. Catal. B Environ. 154 (2014) 285-293.
[28] J. García-Aguilar, I. Miguel-García, Á. Berenguer-Murcia, D. Cazorla-Amorós, ACS Appl. Mater. Interfaces 6 (2014) 22506-22518.
[29] S.C. Pillai, P. Periyat, R. George, D.E. Mccormack, K. Michael, H. Hayden, J. Colreavy, D. Corr, S. Hinder, J. Phys. Chem. C 111 (2007) 1605-1611.
[30] H. Zhang, J.F. Banfield, J. Phys. Chem. B 104 (2000) 3481-3487.
[31] B. Oregan, M. Gratzel, Nature 353 (1991) 737-740.
[32] M. Thommes, K. Kaneko, A.V. Neimark, J.P. Olivier, F. Rodriguez-Reinoso, J. Rouquerol, K.S.W. Sing, Pure Appl. Chem. 87 (2015) 1051-1069.
[33] R.A. Spurr, H. Myers, Anal. Chem. 29 (1957) 760-762.

[34] M.A. Lillo-Ródenas, N. Bouazza, A. Berenguer-Murcia, J.J. Linares-Salinas, P. Soto, A. Linares-Solano, Appl. Catal. B Environ. 71 (2007) 298-309.
[35] L. Cao, D. Chen, W. Li, R. Caruso, ACS Appl. Mater. Interfaces 6 (2014) 13129-13137.
[36] V. Likodimos, A. Chrysi, M. Calamiotou, C. Fernández-Rodríguez, J.M. Dona-Rodríguez, D.D. Dionysiou, P. Falaras, Appl. Catal. B Environ. 192 (2016) 242-252.
[37] L. Cano-Casanova, A. Amorós-Pérez, M. Ouzzine, M.A. Lillo-Ródenas, M.C. Román-Martínez, Appl. Catal. B Environ. 220 (2018) 645-653.
[38] P. Cheng, J. Qiu, M. Gu, Y. Jin, W. Shangguan, Mater. Lett. 58 (2004) 3751-3755.
[39] S. Musić, M. Gotić, M. Ivanda, S. Popović, A. Turković, R. Trojko, A. Sekulić, K. Furić, Mater. Sci. Eng. B, 47 (1997) 33-40.
[40] N.G. Moustakas, A.G. Kontos, V. Likodimos, F. Katsaros, N. Boukos, D. Tsoutsoua, A. Dimoulas, G.E. Romanos, D.D. Dionysiou, P. Falaras, Appl. Catal. B Environ 130 (2013) 14-24.
[41] A. Gribb, J.F. Banfield, Am. Mineral. 82 (1997) 717-728.
[42] L. Lin, Y. Chai, B. Zhao, W. Wei, D. He, B. He, Q. Tang, J. Inorg. Chem. 3 (2013) 14-25.
[43] N. Bouazza, M.A. Lillo-Ródenas, A. Linares-Solano, Appl. Catal. B Environ. 84 (2008) 691-698.

Chapter 4

Photooxidation of Propene with P25 Encapsulated in Silica

In this Chapter, we have performed the encapsulation of a reference TiO_2 material (P25) in spherical silica with hierarchical porosity using a sol-gel methodology. The same P25 material has been encapsulated within a "classical" MCM-41 mesoporous silica and a precipitated silica. The materials synthesized in this Chapter were characterized by ICP-OES, SEM, TEM, EDX, XRD, UV–Vis, TG, and nitrogen adsorption. It has been observed that the P25 samples encapsulated in silica present improved CO_2 production rates per mole of P25 in the photooxidation of propene, compared to P25 alone as well as the physical mixture of the two components. Moreover, the sample with a low content of P25 encapsulated in silica with hierarchical porosity presents the highest CO_2 production rates per mole of P25 with respect to the other P25/silica samples, due to a better accessibility of the titania phase and improved illumination of the active phase. Furthermore, the hierarchical porosity of the silica shell material favours mass transport and an increased concentration of reagents by adsorption near the titania phase. This improvement in photocatalytic activity is obtained by following a simple and reproducible synthesis methodology that employs an established silica preparation protocol. Thus, the choice of a silica with an adequate porosity for this application is proven to be a promising advancement in the development of efficient photocatalysts.

4.1. Introduction

In the last years, significant efforts have been made to increase the porosity of TiO_2 by synthesis of new nanoporous TiO_2 materials, as it was studied and described in Chapter 3 "Photooxidation of Propene with TiO_2 Photocatalyst". Another alternative is the fabrication of TiO_2/Adsorbent composites or supported TiO_2 on the surface of adsorbents to improve the properties of TiO_2, as described in Chapter 1 "Introduction" (focusing on the properties of the adsorbent materials), with the aim of enhancing the photocatalytic activity of TiO_2. The most interesting materials used as adsorbents in these composites are carbon materials, zeolites, mesoporous materials, and polymers, among others [1-4].

TiO_2/SiO_2 materials have attracted a great deal of attention due to the advantages of SiO_2 as support or as component of composites, due to its tunable surface area and pore size, as well as interconnectivity of the pore network facilitating mass transport, high surface acidity species (presence of Ti-O-Si), abundant surface hydroxyl groups and transparency in a broad wavelength range within the UV/Vis region [1,5].

Some studies have pointed out that the photocatalytic activity of TiO_2/SiO_2 composites is worse than that of the pure TiO_2 due to a blocking effect exerted by the silica on the active phase. For example, K. J. Nakamura et al showed a decreased rate of photocatalytic degradation of methylene blue when using TiO_2 encapsulated in SiO_2 [6]. Another report by M. Nussbaum et al demonstrated that as the thickness of the SiO_2 shell increased around the TiO_2 photocatalyst the activity of the active phase decreased [7].

On the other hand, many studies show that the presence of SiO_2 with TiO_2 particles is not deleterious. In fact, several reports point out that silica favours the photoactivity of TiO_2 [5,8-11]. In the last years, many efforts have been made to synthesize a nanostructured photocatalyst with enhanced adsorption and molecular-sieving properties, with tunable conformations, as well as improved mass transfer in order to optimize the activity of the photocatalyst. In this aspect, S. Wang et al synthesised TiO_2@SiO_2 core-shell nanoparticles, with a void interlayer [12]. Another approach was carried out by Y. Kuwahara et al where they developed yolk-shell nanostructured photocatalysts, consisting of TiO_2 nanoparticles in the core of spherical hollow silica shells [13]. In another study, X. Chen et al synthesised TiO_2/SiO_2 and TiO_2/ZrO_2 nanocomposites with hierarchical macro/mesopores [10]. In all cases, the authors intended the preparation of well-defined porous textures of their composites in order to favour mass transport and the selective concentration of reagents on the photoactive surface so as to optimize the photocatalytic activity. Some authors used this type of composites for the selective degradation of molecules due to the textural properties that silica brings forth to the composite [12,14].

Considering the extensive background, this Chapter is focused on the preparation of TiO_2/SiO_2 composites through the encapsulation of commercial P25 in silica

materials with markedly different porous textures (combining micro, meso, and macro-porosity in the best case scenario) in order to improve the photocatalytic activity by enhancing the adsorption characteristics of the composites (see Scheme 4.1). In this respect, the use of a silica shell displaying hierarchical porosity favours the aspects commented previously. Also, this Chapter studies the effect of the percentage of P25 encapsulated in the silica with hierarchical porous texture in order to test the illumination efficiency and to optimize the photocatalytic activity.

The materials studied in this work have been tested as photocatalysts in the removal of VOCs, specifically propene since this molecule might be taken as a representative example of low molecular weight VOCs, as described in Chapter 1 "Introduction" and Chapter 3 "Photooxidation of Propene with TiO_2 Photocatalyst". Moreover, this type of composites (TiO_2/SiO_2) can improve the photooxidation of VOCs as reported in the literature [1,5].

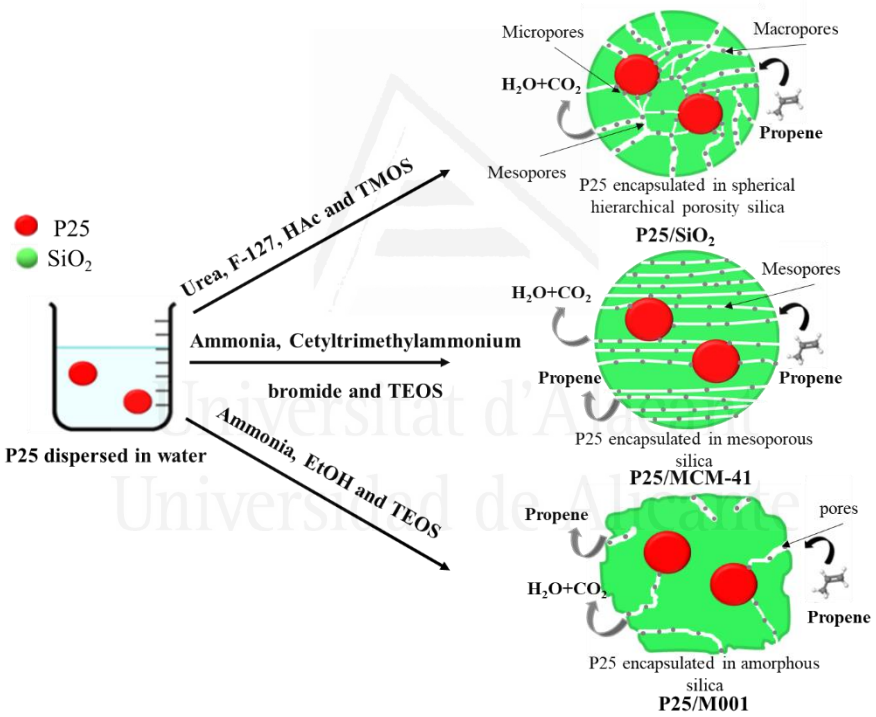

Scheme 4.1. Schematic representation of the synthetic procedure followed for the preparation of silica samples with different porous textures.

4.2. Materials and Methods

4.2.1. Materials

Titanium tetramethyl orthosilicate (TMOS, 99%, Sigma-Aldrich), tetraethyl orthosilicate (TEOS, 99%, Sigma-Aldrich), glacial acetic acid (HAc, 99%, Sigma-Aldrich), Pluronic F-127 (F-127, Sigma-Aldrich), cetyltrimethylammonium bromide (Sigma-Aldrich), urea (99%, Merck), ammonium hydroxide (NH_4OH, 30%, Panreac), absolute ethanol (EtOH, 99.8%, Fisher Scientific), TiO_2 (P25, Rutile: Anatase/30:70, 99.9%, 20-50 nm, Degussa) and deionized water were used in the present work. All reactants were used as received, without further purification. An ultrasonic probe equipment SONOPULS HD 2200 (BANDELIN electronic GmbH & Co. KG) was used to disperse the P25 powder in water.

4.2.2. Preparation of P25 (TiO_2) Encapsulated in Silica with Hierarchical Porosity

Commercial TiO_2 (Evonik P25) was encapsulated in spherical silica with hierarchical porosity following a straightforward sol-gel synthesis adapted from previous reports [15].

The synthesis of the P25/spherical hierarchical silica, done to obtain a nominal loading of 20 wt.% TiO_2, was performed as follows: 0.32 g of P25 were dispersed in 10.1 g of water using an ultrasound probe (Bandelin SONOPULS HD 2200) with a power of 660 W operating at 30% output power for 5 min. In order to prepare the composite material, the P25 dispersion in water was mixed with 0.9 g of urea, 0.81 g of F-127 and 5.8 μl of glacial HAc. This solution was stirred for 80 min. The solution was cooled at 0 ºC and 4 g of TMOS were added dropwise under vigorous stirring. The resulting solution was kept under stirring for 40 min at 0 ºC. The solution was rapidly transferred to a 40 mL autoclave and heated at 40 °C for 20 h to promote gel formation. The temperature was later increased to 120 °C with a dwelling time of 6 hours to promote the decomposition of urea to generate the mesoporosity. The resulting encapsulated P25 was calcined at 500 ºC for 6 h with a heating rate of 1 ºC/ min in order to remove the templates and any leftover reagents used in the synthesis.

To study the effect of the load of P25 in the encapsulation of the samples, the amount of P25 in the synthesis was changed to obtain composites with a nominal TiO_2 loading of 10 and 40 wt.% (0.16 g and 0.64 g, respectively). All samples were calcined as described above. The nomenclature of these samples is P25_10/SiO_2, P25_20/SiO_2 and P25_40/SiO_2 for the samples containing 10, 20, and 40 wt.% of nominal P25 loading, respectively.

4.2.3. Preparation of P25 (TiO_2) in a Precipitated Silica (M001) and a Mesoporous Silica (MCM-41)

With the objective of studying the effect of silica in the encapsulated P25, two more composites of P25 encapsulated (20 wt.% nominal loading) with precipitated silica [16] and a mesoporous silica (MCM-41 type) [17] were also prepared. We used the same methodology as that employed to encapsulate the P25 in hierarchical silica.

The synthesis of the P25 encapsulated in a precipitated silica was performed as follows: 0.4 g of P25 were dispersed in 20 g of water with an ultrasound probe (Bandelin SONOPULS HD 2200) with a power of 660 W operating at 30% output power for 5 min. In order to prepare the composite material, the P25 dispersion in water was mixed with 4 mL of NH_4OH, 85 g of EtOH to favour the precipitation of the silica, 70 g of water and 8 mL of TEOS, at 380 rpm for 1 h. The mixture was filtered and dried overnight at 50 ºC. The resulting encapsulated P25 was calcined at 500 ºC for 6 h with a heating rate of 1 ºC/ min in order to remove the templates and any leftover reagents used in the synthesis. This sample was named P25/M001.

The synthesis of the P25 encapsulated in mesoporous silica was performed as follows: 0.4 g of P25 were dispersed in 20 g of water with an ultrasound probe (Bandelin SONOPULS HD 2200) with a power of 660 W operating at 30% output power for 5 min. The composite material was prepared by dissolving 2 g of the templating agent (cetyltrimethylammonium bromide) in 76 g of deionized water. The mixture was stirred and heated gently until a clear solution was obtained. This mixture was added to the P25 dispersion in water, together with 4 mL of NH_4OH and 8 mL of TEOS. The resulting mixture was stirred at 380 rpm for 1 h. The suspension was filtered and dried overnight at 50 ºC. The resulting encapsulated P25 was calcined as described above. This sample was labelled as P25/MCM-41.

4.2.4. Samples Characterization

The percentages of TiO_2 and SiO_2 present in the samples were analyzed by inductively coupled plasma emission spectroscopy (ICP-OES), in a Perkin-Elmer Optima 4300 system. Dissolution of the samples was carried out by treating them with HF at room temperature.

X-ray diffraction (XRD) analysis was carried out in a Miniflex II Rigaku equipment. Cu Kα (1.54056 Å) radiation was used. The scanning velocity was 2 º/min, and diffraction patterns were recorded in the angular 2θ range of 6-80 º.

Thermogravimetric analysis was done in a thermobalance (SDT 2960 instrument, TA). In these analyses, the sample was heated up at 900 ºC in air (heating rate of 5 ºC min^{-1}).

The UV-VIS/DR spectroscopy analysis was performed in an UV-Visible spectrophotometer (Jasco V-670), with an integrating sphere accessory and powder sample holder. $BaSO_4$ was used as the standard reference and the reflectance signal

was calibrated with a Spectralon standard (Labsphere SRS-99-010, 99% reflectance). The absorption edge wavelength was estimated from the intercept at zero absorbance of the high slope portion of each individual spectrum in the range 200-800 nm (absorbance method). Then, the band gap can be calculated as (eq .4.1):

$$Eg = \frac{1239.8}{\lambda} \quad (4.1)$$

where Eg is the band gap energy (eV) and λ is the edge wavelength (nm).

Nitrogen adsorption-desorption isotherms were performed in an Autosorb-6B apparatus from Quantachrome. Prior to analysis all samples were degassed at 250 ºC for 4 h. BET surface area (S_{BET}) and total micropore volume (V_{N_2}) were determined by applying the Brunauer-Emmett-Teller (BET) equation, and the Dubinin-Raduskevich equation to the N_2 adsorption data obtained at -196 ºC, respectively. Total pore volumes were determined by nitrogen adsorption volume at a relative pressure of 0.95. Mesopore size distributions for all the samples were obtained applying the Barrett-Joyner-Halenda (BJH) equation to the N_2 desorption branch data from the adsorption isotherms at -196 ºC, using the software provided by Quantachrome.

Transmission electron microscopy (TEM) images were taken using a JEOL JEM-2010 equipment. Field-emission scanning electron microscope (FE-SEM) images were taken using a ZEISS, Merlin VP Compact, this equipment has incorporated a microanalysis system by Energy Dispersive X-ray spectroscopy (EDX), BRUKER Quantax 400 for performing elemental mapping of Si and Ti species present in the samples.

4.2.5. Catalytic Tests

The photocatalytic performance of the different materials was studied using an experimental system designed in our laboratory [18], as was mentioned in Chapter 3 "Photooxidation of Propene with TiO_2 Photocatalyst" and Chapter 2 "Experimental Techniques".

The photocatalysts synthesised in this Chapter were used for the oxidation of propene at 100 ppmv in air at room temperature under flow conditions. The calibrated gas cylinder was supplied by Carburos Metálicos, S.A.

The flow rate of the propene-containing stream was 30 (STP) mL/min after purging the reactor with helium.

The weight of photocatalyst used in these experiments was 0.11 g. However, in order to study the illumination efficiency and any possible inter-particle mass transfer issues, tests at different flow rates of propene were done in which the flow of propene and the mass of P25 were both changed in order to keep the space velocity constant (V_{sp} = flow (mL/min)/ mass of photocatalyst (g)) at a value of 257 mL/g·min. The

ratio was 10 mL min^{-1}/0.0367 g, 20 mL min^{-1}/0.0735, 30 mL min^{-1}/0.11 g and 40 mL min^{-1}/0.147 g. This was done in order to properly compare the samples prepared in this study. In addition, the sample P25_40/SiO_2 was measured with the same V_{sp} (257 mL/g·min) with respect to the amount of P25. Additionally, blank tests were performed under the same experimental conditions as the catalytic tests but in absence of the photocatalysts, resulting in non detectable catalytic activity.

To better study the combined effect between the silica and the P25, the reactor was filled with both silica and P25 as separate powders in a configuration in which the silica with hierarchical porosity was either on top or under the titania. The resulting samples were named SiO_2/P25 and P25/SiO_2 respectively. Furthermore, a physical mixture of P25 and silica (containing the appropriate amount of P25) was also prepared with the same purpose, the nomenclature of this sample is PM.

The propene-containing stream was passed through the photocatalyst bed until the propene concentration was stable (after about 3 h). The lamp is then switched on and kept working until a constant propene signal is achieved, that is, steady state conditions (usually after 3 h) and, afterwards the outlet gas is continuously analyzed by mass spectrometry Ommistar (Balzers).

Propene conversion was calculated using the following expression (eq. 4.2):

$$\text{Propene conversion (\%)} = \frac{C_{\text{initial}_{C_3H_6}} - C_{\text{steady state}_{C_3H_6}}}{C_{\text{initial}_{C_3H_6}}} \times 100 \qquad (4.2)$$

where $C_{\text{initial } C_3H_6}$ is the initial propene concentration, 100 ppmv and $C_{\text{steady state } C_3H_6}$ is the propene concentration at steady state conditions in the outlet gas when the UV light is switched on. Moreover, the CO_2 production rate was calculated per mole of P25, taken as the active phase, using the following expression (with the aim to normalize the results with the amount of P25) (eq. 4.3):

$$CO_2 \text{ production rate} = \frac{q_{gen}}{n} \qquad (4.3)$$

where q_{gen} is the molar flow rate of CO_2 generated (moles CO_2/s) and n is the moles of catalyst (moles of P25).

4.3. Results and Discussion

4.3.1. P25/SiO_2 Samples Characterization

In this section of this Chapter, the results on the characterization for the P25 samples encapsulated in spherical silica with hierarchical porosity (SiO_2) are presented, emphasizing the effect of the P25 loading in the composites.

The results obtained by ICP-OES show the discrepancies between the nominal and real loadings analysed by ICP-OES in the samples (Table 4.1). The sample with 10 wt.% nominal loading of TiO_2, results in a 3.8 wt.% loading by ICP-OES analysis. The other samples encapsulated in hierarchical silica present the same trend as showed in Table 4.1. As a result of the analysis of ICP-OES, the samples P25_10/SiO_2, P25_20/SiO_2, P25_40/SiO_2 show a content of 3.8, 8.14 and 15.9 wt.% of P25; these values will be used in the calculations in order to obtain reliable figures. The discrepancies between the nominal loading of TiO_2 and the results obtained for the ICP-OES technique may be due to a fraction of the P25 solid present in the dispersion which was not transferred to the reaction medium. In this aspect, we observed the presence of a significant amount of P25 solid adhered to the walls and in the bottom of the vessel where the dispersion was prepared after transferring this suspension.

Table 4.1. Percentage of titania of the sample prepared in this Chapter.

Samples	% TiO_2 Nominal	% TiO_2 ICP-OES
P25_10/SiO_2	10	3.8 ± 0.9
P25_20/SiO_2	20	8.1 ± 0.2
P25_40/SiO_2	40	15.9 ± 0.3

The XRD pattern of the P25/SiO_2 samples with different P25 loading are showed in Fig. 4.1 a). In all cases, the particles of P25 encapsulated in silica have the same crystalline phases as the benchmark P25 (rutile and anatase) after calcination at 500 ºC, indicating the presence of P25 in all composites (P25_10/SiO_2, P25_20/SiO_2 and P25_40/SiO_2) without any further modification. An elbow in the XRD pattern of all composites due to the presence of amorphous silica is also observed, as showed in the pattern for the naked SiO_2 sample [15]. TG analyses show a small weight loss of approximately 2 wt.% in all samples (see Fig. 4.1b)). This suggests that all organic matter and any leftover reagents present in the synthesis were eliminated in the calcination step. The low weight percentage losses observed might be due to adsorbed water or the possible decomposition reactions of hydroxyl groups at higher temperatures [19].

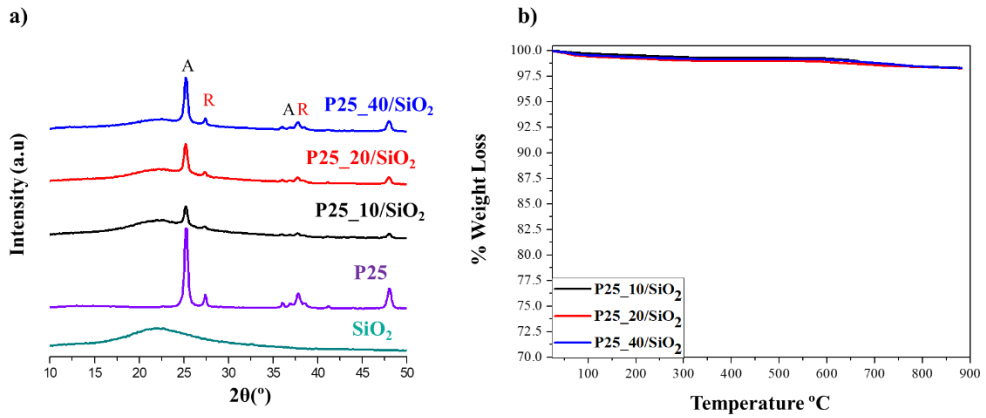

Figure 4.1. a) XRD patterns of all composites prepared with hierarchical porosity silica. The data for the SiO_2 and P25 are showed for comparison. Key: A = anatase; R = rutile and b) TG curves of the P25 encapsulated with hierarchical porosity silica.

The UV-vis spectra obtained for the P25/SiO_2 with different P25 loading samples are showed in Fig. 4.2. All hybrid photocatalysts with different loading of P25 show a similar absorption band edge at 400 nm. This fact indicated that the loading of P25 in the composite does not modify the absorption range and the band gap of the P25. However, the composites show a small discrepancy in the absorbance range and in the band gap with respect to the naked P25 (Fig. 4.2) indicating that the presence of the silica can slightly modify the band gap of P25 from 3.08 to 3.2 eV.

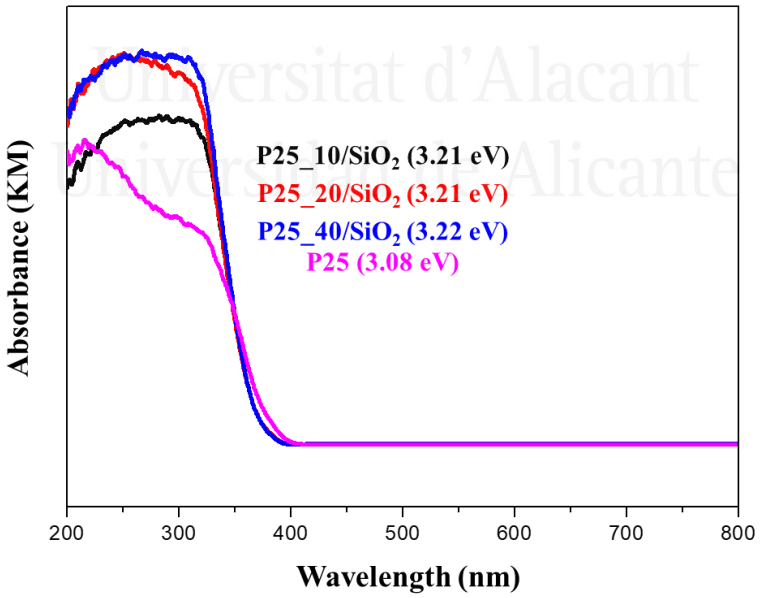

Figure 4.2. UV-Vis absorption spectra and band gap value (Eg) of the P25/SiO_2 with different P25 loading samples. The data for the benchmark material P25 is showed for comparison purposes.

The porous texture of the synthesized samples was investigated by N_2 adsorption measurements as showed in Fig. 4.3. The N_2 physisorption isotherm of P25 shows a typical type-II isotherm, indicative of a non-porous solid. However, the sample does present a hysteresis in the high relative pressure range due to interparticle adsorbate condensation. The SiO_2 prepared in our research group is a combination of type I and IV isotherms, typical of mesoporous materials with a certain degree of microporosity. This silica has hierarchical porosity, presenting micro, meso and macro-porosity [15]. As expected, the composites obtained in this Chapter present similar isotherms to that of the pure hierarchical SiO_2 material, with a noticeable decrease in the adsorption uptake at low relative pressures and the hysteresis loop as the P25 loading increases.

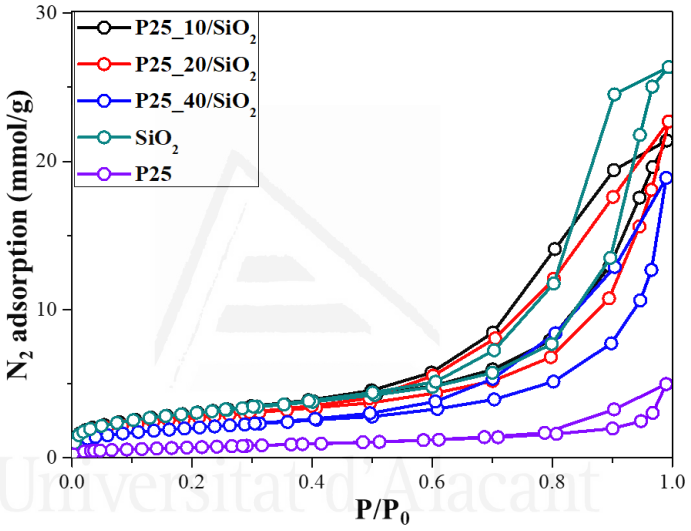

Figure 4.3. N_2 isotherms at 77 K for the different composites with hierarchical porosity silica samples. The adsorption isotherm of SiO_2 and P25 is also shown for comparison purposes.

Concerning the textural properties showed in Table 4.2, the BET surface area and $V_{total\ 0.95}$ decreases with increasing P25 loading, as commented in the previous paragraph. However, the textural parameters cannot help in distinguishing whether the P25 is encapsulated or not in the SiO_2. Comparing the S_{BET} (obtained from the isotherms) and T_S_{BET} (obtained theoretically assuming that the composite is a physical mixture), the samples with lower quantities of P25 (P25_10/SiO_2 and P25_20/SiO_2) show a discrepancy of only 7 % between S_{BET} and T_S_{BET}. Nevertheless, the samples with the highest loading of P25 (P25_40/SiO_2) shows a much higher discrepancy (45 %) between S_{BET} and T_S_{BET}. This difference indicates that high TiO_2 loadings severely affect the final morphology of the obtained composite, resulting not only in a modification of the porous texture, but also in the shaping of the final SiO_2/TiO_2 sample (vide infra). In this sense, it appears that high concentrations of suspended TiO_2 powder prevents the spinodal decomposition of the SiO_2-rich phase,

resulting in a composite with an irregular morphology. As a result, the mixing law fails to apply for this sample.

Table 4.2. Textural properties of the samples prepared in this study. The data for SiO_2 and P25 are showed for comparison purposes.

Samples	S_{BET} (m^2/g)	*T_S_{BET} (m^2/g)	$V_{total,0.95}$ (cm^3/g)	V_{N2DR} (cm^3/g)	Mean Pore Size (nm)
SiO_2	244	-	0.86	0.10	6.2
P25_10/SiO_2	235	252	0.61	0.10	7.9
P25_20/SiO_2	215	230	0.57	0.09	7.9
P25_40/SiO_2	145	219	0.38	0.07	6.2
P25	55	-	0.18	0.02	7.6

*T_S_{BET} represents the theoretical S_{BET} of the composites synthesised in this work (considering the composites as a physical mixture). This value was calculated by the following expression: T_S_{BET} = (S_{BET} (Mesoporous silica) · (SiO_2 present in the composites (ICP-OES)) + (S_{BET} (P25) · P25 present in the composites (ICP-ES)).

TEM images are showed in Fig. 4.4. The TiO_2 crystals are encased in the hierarchical silica matrix (Fig. 4.4 a)). Moreover, SiO_2 is clearly surrounding the P25 particles in the sample P25_20/SiO_2, which corroborates the encapsulation of the TiO_2 inside the SiO_2 matrix. Fig. 4.4 b) shows the presence of P25 in the sample P25_20/SiO_2 as the particle shows the lattice fringes and interplanar distances characteristic of both anatase and rutile present in P25 particles.

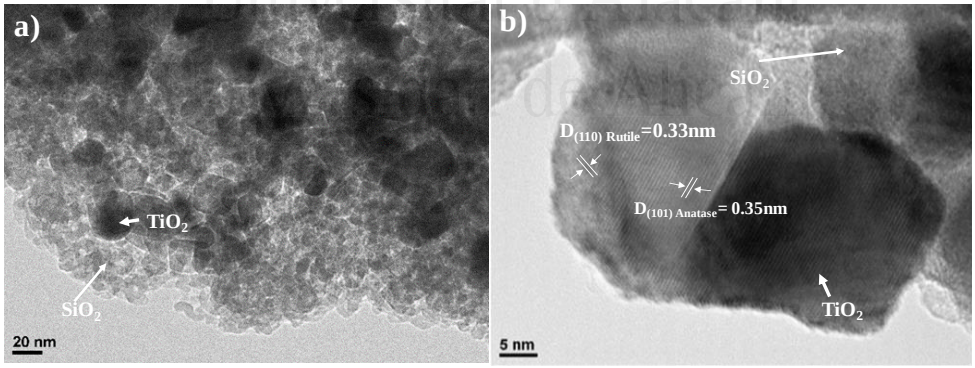

Figure 4.4. TEM images of a representative sample prepared in this study: (a) P25_20/SiO_2, (b) Magnification of P25 NPs (sample P25_20/SiO_2)

SEM images show that the samples with low P25 loadings (3.8 % and 8.14 wt.%) (Fig. 4.5 a) and b)) have a spherical morphology typical for this silica (Fig. 4.5 d)). No particles with irregular morphology (representative of P25 NPs, Fig. 4.5 e)) are observed for these samples, which indicates the encapsulation of P25 inside the SiO_2 matrix, as already hinted at by the TEM images. However, the sample with the highest

P25 loading (P25_40/SiO_2) presents both spherical and irregular particles (Fig. 4.5 c)), in agreement with the comments made from the adsorption isotherms results.

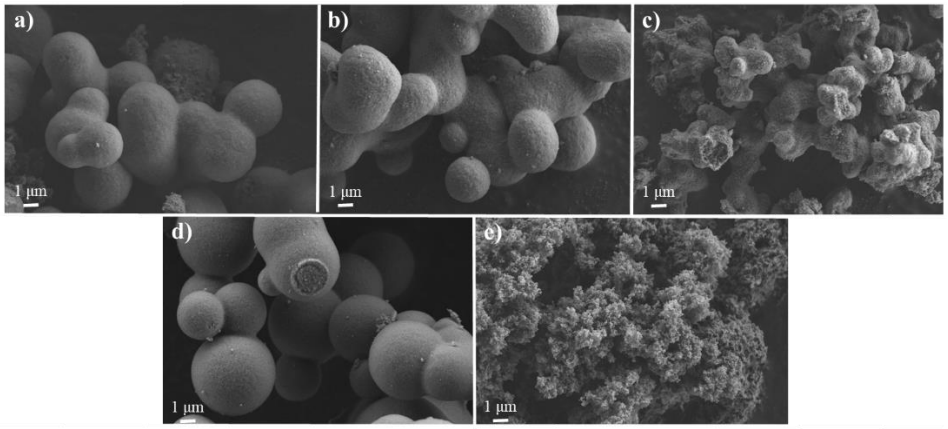

Figure 4.5. SEM of the samples with hierarchical porosity silica: a) P25_10/SiO_2, b) P25_20/SiO_2 and c) P25_40/SiO_2. The SEM images of SiO_2 d) and P25 e) are also showed for comparison purposes.

EDX mapping images are presented in Figs. 4.6 a), b) and c). Sample P25_10/SiO_2 contains Ti in the composites indicating that P25 is probably inside the SiO_2 shell, owing to the composite presenting a spherical structure as observed in the SEM images (Fig. 4.5 a) and 4.6 a)). This is a clear indication that the spinodal decomposition process is not largely affected by the presence of the TiO_2 powder. For sample P25_20/SiO_2 a similar observation can be made although the presence of Ti is more noticeable as showed in Fig. 4.6 b), allowing to conclude that in both composites the P25 particles are encapsulated within the SiO_2 matrix. Nevertheless, the sample with the highest TiO_2 loading (sample P25_40/SiO_2) (Fig. 4.6 c)) presents a morphology distinct from spherical, which shows that the spinodal decomposition is modified in the presence of large concentrations of photocatalyst. In turn, this encapsulated TiO_2 sample shows a significantly different morphology from the other two samples as corroborated by the SEM images and the textural parameters of these composites, in which the mixing law does not apply. In order to better compare the results towards an understanding of the encapsulation phenomenon Fig. 4.7 a) and b) show EDX images mapping of sample P25_20/SiO_2 and a physical mixture in which the two phases are clearly and completely separated, with no observable encapsulation.

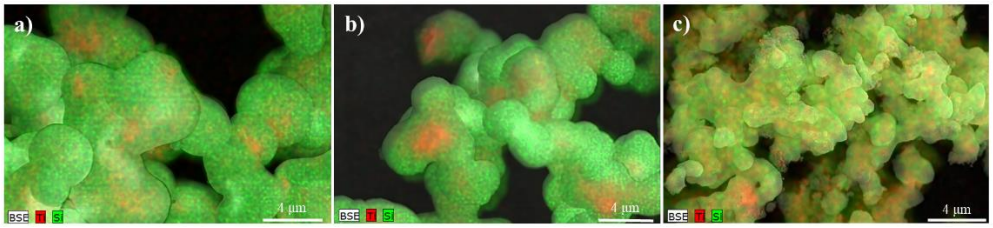

Figure 4.6. EDX images mapping of the samples: a) P25_10/SiO_2, b) P25_20/SiO_2 and c) P25_40/SiO_2.

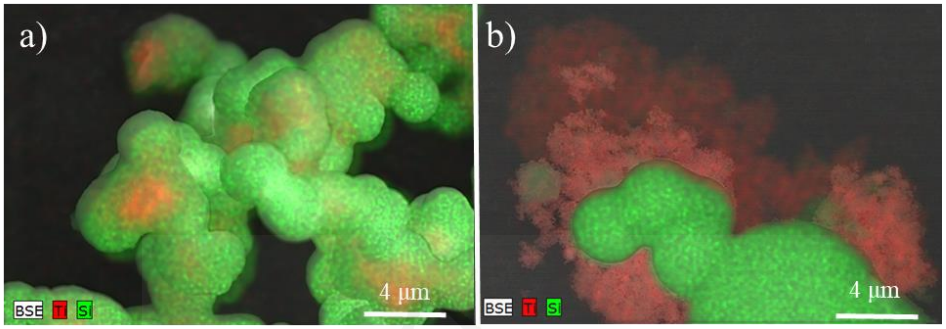

Figure 4.7. EDX images mapping of the composite and the physical mixture with the same percentage of P25: a) P25_20/SiO_2 (composite) and b) PM (Physical mixture).

4.3.2. P25/M001 and P25/MCM-41 Samples Characterization

In this section of the Chapter, the results on the characterization of the P25 samples encapsulated inside precipitated silica (M001) and a mesoporous silica (MCM-41) with a nominal TiO_2 content of 20% are discussed. These results are compared with P25 encapsulated in the aforementioned spherical hierarchical silica (P25_20/SiO_2) to better put the results in perspective.

The results obtained by ICP-OES (Table 4.3) show discrepancies between the samples encapsulated in different silicas where all samples have a 20 wt.% nominal of P25. The sample with P25/M001 presents the lowest TiO_2 loading (3.2 wt.%). The other samples P25/MCM-41 and P25_20/SiO_2 present a similar TiO_2 loading, 6.8 wt.% and 8.1 wt.%, respectively, being the sample with the P25 encapsulated in hierarchical silica the one with the highest loading. These values will be used in the calculations in order to obtain reliable figures.

Table 4.3. Percentage of TiO_2 of the sample prepared in this Chapter.

Samples	% TiO_2 ICP-OES
P25/M001	3.2 ± 0.1
P25/MCM41	6.8 ± 0.9
P25_20/SiO_2	8.1 ± 0.2

The XRD patterns for the samples with P25 encapsulated in different silica samples (M001, MCM-41 and SiO_2) are showed in Fig. 4.8. The particles of P25 encapsulated in the different silicas present the same crystalline phases as the benchmark P25 (rutile and anatase) after calcination at 500 ºC, indicating the presence of P25 in the composites without any further modification as indicated previously in Fig. 1 a) for the composite (P25_20/SiO_2). In these composites with different silicas (P25/M001, P25/MCM-41 and P25/SiO_2) an elbow in each of the XRD patterns was also observed, indicating the presence of the different silicas (M001, MCM-41 and SiO_2) in each composite used in this Chapter.

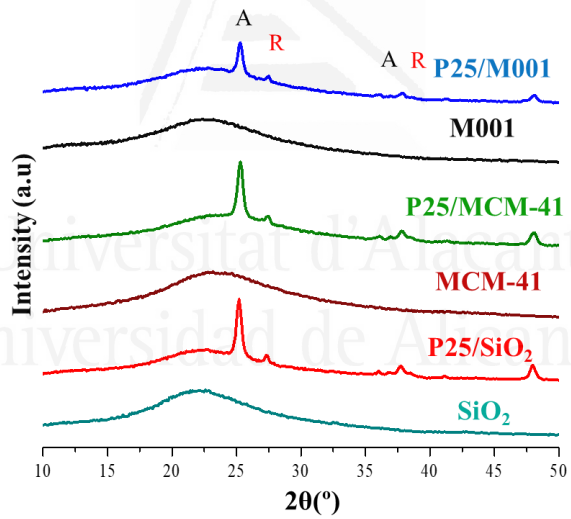

Figure 4.8. XRD patterns of the composites with different silica. The data for the different silicas used in this Chapter are showed for comparison purposes. Key: A = anatase; R = rutile

The UV-Vis spectra obtained for the P25 encapsulated with different silicas (M001, MCM-41 and SiO_2) are showed in Fig. 4.9. All hybrid photocatalysts with different silica samples present a similar absorption band edge at 400 nm and band gap. These values indicate that the use of different silica (M001, MCM-41 and SiO_2) does not modify the light absorption of the P25 encapsulated.

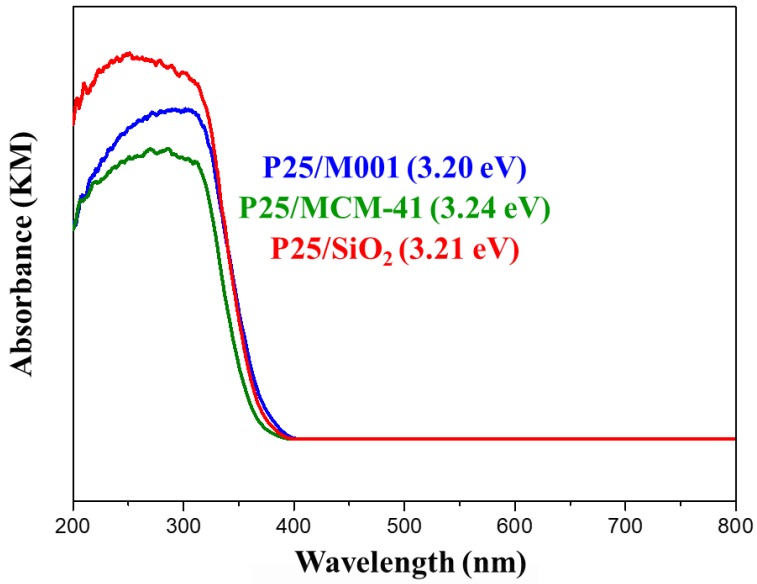

Figure 4.9. UV-Vis absorption spectra and the band gap (Eg) of the P25/SiO_2 with different silica samples.

The N_2 adsorption measurements at -196 ºC are showed in Fig. 4.10. The N_2 physisorption isotherm of sample M001 shows a type-II isotherm, indicative of a non-porous material, with some porosity arising from a small hysteresis in the high relative pressure range due to interparticle condensation. However, the composite P25/M001 presents a combination of type I and type IV isotherms. This fact is remarkable since this composite with P25 (non-porous material) has higher N_2 adsorption capacity with respect to the naked M001, indicating the appearance of additional porosity when the composite is formed probably due to interparticle spacings with sizes in the <1 nanometer region. The MCM-41 silica shows a combination of type I and IV isotherms, typical of mesoporous materials with a certain degree of microporosity as it has been reported in the literature [16]. As expected, the composites obtained with this silica present similar isotherms to that of the pure MCM-41, with a noticeable decrease in the adsorption uptake at low pressures and the hysteresis loop due the presence of a non-porous material (P25).

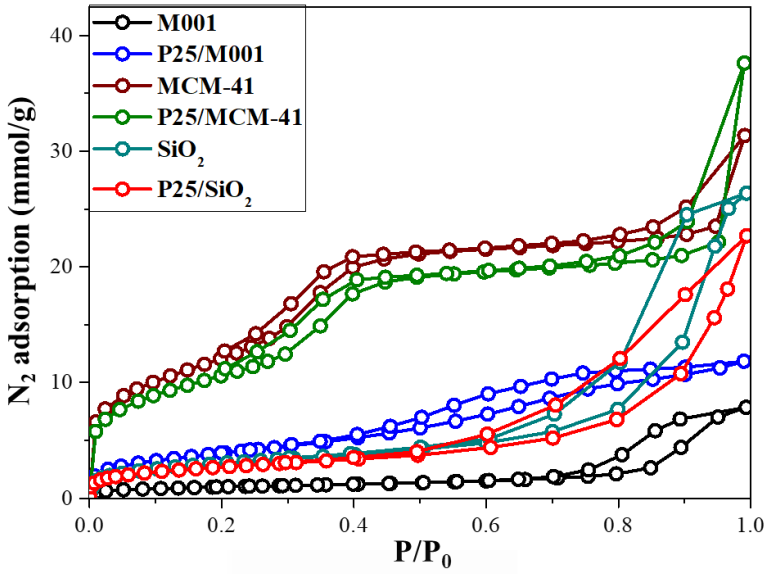

Figure 4.10. N_2 isotherms at 77 K for the samples prepared in this study: P25/M001, P25/MCM-41, and P25_20/SiO_2. The adsorption isotherms of the pure silicas are also showed for comparison purposes.

The textural properties obtained from the adsorption isotherms are showed in Table 4.4. The BET surface area and $V_{total\ 0.95}$ decrease with the incorporation of P25 except in the case of the P25/M001 sample where these values increase. The samples with MCM-41 present the highest surface area and total pore volume.

Table 4.4. Textural properties of the samples prepared in this study derived from the analysis of the N_2 adsorption isotherms. The data for SiO_2 and P25 are showed for comparison purposes

Samples	S_{BET} (m^2/g)	$V_{total,0.95}$ (cm^3/g)	V_{N2DR} (cm^3/g)	Mean Pore Size (nm)
M001	77	0.25	0.033	6.2
MCM-41	973	0.82	0.39	2.9
SiO_2	244	0.86	0.10	6.2
P25/M001	317	0.39	0.17	3.1
P25/MCM-41	875	0.77	0.34	3.1
P25_20/SiO_2	215	0.57	0.09	7.9
P25	54	0.18	0.02	7.6

TEM images show the possible encapsulation of P25 inside the different silicas (Fig. 4.11). SEM images show the morphology of the samples P25/M001, P25/MCM-41 and P25_20/SiO_2 (Fig. 4.12 a-c)). The samples P25/M001 and P25/MCM-41 present an irregular morphology, a feature common for both precipitated silica and P25. EDX mapping images are presented in Figs. 4.12 d), e) and f). All samples present Ti in the composites indicating that P25 is inside the different silicas as observed for sample P25_20/SiO_2.

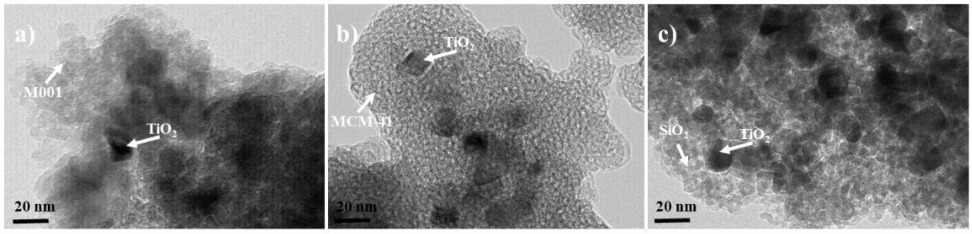

Figure 4.11. TEM of the composite prepared in this study: a) P25/M001, b) P25/MCM-41 and c) P25_20/SiO_2.

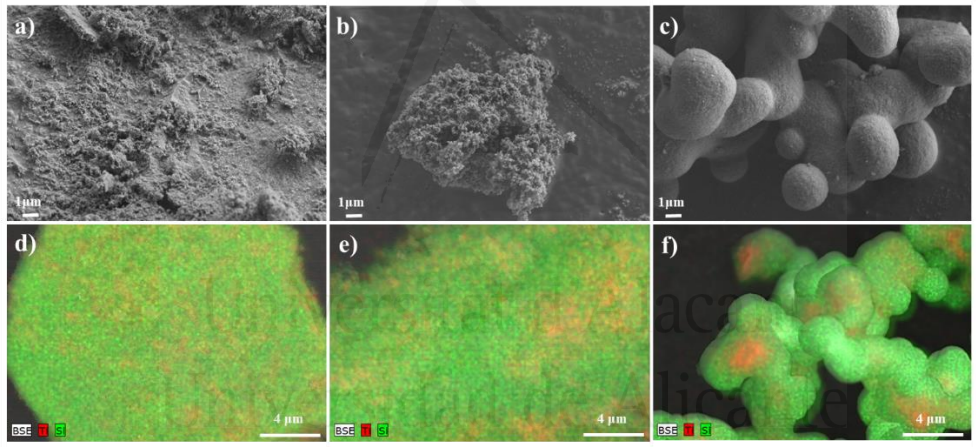

Figure 4.12. SEM of the samples with different silica: a) P25/M001, b) P25/MCM-41 and c) P25_20/SiO_2. Figure 4.12 d-f) present the EDX images mapping d) P25/M001, e) P25_20/MCM-41 and f) P25_20/SiO_2.

4.3.3. Photocatalytic Activity

The photocatalytic activity of the materials prepared in this Chapter was evaluated by studying the mineralization of propene in the gas phase at low concentration (100 ppmv in air) to CO_2 at room temperature.

The results of the effect of different P25 loadings in the photocatalytic activity of the samples with silica with hierarchical porosity are showed in Fig. 4.13 a). The naked P25 presents the best value of propene conversion with respect to the composites where the P25 was encapsulated in the spherical hierarchical silica (SiO_2). In the case of the composites, as the concentration of P25 (active phase) is increased

propene conversion increases. Nevertheless, the samples with 8.1 wt.% and 15.9 wt.% P25 loading present approximately the same propene conversion. This might be due to sample P25_40/SiO_2 presenting a different morphology with respect to the other composites and this factor affects the activity of the composite (Fig. 4.13 a)). When the results of the photocatalytic activity are normalized per mole of active phase (P25) (CO_2 production rate) expressed as moles CO_2/(moles P25 · s), P25 has the lowest photoactivity compared to the composites due to the silica favouring the activity per mole of P25 as showed in the literature [5]. With respect to CO_2 production rate, the composites show a decrease in the conversion of propene upon increasing the percentage of P25 in the composite which might be due to the change in porous texture and morphology of the silica or to another important factor such as the better illumination efficiency [20] of particles of P25 when the composites have lower percentages of active phase as explained below. Moreover, in this section we evaluated the durability of the samples, specifically the P25_10/SiO_2 sample as reference material. The conditions used in this test have been described in the Catalytic Test section but running the propene abatement tests continuously for 14 hours. In this sample, the propene conversion was stable after 14 h of reaction (the initial and final propene conversion values were kept at 14%). In this sense, this sample (P25_10/SiO_2) was also recycled three times. For this purpose, the sample was cycled in the photooxidation of propene as described in the Catalytic Test for three cycles (the conversion values for the three consecutive cycles was 14%). The performance of the sample did not show a noticeable change in the propene conversion value at the end of each cycle.

In order to deepen into the synergy between silica and P25 upon encapsulation in these materials as described in literature [2,4,10], the sample showing the highest TiO_2 loading (P25_40/SiO_2), is compared in propene mineralization with composites in different configurations (PM, SiO_2/P25 and P25/SiO_2) as described in the Catalytic Tests section. As showed above (Fig. 4.13 b)), the naked P25 presents the best propene conversion value with respect to the other samples, due to the composites having a significantly lower amount of P25. In the composites and the mixtures (SiO_2 and TiO_2), the sample with the P25 encapsulated has better propene conversion than the other samples. This result indicates a synergetic effect between the encapsulated P25 and the SiO_2; it seems that hierarchical silica favours mass transport and increases the concentration of reagents near the P25 particles.

Interestingly, P25 has the lowest photocatalytic activity when expressed as rate of CO_2 formation per moles of P25, compared to the composites (Fig. 4.13 b)) even when the P25 sample is not encapsulated. In the case of the composites, the encapsulation of P25 (Fig. 4.13 a)) improved the activity per moles of P25. This is observed in the conversion of propene for the P25_xx/SiO_2 samples, which hints at a synergy between the P25 encapsulated inside the hierarchical silica. In this respect, the coexistence of a silica with hierarchical porosity which favours mass transfer of

reagents and products, the possibility of this same porosity acting as an adsorbent for reagents, and the intimate contact between the SiO_2 and TiO_2 phase results in an improved performance of the encapsulated samples compared with all its physically mixed counterparts (Fig. 4.13 b)).

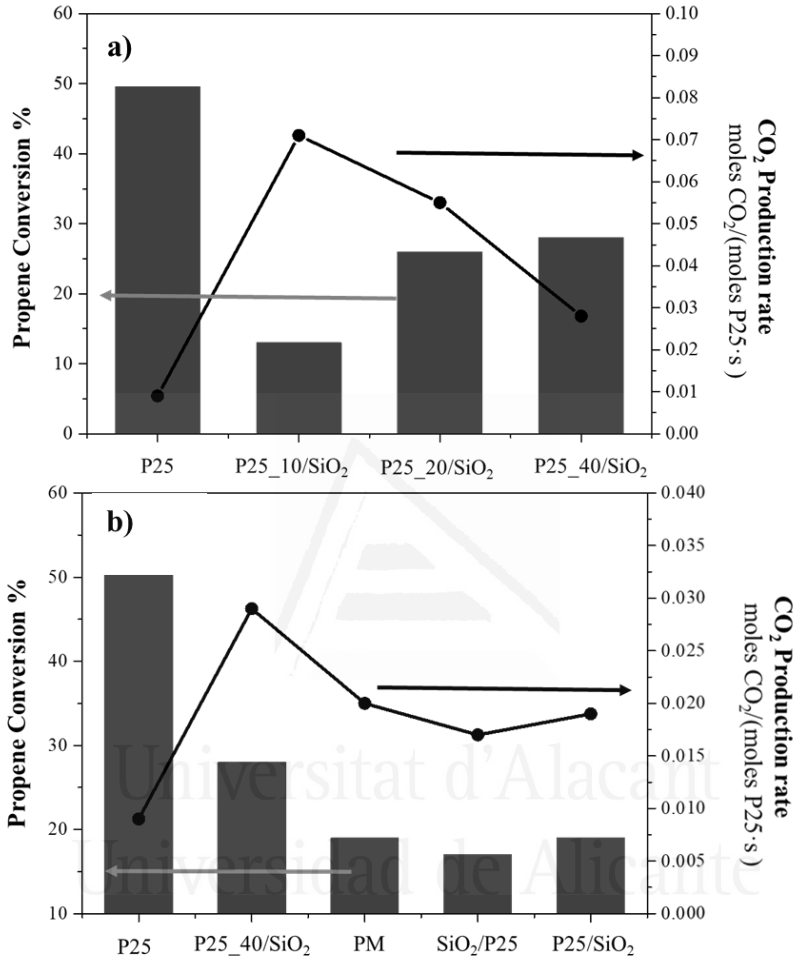

Figure 4.13. Comparison of propene conversion and CO_2 production rates for samples with spherical hierarchical porosity silica and P25 for comparison purposes: a) Photoxidation varying the percentage of P25 in the samples and b) Comparison of the composite P25_40/SiO_2 with samples where the same amount of P25 is not encapsulated.

From our results showed in Table 4.2 and Fig. 13 a), it would appear that there is a correlation between the BET surface area in the composites and their CO_2 production rate in the propene mineralization reaction. With this in mind, from the values showed in Table 4.4, the TiO_2 sample encapsulated in MCM-41 (SiO_2) should outperform all samples. This material should better concentrate the reagents favouring their oxidation by the TiO_2 phase, as explained in the literature [2,10]. In order to probe into this effect in the activity of encapsulated P25, the CO_2 production rates for the samples with silica having different textural parameters (S_{BET}) and morphologies

are showed in Fig. 4.14. Interestingly, the composite with hierarchical silica presents the highest CO_2 production rate, despite having poorer textural properties. It is also observed that the sample encapsulated in mesoporous silica shows better photooxidation of propene than that in precipitated silica. This result evidences the importance of using a silica not only with large surface area but also with hierarchical porosity for optimizing the mass transport in addition to an increased concentration of reagents due to the hierarchical porosity interconnected which allows all the adsorbed propene to arrive at the active phase (P25). This comparison is straightforward comparing these samples with others showing a BET surface area four times larger which lack this hierarchical structure as showed in Scheme 1. In the MCM-41 sample, the porous structure (tubular non-interconnected mesopores) does not guarantee a good access to the active phase via the mesopores, since many of them may not be connected with the P25 particles. On the other hand, in the silica with hierarchical porosity (SiO_2) the interconnected porosity allows a much higher accessibility to the active sites, favouring the oxidation of propene on P25, as showed in Scheme 4.1.

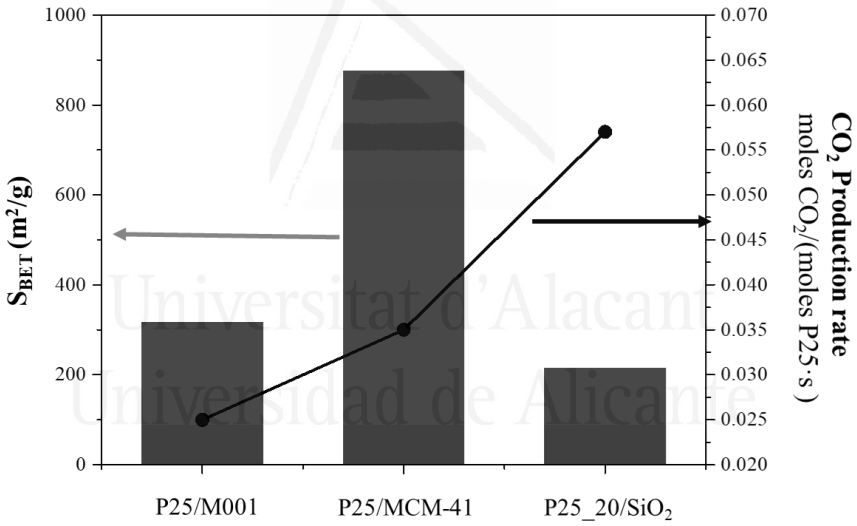

Figure 4.14. Comparison of CO_2 production rates of samples of P25 encapsulated in different silica and their textural parameters (S_{BET}).

With the purpose of studying the possible effect of the better illumination efficiency in the encapsulated P25 particles as mentioned in Chapter 1 and discussed before, the conversion of propene was also obtained by varying the propene flow and the mass of P25 (Fig. 4.15) keeping the space velocity (Vsp) constant with the purpose of comparing the naked P25 samples with different mass as described in the Catalytic Test section. These catalytic tests are usually done to detect diffusional limitations. The results show an increase in propene conversion as the flow of reagents and mass of catalysts are decreased. This is markedly different from the expected results for classic catalysis, where the conversion remains constant until it decreases due to

diffusional problems [21]. This result indicates some contribution of the photonic efficiency [20]. When the weight of the sample (in this case only P25) is decreased (and consequently the catalyst bed size), the propene conversion increases due to a better illumination of the particles. This factor could partially explain the increased photocatalytic activity of the composites compared to P25 as showed in Fig. 13 b). In fact, the results of the comparison of the samples P25 (0.11 g of naked P25) and P25_40/SiO_2 (0.69 g of composite), which represents the worst case scenario in illumination efficiency for the encapsulated P25 particles, performed at the same V_{sp} with respect to the amount of P25 (adding in both cases 0.11 g of P25 in the reactor), indicate a double effect: one arising from the better illumination of the TiO_2 particles because the P25 particles are kept within a UV-transparent shell in the composite; this effect combines with the presence of hierarchical porosity that enhances the conversion of propene as showed Fig. 4.14. These results indicated the difficulty in separating the significant effect brought forth by the porosity of the silica shell (as showed in Fig. 4.14) and the contribution of the improved illumination efficiency in the photocatalyst (as showed in Fig. 4.15).

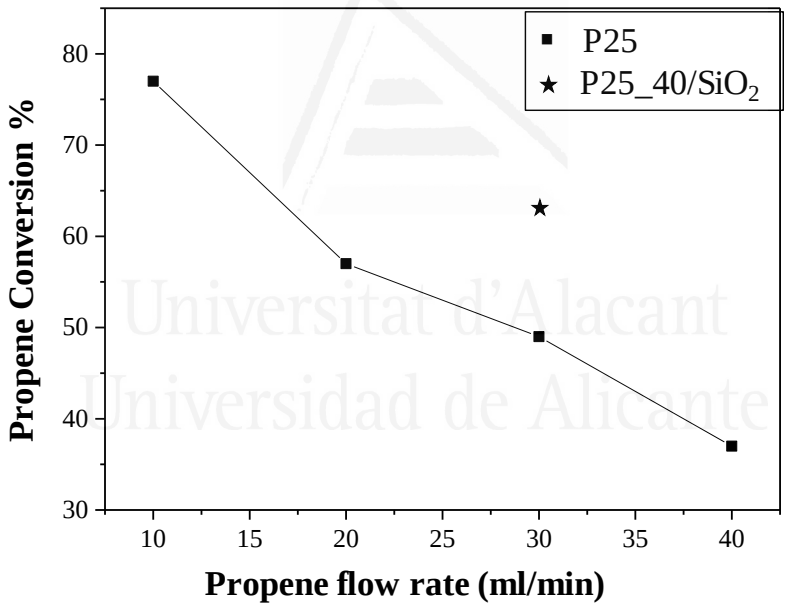

Figure 4.15. Comparison of propene conversion with different flow rates (The mass of the samples is described in Experimental section) maintaining a constant space velocity of 257 $mL \cdot g^{-1} \cdot min^{-1}$ (See Experimental section). The sample P25_40/SiO_2 with the same mass of P25 (0.11g) and space velocity is included for comparison purposes.

Considering the results obtained in this study in terms of characterization of samples and their performance in the photocatalytic oxidation of propene at low concentrations, the most promising outlook seems to be the following: (1) this Chapter presents a facile synthetic protocol for the encapsulation of P25 in different SiO_2 materials through a simple and reproducible sol-gel method, providing a

synergetic effect between the P25 and the silica; (2) the increase in TiO_2 loading decreases the activity of the P25/SiO_2 samples, due to the change in the morphology of the composites (TiO_2_40/SiO_2) and the importance of the illumination efficiency of the active phase; (3) the synergetic effect between the silica and P25 takes place upon encapsulation due to an intimate contact of the P25 with the silica which acts as adsorbent for the propene molecules and this favours photoactivity; (4) The election of a suitable (i.e. interconnected) porous texture of the silica matrix allows the improved photoactivity of the photocatalyst per moles of P25.

With the results discussed above, the encapsulation of P25 (TiO_2) in spherical silica with hierarchical porosity, which can be prepared by a simple, reproducible, and cost-effective sol-gel method displays a remarkable photocatalytic activity with respect to the benchmark P25 and the P25 encapsulated in a standard precipitated silica (M001) or mesoporous silica (MCM41). This approach opens the door to synthetic encapsulation strategies towards materials with high performance in photoactivity for the elimination of VOCs at low concentration using an adequate silica without using convoluted or advanced synthesis methods [13,22].

4.4. Conclusions

In this Chapter, a facile encapsulation of P25 (TiO_2) in different silica materials (spherical silica with hierarchical porosity, mesoporous silica and precipitated silica) was performed from the modification of an established methodology. The sample P25_10/SiO_2 presents the best improvement of CO_2 production rate per moles of P25, because the increase in the loading of P25 causes a modification in the morphology and porosity of the composite and a diminished illumination efficiency affecting photocatalytic activity. Apart from the synergetic effect between the silica and P25, encapsulation provides an added bonus due to an intimate contact of the P25 with the silica which favours photoactivity. Another important factor is the election of a correct porous network for the silica matrix. This fact allows to synthesize new materials with an improved mass transfer and catalytic efficiency for the abatement of contaminants at low concentrations in gas phase

4.5. Referencias

[1] X. Qian, K. Fuku, Y. Kuwahara, T. Kamegawa, K. Mori, H. Yamashita, ChemSusChem. 7 (2014) 1528-1536.
[2] Y. Paz, Solid State Phenom. 162 (2010) 135-162.
[3] R. Leary, A. Westwood, Carbon 49 (2011) 741-772.
[4] Y. Kuwahara, H. Yamashita, J. Mater. Chem. 21 (2011) 2407-2416.
[5] C. Anderson, A.J. Bard, J. Phys. Chem. 99 (1995) 9882-9885.
[6] K.J. Nakamura, Y. Ide, M. Ogawa, Mater. Lett. 65 (2011) 24-26.
[7] M. Nussbaum, Y. Paz, Phys. Chem. Chem. Phys. 14 (2012) 3392.
[8] K. Tanabe, J. Catal. 231 (1974) 225-231.
[9] A. Corma, M.T. Navarro, J.P. Pariente, J. Chem. Soc. Chem. Commun. (1994) 147-148.
[10] X. Chen, X. Wang, X. Fu, Energy Environ. Sci. 2 (2009) 872.
[11] H. Yoshida, C. Murata, T. Hattori, Chem. Commun. (1999) 1551-1552.
[12] S. Wang, T. Wang, W. Chen, T. Hori, Chem. Commun. (2008) 3756-3758.
[13] Y. Kuwahara, Y. Sumida, K. Fujiwara, H. Yamashita, ChemCatChem. 8 (2016) 2781-2788.
[14] P. Nadrah, M. Gaberšček, A. S. Škapin, Appl. Surf. Sci. 405 (2017) 389-394.
[15] J. García-Aguilar, I. Miguel-García, Berenguer-Murcia, D. Cazorla-Amorós, ACS Appl. Mater. Interfaces. 6 (2014) 22506-22518.
[16] A. Berenguer-Murcia, D. Cazorla-Amorós, Á. Linares-Solano, Adsorpt. Sci. Technol. 29 (2011) 443-455.
[17] A. Berenguer-Murcia, A.J. Fletcher, J. García-Martínez, D. Cazorla-Amorós, A. Linares-Solano, K.M. Thomas, J. Phys. Chem. B. 107 (2003) 1012-1020.
[18] M.A. Lillo-Ródenas, N. Bouazza, A. Berenguer-Murcia, J.J. Linares-Salinas, P. Soto, A. Linares-Solano, Appl. Catal. B Environ. 71 (2007) 298-309.
[19] L. Cano-Casanova, A. Amorós-Pérez, M. Ouzzine, M.A. Lillo-Ródenas, M.C. Román-Martínez, Appl. Catal. B Environ. 220 (2018) 645-653.
[20] J.M. Herrmann, J. Photochem. Photobiol. A Chem. 216 (2010) 85-93.
[21] H. S. Fogler, Elements of Chemical Reaction Engineering; Prentice Hall, USA, 2006.
[22] S. Ikeda, Y. Ikoma, H. Kobayashi, T. Harada, T. Torimoto, B. Ohtani, M. Matsumura, Chem. Commun. (2007) 3753-3755.

Chapter 5

Photooxidation of Propene with TiO_2-MWCNT Photocatalysts

In this Chapter, we have performed the synthesis of TiO_2/MWCNT composites focusing on the study of the effect of the dispersion of the photoactive phase and in the carbon active sites generated on the MWCNTs in the properties of the composites for the abatement of propene. We used different approaches for the dispersion of MWCNTs during the composites synthesis; 1) using an ultrasound bath for 5 minutes, 2) using an ultrasound baths for 60 minutes, and 3) using an ultrasound probe for 5 min. The materials synthesized in this Chapter have been characterized by TG, TEM, XRD, XPS, UV-Vis spectroscopy, TPD and PL spectroscopy. It has been observed that the presence of MWCNTs in the composites improves the catalytic activity of all composites prepared in this Chapter in the photooxidation of propene. Moreover, a good dispersion and an increase in the active surface area or oxygen surface functionalities created on the MWCNTs during the synthesis of the composites improve the catalytic activity of the samples.

5.1. Introduction

Significant efforts have been made by the scientific community to change the properties of TiO_2 by synthesizing new nanoporous TiO_2 materials or TiO_2-Adsorbent composites [1-4]. In this sense, in previous Chapters of the present Thesis different approaches to improve the properties of TiO_2 have been described. Chapter 3 "Photooxidation of Propene with TiO_2 Photocatalyst", focused on the synthesis of a TiO_2 with hierarchical porosity which improved some properties of the TiO_2 with respect to the commercial benchmark TiO_2 (P25), showing a slight increase in the photocatalytic activity of TiO_2. Another approach also used in this Thesis was the study of TiO_2 with silica composites (P25 encapsulated in different silica), as described in Chapter 4 "Photooxidation of Propene with P25 Encapsulated in Silica". In this Chapter we observed an increase of the photocatalytic activity in the composites induced by the porosity of the silica. Due to the relevant results obtained previously in Chapter 4, another interesting approach is changing silica by another material for example, carbon materials, zeolites, polymers, among others, with the objective of improving the properties of the TiO_2 [2,5-8].

In the last decades, the use of carbon nanotubes (CNT) has attracted significant interest for their use in composite materials (TiO_2-CNT) in photocatalysis applications due to their interesting properties, such as high electrical conductivity, high electron storage capacity and high surface area (typically between 200-400 m^2/g). Moreover, the presence of CNTs in the photocatalytic system increases the lifetime of generated electron-hole (e^--h^+) pairs in the semiconductor and they can act as a supplementary catalytic active site in certain reactions [5,9-11].

In this sense, Vincent et al reported the inclusion of carbon nanotubes (CNTs) into a TiO_2 matrix prepared by a sol-gel method the authors proposed the possible applications of this type of nanocomposite [12]. Yu et al observed that the presence of CNTs in the TiO_2 can change the properties of TiO_2. In this sense, they observed that the agglomerated morphology and the particle size of the TiO_2 in the composites changed in the presence of CNTs. The addition of CNTs did not affect the mesoporous nature of the TiO_2 and an increase of the hydroxyl groups available on the surface of the composite was observed with respect to pure TiO_2. Also, in this study it was observed that the CNTs can suppress the recombination of photo-generated e^--h^+ pairs. However, excessive CNTs also shield the TiO_2 from absorbing UV light. With respect to the photocatalytic activity of these samples in the degradation of acetone it was observed that the composites have much higher photocatalytic activity than P25 and TiO_2-activated carbon (AC) composites [13]. Wang et al observed a synergy effect in the photocatalytic activities for the composite catalysts (TiO_2-MWCNT) in the conversion of phenol in aqueous solutions. This effect was discussed by the authors in terms of a strong interaction between carbon and TiO_2 phases [14]. Xu et al described the study of carbon nanotubes CNT-TiO_2 nanocomposite prepared by a simple impregnation method for their application in the gas-phase degradation of

benzene. This nanocomposite presented an enhanced photocatalytic activity for benzene degradation with respect to a commercial TiO_2 (P25, Degussa) [15]. Koli et al investigated the photocatalytic activity of the degradation of methyl orange dye and the photo-inactivation of Bacillus subtilis. They observed that the MWCNTs present in the nanocomposite absorbed a high amount of photon energy in the sunlight, effectively driving the photochemical degradation reactions. In both applications, the authors observed a significant enhancement in the degradation/inactivation reaction rate with the TiO_2-MWCNTs (0.5 wt.%) with respect to bare TiO_2 [16].

With this in mind, this Chapter focuses on the preparation of TiO_2-MWCNT composites through the incorporation of dispersed MWCNT in the TiO_2 synthesis solution in order to improve the photocatalytic activity of the pure TiO_2 material. For this reason, in this Chapter we have studied the effect of the dispersion of the photoactive phase and the active sites existing in the MWCNT in the properties of the final composite in terms of their catalytic properties. For studying these effects, in this Chapter we have performed different approaches for the dispersion of MWCNT: 1) using an ultrasound bath for 5 minutes, 2) using an ultrasound bath for 60 minutes and 3) using an ultrasound probe for 5 min. The samples are applied in the abatement of propene to continue the studies previously performed in Chapter 3 "Photooxidation of Propene with TiO_2 Photocatalyst" and 4 "Photooxidation of Propene with P25 Encapsulated in Silica" since the MWCNT can improve the properties of TiO_2 for enhancing its catalytic activity in the photooxidation of VOCs as reported in the literature, as it was described in this Introduction section.

5.2. Materials and Methods

5.2.1. Materials

Titanium (IV) tetrabutoxide (TTB, 97%, Sigma-Aldrich), Multiwall Carbon Nanotubes (MWCNT, Nanoblack, bamboo-type MWCNT with a diameter between 15 and 30 nm), glacial acetic acid (HAc, 99%, Sigma-Aldrich), Pluronic F-127 (F-127, Sigma-Aldrich), absolute ethanol (EtOH, 99.8%, Fisher Scientific), formamide (FA, 99.5%, Sigma-Aldrich), urea (99%, Merck), and deionized water were used in the present work. All reactants were used as received, without further purification.

5.2.2. Sample Preparation

The TiO_2-MWCNT samples were prepared adapting a previously performed synthesis in Chapter 3 "Photooxidation of Propene with TiO_2 Photocatalyst". The main difference was the incorporation of the needed amount of MWCNTs (1 wt. %), dispersed in water and ethanol, in the TiO_2 synthesis solution, with the aim of synthesizing the composite material (TiO_2-MWCNT).

The synthesis of TiO_2-MWCNT composites was performed as follows: 5 g of the titanium precursor (titanium tetrabutoxide, TTB) were weighed and dissolved in

7.9 g of EtOH. This solution ("solution A") was stirred vigorously for 10 min. Then, in this order, 1.6 g of HAc, 0.3 g of F-127, 1.6 g of deionized water, 7.9 g EtOH, 0.4 g of FA, and 0.4 g of urea were weighed and added in a separate vessel. The mixture was stirred for 10 min ("solution B"). Then, the MWCNTs were incorporated in solution B and then dispersed using three different approaches. In the first and second approach the MWCNTs were dispersed for 5 min and 60 min using an ultrasonic bath (Fisherbrand, FB15051) with a power of 200 W and in the third approach the MWCNTs were dispersed with an ultrasound probe (Bandelin SONOPULS HD 2200) for 5 min with a power of 660 W operating at 30% output power. "Solution B" with the dispersed MWCNT was rapidly added dropwise on "solution A" under vigorous stirring. The resulting solution was transferred to an autoclave and heated at 60 °C for 24 h and the temperature was later increased to 120 °C with a dwelling time of 24 h. The samples obtained were calcined at 350 ºC for 6 h with a heating rate of 1 °C/min. The nomenclature of the samples used in this work were TiO_2-MWCNT_UB_5min and TiO_2-MWCNT_UB_60min for the samples where the MWCNTs were dispersed for 5 min and 60 minutes using an ultrasonic bath, respectively, and TiO_2-MWCNT_UP_5min for the samples where MWCNTs were dispersed for 5 min with an ultrasound probe. Moreover, in this Chapter the commercial P25 (TiO_2) and a pure sample of TiO_2, prepared using this synthesis condition but without the incorporation of MWCNT (Chapter 3), were used for comparison purposes.

5.2.3. Sample Characterization

The amount of MWCNTs in the composites was determined by thermogravimetric analysis using a thermobalance (SDT 2960). In these analyses, the sample was heated up to 900 °C in air (heating rate of 5 °C min^{-1}).

The crystal phase composition and crystallinity of TiO_2 were determined by X-ray diffraction (XRD) analysis using a Miniflex II Rigaku. Cu Kα (1.54056 Å) radiation was used. The scanning velocity was 2º/min, and diffraction patterns were recorded in the angular 2θ range of 6-80º. The crystallite size was estimated by applying the Scherrer equation as described in Chapter 2 "Experimental Techniques" and Chapter 3 "Photooxidation of Propene with TiO_2 Photocatalyst".

The optical absorption properties were studied by UV-VIS/DR spectroscopy (Jasco V-670). $BaSO_4$ was used as the reference standard and the reflectance signal was calibrated with a Spectralon standard (Labsphere SRS-99-010, 99% reflectance). The absorption edge wavelength was estimated from the intercept at zero absorbance of the high slope portion of each individual spectrum in the range 200-800 nm (absorbance method). Then, the band gap can be calculated using the absorbance method used as described previously in Chapter 3 and Chapter 4.

The morphology of the samples was analyzed by transmission electron microscopy (TEM, JEOL JEM 2010).

X-Ray Photoelectron Spectroscopy (XPS) was performed using a K-α spectrometer from Thermo-Scientific, equipped with an Al anode.

Photoluminescence measurements at room temperature were taken on a Fluorolog-3 spectrofluorometer (HORIBA). The excitation wavelength used for the photoluminescence analysis was 380 nm.

The ASA (Active Surface Area) of the MWCNT samples prepared in this Chapter was measured using an established method which is based on di-oxygen chemisorption [17,18]. Firstly, 10 mg of MWCNT (only carbon material) were heat-treated up to 920 ºC at a heating rate of 20 ºC/min, N_2 flow rate of 100 mL/min, and kept at 920 ºC for 0.5 h under N_2 to remove all oxygen functional groups on the carbon surface. Afterwards, the temperature is lowered to 250 ºC and kept for 1 h under inert atmosphere. Next, synthetic dry air (20 vol% O_2 in N_2) is fed to the thermobalance for 7 h to perform the oxygen chemisorption step. The ASA was then determined from the weight uptake of the samples by the following equation (eq. 5.1) assuming that each chemisorbed oxygen atom occupies an area of 0.083 nm^2.

$$\mathrm{ASA}\left(m^2/g\right)=\frac{1}{w_0}\cdot\frac{A\cdot N_A\cdot(w_c-w_0)}{N_O} \qquad (5.1)$$

where A is the area that one oxygen atom occupies per edge site (carbon atom), N_A is the Avogadro constant, w_0 is the starting weight of carbon in the chemisorption step, w_c is the weight of carbon after oxygen chemisorption and N_O is oxygen atomic weight.

Temperature-Programmed Desorption (TPD) measurements are extensively used to characterize the surface functionalities of carbon materials [19,20]. Oxygen complexes decompose mostly as CO_2 and CO that can be followed by TPD techniques. TPD experiments were performed in a thermogravimetric system (TA Instruments, SDT Q600 Simultaneous) coupled to a mass spectrometer (Thermostar, Balzers, BSC 200). The MWCNTs were heat-treated up to 920 ºC at a rate of 20 ºC/min followed by keeping this temperature for 0.5 h under a Helium flow rate of 100 mL/min to clean the carbon surfaces. The CO and CO_2 evolved from the samples during the heat treatment was monitored (TPD experiment). TPD experiments were also done for the samples after the heat treatment process (HT-TPD). The amounts of CO and CO_2 desorbed from the samples during the experiments were quantified by calibration of 28 and 44 m z^{-1} signals using calcium oxalate.

5.2.4. Catalytic Tests

The photocatalytic performance of the different photocatalysts was studied using an experimental system designed in our laboratory, as described in Chapter 2 “Experimental Techniques”, Chapter 3 “Photooxidation of Propene with TiO_2 Photocatalyst”, and Chapter 4 “Photooxidation of Propene with P25 Encapsulated in Silica”.

The weight of photocatalyst used in these experiments was 0.11 g for all the samples. The photocatalysts were used for the oxidation of propene at 100 ppmv in air at room temperature, 25 °C. The calibrated gas cylinder was supplied by Carburos Metálicos, S.A. The flow rate of the propene-containing stream was 30 (STP) mL/min in all experiments.

The propene-containing stream was passed through the photocatalyst bed until the propene concentration was stable (after about 3 h). The lamp is then switched on and kept working until a constant propene signal is achieved, that is, steady state conditions (usually after 3 h). Afterwards the outlet gas is continuously analyzed by mass spectrometry Ommistar (Balzers), in the same conditions of the catalytic tests performed in Chapter 3 or Chapter 4. Propene conversion was calculated using the equation showed in Chapter 3 (eq. 3.5) and Chapter 4 (eq. 4.2) for studying the catalytic activity of the materials synthesized in this chapter.

Additionally, blank tests were performed under the same experimental conditions as the catalytic tests, but in the absence of the TiO_2 photocatalysts, and no catalytic activity was detected.

5.3. Results and Discussion

5.3.1. Materials Characterization

The carbon loadings (MWCNTs) incorporated in the composites synthesized in this Chapter are illustrated in the Table 5.1. These results obtained by TG analysis show that all composites present approximately 1wt.% of carbon in the composites using the different dispersion approaches. Moreover, these values are similar to the nominal loading value (1wt.%) indicating that MWCNTs are adequately incorporated in the composites in all approaches studied in this Chapter.

Table 5.1. Loadings of multiwall carbon nanotubes (MWCNTs) of the samples prepared in this study calculated by TG analysis (Determined from the weight loss in the interval 450-600 ^oC).

Samples	wt.% MWCNT TG analysis
MWCNT	100
TiO_2-MWCNT_UB_5min	1.03
TiO_2-MWCNT_UB_60min	0.98
TiO_2-MWCNT_UP_5min	1.06
TiO_2	-

The XRD patterns of the composites prepared using different approaches in the synthesis are showed in Fig. 5.1. In all composites, the TiO_2 presents the characteristic peaks of the anatase phase and they are similar to the bare TiO_2. However, the TiO_2-MWCNT_UB_5min (8.7 nm) TiO_2-MWCNT_UB_60min (9 nm) and TiO_2-MWCNT_UP_5min (9.1), composites have a slight increase in the crystal size with respect to pure TiO_2 (7.6 nm), calculated using the Scherrer equation previously described in Chapter 3 "Photooxidation of propene with TiO_2 photocatalyst".

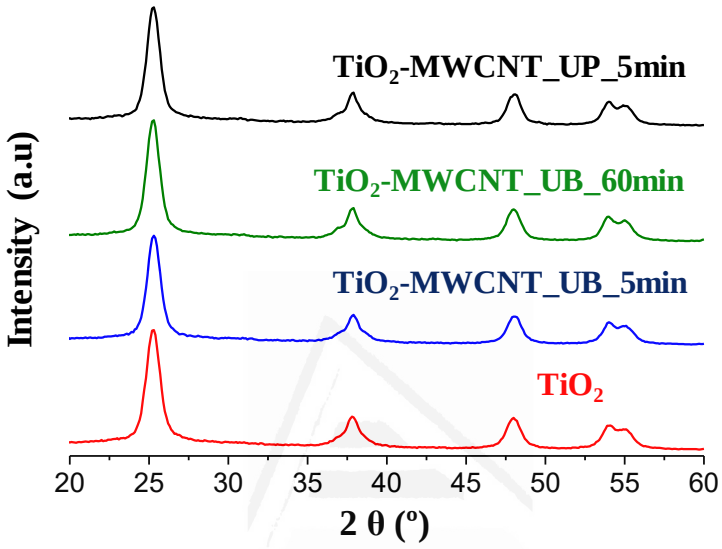

Figure 5.1. XRD patterns of all composites prepared with MWCNT and bare TiO_2 for comparison.

The UV-Vis absorption properties of the composites prepared in this Chapter and the original TiO_2 were evaluated (Fig 5.2 and Table 5.2). The bare TiO_2 presents an absorption edge and band gap (Table 5.2) at 398 nm and 3.12 eV typical of TiO_2 with anatase phase [21]. However, the composites presented a marked increase in the absorption of visible light and a decrease in the value of the band gap, as showed in Fig 5.2 and Table 5.2, since MWCNTs can modify the band gap and the UV-Vis absorption properties of the semiconductor as it has been widely described in the literature [13,22].

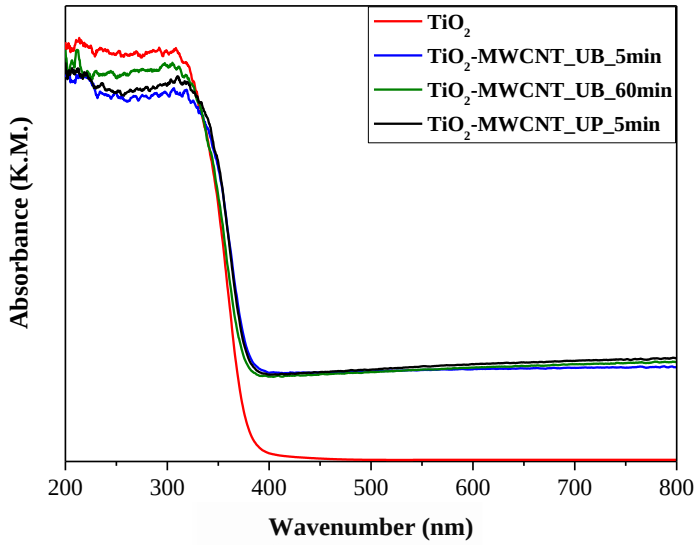

Figure 5.2. UV-Vis absorption spectra of the composites (TiO_2-MWCNT) and pure TiO_2.

Table 5.2. Absorption edge wavelengths (nm) and band gap (Eg) values of the TiO_2-MWCNT composites and bare TiO_2 prepared in this study.

Samples	λ (nm)	Eg (eV)
TiO_2	398	3.18
TiO_2-MWCNT_UB_5min	425	2.91
TiO_2-MWCNT_UB_60min	426	2.90
TiO_2-MWCNT_UP_5min	428	2.89

Fig 5.3 presents TEM images of the composites, which show that the sample with 60 minutes sonication in a bath presents a better dispersion than the same sample after only 5 min sonication. Moreover in the TEM images it is observed that the sample treated using an ultrasound probe for 5 min (TiO_2-MWCNT_UP_5min) presents a better dispersion (smaller aggregates) and shorter MWCNT length with respect to the samples dispersed with a ultrasound bath (TiO_2-MWCNT_UB_5min, TiO_2-MWCNT_UB_60min), indicating that a more intense sonication promotes a better dispersion of the MWCNT and may generate some structural defects in the carbon materials.

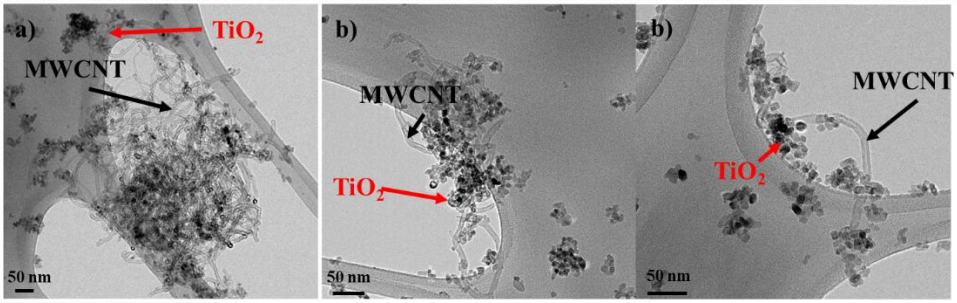

Figure 5.3. TEM images of the different TiO_2-MWCNT composites prepared in this Chapter: a) TiO_2-MWCNT_UB_5min, b) TiO_2-MWCNT_UB_60min, c) TiO_2-MWCNT_UP_5min,

The interaction of the TiO_2 and the MWCNT was studied by XPS analysis, as showed Fig. 5.4. The XPS spectrum of Ti 2p shows a positive displacement of 0.9 eV (bands Ti 2p1/2 and Ti 2p3/2) in presence of the MWCNT (composites) with respect to the pure TiO_2. This displacement can indicate of a good interaction between the MWCNT and the TiO_2 in the composites [23].

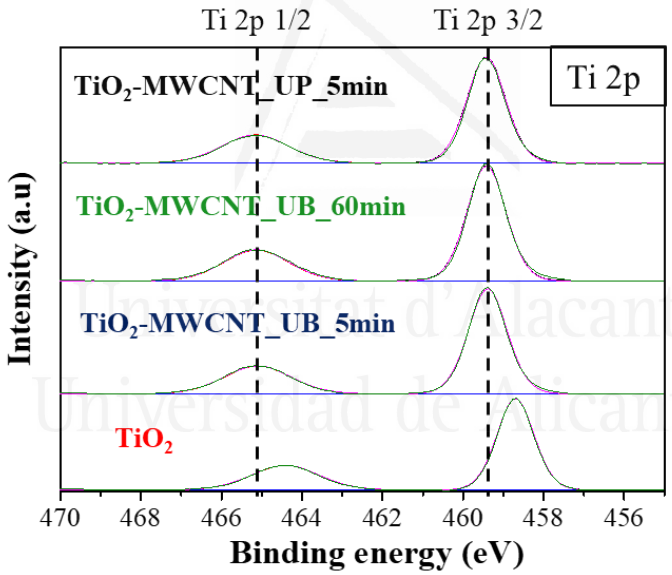

Figure 5.4. Ti 2p XPS spectra of the TiO_2-MWCNT composites prepared in this study and bare TiO_2.

In order to characterize the modification of the surface of the MWCNT with the different sonication treatments, we have determined the active surface area (ASA) and surface composition (TPD) of the bare MWCNT and the MWCNT after the three different dispersion approaches. The active surface area presented in Table 5.3 shows an increase of this parameter when the MWCNTs were sonicated for longer times (MWCNT_UB_60min) or when this carbon material was sonicated with an Ultrasonic probe (MWCNT_UP_5min). Moreover, the results obtained by TPD analysis (Table 5.3) show an increase of surface oxygen groups in the MWCNT

sonicated with an ultrasonic probe (MWCNT_UP_5min) with respect to the MWCNT_UB_60min, MWCNT_UB_5min and pure MWCNT samples. These parameters (ASA and surface composition) and the TEM images show that the increase of the sonication time and power promotes a better dispersion of the MWCNT and generates some structural defects in the carbon materials. This increase in both the dispersion and active surface area (or oxygen content) in the multiwall carbon nanotubes, may be interesting for the synthesis of composite materials with adequate properties for the application of these photocatalysts (photooxidation of propene).

Table 5.3 Active surface area (ASA) and surface composition, obtained by TPD, of the pure MWCNT and only MWCNT using three different approaches used in the synthesis of the composites.

Samples	ASA (m^2/g)	CO (µmol/g)	CO (µmol/g)	O (µmol/g)
MWCNT	8.1	351	95	541
MWCNT_UB_5min	8.5	316	182	679
MWCNT_UB_60min	9.0	415	159	734
MWCNT_UP_5min	13.0	529	149	823

5.3.2. Photocatalytic Activity

The photocatalytic activity of the materials prepared in this Chapter was evaluated by studying the mineralization of propene in the gas phase at low concentration (100 ppmv in air) to CO_2 at room temperature, as it was evaluated previously in Chapters 3 "Photooxidation of Propene with TiO_2 Photocatalyst" and 4 "Photooxidation of Propene with P25 Encapsulated in Silica".

The pure TiO_2 calcined at lower temperature (350 °C) (with the aim of not oxidizing the MWCNT) has a good conversion of propene (around 50%) which surpasses the conversion of propene observed for the reference sample (P25), as showed in Fig. 5.5. One interesting result is that the composites (TiO_2-MWCNT) synthesized in all approaches show higher conversion with respect to pure TiO_2. Moreover, we observed an increase in propene conversion for the samples prepared using an ultrasound bath for 5 min, 60 min and ultrasonic probe for 5 min, in this order (TiO_2-MWCNT_UB_5min < TiO_2-MWCNT_UB_60min < TiO_2-MWCNT_UP_5min) (Fig. 5.5). This fact can indicate that the incorporation of MWCNT favours the photocatalytic activity of the TiO_2 due to the positive properties of the MWCNT described in section 5.1 "Introduction" and in the literature [24]. For a better understanding of the photocatalytic activity of the composites prepared in this Chapter, were compared the propene conversion with the active surface area of the different composites (Fig. 5.6). The data show that an increase in the ASA results in

a higher propene conversion for the photocatalyst. This correlation and the characterization results obtained in this Chapter can indicate that a better dispersion of the carbon materials and the generation of higher active surface area or oxygen species on the MWCNT can improve the photocatalytic activity of the composites, because it will allow a better interaction of the Ti species and the MWCNT during the synthesis of the composites [11,13,24].

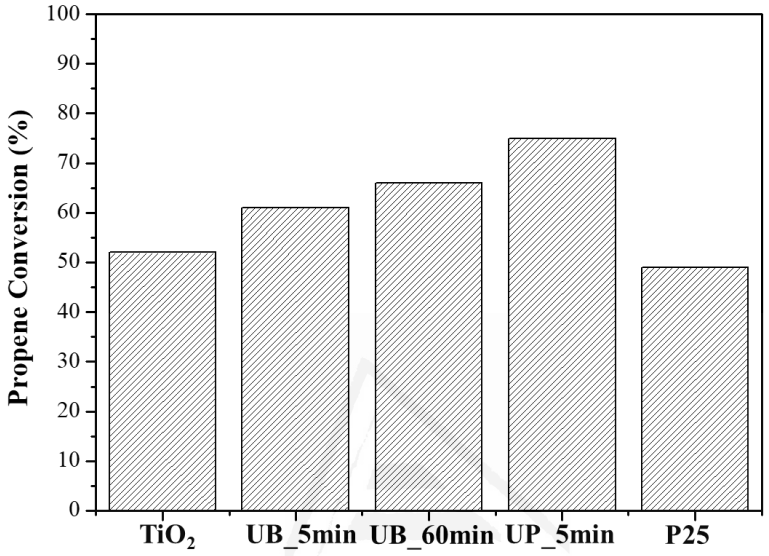

Figure 5.5. Propene conversion of the composites prepared in this study (TiO_2-MWCNT_UB_5min, TiO_2-MWCNT_UB_60min, TiO_2-MWCNT_UP_5min,), pure TiO_2 and commercial P25 for comparison proposed.

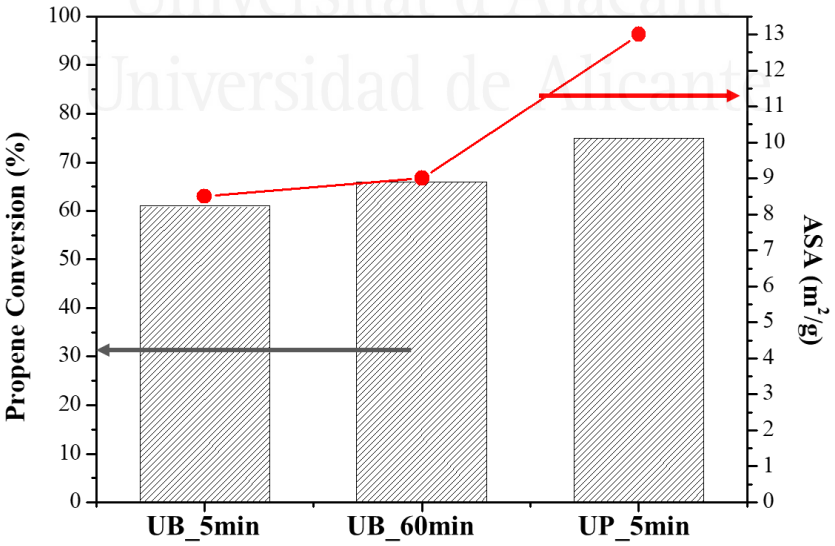

Figure 5.6. Comparison of propene conversion and active surface area (ASA) for the composites prepared in this Chapter

The effect of the electron hole recombination rate in the photocatalytic activity of the composites prepared in this Chapter may be of great relevance. To better understand this effect in the photocatalysts, as it has been reported in the literature [10,22], a photoluminescence analysis was performed to the composite showing the best catalytic performance (TiO_2-MWCNT_UP_5min) and the pure TiO_2 and commercial P25 for comparison purposes (Fig. 5.7). The PL spectrum presents the spectral range from 400 to 550 nm. The band at 416 nm indicates the indirect band-to-band recombination across the band gap. The peak observed at 520 nm is assigned to the recombination of states above the valence band [22,25,26]. The pure TiO_2 sample presents a smaller signal in PL emission than the commercial P25. Moreover, the composite (TiO_2-MWCNT_UP_5min) has a more significant decrease of the PL emission intensity, demonstrating that the incorporation of MWCNT hampers the e^--h^+ recombination rate and this effect can favour the photocatalytic activity of the composite [10,22,27].

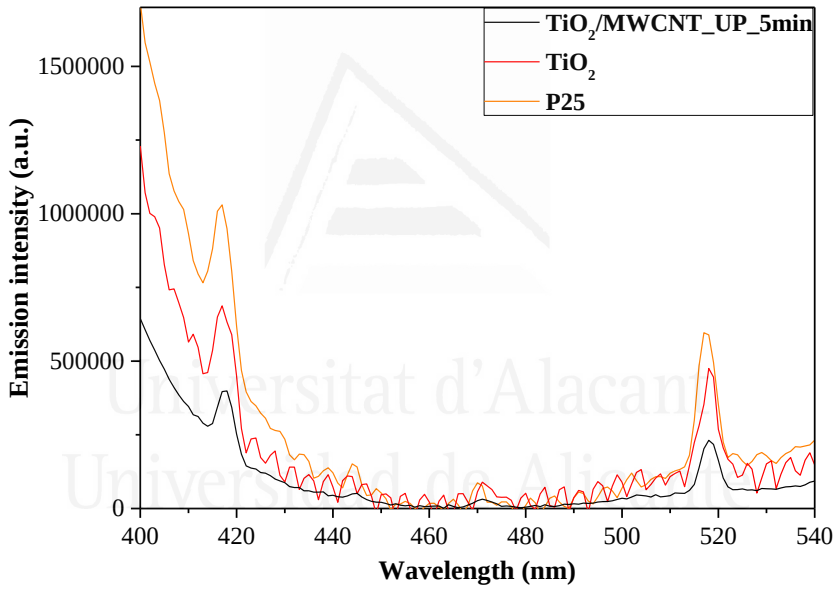

Figure 5.7. Photoluminescence of TiO_2-MWCNT_UP_5min, TiO_2 and P25 photocatalysts. The excitation wavelength used for the photoluminescence analysis was 380 nm.

Considering the results obtained in this Chapter in terms of characterization of composites and their performance in the photocatalytic oxidation of propene at low concentrations, the most promising outlook seems to be the following: 1) this Chapter presents an easy preparation method of TiO_2-MWCNT composites with improved dispersion of the MWCNT in the TiO_2 phase; 2) the incorporation of MWCNT in the TiO_2 synthesis improves the properties of the final composite material in terms of better absorption of Visible light and lower e^--h^+ recombination rate; 3) longer times of sonication or using a more powerful ultrasound source in the dispersion of the MWCNT generates a better dispersion of the carbon materials and higher active

surface area or oxygen species are created on the MWCNT; 4) a good interaction between the titanium oxide and the carbon material in the composite synthesis improves the photocatalytic activity

With the results presented and discussed above, TiO_2-MWCNT composites, which can be prepared by a simple, reproducible, and cost-effective sol-gel method display a remarkable photocatalytic activity with respect to the bare TiO_2 and the benchmark P25. Moreover the sample prepared using an ultrasound probe for dispersing the MWCNT presents better dispersion, higher active surface area and surface oxygen groups with respect to the other composites, what is favorable to increase the catalytic activity of this sample (TiO_2-MWCNT_UP_5 min).

5.4. Conclusions

In this Chapter, we have studied the synthesis of TiO_2-MWCNT composites focusing on the study of the effect of the dispersion of the components and in the carbon active sites generated on the MWCNT, in the properties of the composites for the abatement of propene, using different approaches for the dispersion of MWCNT; 1) using an ultrasound bath for 5 minutes, 2) using an ultrasound bath for 60 minutes and 3) using an ultrasound probe for 5 min. The most relevant results obtained were that sonicating for longer times or using a more powerful ultrasound source generates a better dispersion of the carbon materials and higher active surface area or oxygen species are created on the MWCNT. These features are beneficial for a better interaction between the titanium oxide and the carbon material in the composite synthesis, resulting in an improved photocatalytic activity, as shown in Scheme 5.1.

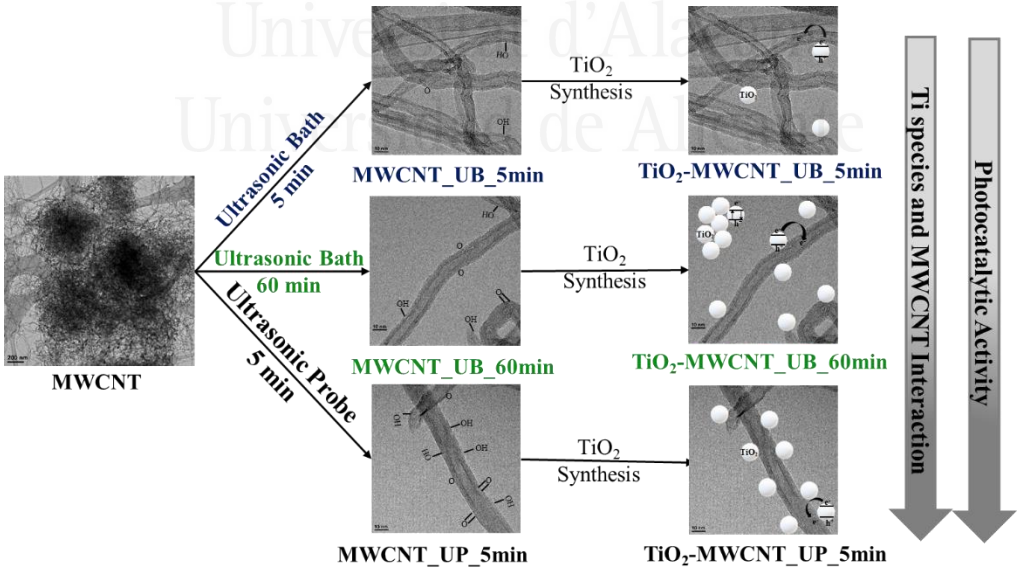

Scheme 5.1. Schematic representation of the synthesis procedure followed for the preparation of MWCNT-TiO_2 and the interesting results obtained in this Chapter.

5.5. References

[1] J. Schneider, M. Matsuoka, M. Takeuchi, J. Zhang, Y. Horiuchi, M. Anpo, D.W. Bahnemann, Chem. Rev. 114 (2014) 9919-9986.
[2] Y. Paz, Solid State Phenom. 162 (2010) 135-162.
[3] M. Humayun, F. Raziq, A. Khan, W. Luo, Green Chem. Lett. Rev. 11 (2018) 86-102.
[4] H. Park, Y. Park, W. Kim, W. Choi, J. Photochem. Photobiol. C Photochem. Rev. 15 (2013) 1-20.
[5] R. Leary, A. Westwood, Carbon. 49 (2011) 741-772.
[6] T. Torimoto, S. Ito, S. Kuwabata, H. Yoneyama, Environ. Sci. Technol. 30 (1996) 1275-1281.
[7] N. Yahya, F. Aziz, N.A. Jamaludin, M.A. Mutalib, A.F. Ismail, W.N. Salleh, J. Jaafar, N. Yusof, N.A. Ludin, J. Environ. Chem. Eng. 6 (2018) 7411-7425.
[8] M. Dahl, Y. Liu, Y. Yin, Chem. Rev. 114 (2014) 9853-9889.
[9] A.M. Kamil, H.T. Mohammed, A.A. Balakit, F.H. Hussein, D.W. Bahnemann, G.A. El-Hiti, Arab. J. Sci. Eng. 43 (2018) 199-210.
[10] K. Woan, G. Pyrgiotakis, W. Sigmund, Adv. Mater. 21 (2009) 2233-2239.
[11] Z. Li, L. He, L. Jing, J. Lin, Y. Luan, Chempluschem. 78 (2013) 670-676.
[12] P. Vincent, A. Brioude, C. Journet, S. Rabaste, S.T. Purcell, J. Le Brusq, J.C. Plenet, J. Non. Cryst. Solids. 311 (2002) 130-137.
[13] Y. Yu, J.C. Yu, J.G. Yu, Y.C. Kwok, Y.K. Che, J.C. Zhao, L. Ding, W.K. Ge, P.K. Wong, Appl. Catal. A Gen. 289 (2005) 186-196.
[14] W. Wang, P. Serp, P. Kalck, C.G. Silva, J.L. Faria, Mater. Res. Bull. 43 (2008) 958-967.
[15] Y.J. Xu, Y. Zhuang, X. Fu, J. Phys. Chem. C. 114 (2010) 2669-2676.
[16] V.B. Koli, A.G. Dhodamani, S.D. Delekar, S.H. Pawar, J. Photochem. Photobiol. A Chem. 333 (2017) 40-48.
[17] A. Gabe, R. Ruiz-Rosas, E. Morallón, D. Cazorla-Amorós, Carbon. 148 (2019) 430-440.
[18] J. Lahaye, P. Ehrburger, Pure Appl. Chem. 61 (1989) 1853-1858.
[19] J.L. Figueiredo, M.F.R. Pereira, M.M.A. Freitas, J.J.M. Órfão, Carbon. 37 (1999) 1379-1389.
[20] Y. Otake, R.G. Jenkins, Carbon. 31 (1993) 109-121.
[21] V.N. Kuznetsov, N. Serpone, J. Phys. Chem. B. 110 (2006) 25203-25209
[22] S. Da Dalt, A.K. Alves, F.A. Berutti, C.P. Bergmann, Part. Sci. Technol. 33 (2015) 308-313.
[23] L.A.A. Rodriguez, D.N. Travessa, Adv. Mater. Sci. Eng. 2018 (2018).
[24] G. Jiang, X. Zheng, Y. Wang, T. Li, X. Sun, Powder Technol. 207 (2011) 465–469.
[25] N.O. Ramoraswi, P.G. Ndungu, Nanoscale Res. Lett. 10 (2015) 427.
[26] A. Saha, A. Moya, A. Kahnt, D. Iglesias,S. Marchesan, R. Wannemacher, M. Prato, J.J. Vilatela, D.M. Guldi, Nanoscale. 9 (2017) 7911-7921.
[27] M. Shaban, A.M. Ashraf, M.R Abukhadra, Sci. Rep. 8 (2018) 781.

Chapter 6

Propylene Epoxidation with Ni-$TiSiO_2$ Catalysts

In this Chapter, we have presented a novel catalyst based on well-dispersed Ni nanoparticles loaded on a Ti-SiO_2 support for the propylene epoxidation reaction using H_2/O_2 mixtures. XPS, advanced electron microscopy techniques including High Resolution Transmission Electron Microscopy (HREM), and UV-Vis corroborate both the small size of Ni particles and the excellent dispersion and the incorporation of Ti as tetrahedral single-site species into the silica framework. The catalytic results under steady-state conditions at low temperature (200 ºC) show high selectivity towards propylene oxide (around 85 %) with a substantial propylene conversion (over 6 %) and excellent H_2 efficiency (~37 %) using only 0.5 wt. % of Ni on Ti-SiO_2 (Ti/Si=0.01 molar ratio). In this Chapter, we have also carried out a preliminary DFT study to gain understanding of the characteristics that make this nickel catalyst active and selective for the propylene epoxidation reaction.

6.1. Introduction

The worldwide production of propylene oxide (PO) is increasing each year due to its use as a pre-polymer for polyurethanes or polyether polyols synthesis [1]. At present, PO is mainly produced in liquid phase by the chlorohydrin process (40% of PO production) or by the organic hydroperoxide processes. However, some problems are associated to these commercial processes: for example, the use of dangerous and highly oxidizing reagents such as Cl_2 or organic peroxides (R-OOH) and the generation of by-products which are difficult of separate [2,3]. One alternative to overcome these shortcomings is to produce PO by the oxidation of propylene via heterogeneous catalysis, since this methodology can avoid the use of Cl_2 or organic peroxides enabling the use of other more sustainable and environmentally friendly reagents like H_2/O_2 or O_2.

In the last decades, the scientific community has strongly focused on gold supported on titanosilicates catalysts for PO production in gas phase ever since Haruta et al showed that their Au/TiO_2 catalysts (gold particles dispersed on TiO_2) could perform the propylene epoxidation reaction using H_2/O_2 mixtures with very high PO selectivity (>95%) at low propylene conversions (1%) [4]. Nevertheless, this Au-based catalyst suffered from a fast deactivation over time. Stangland et al found an active and stable catalyst based on Au supported on a microporous titanium silicalite-1 (TS-1) [5]. This catalyst presented a propylene conversion of 8.8% and a PO selectivity of 81% at 473 K. This type of catalyst has been studied by the scientific community until reaching a PO selectivity about 90 % with a propene conversion around 10 % at mild temperatures using H_2/O_2 mixtures. These results show that Au-based titanosilicate (Ti-SiO_2) catalysts are very interesting for propylene epoxidation. It must be noted, however, that under these conditions a PO selectivity around 90 % must be reached and maintained since this type of catalysts present a relatively low conversion (10%) [6-9].

In this sense, there are some theoretical and experimental studies in the literature where the authors try to clarify the reaction mechanism using Au-based catalysts. The reaction mechanism of the propylene epoxidation reaction over Au-based Ti-SiO_2 is still hitherto unclear [10]. Most of the authors propose the formation of H_2O_2 or -OOH species on the Au nanoparticles surface which migrate or spill-over towards the tetrahedral Ti incorporated in the silica framework, where propylene can be adsorbed [11,12]. Then the catalytic reaction takes place between the peroxide-like species and the adjacent Ti site [8].

With this in mind, even though Au-based Ti-SiO_2 catalyst is a good candidate for its use in the propylene epoxidation, the use of a noble metal, in this case Au, presents some drawbacks, such as high catalyst price (due largely to the use of gold), low H_2 efficiency and also relatively low propylene conversion. For this reason, it is crucial to develop a new catalyst that uses a non-noble (i.e. transition) metal as an

active phase, such as Ni, Cu, or Fe among others, due to the low price of these metals with respect to noble metals. In this aspect, one alternative can be the use of Ag-based catalysts, with proven performance in ethylene epoxidation. Unfortunately, these catalysts cannot be used for propylene epoxidation because activation of the allylic hydrogen atoms in propylene results in total combustion of the substrate [13,14]. To solve this problem, the scientific community has dedicated significant efforts towards developing transition metal (Ag/Ni [15,16], Fe [17,18] and Cu [19], among others) based catalysts with different oxidants (NO_2, O_2 and O_2/H_2). However, no catalysts with transition metals have reached acceptable selectivities compared to the benchmark Au/Ti-SiO_2 catalysts.

In this work, we present a Ni-based titanosilicate catalyst, which is very promising for the gas-phase catalytic epoxidation of propylene in terms of propylene conversion, PO selectivity and H_2 efficiency, with respect to Au-loaded catalysts. For comparison purposes, the catalytic performance will be compared with that of another transition metal-based catalyst (Fe), due to the low cost of this transition metal and the resulting interest for the scientific community [17]. Furthermore, and since the vast majority of information found in the literature regarding the theoretical investigation of the epoxidation reaction refers to gold-based catalysts as the active phase, in this work we have carried out a preliminary DFT study of the characteristics that make this nickel catalyst active and selective for propene epoxidation.

6.2. Materials and Methods

6.2.1. Materials

Titanium (IV) ethoxide (Sigma-Aldrich), tetramethyl orthosilicate (Sigma-Aldrich), nickel nitrate ($Ni(NO_3)_2 \cdot 6H_2O$, 99.99%, Sigma-Aldrich), iron nitrate ($Fe(NO_3)_2 \cdot 9H_2O$, 99.95%, Sigma-Aldrich), Pluronic F-127 (Sigma-Aldrich), urea (99%, Merck), glacial acetic acid (HAc, 99%, Sigma-Aldrich), sodium hydroxide (NaOH, 99.99%, Sigma-Aldrich) and deionized water were used in the present work. All reactants were used as received without further purification.

6.2.2. Sample Preparation

Synthesis of $Ti_{0.01}$-SiO_2. The mesoporous silica has been prepared adapting a synthetic protocol described elsewhere [20]. For the synthesis, 0.400 g of surfactant (Pluronic F-127), 0.452 g of urea, and 5.052 g of aqueous acetic acid (0.01 M) were mixed under vigorous stirring for 80 min, the final pH of the solution being around 4. Then the solution was cooled in an ice-water bath under continuous stirring and the silica precursor (Tetramethyl orthosilicate) and titanium precursor (Titanium(IV) ethoxide) were added dropwise. This solution was kept under stirring for 40 min at 0°C. The sol was introduced in a teflon-lined autoclave. Then, the autoclave was heated at 40°C for 20 h to produce the aging of the sol (the pH after this step was around 4) followed by a hydrothermal treatment at 120°C for 6 h, to produce the urea

decomposition (the final pH of the supernatant liquid was around 9-10). The final product was then calcined at 550ºC for 6 h (heating rate 3ºC/min).

Transition metal impregnation. For the Ni impregnation, the necessary amount of $Ni(NO_3)_2 \cdot H_2O$ was dissolved in 20 ml of deionized water to prepare the catalysts with the different loadings. After dissolution, 1.0 g of Ti-SiO_2 were added to the solution. Then, a freshly prepared NaOH solution (2 M) was added dropwise until a pH of 10.5 was reached producing a color change from colourless to light green. The suspension was stirred at room temperature for 2 hours, filtered and washed with water until neutral pH was obtained in the filtration water. Finally, the catalysts were dried at 100ºC before their use in the catalytic tests. Four different Ni loadings (wt. %) were prepared: 0.5, 1, 2, and 5 wt. % Ni/Ti-SiO_2. For comparison purposes in terms of performance in the propylene epoxidation reaction, iron-based catalyst was also prepared with 1 wt. % loading following the same procedure using the corresponding metal salt (see Materials Section).

6.2.3. Sample Characterization

All the prepared catalysts have been characterized by Transmission Electron Microscopy (TEM) with a JEOL JEM-2010 microscope operating at 200 kV with a space resolution of 0.24 nm coupled to Energy Dispersive X-Ray Analysis (EDX). TEM analyses allowed the evaluation of the metal species incorporation, the formation of small particles of metal and the quantification of the metal loading by the coupled EDX.

Spectroscopic techniques were also used for characterization purposes. The prepared materials were analyzed using an UltraViolet-Visible-Near-Infrared (UV-Visible-NIR, V-670, JASCO) equipped with a double monochromator system, a photomultiplier tube detector and an integrating sphere (ISN-723 UV-Visible-NIR, JASCO) which enables the possibility of measuring the diffuse reflectance or diffuse transmittance of a solid powder. In situ Fourier Transform Infrared Spectroscopy (FTIR, FTIR-4100, JASCO) was also used for the study of the solid-gas reaction in the different catalysts. The results have been presented by subtracting the spectrum corresponding to the pure catalyst to that obtained at the same temperature.

Inductively coupled plasma-optical emission spectroscopy (ICP-OES), in a Perkin-Elmer Optima 4300 system was used to obtain the metal loading of the catalysts (Ni). The necessary amount of sample was dissolved in 0.1 ml of HF (5 vol.%) at room temperature, in order to ensure the total dissolution of the samples, and then diluted to the linear iron detection range (0.05-10 ppm).

The electronic states were determined by X-ray Photoelectron Spectroscopy (XPS) using a K-Alpha spectrometer from Thermo-Scientific, equipped with an Al anode. The X-Ray penetration depth for this equipment is between 2 and 3 nm under the operating conditions. The analysis of the reduced samples was performed as

following: Firstly, the reduction of the formed $Ni(OH)_2$ nanoparticles was performed by doing a pre-treatment up to 500ºC (10 ºC/min) with 5 vol. % H_2 in He to reduce the formed $Ni(OH)_2$. After that, the sample after reduction were analyzed by XPS technique.

High-Resolution Transmission/Scanning Transmission Electron Microscopy, (S)TEM, studies were performed on a double aberration-corrected FEI Titan^3 Themis 60-300 microscope operated at 200 kV in High-Resolution TEM mode, additionally the microscope was operated at 80 kV to minimize sample damage effects for elemental mapping with energy dispersive X-ray spectrometry (XEDS) in STEM mode. This instrument is equipped with a monochromated, high brightness XFEG source and a high sensitivity, high efficiency Super-X EDS system, integrated by 4 window-less SDD detectors symmetrically arranged around the sample and the objective lens pole pieces.

The acquisition of XEDS maps was carried out using an electron probe less than 0.5 nm in diameter, beam current of 60-70 pA, convergence angle of 19 mrad and 20 keV of range. Each chemical map was collected as a series of frames, where the same region, typically 350 x 350 pixels, was scanned 50 times, employing a spatially drift-compensation tool, with a dwell time per pixel of 100 μs, taking approximately 10-12 minutes per spectral image dataset. STEM-HAADF images were recorded under analogous conditions employing an annular dark field detector with a collection range of 50 -200 mrad.

HREM images were analyzed in reciprocal space by measuring on the corresponding Digital Diffraction Patterns (DDPs) using Velox and Gatan Digital Micrograph (DM) software. Resolution in the order of 0.12 nm is achieved under the employed low voltage operating conditions. In addition, Eje-Z program [21] was used for the interpretation of HREM images and modeling the possible nickel phases present in the samples.

The XEDS- spectrum image post-treatment data was performed using Velox software, which allows quantification by Cliff-Lorimer (K-factor) method including absorption correction. The elemental maps of Silicon, Titanium and Nickel, were generated using the family of the Si-Kα, Ti-Kα and Ni-Kα lines at 1.74, 4.51 and 7.47 keV respectively.

The electron microscopy samples were performed by directly depositing a portion of the fine powder of the catalyst samples onto holey-carbon coated Cu grids, to avoid any contamination due to the use of solvents.

6.2.4. Catalytic Tests

Prior to the catalytic tests, all catalysts were pre-treated up to 500ºC (10ºC/min) with 5 vol. % H_2 in He to reduce the formed $Ni(OH)_2$ nanoparticles. The catalysts were tested for at least 4 h under steady-state conditions at 200ºC. The standard

conditions were WHSV of 10,000 ml·g^{-1}·h^{-1} and a gas stream composed of 10% C_3H_6, 10% H_2, 10% O_2 in 70% He was used in the catalytic tests. The outlet gas composition was analyzed with a MS (Pfeiffer Vacuum, Thermostar) and a GC chromatograph (Agilent 7820A) equipped with two columns, PoraBond Q (Agilent) and CTR-I (Alltech), for the separation of the organic (propylene, propane, propylene oxide, acetaldehyde, acetone) and the inorganic (mainly, O_2 and CO_2) compounds, respectively. Propylene conversion, PO yield, PO selectivity and H_2 efficiency were determined and calculated in all catalytic tests following the previously published equations (eq. 5.1, 5.2, 5.3 and 5.4) [22].

$$\text{Propylene Conversion (\%)} = \frac{C_{C_3H_6-\text{in}} - C_{C_3H_6-\text{out}}}{C_{C_3H_6-\text{in}}} \times 100 \quad (5.1)$$

$$\text{PO Yield (\%)} = \frac{C_{\text{PO-out}}}{C_{C_3H_6-\text{in}}} \times 100 \quad (5.2)$$

$$\text{PO Selectivity (\%)} = \frac{C_{\text{PO-out}}}{C_{C_3H_6-\text{in}} - C_{C_3H_6-\text{out}}} \times 100 \quad (5.3)$$

$$H_2\text{Efficiency (\%)} = \frac{C_{\text{PO-out}}}{C_{H_2O-\text{out}}} \times 100 \quad (5.4)$$

6.2.5. Computational Details

DFT calculations were conducted by means of the CP2K package code in its 4.1 version using the QUICKSTEP module [23]. Dispersion corrected (D3) [24] GGA-PBE [25] exchange correlation functional under periodic boundary conditions (PBC) were used for all simulations. During geometry optimizations all the system was allowed to relax to find its local minimum. Adsorption energies were calculated by using the equation (eq. 5.5):

$$E_{ads} = E_{slab/molecule} - (E_{slab} + E_{molecule}) \quad (5.5)$$

Additional information is mentioned in this section for better understanding, CP2K uses a mixed gaussian planewave approach and MOLOPT [26] double-ζ plus polarization optimised basis sets with auxiliary planewave basis. Goedecker-Teter-Hutter GTH pseudopotentials [27] with 4, 6, 12, 18, 5 and 1 valence electrons for Si, O, Ti, Ni, C, and H, respectively have been used.

For all the calculations a periodic slab of 24.9 x 26.2 x 40 Å has been used. A vacuum gap perpendicular to the surface has been added in order to minimise the interaction between periodic images. Due to the size and the nature of the model used, all calculations were performed at the Γ-point. The auxiliary planewave energy was defined by an energy cutoff of 400 Ry. Self-consistent field cycles were converged at $1x10^{-6}$ Ha using OT (CG) method.

During the geometry optimization calculations all the atoms were allowed to relax without any constraint. Conjugate gradient method has been used to minimize the internal forces below force threshold of $9x10^{-4}$ Ry/Bohr.

6.3. Results and Discussion

6.3.1. Materials Characterization

The Ti-SiO_2 catalyst support was first characterized by HR-STEM HAADF and HR-STEM-XEDS (Fig. 6.1). STEM-XEDS elemental maps showed that Ti was highly dispersed, mixed at atomic level with Si in the support, as shown in Fig. 6.1b). Quantification of the elemental maps indicated in this case a Ti content slightly below the average composition, 0.8% at. As expected, other areas with higher Ti contents were also detected, as shown in Fig. 6.2. In all cases, Ti was found well dispersed in the SiO_2 matrix. No evidence of separate TiO_2-like areas could be detected.

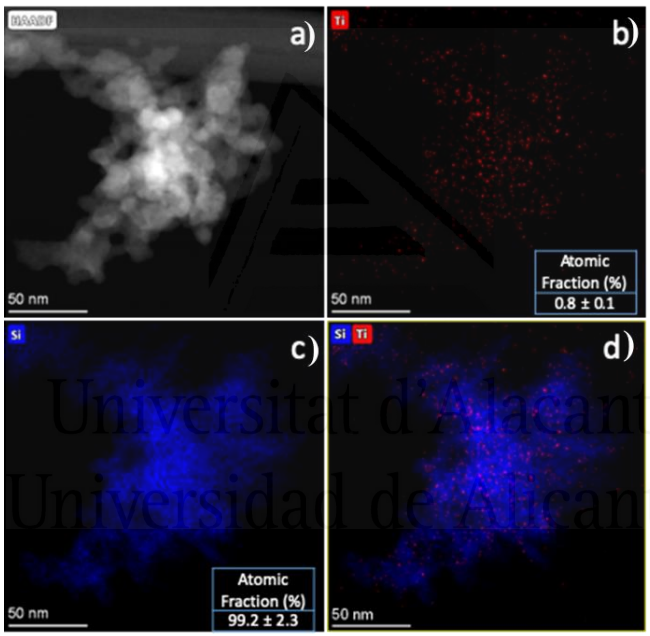

Figure 6.1. a) Representative STEM-HAADF image of the Ti-SiO_2 support, b-d) Ti, Si and overlaid maps obtained by STEM-XEDS.

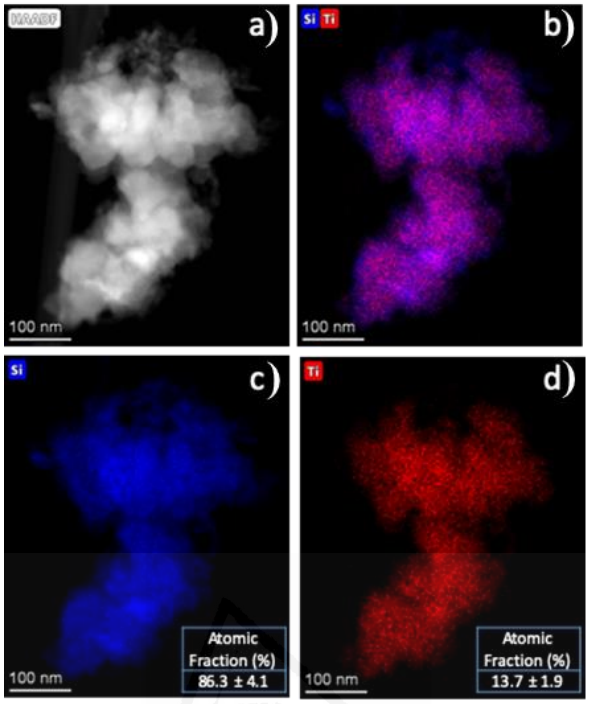

Figure 6.2. a) Representative STEM-HAADF image of the Ti-SiO$_2$ support in a Ti-rich area and b-d) Ti, Si and overlaid maps obtained by STEM-XEDS.

Moreover, as shown in Fig. 6.3, HREM images indicated that the support was formed by nanosized amorphous aggregates (Fig. 6.3 a)) Additional HREM images, including Digital diffractograms (DDPs) depicting the amorphous structure of the support have been gathered in Fig. 6.4. No evidence of crystalline areas could be obtained in the HREM study of the support.

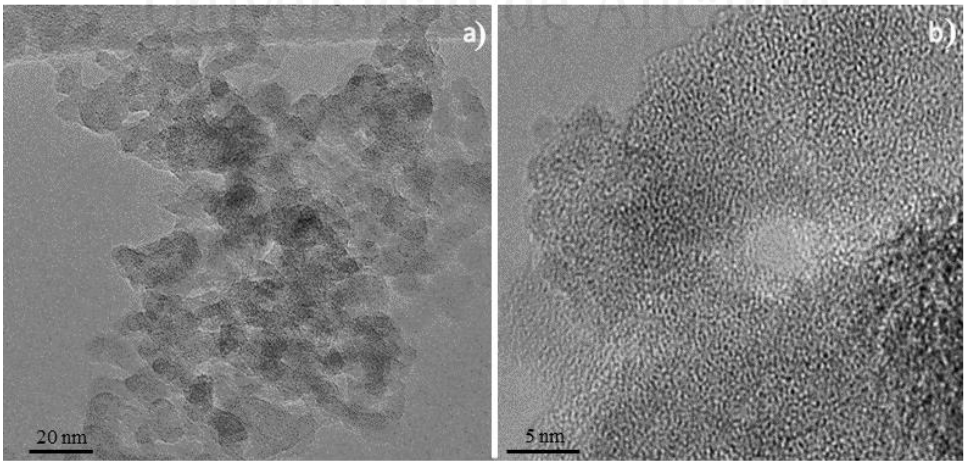

Figure 6.3. Representative medium a) and high b) magnification HREM images of the Ti-SiO$_2$ support.

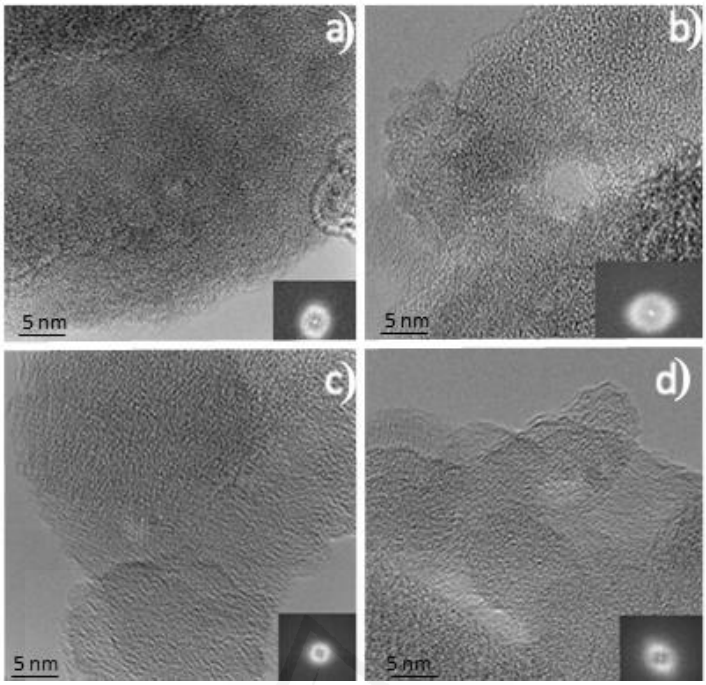

Figure 6.4. Additional HREM views of different regions of the Ti-SiO_2 support. DDPs where no reflection due to a crystalline material are included in each case as insets images.

The transition metal-based catalysts were synthesized by controlled precipitation of $Ni(OH)_2$ and $Fe(OH)_2$ in basic media (see Sample Preparation), on the surface of Ti-SiO_2. This support was prepared by one-step procedure following a well-known methodology [20]. All catalysts prepared in this Chapter were characterized with ICP-OES, in order to determine the metal loading. In all cases, the real Ni and Fe loadings were very close to their respective nominal loadings. UV-Vis absorption is a characterization technique very useful to study the incorporation of Ti into the silica framework [28]. The UV-Vis analysis revealed that Ti is incorporated as single sites into the silica framework mainly in tetrahedral coordination even though a small fraction of Ti in octahedral coordination is obtained in all samples (Fig. 6.5) [20]. As an example, a slight increase of the absorption at about 380 nm is observed after the incorporation of Ni in the catalysts, in all cases (Fig. 6.5). This band further increases after the reduction pretreatment of the Ni NPs indicating the presence of Ni^0 in the catalyst. The increase of the band at 380 nm is accompanied by a broadening of the band at 220 nm, which may indicate that a small fraction of the tetrahedrally coordinated Ti adopts an octahedral coordination after the reductive pretreatment.

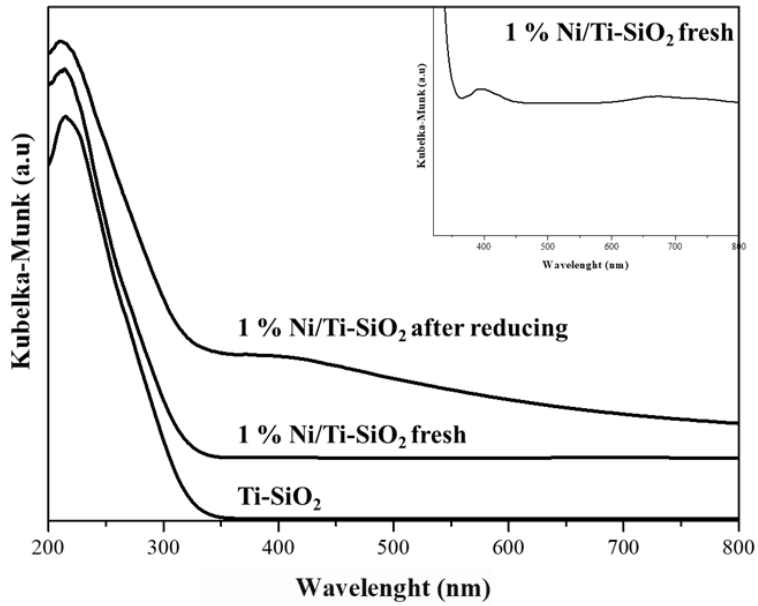

Figure 6.5. Solid UV–Vis reflectance spectra (presented in Kubelka-Munk units) for the raw Ti-SiO$_2$ and 1% Ni/Ti-SiO$_2$ fresh and after reducing. Inset: Magnified view of 300-800 nm region for sample 1% Ni/Ti-SiO$_2$ showing a small band at 380 nm.

TEM characterization (Fig. 6.6) shows a really good dispersion of the metal for the Ni-based catalysts for loadings between 0.5 and 1 wt. % Ni/ Ti-SiO$_2$. On the other hand, for 2 and 5 wt. % Ni catalysts, a more distinct presence of the Ni particles can be observed due to the high metal loading (Fig. 6.6). The EDX analysis confirmed the presence of the metal in all cases.

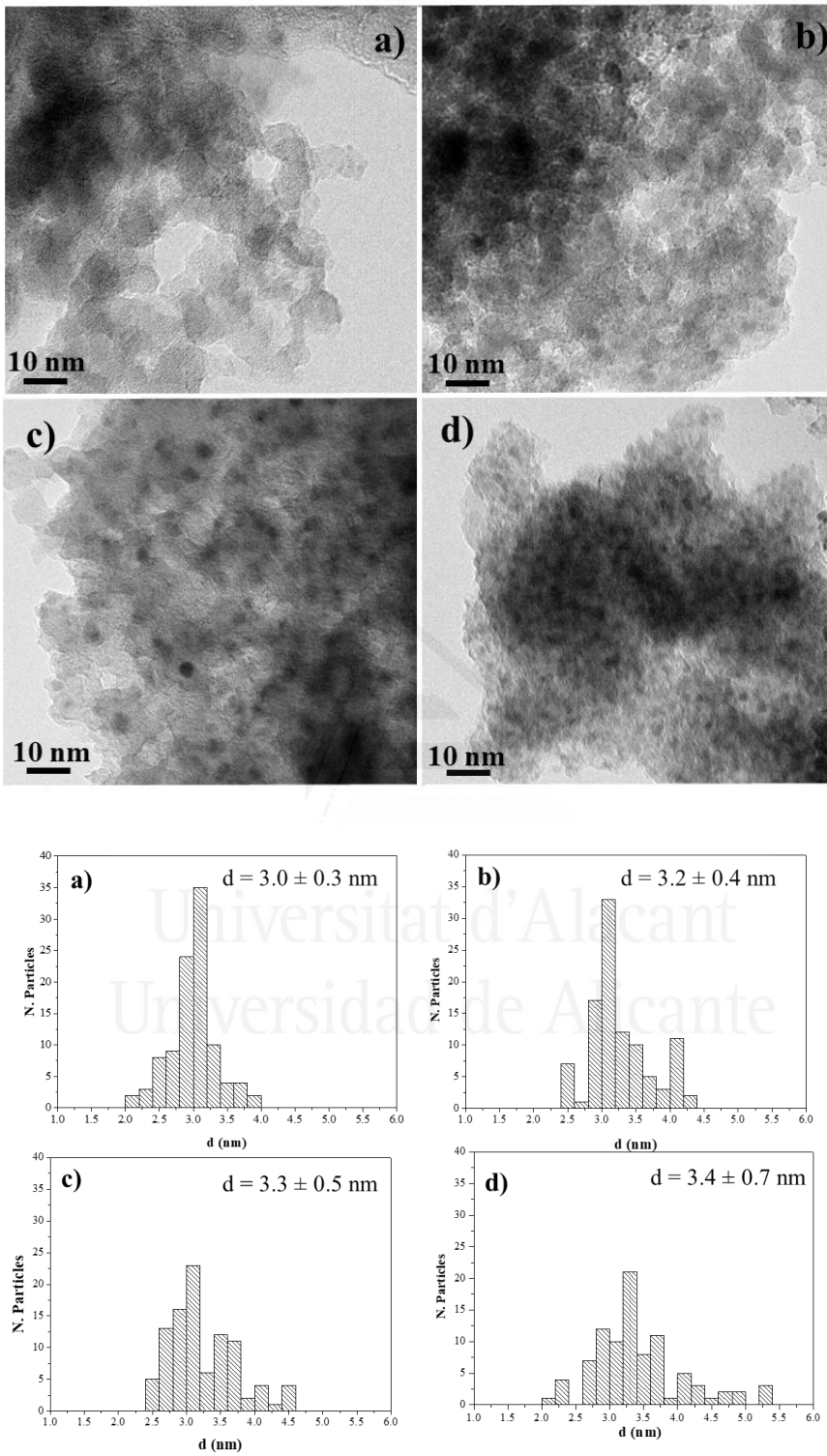

Figure 6.6. TEM images of a) 0.5 % Ni/Ti-SiO_2, b) 1 % Ni/Ti-SiO_2, c) 2 % Ni/Ti-SiO_2 and d) 5 % Ni/Ti-SiO_2 and their corresponding histograms.

The STEM-XEDS analytical investigation of the fresh 0.5% Ni loaded catalyst, (Fig. 6.7 a-e)), showed that the metal was finely dispersed over the surface of the support, in good contact with the underlying Ti areas. HREM images allowed detecting the presence of Ni in this catalyst in the form of 1.5-3.5 nm NiO particles (see Fig. 6.8). Characteristic fringe patterns of Ni were also observed in some particles most likely due to reduction of the small NiO particles under the electron beam (Fig. 6.9). No significant changes were detected in the nanostructure of the 0.5% Ni/Ti-SiO_2 catalyst after reaction, either in terms of the spatial distribution of the different elements present in the catalyst, as revealed by STEM-XEDS, Fig. 6.7f-j), or in the nature of the supported Ni phase, Fig. 6.8 d). Only a small increase in the size of these particles, now closer in average to 3 nm, could be observed.

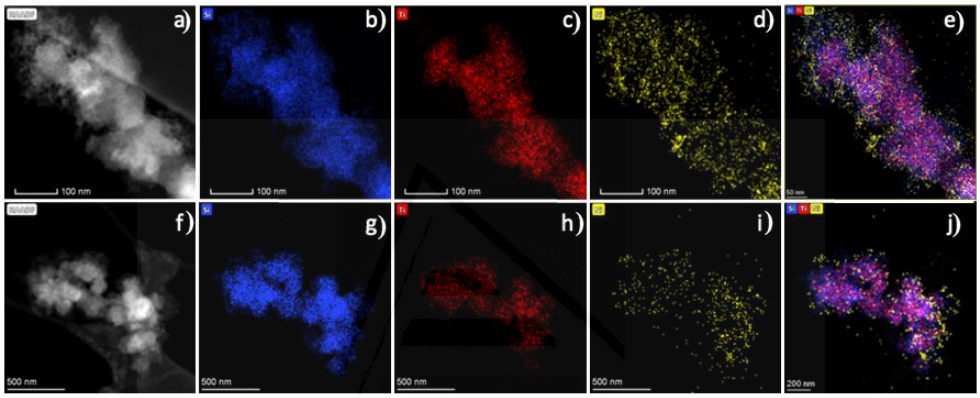

Figure 6.7. HR STEM-XEDS analytical study of the 0.5% Ni/Ti-SiO_2 catalyst as prepared (upper row) and after reaction (bottom row). STEM-HAADF a,f), Si b,g), Ti c,h), Ni d,i) and overlaid e,j) maps are included.

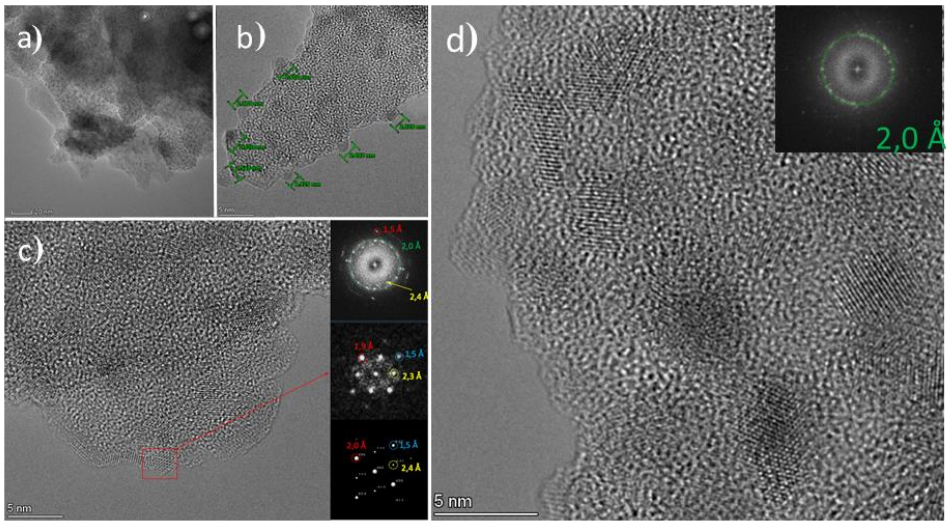

Figure 6.8. a-b) Medium and high magnification views of the fresh 0.5% Ni/Ti-SiO_2 catalyst. Different nanosized particles are marked in b), c) HREM view of the fresh catalysts where the structure of the particles is revealed. A DDP from the whole area (top-right inset), showing the 0.24 nm reflections characteristic of NiO is included. The DDP at the middle corresponds to a NiO down the [110] zone axis. A simulated DDP of NiO down [110] is shown at the bottom for comparison and d) representative HREM image of the 0.5% Ni/Ti-SiO_2 catalyst after reaction. A DDP showing a 0.2 nm reflection ring characteristic of Ni is included as inset.

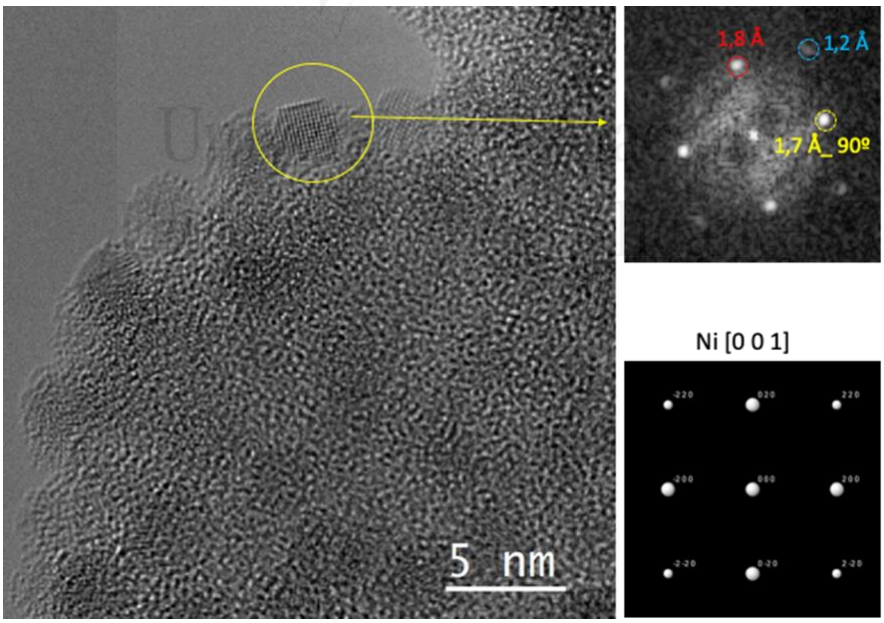

Figure 6.9. HREM image of an area of the 0.5% Ni/Ti-SiO_2 catalyst after reaction. The DDP of the nanoparticle encircled in yellow is shown at the right. Different reflections characteristic of metallic Ni are detected. A simulated DDP of Ni along the [001] zone axis is shown below for comparison.

The fresh catalysts with the highest Ni loading were also analyzed in detail by HR(S)TEM. In this case STEM-XEDS results, Fig. 6.10 a-e), showed a rather uniform and nearly complete coverage of the support particle surfaces by the metallic phase, as expected from the large increase in metal loading. HREM images (Fig. 6.11) showed once again a system of nanosized Ni-containing particles which eventually form long units which decorate in an almost continuous way the surface of the support particles, as marked with deep blue arrows in Fig. 6.11 a,c). The analysis of the lattice fringes revealed the presence of both NiO and Ni, as in the low loading catalyst. As in the case of the lowest loading catalyst, the major nanostructural features of the 5% Ni/Ti-SiO$_2$ catalysts did not significantly modify after reaction, as shown in Fig. 6.10 f-j) and 6.11d). Nevertheless, it must be mentioned that some degree of Ni particle agglomeration is observed, as shown in Figs 6.10 f). As with the catalyst, with a low Ni loading, fringe patterns characteristic of Ni were also observed in some particles (Fig. 6.12).

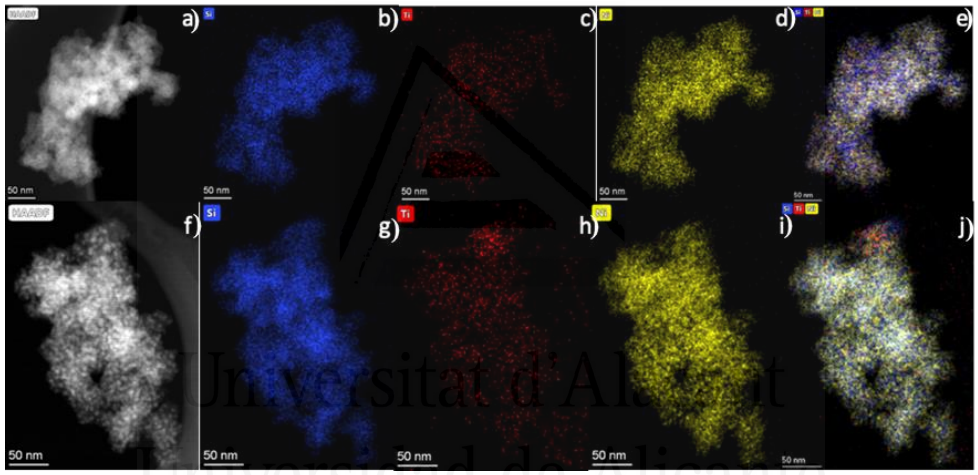

Figure 6.10. HR STEM-XEDS analytical study of the 5% Ni/Ti-SiO$_2$ catalyst as prepared (upper row) and after reaction (bottom row). STEM-HAADF a,f), Si b,g), Ti c,h), Ni d,i) and overlaid e,j) maps are included

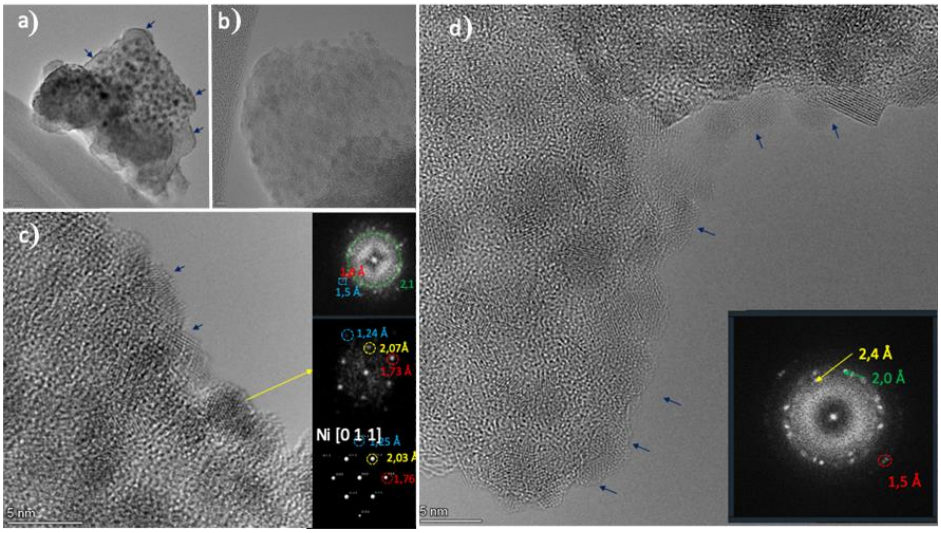

Figure 6.11. a-b) Medium and high magnification views of the fresh 5% Ni/Ti-SiO_2 catalyst. Deep blue arrows point to areas where a nearly continuous coverage of the support by Ni particles is observed. Individual nanosized particles are clearly observed in b); c) HREM view of the fresh catalysts where the structure of the particles is revealed. A DDPs from the whole area (top inset), showing the different reflections characteristic of Ni. The DDP at the middle corresponds to a Ni particle along the [110] zone axis. The DDP at the bottom corresponds to a simulated DDP for Ni along the [110] axis; d) representative HREM image of the 5% Ni/Ti-SiO_2 catalyst after reaction. A DDP of the whole area showing different NiO reflections is included as inset.

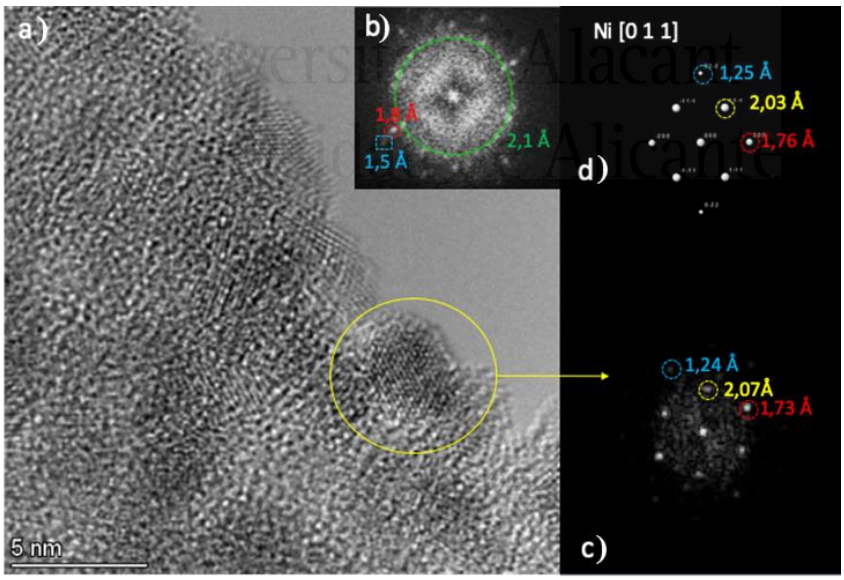

Figure 6.12. a) HREM image recorded on the 5% Ni/Ti-SiO_2 catalyst after reaction. A DDP of the whole area is shown in b). Different reflections corresponding to Ni are marked. Thus, the DDP from the particle encircled in yellow can be indexed to a Ni [110] image c). A simulated DDP is shown in d) for comparison purposes.

Ni and Ti XPS analysis offered information about the different Ni and Ti species present on the surface for the catalysts (see Fig. 6.13 a) and b)). The observed Ni 2p binding energies present some interesting data for nickel catalysts supported on titanosilicates materials. The fresh sample with 1 wt. % Ni/Ti-SiO$_2$ (without pretreatment) does not present a band at a binding energy of 852.8 eV characteristic of zerovalent nickel. However, the sample with 1 wt. % Ni/Ti-SiO$_2$ pretreated in H$_2$ at 500 ºC has the characteristic band of Ni^0 (Fig 6.11 a)). This fact indicates the reduction of the Ni(OH)$_2$ species (band at 856.7 eV) supported on the titanosilicate to metallic species (Ni^0) [29,30]. Moreover, the presence of Ni species on the surface of titanosilicate shifted the Ti 2p$_{3/2}$ BE signal from 460.48 eV (in the support) to 459.3 eV (after Ni loading) (Fig. 6.13 a)), indicating the existence of Ni species with a strong interaction with Ti species [31]. The presence of metallic particles on the support has a relevant effect in the catalytic properties of the catalyst as it has been described in the literature [8] and below in this work. The XPS spectrum collected after reaction showed that the Ni species supported on the catalyst come back to the oxidized species given that the post-reaction sample did not show the characteristic band of Ni^0 at 852.8 eV (Fig. 6.13 b)). The same XPS analyses were also performed in the 0.5 wt. % and 5 wt. % Ni/ Ti-SiO$_2$ and the results obtained (not shown) were very similar to those shown in Fig. 6.13.

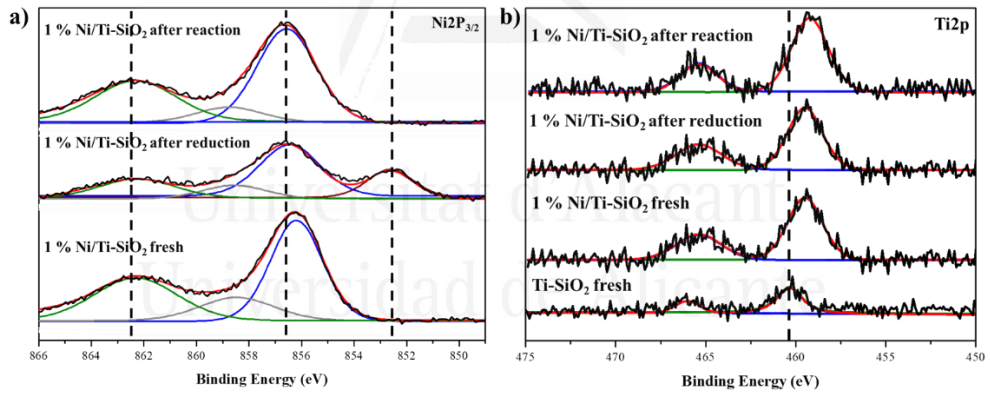

Figure 6.13. XPS of the sample 1% Ni/Ti-SiO$_2$: a) Ni2P$_{3/2}$ XPS spectra of the raw 1% Ni/Ti-SiO$_2$, 1% Ni/Ti-SiO$_2$ after reduction and Ni/Ti-SiO$_2$ after reaction and b) Ti2p XPS spectra of the raw Ti-SiO$_2$, 1% Ni/Ti-SiO$_2$ fresh, 1% Ni/Ti-SiO$_2$ after reduction and Ni/Ti-SiO$_2$ after reaction.

6.3.2. Propylene Epoxidation Reaction

The catalytic results under steady-state conditions for the gas-phase propylene epoxidation reaction at 200ºC for all the catalysts prepared in this Chapter are shown in Table 6.1.

Table 6.1. Catalytic results under steady-state for the gas-phase propylene epoxidation reaction at 200ºC.

Catalyst	C_3H_6 Conversion (%)	PO Yield (%)	H_2 Efficiency (%)	PO Selectivity (%)	Others[a] (%)	CO_2 Selectivity (%)
0.5 % Ni /Ti-SiO_2	6.3	5.4	36.9	85.5	4.5	10
1 % Ni/Ti-SiO_2	7.5	6.9	16.3	90.7	6.3	3
2 % Ni/Ti-SiO_2	5.8	3.0	10.6	52.2	6.7	41
5 % Ni/Ti-SiO_2	9.3	1.4	1.5	14.4	9.6	76
0.05 Au/TS-1[30]	8.8	n/d	n/d	81	14.7	4.4
1% Fe/Ti-SiO_2	1.1	<0.1	n/d	3	<1	~96

[a] Propane, Acetone and Acetaldehyde are the main organic by-products obtained in the catalytic reaction for Ni-based catalysts. Propanal, acrolein, and propanol were not detected in any of the experimental runs.

In this work a reaction temperature of 200º C was selected because the Ni-based catalysts studied in this chapter present the best catalytic results in the gas-phase propylene epoxidation reaction at that temperature, as shown in Table 6.2, and thus this was also the temperature of choice to test the Fe-based catalyst. An increase in the reaction temperature can favor the sintering of the Ni nanoparticles, thus having a negative impact on the catalytic activity and selectivity.

Table 6.2. Catalytic results under steady-state for the gas-phase propylene epoxidation reaction at different temperatures of the catalyst 1% Ni/Ti-SiO$_2$.

Catalyst	Temperature (ºC)	C_3H_6 Conversion (%)	PO Generation (%)	PO Selectivity (%)
1 % Ni/Ti-SiO$_2$	100	1.2	0.3	28
1 % Ni/Ti-SiO$_2$	150	6.3	5.4	85.5
1 % Ni/Ti-SiO$_2$	200	7.5	6.9	90.7
1 % Ni/Ti-SiO$_2$	250	5.8	3.0	52.2

The results of the Ti-SiO$_2$ and Ni/SiO$_2$ samples in the catalytic test are not presented in Table 6.1 because these catalysts did not present any catalytic activity for this reaction. This clearly shows that both well-dispersed Ni and Ti species with a strong interaction are needed in the catalysts to obtain suitable PO generation values in the presence of H_2/O_2 mixtures. Table 6.1 shows that all Ni catalysts present a conversion of propylene below 10% irrespective of the metal loading at 200ºC under steady-state conditions after the reduction treatment. It must be noted that all catalysts showed a stable catalytic performance throughout each epoxidation reaction (which, as mentioned in the experimental section lasted 4 hours). The Ni-based catalysts have similar propylene conversion compared to Au-based catalysts (e.g. Au supported on Ti-SiO$_2$) described in the literature (Table 6.1). Addressing the selectivity towards PO, the catalysts with low Ni loading (0.5% and 1%) present an excellent PO selectivity of around 90%. However, higher loadings of Ni on the surface of the titanosilicate decreased the selectivity towards PO as reported for the catalysts based on Au. This effect could be due to the different loadings of the catalysts (this is clearly shown by comparing Fig. 6.7 and 6.10). As a result, high amounts of Ni in the catalyst may block the Ti single site species on the surface of the support. As a result, these catalysts are not efficient in the propylene oxide generation due to a blocking of the active site, as we will discuss below. It must be noted that a similar active site engineering has been recently reported by Hutchings et al, in which they state that a suitable thermal treatment followed by reduction at 450 ºC is essential for the development of peripheral Pt/TiO$_2$ sites, which are "most likely active sites" in the selective hydrogenation of 3-nitrostyrene [32].

With respect to H_2 efficiency, an increase in the loading of Ni on the surface of the support causes a drop in this parameter. These results show the outstanding performance of the catalysts with low Ni loadings (0.5 wt. and 1% wt.) for this reaction. These catalysts present the best dispersion of nickel and titanium species on

and into the silica (see Fig. 6.6) which results in excellent catalytic properties with respect to other catalysts with higher amounts of Ni (2 wt. % and 5 wt. % Ni/ Ti-SiO_2). Moreover, these catalysts (0.5 wt. % and 1 wt. % Ni/ Ti-SiO_2) show similar catalytic properties than Au-based catalysts (7% of C_3H_6 Conversion and 90 % of PO Selectivity) being the catalyst based on Au the most attractive for this reaction reported in the literature [6,7]. In this aspect, the catalysts described in this Chapter present similar catalytic performance but using a significantly cheaper non-noble metal thus being more cost-effective than the catalyst based on gold. Another important factor is that the PO formation rate for the best Ni-based catalyst described in this work is 112 g PO/(kg_{cat}·h), similar to the benchmark Au-based catalysts described in the literature (116 g PO/(kg_{cat}·h)) [33,34]. This result of PO formation rate makes the nickel-based catalysts described in this work a competitive candidate for their use in the production of propylene oxide at an industrial scale. In this respect, the most promising catalysts were recovered and reused for at least three catalytic cycles, displaying no significant loss of performance after each cycle.

Table 6.1 also presents the data obtained using the Fe-impregnated catalyst. It is clear that the catalyst performs very poorly in this reaction. In the case of the Fe-based catalyst, apart from a very low propene conversion, the most noticeable result was that the predominant reaction was the complete oxidation of propene to CO_2 and water, which is consistent with literature data, which indicates that Fe is too acidic and thus promotes the abstraction of the allylic hydrogen of propylene, favoring its complete oxidation [17,18]. For the sake of comparison, and despite not being economically competitive to 3d transition metals, a Ru catalyst (prepared in the same way as that reported in our study, results not shown) was also tested. While the conversion increased significantly over the Fe-based catalyst, the selectivity towards the desired product was very low, with propane, isopropanol and acetaldehyde being predominant over propylene oxide. In this respect, the Ni/Ti-SiO_2 catalysts possesses the optimum interplay between oxygen and propylene activation, with very high selectivity (over 90%) towards the desired product.

In order to clarify the performance during reaction for the best catalyst, FTIR measurements before and after the reaction with the 1 wt. % Ni/ Ti-SiO_2 catalyst were carried out to investigate the surface species formed during reaction (Fig. 6.14). In the fresh catalyst (1 wt. % Ni/ Ti-SiO_2) no bands were observed at 2980, 2939 and 2880 cm^{-1}. These bands are assigned to the C–H stretching vibrations of bidentate propoxy species. After reaction these bands appear, which can result from PO adsorption on Ti sites [8]. This is also observed in the Au based catalysts indicating that the performance of these two catalysts converting propylene into propylene oxide may be similar [8,12]. In this respect, it would appear that the Ni species located near tetrahedral Ti would be performing the same role as Au nanoparticles in the benchmark catalyst. In this respect, the DFT results obtained in this study (vide infra) imply that the active sites are the interfaces between the nickel particles and the

tetrahedral Ti of the support, which, as evidenced from our catalytic data together with the FTIR experiments, perform similarly to the benchmark Au-based catalyst, suggesting the possibility that both catalysts follow a similar reaction mechanism to produce propylene oxide.

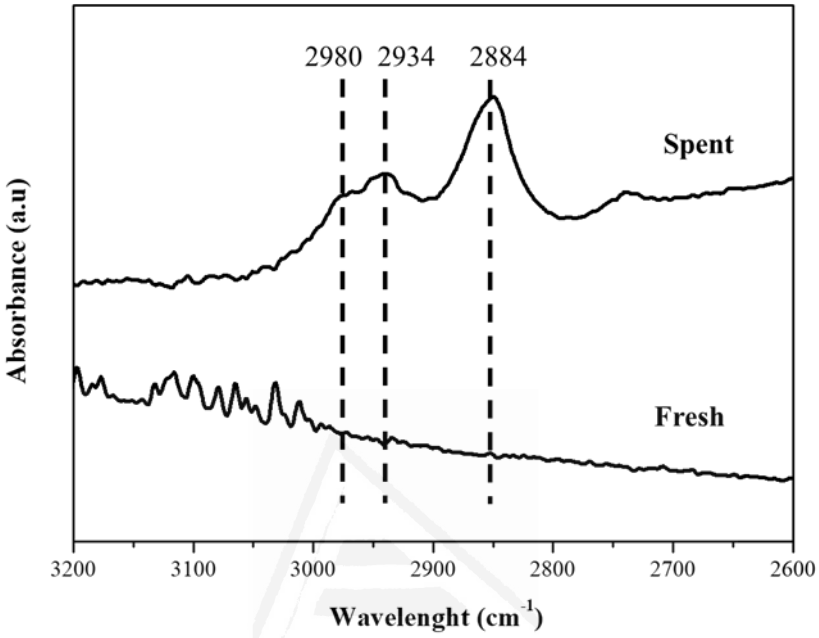

Figure 6.14. FTIR spectra of the fresh and the spent 1 wt. % Ni/ Ti-SiO$_2$ catalyst.

6.3.3. Computational Study

The majority of theoretical chemistry papers found in the literature are focused on the study of Au/TS-1 and Au/TiO$_2$ catalysts [35-37]. It is known that one of the characteristics of Au as active phase is its low capacity to promote catalytic reactions compared to other transition metals. Specifically, the capacity that gold possesses for oxygen chemisorption is limited [38-40]. Special conditions are needed in the structure of the gold particle (clusters with odd number of atoms, flexible geometries, alloys, hydrogen pre-chemisorption) [10] to activate the oxygen molecule for further reaction.

It is precisely this low ability to activate reactive molecules, which has made gold-based catalysts effective in reactions in which selectivity prevails over total catalytic activity [38,41] such as the propylene epoxidation reaction. The use of more reactive metal phases in the epoxidation reaction usually promotes the total oxidation of the hydrocarbon to carbon dioxide and the hydrogen to water (as is the case of the Fe-based catalyst [17,22] used in this study, see Table 6.1).

However, the results presented in this study show that the epoxidation reaction can be carried out with high selectivity using nickel as metal phase. Then, here we present a preliminary theoretical DFT study to try to understand the role of Ni species.

Description of the computational system

The molecular system used is based on an amorphous SiO_2 model. Specifically, a model of a MCM-41 wall silica structure presented in reference [42] has been modified and adapted as support for our catalyst model (424 atoms per unit cell). In the model used (Fig. 6.15), one surface silanol has been replaced by a Ti-OH group leading to a Ti tetrahedral single site placed in the silica framework, as it was deduced from the solid UV-Vis experiments. Some authors [35,43] demonstrated that tetrahedral Ti-OH are the active species to produce hydroperoxide intermediates (Ti-OOH) that is one of the key intermediates in the epoxidation reaction. It is also expected that this titanium site would be more accessible to reactants than non-hydroxylated titanium.

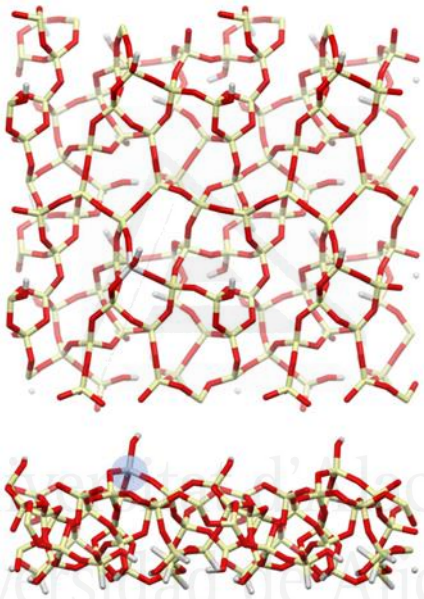

Figure 6.15. Top view and side view of the silica structure with intercalated Ti atom (Light blue circle in the lower diagram) in a Ti-OH site.

The TEM results conclude that the catalyst is comprised of very small nickel particles (1.5-3.5nm) for the low metal content catalysts (0.5 wt.%) as well as for the other catalysts. Thus, after optimization of the Ti/SiO_2 structure, a 10 atoms nickel particle (approx. 0.5 nm in diameter) has been added to the silica surface close to the titanium site and the geometry of the full structure was optimized. From our observations the Ni-Ti interface, where the epoxidation reaction is taking place (see below), is well represented in this model. Fig. 6.16 shows a detail of the interface between the nickel particle and the Ti/SiO_2 structure. It can be observed that nickel presents a strong interaction with the silica surface. This behavior is observed in the displacement of the oxygen atoms of silica structure in contact with the metal interface (marked in yellow).

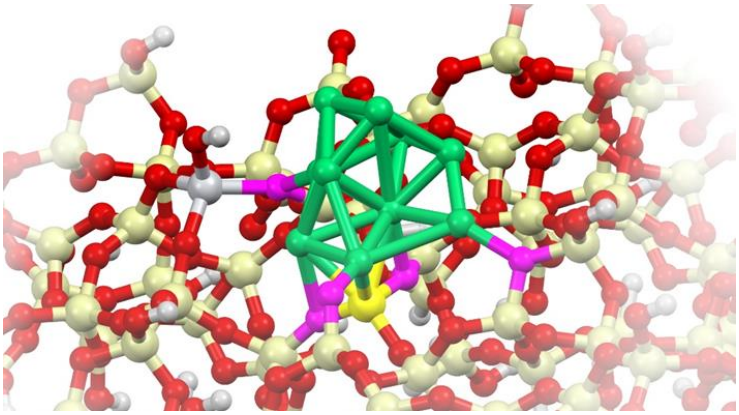

Figure 6.16. Detail of the interaction of the nickel particle with the Ti/SiO_2 framework. The distortion of the silica structure can be seen in the atoms marked in purple (oxygen) and in bright yellow (silicon).

Molecular interaction study

To understand the interaction of the reactive molecules with the model system, several geometry optimizations with H_2, O_2, and C_3H_6 have been carried out and the adsorption energies have been calculated. Different departure geometries have been studied to ensure that a representative energy potential space with different local minimum is sampled. Also, for comparative purposes, the optimization of some molecular adsorption geometries with the Ti/SiO_2 structure without nickel atoms was also calculated.

- Interaction with H_2 and C_3H_6

The interaction of H_2 with the system occurs mainly through the adsorption and dissociation of the hydrogen molecule over the nickel particle. The energies obtained in several attempts of chemisorbing H_2 on nickel atoms range between -0.9 and -1.2 eV. Different configurations have been studied with the adsorbed hydrogen on top, bridge and in hole positions and the values are in the order of the chemisorption energies obtained using Ni(111) as metallic surface [44]. The interaction of H_2 with the system without nickel leads to a low energy value typical of physisorption processes.

In the case of propylene, also several optimizations have been carried out with different starting geometries. The approximation of the olefin to the Ti site does not produce an optimized state with high adsorption energies: -0.05eV for the system without nickel, and -0.22 eV to the system with the nickel particle. However, the adsorption on the nickel atoms produces a strong interaction with an adsorption energy up to -2.02 eV. The carbon double bond length increases from 1.34 to 1.40Å indicating the activation of the molecule in the vicinity of nickel. However, this activation is far from the interface between nickel and Ti site, so an optimization approach with the propene close to the interface has been carried out. In this

optimization, the molecule is less activated than in the previous case. However, an adsorption energy of -0.92 eV indicates that some activation is taking place and it may be sufficient to facilitate the formation of propylene oxide. For comparison purposes, Driscoll et al. [45] found adsorption energies between -0.4 and -0.6 eV approximately for an active Au/TiO_2 catalyst.

- Interaction with oxygen

One of the key aspects in the epoxidation process, is the interaction of the oxygen molecule with the active phase. Firstly, the direct interaction of oxygen with the Ti/SiO_2 surface (without nickel) leads to a weak adsorption. Only a physisorption-like behavior and energies have been achieved after different attempts in geometry optimization.

The oxygen adsorption simulations show that the nickel nanoparticle used in the system has a strong interaction with molecular oxygen. Two different optimizations have been done with different starting departure geometries. Fig. 6.17 shows the final atom positions. Oxygen was adsorbed over two different zones of the nickel particle: far from Ti site (geometry I), and close to Ti site (geometry II). Adsorption energies are shown also in Fig. 6.17.

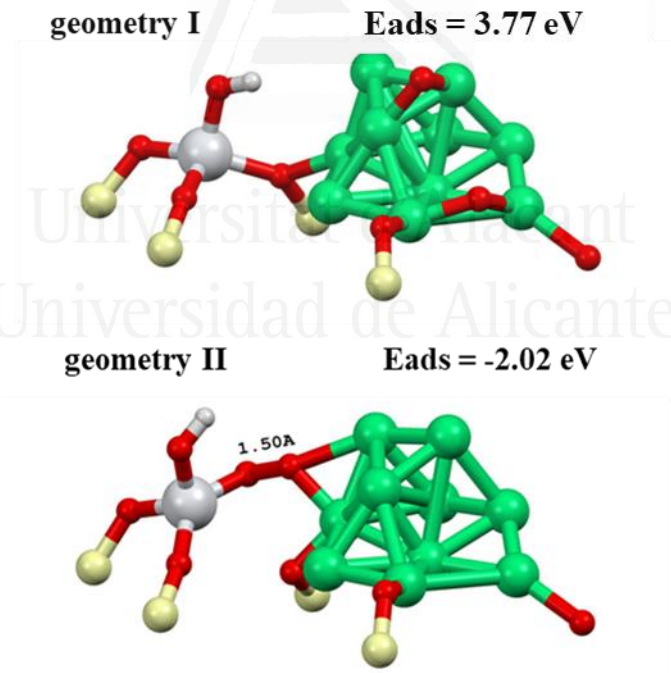

Figure 6.17. Detail of the two final geometries obtained during the adsorption of oxygen. Adsorption energies are also shown in eV.

The dissociation of the molecular oxygen during its adsorption on nickel that occurs in the geometry I takes place without any apparent activation barrier. A high adsorption energy (-3.77 eV) has been achieved. This dissociated atomic oxygen is more able to promote the oxidation of chemisorbed H_2 having a strong effect on the selectivity of the epoxidation reaction [46]. Furthermore, the absence of dissociation energy plus the higher adsorption energies obtained, implies that the metallic chemisorption sites available would be, practically, occupied with oxygen atoms, instead of hydrogen or hydrocarbon intermediates. That is why it is expected that during the epoxidation reaction, the nickel particles would be superficially oxidized. This catalytic behavior is in agreement with the XPS results obtained in Fig. 6.13 a), in which the spent catalysts show an oxidized nickel surface.

The geometry II in Fig. 6.17 shows that, when an oxygen molecule is placed in the space between the Ti site and the nickel particle a synergistic co-adsorption of the molecule occurs. The O-O bond length increases from 1.23Å in molecular oxygen to 1.50Å that corresponds to a bond distance typical of peroxide species (H_2O_2 has a bond distance of 1.54Å). The previous geometry is a structure in which the total dissociation of the O_2 molecule has not been carried out. Thus, it could be an intermediate whose reactivity towards the total oxidation of H_2 or the hydrocarbon could be limited. In addition, the adsorption energy is lower than in the previous case, so it would be a more suitable species to be an intermediate in epoxidation reaction [36-43].

To illustrate this, during the formation of this peroxide structure, a cleavage of one of the Ti-O bonds is proposed. Then, another free nickel atom participates in this co-adsorption forming a new Si-O-Ni species with the liberated Si-O bond (see Fig. 6.18, the Si-O-Ni species is highlighted in yellow). These results show that the open structure of the Ti-OH site and the flexibility of the amorphous silica play an important role to favor the formation of the peroxide structure found.

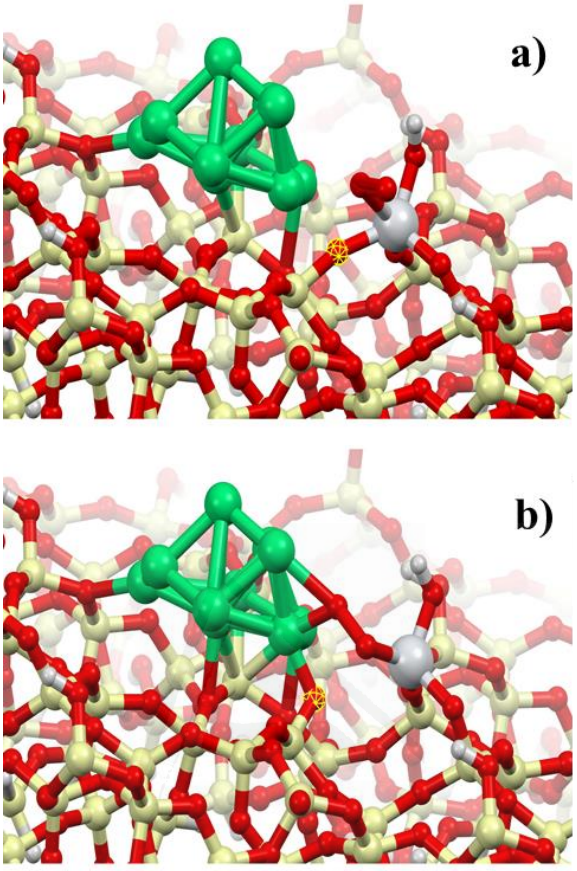

Figure 6.18. Initial a) and final b) geometries in the oxygen adsorption experiment. The moving oxygen is marked in yellow.

The strong interaction observed between nickel and oxygen agrees with the experimental fact that the nickel particles seem to be mainly oxidized during and after the epoxidation reaction. To understand how the nickel oxidation degree affects the Ti-Ni interface behavior, one and two oxygen molecules have been absorbed on the nickel particle. Then, another oxygen molecule has been relaxed on the Ti-Ni interface leading to the peroxide structure of geometry II in Fig. 6.17. These structure optimizations finally show that the adsorption of up to two oxygen molecules does not exert a significant effect on the formation energy of the peroxide structure.

With the aim of investigating if the geometry II structure could be an intermediate of the epoxidation reaction, the hydroperoxide (TiOOH) structure represented in Fig. 6.19 has been proposed and optimized. This structure consists of a migration of one of the oxygen atoms of the previous O-O peroxide structure (geometry II) and the formation of the titanium hydroperoxide species and a Ti-O-Ni link. This intermediate has been proposed by other authors [35,36] as the most probable intermediate for the epoxidation reaction in TS-1 and Au/TiO_2 catalyst,

being the closest oxygen to Ti the one abstracted by the propylene to form the epoxide molecule.

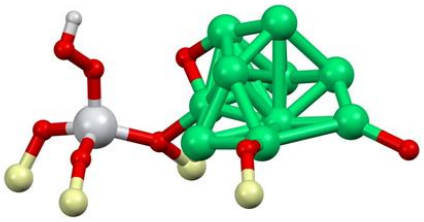

Figure 6.19. Optimized titanium hydroperoxide intermediate derived from geometry II structure shown in the Fig. 6.17.

The energy calculations carried out with these two species show that the hydroperoxide structure is thermodynamically less stable than the peroxide Ti-O-O-Ni one. Therefore, the transformation from one intermediate to another results in an endothermic change of +1.18 eV, so an energy barrier higher than this energy is expected for this transformation.

In several studies [35,36] it has been proposed that the Mulliken populations of the intermediates can act as indirect indicators to evaluate the reactivity of peroxide/hydroperoxide intermediate towards epoxidation. These authors suggest that the presumed mechanism for oxygen abstraction by the olefin is the electrophilic attack of the carbon double bond. So, the oxygen atoms available should be electron deficient to be reactive.

Fig. 6.20 shows the Mulliken charges of the two possible intermediates presented. The oxygen atom near the Ti site that was proposed as the active oxygen in the epoxidation mechanism by gold presents populations of -0.25 and -0.28 for the TiOOH and TiOONi structures, respectively. The oxygen atoms outside the peroxide group, present Mulliken charges of -0.5 approximately, so a loss in the electron density is found in the peroxide species. This loss allows the olefin molecule to approach the oxygen without producing an electronic repulsion effect, so the electrophilic attack stated above can take place. However, the similarity in the Mulliken charges in the two structures does not give a valuable criteria to choose the most probable intermediate in the epoxidation reaction.

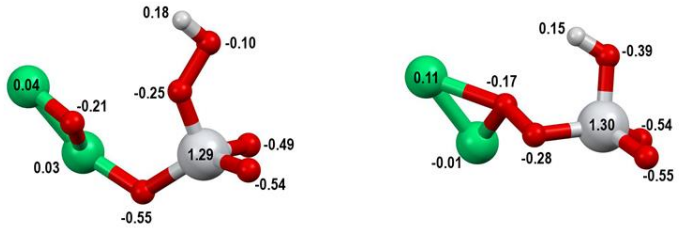

Figure 6.20. Mulliken populations of the two proposed intermediates.

Thus, further calculation work is being performed with the catalytic system with the aim of clarifying the mechanism of epoxidation of propylene using nickel as active metal and a Ti/SiO_2 as active site surface.

6.4. Conclusions

In summary, we have studied the use of Ni-based titano-silicate catalysts for the gas-phase catalytic epoxidation of propylene. The results show excellent catalytic results under steady-state. The best catalysts (0.5% and 1% $Ni/Ti\text{-}SiO_2$) described in this work show a conversion of propylene of about 6 %, a selectivity over 85 % and a PO formation rate of 112 g PO/(kg_{cat}·h). These values are very interesting because (1) these are similar to the best catalysts described in the literature (Au-based $Ti\text{-}SiO_2$) being the latter the ones that have the best catalytic properties to date and (2) they use a transition metal instead of a noble metal with stable (4 h of reaction) and cyclability (3 cycles) catalytic performance. This latter advantage can reduce the cost of PO production significantly. Thus, this work can open a new route towards the use of catalysts based on non-noble metals with catalytic properties similar to Au-based catalysts in epoxidation processes. Moreover, the preliminary study done using DFT calculations with the aim of clarifying the epoxidation mechanism of propylene using nickel as active metal and a Ti/SiO_2 as support, show that the interplay between Ni and Ti species with a good interaction is very important for produce the peroxide-species intermediate which results in the production of propylene oxide, as it has been reported for the Au-based catalyst. Thus, the cornerstone for the outstanding performance of these catalysts lies in the optimization of the amount of Ni-Ti interfacial sites, which relies on the interplay between an adequate development of Ti single sites in tetrahedral coordination and a low loading of Ni on the $Ti\text{-}SiO_2$ support to avoid any detrimental Ti blocking.

6.5. References

[1] J. Huang, M. Haruta, Res. Chem. Intermed. 38 (2012) 1-24.

[2] S.J. Khatib, S.T. Oyama, Catal. Rev. 57 (2015) 306-344.

[3] T. A. Nijhuis, M. Makkee, J. A. Moulijn and B. M. Weckhuysen, Ind. Eng. Chem. Res. 45 (2006) 3447-345.

[4] T. Hayashi, K. Tanaka, M. Haruta, J. Catal. 178 (1998) 566-575.

[5] E.E. Stangland, B. Taylor, R.P. Andres, W.N. Delgass, J. Phys. Chem. B. 109 (2005) 2321-2330.

[6] A. K. Sinha, S. Seelan, S. Tsubota, M. A. Haruta, Angew. Chem. Int. Ed. 43 (2004) 1546-1548.

[7] B. Chowdhury, J. J. Bravo-Suárez, M. Daté, S. Tsubota, M. Haruta, Angew. Chem. Int. Ed. 45 (2006) 412-415.

[8] J. Lu, X. Zhang, J.J. Bravo-Suárez, T. Fujitani, S.T. Oyama, Catal. Today. 147 (2009) 186-195.

[9] M. Haruta, J. Kawahara, Mechanisms in Homogeneous and Heterogeneous Epoxidation Catalysis, Elservier Science, 2008, pp. 297-313.

[10] J. Ji, Z. Lu, Y. Lei, C. H. Turner, Catalyst. 4 (2018) 421.

[11] A.K. Sinha, S. Seelan, S. Tsubota, M. Haruta, Top. Catal. 29 (2004) 95-102.

[12] G. Mul, A. Zwijnenburg, B. van der Linden, M. Makkee, J.A. Moulijn, J. Catal. 201 (2001) 128-137.

[13] M. A. Barteau, R. J. Madix, J. Am. Chem. Soc. 105 (1983) 344-349.

[14] J. T. Roberts, R.J. Madix W.W. Crew, J. Catal. 141 (1993) 300-307.

[15] A. Takahashi, N. Hamakawa, I. Nakamura, T. Fujitani, Appl. Catal. A: Gen. 294 (2005) 34-39.

[16] B. Yua, T. Ayvalı, E. Raine, T. Li, M.M.J Li, J. Zheng, S. Wu, A. A. Bagabas, S. C. E Tsang, Appl. Catal. B: Envir. 243 (2019) 304-312.

[17] V. Duma, D. Hönicke, J. Catal. 191 (2000) 93-104.

[18] B. Horváth, M. Hronec, R. Glaum, Top. Catal. 46 (2007) 129-135.

[19] X. Yang, S. Kattel, K. Xiong, K. Mudiyanselage, S. Rykov, S.D. Senanayake, J.A. Rodriguez, P. Liu, D.J. Stacchiola, J. G. Chen, Angew. Chem. Int. Ed. 54 (2015) 11946-11951.

[20] J. García-Aguilar, M. Navlani-García, Á. Berenguer-Murcia, K. Mori, Y. Kuwahara, H. Yamashita, D. Cazorla-Amorós, RSC Adv. 6 (2016) 91768-91772.

[21] S. Bernal, F.J. Botana, J.J. Calvino, C. Lopez-Cartes, J.A. Pérez-Ómil, J.M. Rodríguez-Izquierdo, Ultramicroscopy. 72 (1998) 135-164.

[22] J. García-Aguilar, D. Cazorla-Amorós, Á. Berenguer-Murcia, Appl. Catal. A: Gen. 538 (2017) 139-147.

[23] A. Kohlmeyer, C. J. Mundy, F. Mohamed, F. Schiffmann, G. Tabacchi, H. Forbert, W. Kuo, J. Hutter, M. Krack, M.Iannuzzi, et al. CP2K. CP2K Developers Group 2004.

[24] S. Grimme, Semiempirical GGA-Type Density Functional Constructed with a Long-Range Dispersion Correction. J. Comput. Chem. 27 (2006) 1787-1799.

[25] J. P. Perdew, K. Burke, M. Ernzerhof, Phys. Rev. Lett. 18 (1996) 3865-3868.

[26] J. VandeVondele, J. Hutter, J. Chem. Phys. 127 (2007) 114105.

[27] S. Goedecker, M. Teter, J. Hutter, Phys. Rev. B Condens. Matter 54 (1996) 1703-1710.

[28] X.H. Tang, X. Wen, S.W. Sun, H.Y. Jiang, Stud. Surf. Sci. Catal. 141 (2002) 167-172.

[29] T. Lehmann, T. Wolff, C. Hamel, P. Veit, B. Garke, A. S. Morgenstern, Micropor. Mesopor. Mat. 151 (2012) 113-125.
[30] A. P. Grosvenor, M. C. Biesinger, C. Smart, N.S. McIntyre, Surface Science. 600 (2006) 1771-1779.
[31] B.V. Senkovskiy, D. Y. Usachov, A.V. Fedorov, O.Y. Vilkov, A.V. Shelyakov, V.K. Adamchuk, J. Alloys Compd. 537 (2012) 190-196.
[32] M. Macino, A.J. Barnes, S.M. Althahban, R. Qu, E.K. Gibson, D.J Morgan, S.J. Freakley, N. Dimitratos, C.J. Kiely, X. Gao, A.M. Beale, D. Bethell, Q. He, M. Sankar, G.J. Hutchings, Nature Catalysis 2 (2019) 873-881.
[33] B. Taylor, J. Lauterbach, W.N. Delgass, Appl. Catal. A. 291 (2005) 188-198.
[34] T. Ishida, T. Murayama, A. Taketoshi, M. Haruta Chem. Rev. 120 (2020) 464-525.
[35] D. H. Wells, W.N. Delgass, K.T. Thomson, J. Am. Chem. Soc. 16 (2004) 2956-2962.
[36] C.R. Chang, Y.G. Wang, J. Li, Nano Res. 4 (2011) 131-142.
[37] A. Roldan, D. Torres, J. M. Ricart, F. Illas, J. Mol. Catal. A Chem. 306 (2009) 6-10.
[38] Z.P. Liu, P. Hu, A. Alavi, J. Am. Chem. Soc. 124 (2002) 14770-14779.
[39] J. Guzman, B.C.J. Am. Chem. Soc. 126 (2004) 2672-2673.
[40] B. Yoon, H. Häkkinen, U. Landman, A.S. Wörz, J.M. Antonietti, S. Abbet, K. Judai, U. Heiz, Science 307 (2005) 403-407.
[41] M. S. Chen, D.W. Goodman, Science 306 (2004) 252-255.
[42] P. Ugliengo, M. Sodupe, F. Musso, I.J. Bush, R. Orlando, R. Dovesi, Adv. Mater. 20 (2008) 4579-4583.
[43] D.H. Wells, W.N. Delgass, K.T. Thomson, J. Catal. 225 (2004) 69-77.
[44] G.W. Watson, R.PK. Wells, D.J. Willock, G.J.A Hutchings, J. Phys. Chem. B. 105 (2001) 4889-4894.
[45] D. M. Driscoll, W. Tang, S. P. Burrows, D. A. Panayotov, M. Neurock, M. McEntee, J. R. Morris, J. Phys. Chem. C 121 (2017) 1683-1689.
[46] H.Y. Su, X.H. Bao, W.X. Li, J. Chem. Phys. 128 (2008) 194707.

Chapter 7

Ammonia-Borane Decomposition with Cu/TiO_2-MWCNT Photocatalysts

In this Chapter, we have studied the effect of the incorporation of MWCNT on a TiO_2 support and the use of different metals (acting as active phase) to obtain Metal/TiO_2-MWCNT photocatalytic systems. The materials prepared in this Chapter were characterized by ICP-OES, TEM, EDX, XRD, PL, UV-Vis, and nitrogen adsorption techniques. Among those investigated metals, Cu has shown to be the most promising for the present application. The assessment of the photocatalytic performance of Cu/TiO_2-MWCNT with various Cu contents revealed that the catalytic activity depends on the Cu loading. The photocatalyst with 1 wt.% Cu loading displayed the best performance. The incorporation of MWCNT in the support enhanced the photocatalytic activity towards the production of H_2 under visible and UV-Visible light irradiation at room temperature.

7.1. Introduction

One of the important challenges for the scientific community is changing the energy scenario, currently based on carbon economy, towards a sustainable alternative. Carbon economy relies on limited resources, such as fossil fuels, which are associated to serious environmental problems. The drive towards a renewable and clean energy vector, with the objective of ensuring a sufficient worldwide energy supply while minimizing the environmental impact, is now stronger and more necessary than ever. In this sense, Hydrogen (H_2) is nowadays recognized as a candidate for a renewable and clean energy economy because it has high energy density and clean burning [1]. However, important limitations related to the safe storage, handling and distribution of H_2 are still under consideration [2]. An interesting alternative to solve these problems is the use of hydrogen carrier molecules, such as formic acid or ammonia borane (AB), through straightforward storage and delivery by their decomposition producing H_2 [3-6].

In the last years, the scientific community has paid attention to the production of H_2 from AB due to its interesting properties such as high hydrogen content (19.6 wt. %), high gravimetric and volumetric densities (196 $gH_2\ kg^{-1}$ and 146 $gH_2\ L^{-1}$, respectively), low molecular weight (30.87 g mol^{-1}), high stability and low toxicity [7-9], etc. The decomposition of AB to generate H_2 can follow two different pathways: 1) Pyrolysis that needs high temperatures and only reaches a yield of 6.5 wt. % of hydrogen (1 mol per mol of AB), and 2) Hydrolysis of AB that can produce a yield of 19.6 wt. % of hydrogen (3 moles per mol of AB) under mild reaction conditions using an adequate catalyst [10,11], as shown in eq. 7.1.

$$NH_3BH_3 + 2H_2O \rightarrow NH_4BO_2 + 3H_2 \quad (7.1)$$

Numerous studies have already been reported by investigating the performance of noble-metal based catalysts with various compositions (Au, Ru, Pt, Rh, and Pd) [12-15]. Such catalysts usually show interesting results under mild conditions, but they have drawbacks related to the scarcity and high price of noble metals.

With this problem in mind, the scientific community is focused on designing catalysts based on transition metals, such as Cu, Ni, Co, and Fe, among others, both in the form of monometallic or bimetallic nanoparticles combined with noble metals [16,17].

As for the support, a wide variety of materials has already been studied (carbon materials, oxides, zeolites, or metal organic frameworks (MOFs)), with the purpose of minimizing the load of metal used, stabilizing the nanoparticles and improving their catalytic activity [18-24]. An interesting and fruitful approach has been the use of photocatalytically-driven AB decomposition [13,14].

Despite the importance of titanium dioxide (TiO_2) in photocatalysis, described widely in this Thesis (Chapters 3, 4, and 5), the role of TiO_2-based catalysts as photoactive materials in this application has not been widely investigated so far due to its inherent deficiencies in terms of high band gap energy which can only be excited by UV light (λ<380 nm) and high recombination rate of electron–hole pairs, which results in low photocatalytic efficiency. Instead, those studies reporting on TiO_2-based catalysts for the present application, highlight other aspects such as the effect of the composition of the nanoparticles [17] or the plasmonic effect displayed by certain metals [14].

An interesting alternative to improve the properties of the TiO_2 as photocatalyst and support is the incorporation of carbon materials to form TiO_2-carbon systems [25,26]. In this sense, the use of carbon nanotubes (CNT) has attracted a great interest in the last decades due to their interesting properties, such as high electrical conductivity, high electron storage capacity and high-surface area (typically between 200-400 m^2/g). Moreover, the presence of CNTs in the photocatalytic system increases the lifetime of e^--h^+ pairs generated in the semiconductor and they can act as a supplementary catalytic active site in certain reactions [27-30]. These composites TiO_2-MWCNT have been described and tested before in this Thesis in Chapter 5 "Photooxidation of Propene with TiO_2-MWCNT Photocatalyst" for the abetement of pronene obtaining an enhancement of the catalytic activity with respect to pure TiO_2.

With this in mind, in this Chapter the TiO_2-CNTs composites with improved properties, previously reported in Chapter 5, are used as supports for transition metal photocatalysts for their use towards the production of H_2 from AB decomposition. Among the different transition metals investigated (Cu, Ni and Co), Cu-based systems showed the best activity under the experimental conditions used. The role of the carbon material was also herein assessed.

7.2. Materials and Methods

7.2.1. Materials

Titanium (IV) butoxide (TTB, 97%, Sigma-Aldrich), multiwall carbon nanotubes (MWCNT, Nanoblack, bamboo-type MWCNT with a diameter between 15 and 30 nm), glacial acetic acid (HAc, 99%, Sigma-Aldrich), Pluronic F-127 (F-127, Sigma-Aldrich), absolute ethanol (EtOH, 99.8%, Fisher Scientific), formamide (FA, 99.5%, Sigma-Aldrich), urea (99%, Merck), sodium borohydride ($NaBH_4$, 98%, Sigma-Aldrich), copper nitrate ($Cu(NO_3)_2{\cdot}3H_2O$, 99%, Nacalai Tesque), nickel nitrate ($Ni(NO_3)_2{\cdot}6H_2O$, 99.99%, Sigma-Aldrich), cobalt nitrate ($Co(NO_3)_2{\cdot}6H_2O$, 98%, Sigma-Aldrich), ammonia borane (AB, $H_3N{\cdot}BH_3$, 97%, Sigma-Aldrich), Commercial TiO_2 (P25, Rutile:Anatase / 70:30, 99.9%, Degussa) and deionized water were used in the present work. All reactants were used as received, without further purification.

7.2.2. Preparation of Supports (TiO_2 and TiO_2-MWCNT Composites)

The TiO_2 support was prepared using the synthesis developed and described in Chapter 3 "Photooxidation of Propene with TiO_2 Photocatalyst". For the synthesis of the TiO_2, 5 g of the titanium precursor (TTB) were dissolved in 7.9 g of EtOH. This solution (labelled "Solution A") was stirred vigorously for 10 min. Then, 1.6 g of HAc, 0.3 g of F-127, 1.6 g of H_2O, 7.9 g EtOH, 0.4 g of FA, and 0.4 g of urea were added in another vessel (labelled "Solution B"). The mixture was stirred for 10 min. "Solution B" was added dropwise to "Solution A" under vigorous stirring. The obtained solution was quickly transferred to an autoclave and heated at 60 °C for 24 h to promote the gel formation and the temperature was then increased to 120 °C for 24 h with the objective of promoting the decomposition of urea. The solid obtained was calcined at 350 ºC with the purpose of removing the template.

For the TiO_2/MWCNT composites, we have used an adaptation of the synthesis of TiO_2 described before (using the most interesting approach studied and described in Chapter 5 "Photooxidation of Propene with TiO_2-MWCNT Photocatalyst"), incorporating the needed amount of MWCNTs (1 wt. %) in "Solution B". The MWCNTs were then dispersed in "Solution B" with an ultrasound probe (Bandelin SONOPULS HD 2200) with a power of 660 W operating at 30 % power for 5 min. After this step, the synthesis was performed under the same conditions described for the support based on bare TiO_2 and in the synthesis described in Chapter 5.

The supports obtained in this Chapter were named as TiO_2 and TiO_2-MWCNT, respectively.

7.2.3. Preparation of Transition Metal (Cu, Co, and Ni) Based Photocatalysts

Photocatalysts based on as-synthesized TiO_2 and TiO_2-MWCNT, as well as on commercial P25 were prepared by following a standard impregnation protocol followed by a reduction step with $NaBH_4$. For that, 500 mg of support (TiO_2, TiO_2-MWCNT or commercial P25) were suspended in 10 mL of deionized water and stirred for 1 h. After that, the necessary amount of a solution of the metal precursor was added so as to have a final metal loading of 1 wt.% and the mixture was stirred for 1 h at room temperature. Then, the metal ions were reduced by incorporation of a freshly prepared $NaBH_4$ aqueous solution (molar ratio between metal and $NaBH_4$ was 1:10) and the solution was stirred for 1 h. Finally, the mixtures were centrifuged (5000 rpm) to collect the catalysts and they were quickly washed with a mixture of water and ethanol (1:1 in volume) three times in order to totally remove the $NaBH_4$ present in the samples. The washed catalysts were kept under vacuum to prevent the oxidation by air. In the case of Cu-containing samples, additional photocatalysts with different Cu loadings (1, 2, and 5 wt.%) were obtained by the same procedure. The obtained photocatalysts were denoted as (CuX%/TiO_2-MWCNT)

7.2.4. Samples Characterization

Thermogravimetric analysis was performed in a TA SDT 2960 thermobalance. In these analyses, the samples were heated up at 900 °C in air (heating rate of 10 °C min^{-1}).

X-ray diffraction (XRD) at room temperature was performed using a Rigaku Miniflex II equipment (30 kV/15 mA) with Cu Kα radiation and a scanning rate of 2º/min, in the 2θ range 6-80º.

Nitrogen adsorption-desorption isotherms at -196 ºC were performed in an Autosorb-6B apparatus from Quantachrome Corporation. Prior to the analysis, samples were degassed at 250 °C for 4 h under vacuum. BET surface area (S_{BET}) and total micropore volume (V_{DR}) were determined by applying the Brunauer-Emmett-Teller (BET) equation, and the Dubinin-Raduskevich equation to the N_2 adsorption data obtained at -196 °C, respectively. Total pore volumes (V_t) were determined from the adsorbed nitrogen volume at a relative pressure of 0.95.

X-Ray Photoelectron Spectroscopy (XPS) was performed using a K-α spectrometer from Thermo-Scientific, equipped with an Al anode.

Transmission electron microscopy (TEM) images were recorded using a JEOL JEM-2010 equipment. The metal loading was determined by inductively coupled plasma-optical emission spectroscopy (ICP-OES) with a Perkin-Elmer Optima 4300 system.

UV-Vis diffuse reflectance spectra were collected in a Shimadzu UV-2600 spectrophotometer. $BaSO_4$ was used as background, and the absorption spectra were obtained using the Kubelka-Munk function.

Photoluminescence measurements at room temperature were taken on a Fluorolog-3 spectrofluorometer (HORIBA). The excitation wavelength used for the photoluminescence analysis was 380 nm.

7.2.5. Catalytic Tests

The performance of the prepared photocatalysts towards the production of H_2 from AB dehydrogenation reaction was evaluated as follows: 20 mg of photocatalyst were suspended in 5 mL of deionized water in a sealed test tube (66 mL) and the system was purged with argon gas in the suspension for 30 min under stirring. Then, a solution of AB (500 μL, 0.04 M) was introduced in the mixture under stirring. The activity of the materials was assessed under dark, UV-Visible light irradiation or Visible light irradiation conditions ($\lambda > 420$ nm). The photocatalytic tests were performed by using a 500 W Xenon lamp (San-Ei Electric Co. Ltd.XEF-501S). The photoreactor was cooled by a fan in order to maintain a constant temperature (26 ± 0.5 ºC) during the photocatalytic reaction, as was described briefly in Chapter 2 "Experimental Techniques".

The H_2 evolution profiles were obtained by analyzing the evolved gas with a GC8A (Shimadzu) gas chromatograph equipped with a MS-5A column and a TCD detector. The reusability of the catalysts was evaluated by performing three consecutive runs. For that, the solvent was removed by centrifugation and the spent catalyst was placed in the reactor, purged with argon gas, and a fresh AB solution was injected. The reaction was monitored under the same experimental conditions as those used in the first reaction run.

7.3. Results and Discussion

7.3.1. Support Characterization

Table 7.1 includes the most relevant results of the characterization of the support materials since the characterization of these materials was described extensively in Chapter 5 "Photooxidation of Propene with TiO_2-MWCNT photocatalyst". The content of MWCNTs in the TiO_2-MWCNT support was determined by thermogravimetric analysis. The carbon content was calculated to be around 1 wt. %, which was in good agreement with the nominal MWCNTs loading. With respect to the crystallite size obtained by XRD analysis of the supports (Table 7.1), TiO_2 and TiO_2-MWCNT have the characteristic peaks of the anatase phase and smaller crystallite TiO_2 size with respect to the commercial P25. Moreover, the incorporation of MWCNT in the synthesis leads to a slight increase of the TiO_2 crystallite size in the composite support. The N_2 adsorption-desorption isotherms are shown in Fig. 7.1. The N_2 physisorption isotherm of commercial P25 shows a type-II isotherm, characteristic of a nonporous solid. As-synthesized TiO_2 and TiO_2-MWCNT showed a combination of type I and IV isotherms, which is typical of mesoporous materials with a certain degree of microporosity. However, TiO_2-MWCNT has a more developed mesoporosity because it presents an increase in the hysteresis and an increase of the V_t value as showed in Table 7.1. As for the textural properties, the results obtained from the adsorption-desorption experiments revealed that BET surface area and V_t increase for the as-synthesized TiO_2 and TiO_2-MWCNT as compared to the commercial P25. TEM images are presented in Fig. 7.2. The supports TiO_2 and TiO_2-MWCNT have a smaller TiO_2 particle size with respect to the commercial P25. Moreover, it is possible to observe the presence of MWCNT in the sample TiO_2-MWCNT and the good contact between both components of the composite. In this sense, the XPS spectrum of Ti 2p (Fig. 7.3) shows a positive displacement of 0.9 eV in presence of the MWCNT with respect to the raw TiO_2. This displacement is indicative of a good interaction between the MWCNT and the TiO_2 in the composites [31].

Table 7.1 MWCNT content (wt. %), crystallite size of TiO_2 and textural properties of the supports used in this work.

Support	MWCNT (wt. %)[a]	TiO_2 crystal size (nm)[b]	Surface area (m^2/g)	V_t (cm^3/g)	V_{DR} (cm^3/g)
P25	-	25	50	0.05	0.01
TiO_2	-	7.6	170	0.35	0.06
TiO_2-MWCNT	1.06	9.1	176	0.46	0.07

[a] Determined from the weight loss in the interval 450-680 ºC
[b] Determined from the Scherrer equation

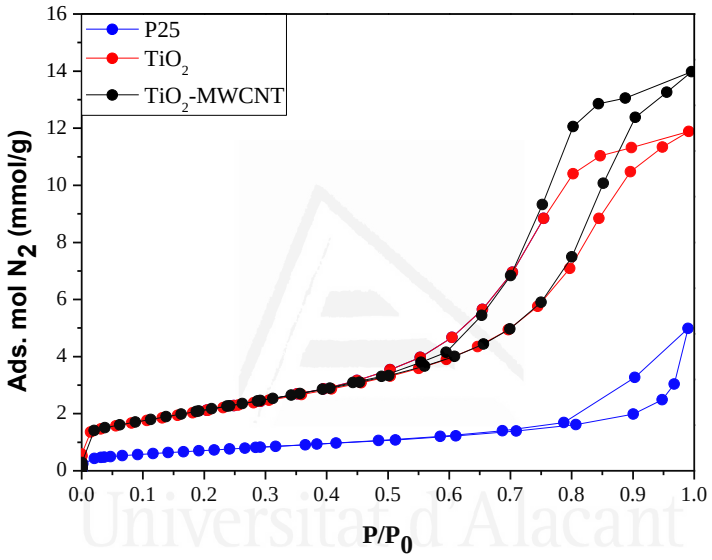

Figure 7.1. N_2 adsorption-desorption isotherms at - 196 ºC for the different supports (P25, TiO_2 and TiO_2-MWCNT).

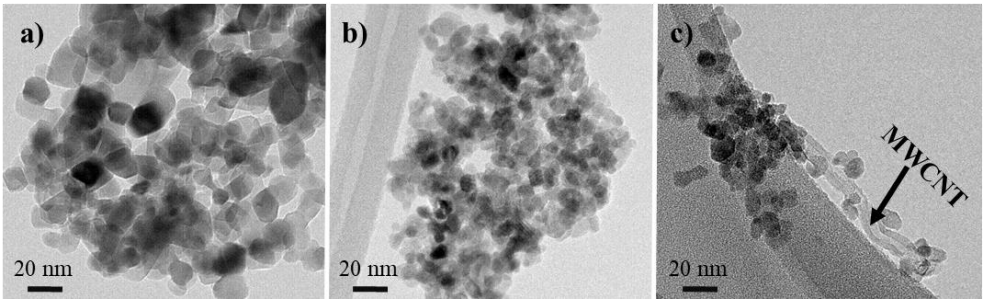

Figure 7.2. TEM images of the support: a) P25, b) TiO_2, c) TiO_2-MWCNT.

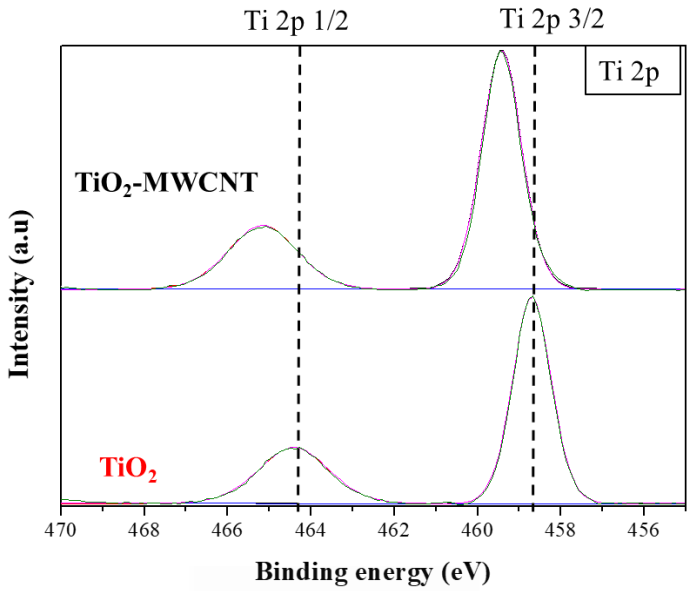

Figure 7.3. Ti 2p XPS spectra of the supports TiO_2 and TiO_2-MWCNT.

7.3.2. Study of the Effect of MWCNT in the Metal/TiO_2-MWCNT System

The evaluation of the composition of the catalysts was initiated with the study of the performance of various transition-metal-based photocatalysts supported on TiO_2-MWCNT for H_2 generation from AB dehydrogenation under visible light irradiation conditions. The metal content was ~1 wt.% in all cases by ICP-OES analysis (See Table 7.2). The comparison of the H_2 evolution profiles achieved with Cu, Ni, and Co photocatalysts is plotted in Figure 7.4. As it can be seen, Co-based photocatalysts displayed a very poor performance, producing 1.8 μmol after 35 min of reaction. In the case of Ni-based photocatalysts, a long reaction time was needed to achieve a total conversion of AB to H_2, while it was achieved after only 15 min for the Cu-based photocatalysts, revealing the superior performance of Cu1%/TiO_2-MWCNT over the Ni and Co counterparts. Such observation might be related to the more favored reduction of copper species under reaction conditions and the subsequent generation of metal active sites as compared to other composition of the catalysts.

Table 7.2. Percentage of metal (Cu, Ni or Co) on the TiO_2/MWCNT-photocatalyst.

Sample	Metal loading (wt. %)
Cu1%/TiO_2-MWCNT	0.91
Ni1%/TiO_2-MWCNT	0.83
Co1%TiO_2-MWCNT	0.81

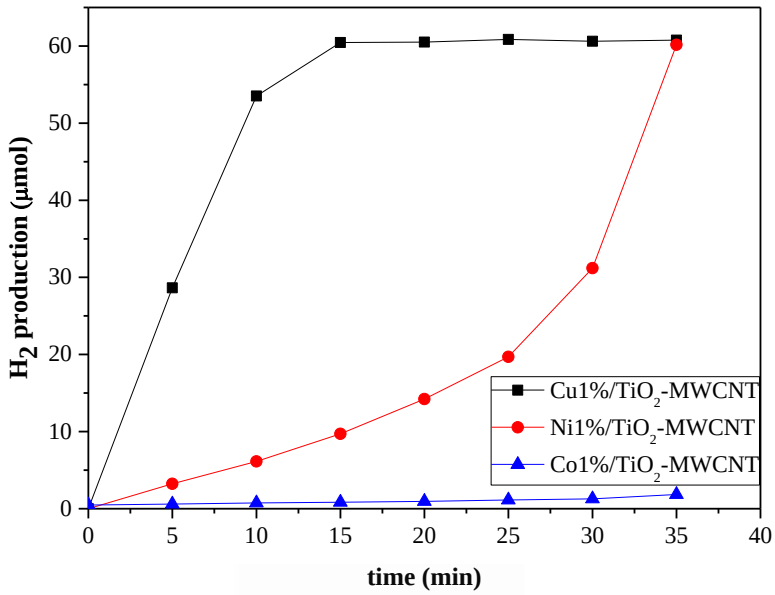

Figure 7.4. H_2 generation from AB dehydrogenation over TiO_2/MWCNT-based photocatalysts (Cu1%/TiO_2-MWCNT, Ni1%/TiO_2-MWCNT and Co1%/TiO_2-MWCNT) under visible light irradiation ($\lambda > 420$ nm) at ambient temperature.

Once the best-performing transition metal (among those investigated in this Chapter) was identified, the effect of MWCNTs in the final materials was also analyzed by comparing the properties and photocatalytic activity of Cu1%/P25, Cu1%/TiO_2, and Cu1%/TiO_2-MWCNT.

With respect to the characterization results of the photocatalyst, ICP-OES analysis shows that all photocatalysts have around 0.90 wt.% of Cu (0.87, 0.89, and 0.91 wt.%, for Cu1%/P25, Cu1%/TiO_2, and Cu1%/TiO_2-MWCNT, respectively), being the amount of copper similar to the nominal loading (1 wt.%). The XRD patterns of the Cu-containing photocatalysts are very similar to those of the Cu-free counterparts (Fig. 7.5). The presence of anatase in the TiO_2 and TiO_2-MWCNT supports was identified, while for the P25 support a mixture of anatase and rutile was detected, as was observed in Chapter 5. No peaks ascribed to the presence of Cu (or copper oxide) species (Fig. 7.5) were observed, which could be due to the presence of very small Cu (or copper oxide) particles and/or the low copper content in the samples [32]. Such observation agrees with TEM results, in which the presence of Cu particles was not observed (Fig. 7.6).

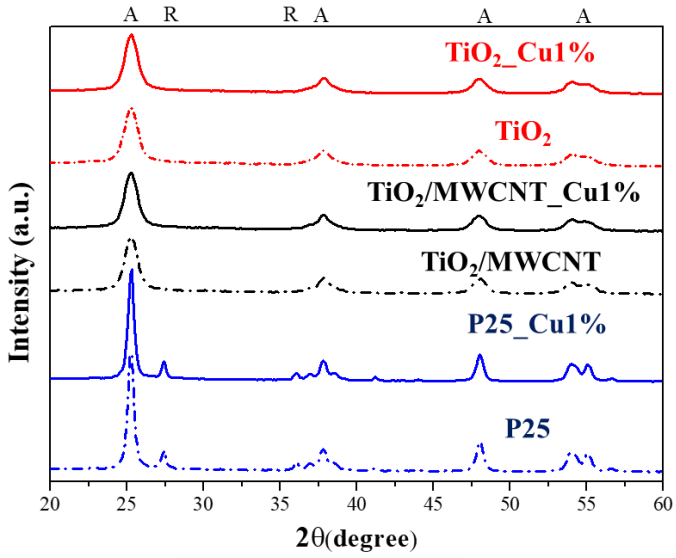

Figure 7.5. XRD patterns of the raw supports (P25, TiO_2, and TiO_2/MWCNT) and the counterpart Cu-containing photocatalysts.

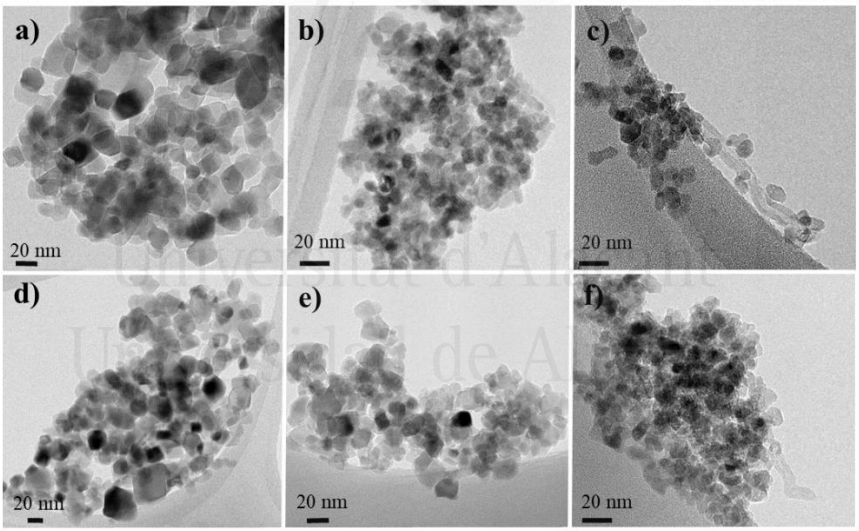

Figure 7.6. TEM images of the supports and the photocatalysts with 1 wt. % of Cu: a) P25, b) TiO_2, c) TiO_2-MWCNT, d) Cu1%/P25, e) Cu1%/TiO_2, and f) Cu1%/TiO_2-MWCNT.

Fig. 7.7 shows the UV-Vis absorption spectra of the supports and photocatalyst with Cu 1 wt.%. TiO_2 support with the crystal phase anatase and commercial P25 with an anatase/rutile mixture (as shown in the XRD spectra Fig. 7.5), present a similar absorption edge. However, the support that contains MWCNT presents a marked increase in the absorption of visible light. Moreover, UV-Vis absorption spectra of Cu-containing photocatalysts show an increase in the visible light in the 600-900 nm range with respect to the Cu-free supports, which is due to the presence of Cu species [32].

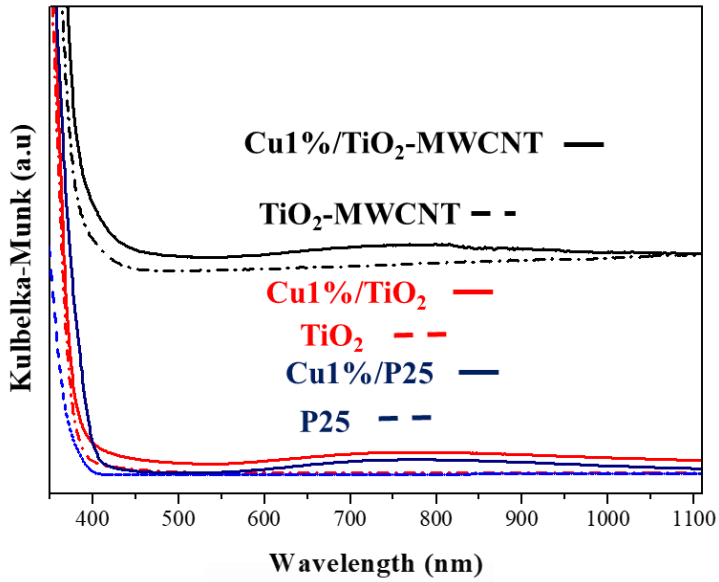

Figure 7.7. UV-Vis absorption of the bare supports (P25, TiO_2, and TiO_2-MWCNT) and the photocatalyst of all supports with 1% of Cu NPs (Cu1%/P25, Cu1%/TiO_2, and Cu1%/TiO_2-MWCNT).

The Cu 2p XPS spectra usually shows the characteristic peaks of Cu^0 and Cu^+ at 932.6 and 932.18 eV, respectively which hampers the proper identification of these two species. However, the satellite peak of Cu^{2+} appears at 943 eV, making the analysis of such species possible [33,34]. From the Cu 2p XPS spectra of the catalysts studied in this work, it could be extracted that Cu1%/TiO_2-MWCNT photocatalyst has only Cu^0 or Cu^+ (Fig. 7.8), while Cu^{2+} is detected in both Cu1%/TiO_2 and Cu1%/P25. That observation indicates that the incorporation of MWCNT in the composite material might favor the existence of less oxidized Cu species (Cu^+) or even stabilize the metal in its zerovalent state (Cu^0).

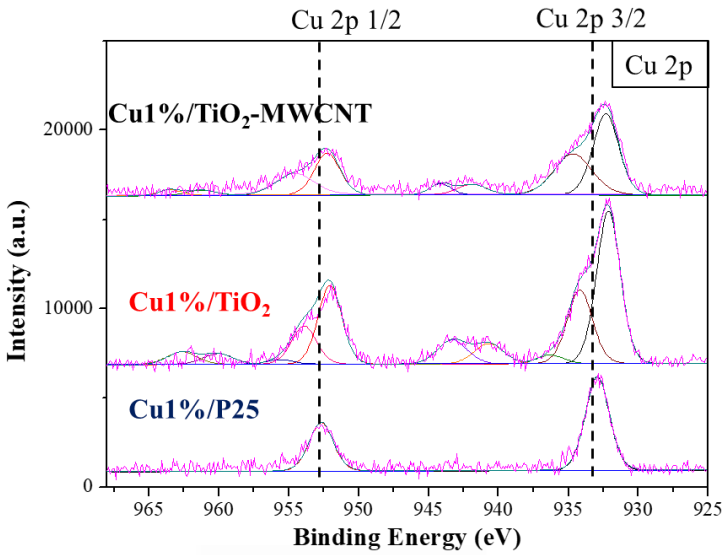

Figure 7.8 Cu 2p XPS spectra of Cu1%/P25, Cu1%/TiO_2, and Cu1%/TiO_2-MWCNT photocatalysts.

Fig. 7.9 compares the Photoluminescence (PL) spectra of the supports (P25, TiO_2, and TiO_2-MWCNT) and the photocatalysts with 1 wt. % of Cu (Cu1%/P25, Cu1%/TiO_2, and Cu1%/TiO_2-MWCNT). The photoluminescence measurements present the spectral range from 400 to 540 nm. The band at 416 nm indicates the indirect band-to-band recombination across the band gap. The peak observed at 520 nm is assigned to the recombination of states above the valence band [35-38]. As compared to P25, PL emission intensity decreased for as-synthesized TiO_2. The incorporation of MWCNT leads to a more significant decrease of the PL emission intensity, demonstrating that the incorporation of MWCNT hampers the e^--h^+ recombination rate. This effect was studied in Chapter 5 "Photooxidation of Propene with TiO_2-MWCNT photocatalyst" and has been reported previously in the literature [39,40]. Moreover, it was observed that such decrease in the PL emission intensity is even more marked for the Cu1%/TiO_2-MWCNT, which suggests the positive role of the presence of Cu in the resulting material.

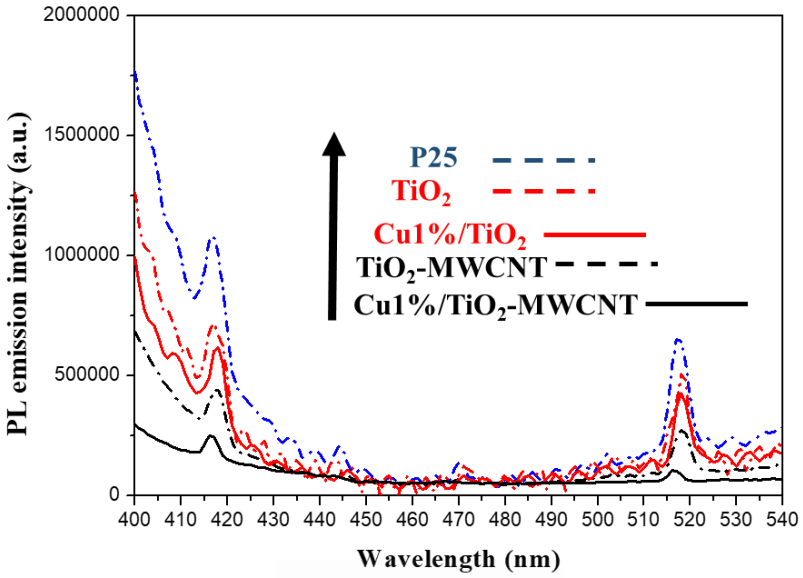

Figure 7.9. Photoluminescence of P25, TiO_2, and TiO_2-MWCNT supports and Cu1%/P25, Cu1%/TiO_2, and Cu1%/TiO_2-MWCNT photocatalysts. The excitation wavelength used for the photoluminescence analysis was 380 nm.

The photocatalytic performance towards the production of H_2 from AB is displayed in Fig.7.10 and Fig. 7.11. As it can be seen in Fig. 7.10, Cu-free photocatalysts showed a very poor activity, generating less than 5 μmol of H_2 after 35 min of reaction. However, Cu-containing photocatalysts showed a significant enhancement under dark conditions, visible light irradiation ($\lambda > 420$ nm) and UV-visible light at ambient temperature (Fig. 7.10), indicating the important role of Cu species in catalyzing the decomposition of AB [18,19,22]. Moreover, the superior performance of the materials under illumination (with both UV and UV-Vis irradiations), as expected for photoactive materials, is also evidenced in Fig. 7.10. The positive role of the incorporation of MWCNTs in the photocatalysts is demonstrated by comparing the results shown in Figure 7.10 (b) and (c), as well as in Fig. 7.11. As it can be observed, a better initial activity was displayed by Cu1%/TiO_2-MWCNT as compared to the MWCNT-free counterpart. However, since such an enhancement is not only observed under irradiation conditions, but also under dark conditions (See Fig. 7.11), it might not be exclusively related to the photocatalytic response of the final material, but also to the intrinsic properties of the composite material.

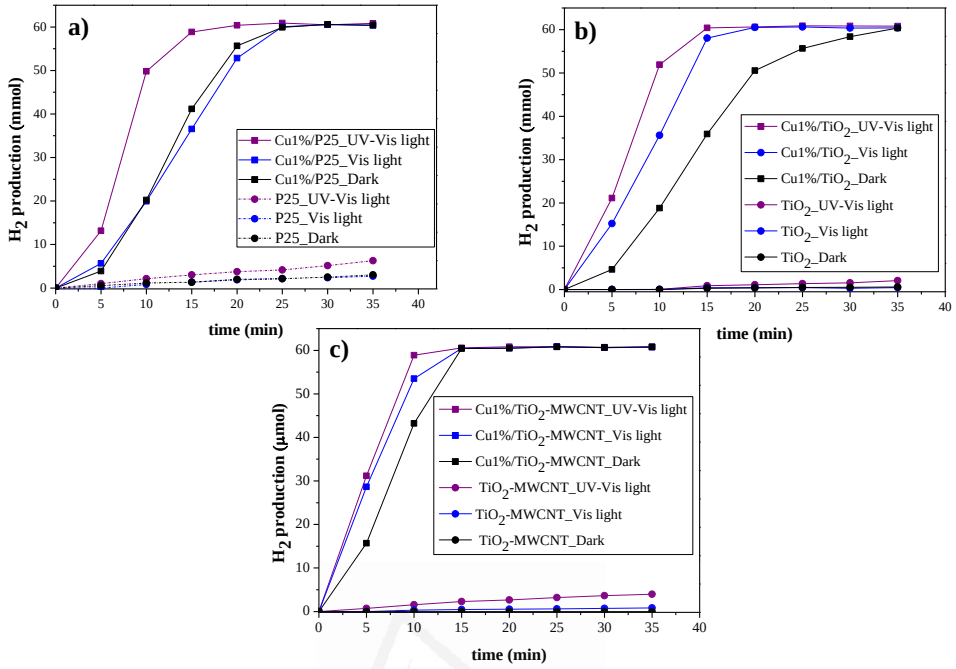

Figure 7.10. H_2 generation profiles from AB dehydrogenation under visible light irradiation (λ > 420 nm), UV-visible light and dark conditions at ambient temperature over the photocatalysts: a) Cu1%/P25, b) Cu1%/TiO_2, and c) Cu1%/TiO_2-MWCNT.

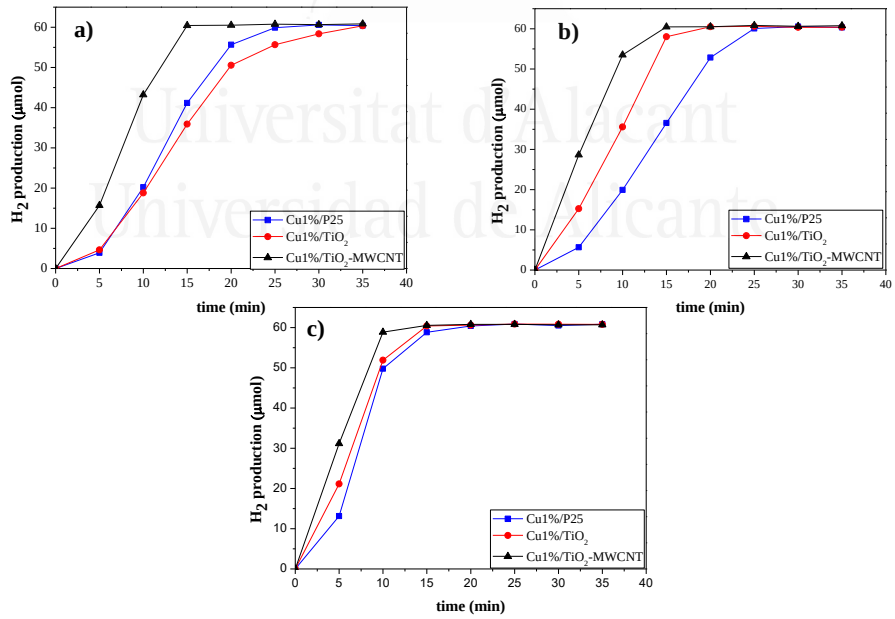

Figure 7.11. H_2 generation from AB dehydrogenation over Cu1%/P25, Cu1%/TiO_2, and Cu1%/TiO_2-MWCNT photocatalysts under: a) dark conditions, b) visible light irradiation (λ > 420 nm), and c) UV-visible light at ambient temperature (~ 60 μmol H_2 represents approximately 100 % conversion of AB).

The results obtained confirmed the great importance of the support in the catalytic activity of the resulting materials. It is observed that the presence of MWCNT in the support improves the catalytic activity towards AB dehydrogenation due to its good interaction with the TiO_2 as well as to the response of the final materials in the visible light region. Moreover, the presence of MWCNT also reduces the e^--h^+ recombination rate in the sample, leading to better photocatalytic performance as compared to the MWCNT-free counterpart photocatalysts.

7.3.3. Effect of Different Cu Loadings on TiO_2-MWCNT Samples

The present section is focused on the optimization of the Cu content of TiO_2-MWCNT-based photocatalysts. For that, catalysts with a nominal Cu loading of 1, 2, and 5 wt.% were synthesized. ICP-OES results revealed that the Cu loading was 0.9, 1.8, and 5.2 wt.%, respectively.

XRD patterns of TiO_2-MWCNT and Cu-containing photocatalysts are depicted in Fig. 7.12 a). It can be observed that while the sample with 1 and 2 wt. % of copper showed the same pattern as the Cu-free counterpart and only the characteristic peaks of the TiO_2 anatase phase were observed, the pattern for sample Cu5%/TiO_2-MWCNT displayed the characteristic peak of zerovalent Cu (111) at 43.2º, indicating the presence of metallic Cu particles of significant size. Nevertheless, it must be noted that in Fig. 7.12 a) no characteristic peaks of CuO at 36 º or Cu_2O at 39º are observed. This may be because these peaks are overlapping with those of the TiO_2 anatase phase [32]. As it was previously mentioned for samples with 1 wt.% of Cu, signals related to Cu species might have not been detected in Cu1%/TiO_2-MWCNT and Cu2%/TiO_2-MWCNT due to their small size and/or the lower Cu content. The UV-Vis absorption spectra of the photocatalysts with different Cu loading is shown in Fig 7.12 b). A significant increase in absorption in the range from 600 to 900 nm (visible light) is observed with the increase of copper loaded in the photocatalyst, which is related to the better light absorption in the visible range of Cu-containing samples [35].

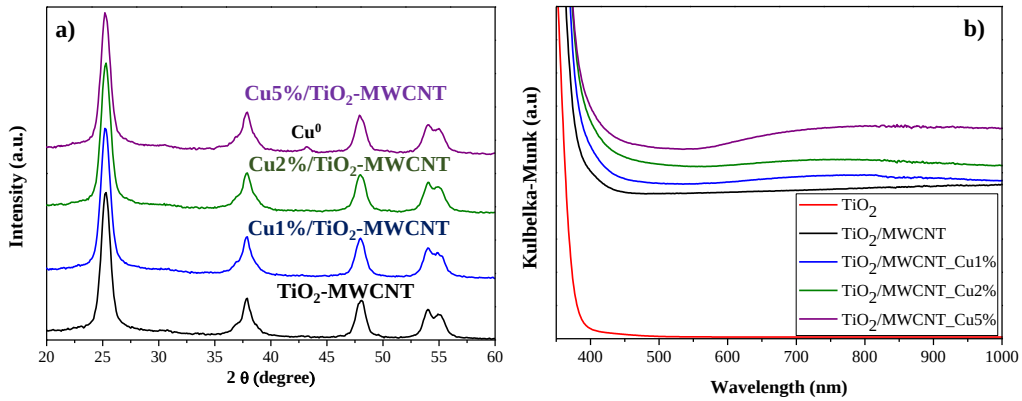

Figure 7.12. Characterization of TiO_2-MWCNT support and TiO_2-MWCNT photocatalysts with different Cu loadings: a) XRD patterns, and b) UV-Vis absorption spectra.

TEM images of the photocatalysts with different Cu loadings are displayed in Fig. 7.13. The images show that the presence of Cu (and copper oxide) nanoparticles increased with the copper loading. In this sense, such Cu species could not be distinguished from the support matrix in Cu1%/TiO_2-MWCNT, while some agglomerates were observed in Cu2%/TiO_2-MWCNT and Cu5%/TiO_2-MWCNT photocatalysts.

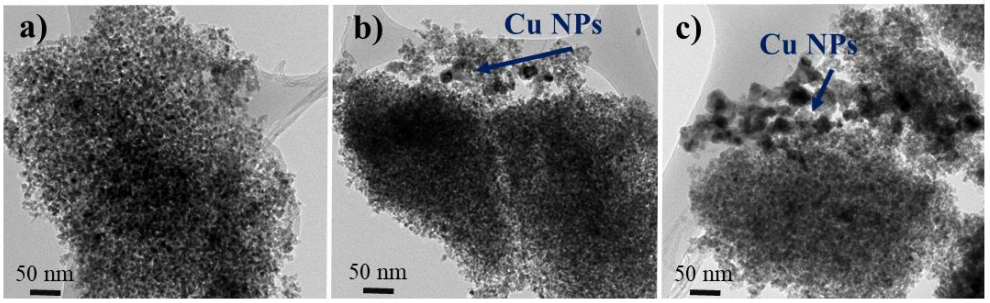

Figure 7.13. TEM images of TiO_2-MWCNT-based photocatalysts with different Cu loadings: a) Cu1%/TiO_2-MWCNT, b) Cu2%/TiO_2-MWCNT, and c) Cu5%/TiO_2-MWCNT.

As it can be seen in Fig. 7.14, N_2 physisorption isotherms of the TiO_2-MWCNT support and photocatalysts with different Cu loadings Cu (1% wt., 2% wt. and 5% wt.) show a combination of type I and IV isotherms in all cases, indicating that the Cu loading did not change the porous texture considerably. However, a decrease in the hysteresis loop was observed in the Cu-containing photocatalysts, indicating that the Cu species are partially blocking or filling the mesoporosity of the support. The textural properties are listed in Table 7.3. As observed, photocatalysts with different Cu loadings have similar BET surface areas and total pore volumes (V_t). Nevertheless, both parameters are lower than those values obtained for the support material, confirming that Cu species are partially blocking or filling the porosity of the support. Another interesting factor is that the V_{DR} does not decrease in the samples with Cu suggesting that the Cu species are not located in the microporosity of the support.

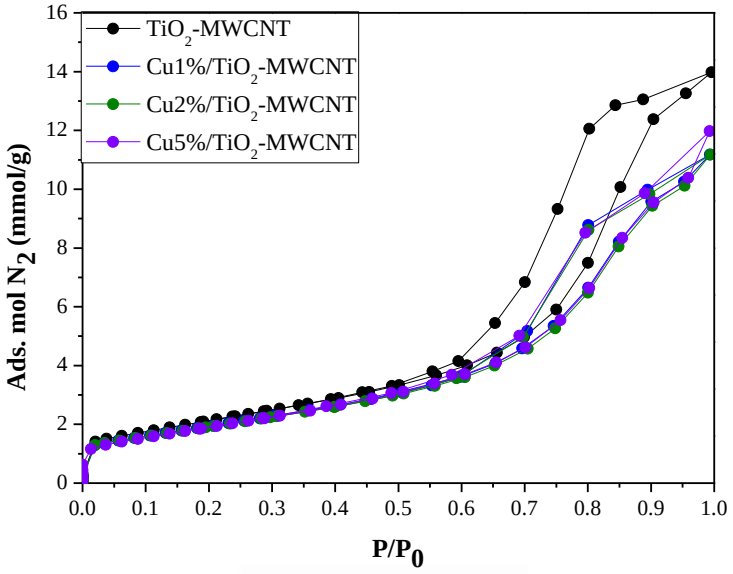

Figure 7.14. N_2 adsorption-desorption isotherms at -196 ºC for the raw support TiO_2/MWCNT and photocatalysts with different Cu loadings (Cu1%/TiO_2-MWCNT, Cu2%/TiO_2-MWCNT, and Cu5%/TiO_2-MWCNT).

Table 7.3. Textural properties of the TiO_2-MWCNT support and Cu-containing photocatalysts.

Sample	Surface area (m^2/g)	V_t (cm^3/g)	V_{DR} (cm^3/g)
TiO_2-MWCNT	176	0.46	0.07
Cu1%/TiO_2-MWCNT	158	0.36	0.06
Cu2%/TiO_2-MWCNT	156	0.35	0.06
Cu5%/TiO_2-MWCNT	155	0.36	0.06

The photocatalytic activity results of this series of photocatalysts (expressed as TOF values in mol H_2·mol Cu^{-1}·min^{-1}) from AB decomposition reaction is depicted in Fig. 7.15. The results revealed that, as expected, the photocatalytic performance depends on the amount of Cu present in the catalyst. In this sense, the photocatalyst with the lowest amount of Cu species displayed the best photocatalytic activity (TOF values) among those investigated and an increase of Cu loading in the photocatalysts brings forth a decrease in the values of TOFs under all experimental conditions used in this study (dark and visible and UV-Vis irradiation). This effect might be ascribed to the larger size of the Cu species with increasing Cu loading in the photocatalysts (as shown in the TEM images (Fig.7.13)) and the subsequent less favored contact among the components of the photocatalysts [18].

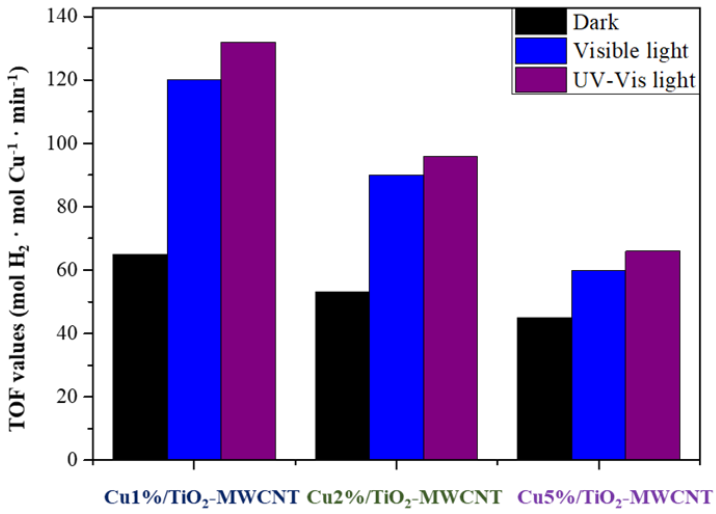

Figure 7.15. TOFs values of TiO_2-MWCNT photocatalysts with different Cu loadings calculated after 2.5 minutes under dark, and visible and UV-Vis irradiation conditions.

According to the results obtained in this study, an increase in the copper loading on TiO_2-MWCNT-based photocatalysts favors the formation of larger metal particles and increases the absorption of visible light without changing the textural properties of the catalyst. However, an increase in the Cu loading decreases the photocatalytic activity (TOF values) of the sample due the agglomeration of Cu species.

7.3.4. Evaluation of the Stability of the Cu1%/TiO_2-MWCNT Photocatalyst and Mechanism of H_2 Production from AB Hydrolysis

In this section, the study is focused on the stability of the most interesting photocatalyst under investigation (Cu1%/TiO_2-MWCNT) for H_2 generation from AB dehydrogenation under visible light irradiation ($\lambda > 20$ nm). Moreover, the role of the hydroxyl radical and superoxide anion in the photocatalytic performance of Cu1%/TiO_2-MWCNT under visible light irradiation has been also evaluated in order to get insight into the possible reaction mechanism.

The stability of Cu1%/TiO_2-MWCNT photocatalyst under visible light irradiation was investigated by performing three consecutive reaction cycles. After each cycle, the spent catalyst was collected by centrifugation, placed in the reactor, and purged with argon gas. Subsequently, 500 μL of AB solution 0.04 M were injected as described in Section 2.4. Fig. 7.16 shows that the Cu1%/TiO_2-MWCNT displayed high stability and the catalytic activity is preserved after three consecutive reaction cycles. It should be mentioned that despite the intense investigation on the development of efficient catalysts and photocatalysts for the production of H_2 from AB, the deactivation issue is still an important limitation for some systems [18,41,42]. Therefore, the high stability achieved in this case makes the present photocatalytic system a promising material for the decomposition of AB.

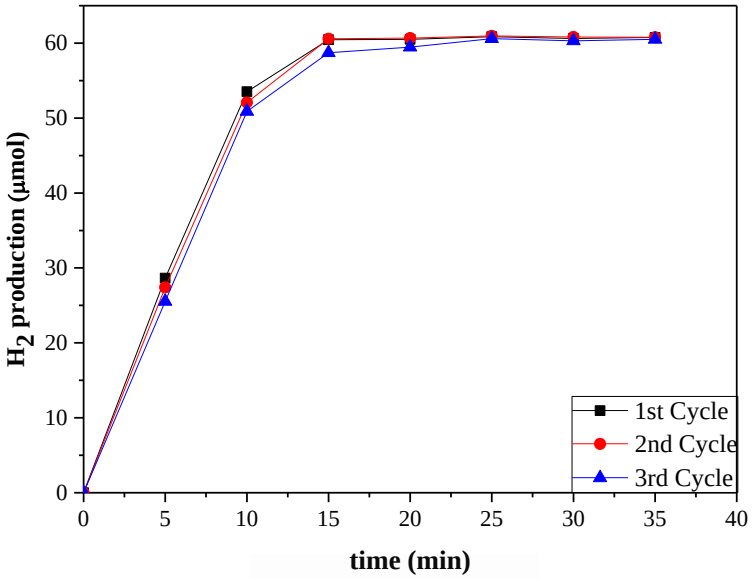

Figure 7.16. Stability tests on the photocatalytic performance of Cu1%/TiO_2-MWCNT for H_2 generation from AB dehydrogenation under visible light irradiation conditions ($\lambda > 20$ nm).

An important factor in photocatalysis is the formation of radical intermediates upon light irradiation of photoactive materials in aqueous media. For this reason, in this Chapter the effect of the hydroxyl radical in the photocatalytic H_2 generation from AB dehydrogenation over Cu1%/TiO_2-MWCNT under visible light irradiation was studied. To perform this analysis, 2-propanol (0.1 mL) was injected into the reaction mixture after purging with argon for 30 min to act as hydroxyl radical scavenger. Also, the effect of the superoxide anions formed by the reactions between the generated electrons and the dissolved oxygen was also assessed. For that, the photocatalyst was bubbled with oxygen gas for 10 min. Fig. 7.17 shows the H_2 evolution profiles achieved using the experimental conditions mentioned (reactor purged with Ar gas, in presence of 2-propanol, and reactor bubbled with oxygen gas). As observed, the presence of 2-propanol (hydroxyl radical scavenger) has an effect in the performance of the photocatalysts due to the decrease of the concentration of hydroxyl radical in the reaction medium (the initial production of H_2 decreased from 28.5 to 15.4 µmol of H_2 after 5 min of reaction when 2-propanol is present in the reaction medium). On the other hand, an important photocatalytic activity decay is observed when oxygen is present in the reaction medium. Such effect might be due to the oxidation of Cu and the formation of less active copper oxide species.

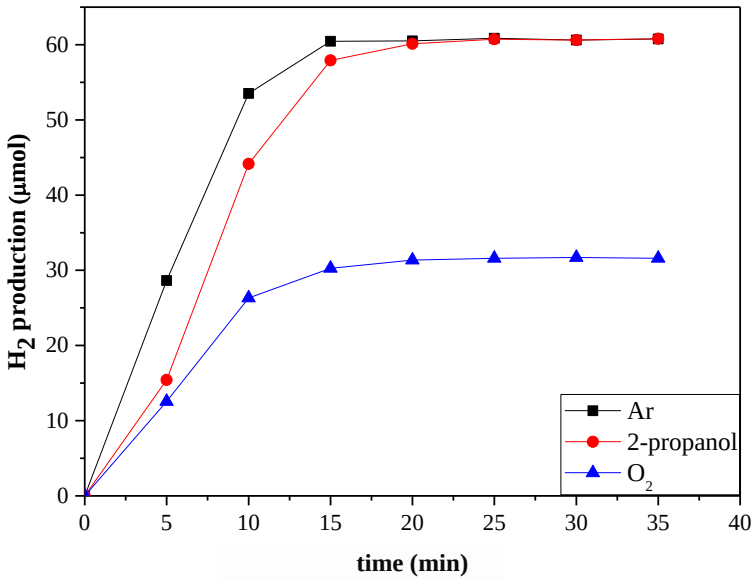

Figure 7.17. Role of hydroxyl radical and superoxide anion on the photocatalytic performance of Cu1%/TiO_2-MWCNT for H_2 generation from AB dehydrogenation under visible light irradiation ($\lambda > 20$ nm).

A possible mechanism for visible light-driven H_2 production from AB decomposition over Cu1%/TiO_2-MWCNT is proposed in Scheme 7.1. Upon light absorption by TiO_2 and generation of e^--h^+ pairs, holes may react with the solvent (H_2O) to form the hydroxide radicals. These species can react with AB molecules adsorbed on the surface of the catalyst and favor the B-N bond cleavage (pathway a)) [19]. On the other hand, the reaction could be driven through a second pathway via the e^- generated by the absorption of light (pathway b)). These e^- can be transferred from the semiconductor (TiO_2) to the carbon material (acting as an electron scavenger) and then to the metal nanoparticles. This effective charge separation might enhance the electrostatic interaction between the AB molecules and the copper nanoparticles, favoring the dehydrogenation reaction through the interaction of the AB molecules with the solvent (water) [13]. The interesting contribution of MWCNTs is that they can serve as an electron scavenger, transferring the e- to the Cu NPs, avoiding the e^--h^+ recombination and favoring a good interaction between the metal particles and AB molecules.

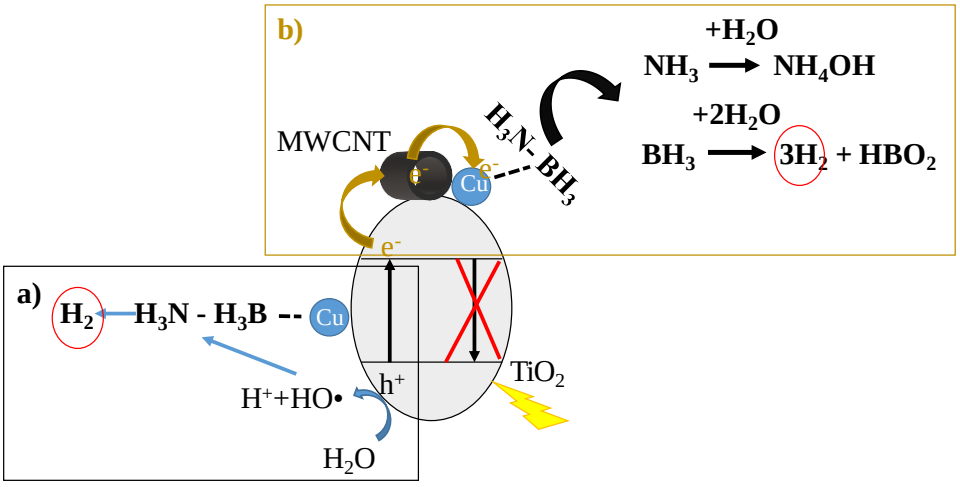

Scheme 7.1. Possible mechanisms for the photocatalytic enhancement of AB dehydrogenation under Visible Light Irradiation over Cu1%/TiO_2-MWCNT photocatalysts.

7.4. Conclusions

In this Chapter, TiO_2-MWCNT composites, previously described in Chapter 5, were used as supports for transition metal photocatalysts for their use towards the production of H_2 from AB decomposition. The most relevant conclusions extracted from this work are that the support presents a great importance in the catalytic activity of the active phase (Cu nanoparticles) observing that the presence of MWCNT improves the catalytic activity of the AB dehydrogenation under visible light irradiation due to the electron scavenging properties of this carbon material. It has also been observed that the catalytic activity depended on the Cu content and the sample with lower copper loading displayed better catalytic activity than those catalysts with higher copper loadings (2 and 5 wt.%). Another important factor is that the most interesting sample (Cu1%/TiO_2-MWCNT) presents high cyclability (3 cycles), which makes it a promising candidate for the present application.

7.5. References

[1] I.P. Jain, Int. J. Hydrogen Energy. 34 (2009) 7368-7378.
[2] N. Armaroli, V. Balzani, Chem. Sus.Chem. 4 (2011) 21-36.
[3] M. Grasemann, G. Laurenczy, Energy Environ. Sci. 5 (2012) 8171-8181.
[4] M. Navlani-García, D. Salinas-Torres, D. Cazorla-Amorós, Energy 12 (2019) 4027.
[5] C.W. Hamilton, R.T. Baker, A. Staubitz, I. Manners, Chem. Soc. Rev. 38 (2009) 279-293.
[6] M. Navlani-García, K. Mori, Y. Kuwahara, H. Yamashita, NPG Asia Mater. 10 (2018) 277-292.
[7] Z. Huang, T. Autrey, Energy Environ. Sci. 5 (2012) 9257-9268.
[8] Q.L. Zhu, Q. Xu, Energy Environ. Sci. 8 (2015) 478-512.
[9] U.B. Demirci, Int. J. Hydrogen Energy. 42 (2017) 9978-10013.
[10] T. Kamegawa, T. Nakaue, Chem. Commun. 51 (2015) 16802-16805.
[11] M. Navlani-García, K. Mori, A. Nozaki, Y. Kuwahara, H. Yamashita, Appl. Catal. A-Gen. 227 (2016) 45-52.
[12] H. Yin, Y. Kuwahara, K. Mori, H. Yamashita, J. Mater. Chem. A. 6 (2018) 10932-10938.
[13] M. Navlani-García, P. Verma, Y. Kuwahara, T. Kamegawa, K. Mori, H. Yamashita, J. Photochem. Photobiol. A Chem. 358 (2018) 327-333.
[14] S. Jo, P. Verma, Y. Kuwahara, K. Mori, W. Choi, H. Yamashita, J. Mater. Chem. A. 5 (2017) 21883-21892.
[15] M. Chandra, Q. Xu, J. Power Sources. 168 (2007) 135-142.
[16] J. García-Aguilar, M. Navlani-García, Á. Berenguer-Murcia, K. Mori, Y. Kuwahara, H. Yamashita, D. Cazorla-Amorós, RSC Adv. 6 (2016) 91768-91772.
[17] K. Mori, K. Miyawaki, H. Yamashita, ACS Catal. 6 (2016) 3128-3135.
[18] D. Salinas-Torres, M. Navlani-García, Y. Kuwahara, K. Mori, H. Yamashita, Catal. Today. (2019) 1-6.
[19] M. Wen, Y. Cui, Y. Kuwahara, K. Mori, H. Yamashita, ACS Appl. Mater. Interfaces. 8 (2016) 21278-21284.
[20] J. Li, Q.L. Zhu, Q. Xu, Catal. Sci. Technol. 5 (2015) 525-530.
[21] A. Yousef, R.M. Brooks, M.M. El-Halwany, M.H. El-Newehy, S.S. Al-Deyab, N.A.M. Barakat, Ceram. Int. 42 (2016) 1507-1512.
[22] M. Zahmakiran, F. Durap, S. Özkar, Int. J. Hydrogen Energy. 35 (2010) 187-197.
[23] S.B. Kalidindi, U. Sanyal, B.R. Jagirdar, Phys. Chem. Chem. Phys. 10 (2008) 5870-5874.
[24] Y.W. Yang, Z.H. Lu, X.S. Chen, Mater. Technol. 30 (2015) 89-93.
[25] R. Leary, A. Westwood, Carbon. 49 (2011) 741-772.
[26] M.A. Andrade, R.J. Carmona, A.S. Mestre, J. Matos, A.P. Carvalho, C.O. Ania, Carbon. 76 (2014) 183-192.
[27] K. Woan, G. Pyrgiotakis, W. Sigmund, Adv. Mater. 21 (2009) 2233-2239.
[28] W. Wang, P. Serp, P. Kalck, C.G. Silva, J.L. Faria, Mater. Res. Bull. 43 (2008) 958-967.
[29] J. Ge, Y. Zhang, S.J. Park, Materials. 12 (2019) 1916.
[30] P. Vincent, A. Brioude, C. Journet, S. Rabaste, S.T. Purcell, J. Le Brusq, J.C. Plenet, J. Non. Cryst. Solids. 311 (2002) 130-137.
[31] L.A.A. Rodriguez, D.N. Travessa, Adv. Mater. Sci. Eng. 2018 (2018) 11.
[32] A.K. Chatterjee, R.K. Sarkar, A.P. Chattopadhyay, P. Aich, R. Chakraborty, T. Basu, Nanotechnology. 23 (2012) 1-11.
[33] M.C. Biesinger, Surf. Interface Anal. 49 (2017) 1325-1334.
[34] Z. Zhang, P. Wang, J. Mater. Chem. 22 (2012) 2456-2464.
[35] D. Wang, X. Pan, G. Wang, Z. Yi, RSC Adv. 5 (2015) 22038-22043.
[36] N.O. Ramoraswi, P.G. Ndungu, Nanoscale Res. Lett. 10 (2015) 427.

[37] A. Saha, A. Moya, A. Kahnt, D. Iglesias,S. Marchesan, R. Wannemacher, M. Prato, J.J. Vilatela, D.M. Guldi, Nanoscale. 9 (2017) 7911-7921.
[38] C. C. Mercado, F. J. Knorr, J. L. McHale, S. M. Usmani, A. S. Ichimura and L. V. Saraf, J. Phys. Chem. C. 116 (2012) 10796-10804.
[39] M. Shaban, A.M. Ashraf, M.R Abukhadra, Sci. Rep. 8 (2018) 781.
[40] T.S. Natarajan, J.Y. Lee, H.C. Bajaj, W.K. Jo, R.J. Tayade, Catal. Today. 282 (2017) 13-23.
[41] Q. Zhou, H.Yang ,C. Xu, Int. J. Hydrogen Energy.41 (2016) 127174-12721.
[42] Q. Zhou, C. Xu, J. Colloid Interface Sci. 496 (2017) 235-242.

Chapter 8

Photooxidation of Propene Using Capillary Microreactors with TiO_2 Fillings

In this Chapter, we have developed an easy methodology to immobilize a benchmark photocatalyst (P25) inside a capillary microreactor (Fused silica capillary with UV transparent coating) without any previous treatment. For this purpose, a dispersion of the sample (P25) in EtOH was used to obtain a packed bed configuration. We have improved the immobilization of the benchmark photocatalyst (P25) inside the capillary incorporating a surfactant (F-127) to generate porosity inside the microreactor to avoid severe pressure drops ($\Delta P < 0.5$ bar). These microreactors show a good performance in the abatement of propene (VOC) under flow conditions per mole of active phase (P25) due to an improved mass transfer when the photocatalyst is inside the capillary. Moreover, the prepared microreactors present a higher CO_2 production rate (moles CO_2/(moles P25·s)) with respect to the same TiO_2 operating in a conventional reactor. The microreactor with low pressure drop is very interesting for the abatement of the VOCs since it improves the photoactivity of P25 per mole of TiO_2 operating at near atmospheric pressure.

8.1. Introduction

In recent decades, the use of microreactor technology has experienced a great increase in diverse fields of scientific disciplines such as medicine [1], chemistry [2-4], materials science [5,6], and energy [7], among others. In the field of heterogeneous catalysis, the use of these devices has focused primarily in organic synthesis [8] and the abatement of contaminants in microfluidic reactors [9] mainly due to the benefits of microreactors with respect to conventional reactors. These include large surface-to-volume ratio, higher mixing efficiency, faster heat and mass transfer rates, shorter reaction times, and faster reaction rates [5,8,10]. Concerning photochemistry, another important factor may be the enhanced efficiency and homogeneity in light irradiation in the microreactor due to the small dimensions characteristic of these devices. This in turn allows the use of lighting sources which consume less power such as LEDs [8]. With these advantages in mind, an interesting approach for the efficient elimination of VOCs (more specifically propene) widely described and studied in the present thesis (see Chapters 3 "Photooxidation of Propene with TiO_2 Photocatalyst", 4 "Photooxidation of Propene with P25 Encapsulated in Silica", and 5 "Photooxidation of Propene with TiO_2-MWCNT Photocatalyst") would be the use of photomicroreactor technology.

In this sense Matsushita et al showed that several different reactions (photocatalytic degradation, reduction, and amine N-alkylation) can be performed very rapidly with considerably large photonic efficiencies in a photocatalytic microreactor with an immobilized TiO_2 layer. Moreover, they observed that the photocatalytic micro-reactor was successful in the N-alkylation reaction in contrast to the results observed in a batch reactor [11]. Krivec et al presented a TiO_2-based microreactor with a highly efficient degradation of caffeine dissolved in water. This system consists of a double-layered TiO_2 anatase film immobilized on the inner walls of the photoreactor [12]. In another study by Krivec et al, a study of hydrodynamics, mass transfer, and photocatalytic activity of phenol oxidation reaction in a fixed TiO_2 microreactor was performed. The authors observed that photocatalytic phenol decomposition inside the microreactor system presented a high conversion of 79.5% with a residence time of 7.22 min [13]. Shen et al developed glass capillaries with TiO_2 supported on the inner wall by immobilized TiO_2 nanoparticles with small particle size. This microreactor reached a total conversion of benzothiophene in 2.8 min and methyl orange in 40 s [14]. More recently Suhadolnik et al showed that the photoelectrocatalytic degradation in microreactors is very interesting due to a strong synergistic effect between the photocatalytic and electrocatalytic processes [15,16].

Usually, the most widely reported configuration in the literature for the microreactor is the wall-coated configuration and the reactions are performed in liquid phase [6]. Another interesting configuration in the microreactors is the packed-bed configuration, due to the improvement of micro-mixing performance in the catalytic bed compared to wall-coated or other type of non-packed microchannels. Moreover,

this configuration ensures a better contact of the reagent (liquid or gas) with the photocatalyst [17]. Nevertheless, this type of configuration has the immobilization of the catalyst inside the reactor as main drawback. In this situation, the in-situ synthesis of a catalytic filling is not straightforward. Furthermore, it is very important to properly control the synthesis conditions in order to generate an adequate interparticle spacing, in order to avoid high pressure drops in the system [6,18].

This Chapter presents a straightforward methodology for the incorporation of a benchmark TiO_2-based photocatalyst (Evonik P25) inside a capillary microreactor (Fused silica capillary with UV transparent coating) without prior treatment, using a dispersion of the active sample in EtOH with and without the use of surfactants. This photomicroreactor was tested in the removal of propene at low concentrations in the gas phase, due to the problems associated for humans and the environment (widely described in Chapters 1 "Introduction", 3 "Photooxidation of Propene with TiO_2 Photocatalyst",4 "Photooxidation of Propene with P25 Encapsulated in Silica", and 5 "Photooxidation of Propene with TiO_2-MWCNT Photocatalyst"), obtaining an improvement of the net photocatalytic activity (CO_2 production rate) with respect to the photoactivity of the P25 in a conventional reactor. The capillary prepared with P25 and a surfactant (Pluronic F-127), with the purpose of creating porosity among the particles of P25 incorporated inside the microreactor, resulted in a photomicroreactor having a lower pressure drop (0.5 bars) than the microreactor filled with P25 only (4 bars), which is a substantial practical improvement. This photomicroreactor was tested in the removal of propene at low concentrations in the gas phase obtaining an improved photocatalytic activity (CO_2 production rate) per mole of active phase than the microreactor filled with P25 only.

8.2. Materials and Methods

8.2.1. Materials

Fused silica capillaries with a UV transparent coating (i.d. 0.1 mm) and a length of 25 cm were purchased from PHOTON LINES and used as capillary microreactors. The reactants utilized in this work without further purification were commercial titanium oxide (P25, Evonik) absolute ethanol (EtOH, 99.8%, Fisher Scientific), Pluronic F-127 (F-127, Sigma-Aldrich), and deionized water.

8.2.2. Incorporation of P25 inside Silica Capillary

The incorporation of a benchmark TiO_2 sample such as P25, without any treatment, inside the fused silica capillaries was carried out by using a dispersion of the P25 in EtOH. This approach is a straightforward methodology to incorporate already synthesized catalysts compared to the methodology of synthesizing the catalyst inside the microreactor in packed-bed, monolithic or wall-coated configuration, which is the usual process reported in the literature [2,14,18].

The incorporation of P25 previously synthesized inside the capillary was performed as follows: 100 mg of titanium oxide (P25) were weighed and dispersed in 600 mg of EtOH. This dispersion was stirred vigorously for 30 min using a magnetic stirrer. The dispersion was injected into the capillary using a syringe (1 mL of capacity). The filled capillary was sealed and set on a device which rotated the capillary around its longitudinal axis for 6 h. The sealed capillary was then annealed at 120ºC for 3 h. After annealing, the capillary was opened and dried overnight at 120ºC. This capillary was labelled Cap. P25.

In this Chapter we also prepared a P25 filled capillary creating porosity among the active particles inside the microreactor by incorporating the surfactant Pluronic F-127 in the dispersion. This capillary was prepared as follows: 20 mg of F-127 (16% wt. with respect to the mass of P25) was dissolved in 600 mg of EtOH (solution A). Then, 100 mg of the titanium oxide (P25) were weighed and dispersed in solution A. This dispersion was stirred vigorously for 30 min. The dispersion was injected into the capillary using a syringe (1mL of capacity). The filled capillary was sealed and set on a device which rotated the capillary around its longitudinal axis for 6 h. The sealed capillary was then annealed at 120 ºC for 3 h. After annealing, the capillary was opened and dried overnight at 120 ºC. The filled capillary was washed with cold water at 0 ºC for 3 days, with the purpose of removing the surfactant F-127 and generate porosity among the particles of P25 inside the microcapillary. This sample was labelled Cap. P25/F-127.

8.2.3. Sample Characterization

Optical microscopy and Scanning Electron Microscopy techniques were employed for the characterization of the TiO_2 (P25) inside the fused silica capillaries. The fillings (P25) of the capillaries were observed by a stereo microscope (EZ4 HD, Leica). The morphology of the particles inside the capillaries was analyzed by scanning electron microscopy (JSM-840, JEOL). In addition, in this Chapter a ME Micro Balance ME36S micro balance (Sartorius) with a weight resolution of up to 0.0001 mg was used for calculating the mass (mg) of P25 incorporated inside the microcapillaries from the difference in weight of the filled and empty capillaries.

8.2.4. Catalytic Tests

The photocatalytic performance of the P25 incorporated in the fused silica capillaries (microreactor) or in a conventional reactor (previously described and studied in Chapter 3), were studied using two different experimental systems designed in our laboratory.

The system for the analysis of the catalytic activity of P25 incorporated inside fused silica capillary microreactors for the abatement of propene, consisted in connecting the capillary in a GC chromatograph (GC-2010, Shimadzu). With the finality of studying the possible effect of the better illumination efficiency in

microreactor systems, different types of UV light sources were used. On one hand, one UV LED or 6 UV LED lights NSSU123T (Nichia Corporation) were used (the power of one LED is 0.015 W and the radiation peak appears at 375 nm). A factor to be considered in photocatalysis is the illumination (radiation power) reaching the photocatalyst. Since illumination depends on the distance from the LED to the sample as described by the Inverse-square law, we have used this law to get an estimate of the illumination of UV radiation reaching the photocatalyst. With the capillary being placed at a distance of 4 cm from the LEDs, the illumination decreased approximately by a factor of 16 using this configuration. A scheme of the system for capillaries is presented in Fig. 8.1. On the other hand, a commercial UV lamp (Philips) with a power of 1 W with its radiation peak appearing at 365 nm, was also employed. This lamp is the one used for the conventional reactor and the illumination using this configuration is unaffected due to the proximity between the light source and the reactor (1 cm), this system was widely described in Chapter 3 "Photooxidation of Propene with TiO_2 Photocatalyst".

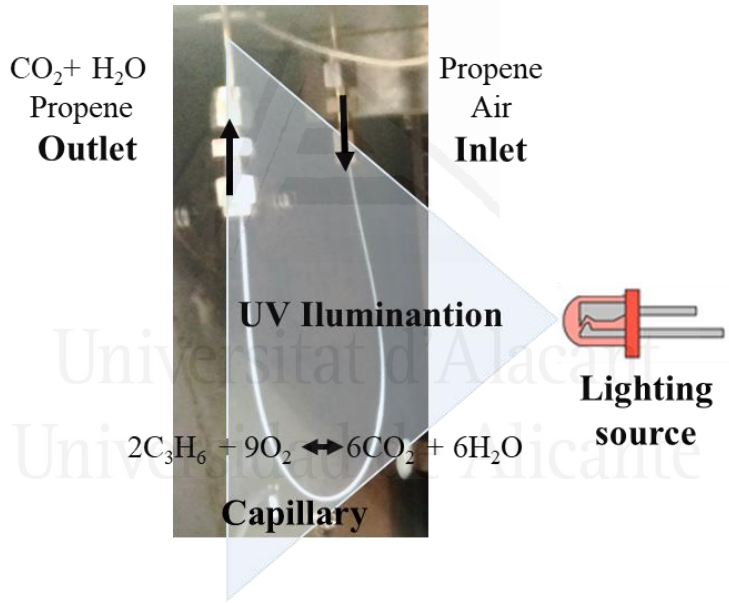

Figure 8.1. Illustration of the experimental set up used for photocatalytic oxidation of VOCs (propene).

The microreactors prepared in this Chapter (Cap. P25 and Cap. P25/F-127) were used for the oxidation of propene at 100 ppmv in air at room temperature, 25 ºC. The calibrated gas cylinder was supplied by Carburos Metálicos. The propene-containing stream had 100 ppmv of propene diluted in synthetic air and without the addition of any humidity. The flow rate of the propene-containing stream was 0.35 (STP) mL/min for the Cap. P25 and 1 (STP) mL/min for the Cap. P25/F-127 and the mass of P25 used in this study was 0.116 mg for Cap. P25 and 0.103 mg for Cap. P25/F-127 (Table 8.1). The difference in flow was caused by the high pressure drop of the former. In

this Chapter, we also studied the performance of the P25 in a conventional reactor using a system previously described in Chapter 2, 3, 4 and 5. The flow rate of the propene-containing stream was 30 (STP) mL/min and the mass of P25 used is 0.11 g in the experiment as shown in Table 8.1.

Table 8.1. Mass of P25 inside the microreactors and the conventional reactor, flow rate of propene and the residence time used in the photooxidation experiments and registered pressure drop.

Samples	Mass of P25 (mg)	Propene Flow rate (mL/min)	Residence Time (mg·min/mL)	Pressure Drop (bar)
Cap. P25	0.116	0.35	0.33	4.5
Cap. P25/F-127	0.103	1	0.103	0.5
P25 in conventional reactor	110	30	3.66	0

The propene-containing stream was passed through the capillary or conventional reactor with photocatalyst. The outlet was injected into a GC chromatograph (6890N Agilent,) equipped with a CTR-I column (Alltech) operating at 75 ºC. GC chromatography permits to follow the evolution of the concentration of propene in the outlet gas. Propene conversion was calculated using the following expression (eq. 8.1):

$$\text{Propene conversion (\%)} = \frac{C_{initial_{C_3H_6}} - C_{steady\ state_{C_3H_6}}}{C_{initial_{C_3H_6}}} \times 100 \qquad (8.1)$$

where $C_{initial\ C3H6}$ is the initial propene concentration, 100 ppmv and $C_{steady\ state\ C3H6}$ is the propene concentration at steady state conditions in the outlet gas when the UV light is switched on. Moreover, the CO_2 production rate was calculated per mole of P25, taken as the active phase, using the following expression (with the aim to normalize the results with the amount of P25) (eq. 8.2):

$$CO_2 \text{ production rate} = \frac{q_{gen}}{n} \qquad (8.2)$$

where q_{gen} is the molar flow rate of CO_2 generated (moles CO_2/s) and n is the moles of catalyst (moles of P25). The mass balances were checked in all reactions to corroborate that CO_2 was the only reaction product, thus corroborating the selectivity of the photocatalytic process.

Additionally, blank tests were performed under the same experimental conditions as the catalytic tests but in the absence of the TiO_2 photocatalysts. No catalytic activity was detected in any of the two reactor configurations.

8.3. Results and Discussion

8.3.1. Study of the Capillary Filled with P25 (Cap. P25)

In this section, we present the characterization results obtained with the capillary filled with a dispersion of P25 in EtOH as described in the Materials and Methods section. The photocatalytic activity results comparing the results obtained with microreactors (Cap. P25) with respect to those obtained in a conventional reactor are also presented and discussed.

With respect to the characterization results obtained, a general top view of the P25 filling inside the microcapillary is presented in Fig. 8.2 a). The optical microscope image shows a homogenous filling of the particles within the microcapillary of 100 μm in diameter. This figure shows an adequate filling and immobilization of the P25 particles inside the capillary with this methodology without any previous treatment. This procedure results in homogeneous P25 fillings inside 25 cm of length of the capillaries. However, this homogenous filling can block the capillary and produce high pressure drops, as it will be presented below. Another proof of the filling of P25 particles inside the microcapillaries is observed in the SEM images obtained from the Cap. 25 sample as shown in Fig. 8.2 b) and c).

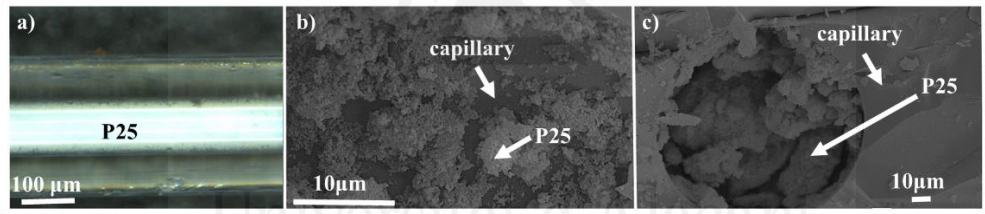

Figure 8.2. Microscopy images of the capillary sample Cap. 25 prepared in this Chapte a). Figure 8.2. b) and c) present the SEM images of the P25 inside the microcapillary for the same sample.

The photocatalytic activity of the capillary filled with P25 (Cap. P25) prepared in this Chapter and the same active phase used in a conventional reactor were evaluated separately for comparison purposes.

It must be noted that in this study, we have not studied the mechanism of total photooxidation of VOCs since it has been extensively studied and reported in the literature [19,20]. Given that our samples do not differ significantly from those studies, it is safe to assume that the mechanism will be identical to that previously reported.

With the purpose of studying the effect of the illumination efficiency in the capillary microreactor, the conversion of propene using the microcapillary filled with P25 was measured using UV light sources with different power outputs (Fig. 8.3), as mentioned in the Catalytic Test section. The results show that the 6 UV LEDs (with a total power of 0.09 W) and the 1 W UV lamp (normally used in conventional reactors in our previous studies (Chapter 3, 4 and 5)), produce very similar conversion

levels. However, the conversion of propene decreased when only 1 UV LED (with a power of 0.015 W) was used.

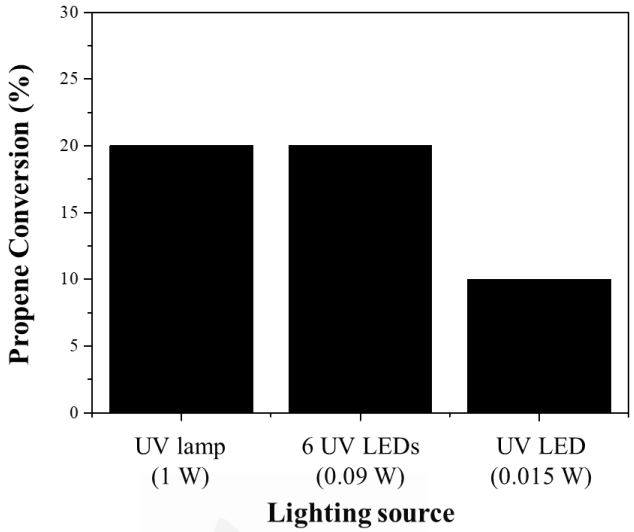

Figure 8.3. Study of the effect of the light source power in propene conversion using a UV lamp, 6 UV LEDs and 1 UV LED with 1W, 0.09 W and 0.015 W of power, respectively as light source.

With the aim of better understanding the differences between the use of microcapillaries and conventional reactors, we compared the propene conversion in both reactor configurations as shown in Fig. 8.4. The P25 powder placed in a conventional reactor presents a significantly higher value of propene conversion with respect to the P25 incorporated inside the microcapillary in absolute terms. This agrees with the higher residence time under the experimental conditions used in the conventional reactor (see Table 8.1). Sample Cap. P25 and sample P25 in a conventional reactor present a residence time of 0.33 mg·min/mL and 3.66 mg·min/mL respectively, the residence time of sample Cap. P25 being one order of magnitude lower than the P25 placed in the convectional reactor. However, if we compare the CO_2 production rate per mole of active phase (Fig. 8.4), the capillary outperforms the conventional reactor. The CO_2 production rate per mole of P25 in the Cap. P25 sample illuminated with 6 UV LEDS lights (0.09 W of power) is three times (0.0305 moles CO_2/(moles P25·s) greater than the conventional reactor illuminated with a commercial UV (Philips) light (1 W of power) (0.0096 moles CO_2/(moles P25·s). Nevertheless, it must be noted that in these calculations we did not consider the different pressures in the conventional reactor and the microreactor and in this case the sample Cap. P25 presents a pressure drop of 4.5 bars (Table 8.1), which is a usual condition in this configuration [5,10].

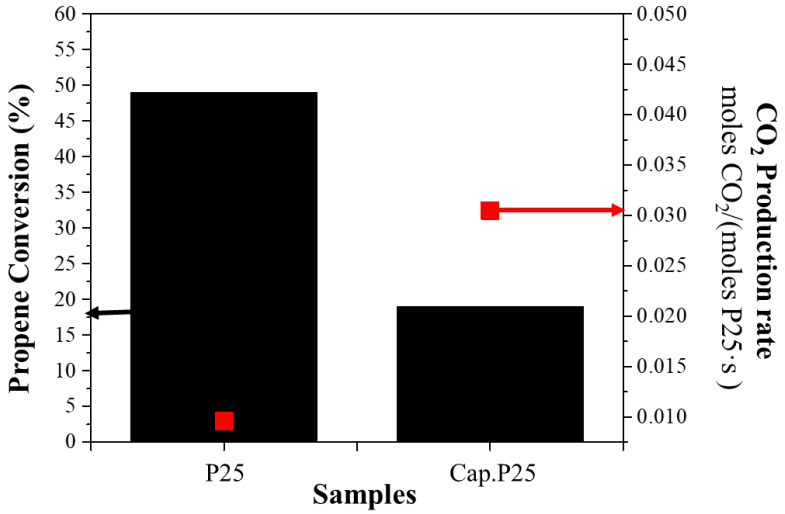

Figure 8.4. Comparison of propene conversion and normalized CO_2 production rates for P25 incorporated in a conventional reactor (P25), and for sample Cap. P25.

In this Chapter, we also tested the durability of the sample Cap. P25 in the conditions described in the Catalytic Test section, in propene abatement tests running for 12 h. The propene conversion decreased 3% after 12 h of reaction. This result is interesting because the sample Cap.P25 can operate in the propene conversion reaction in a stable way. No mass loss was observed inside of the capillary, indicating a good stability of the P25 filling.

8.3.2. Study of the Capillary Filled with P25 and F-127 (Cap. P25/F-127)

The characterization results obtained with the capillary filled with a dispersion of P25, EtOH and F-127 as described above in the Materials and Methods section are presented below. This approach was carried out with the aim of overcoming the issues arising from high pressure drops (see above). By removing the surfactant (F-127), porosity is generated among the P25 particles inside the capillary which reduces the pressure drop (see Table 8.1). In this section, we have also studied and discussed the photocatalytic activity results obtained using this new approach compared with those of Cap. P25 and P25 incorporated in a conventional reactor.

The optical microscopy images for Cap. P25/F-127 and Cap. P25 samples are included in Fig. 8.5. The Cap. P25/F-127 sample presents less P25 inside the microcapillary with respect to the Cap. P25 sample. This result was also corroborated by the weights obtained using a microbalance (see Table 8.1). Moreover, Fig. 8.5 shows that sample Cap. P25/F-127 has a more heterogeneous filling due to interparticle spacing of the P25 produced by the use of the surfactant. This photocatalyst has a low pressure drop (0.5 bar) under operation conditions, which is similar to the P25 powder in the conventional reactor. This result is interesting from an application point of view and for comparison purposes.

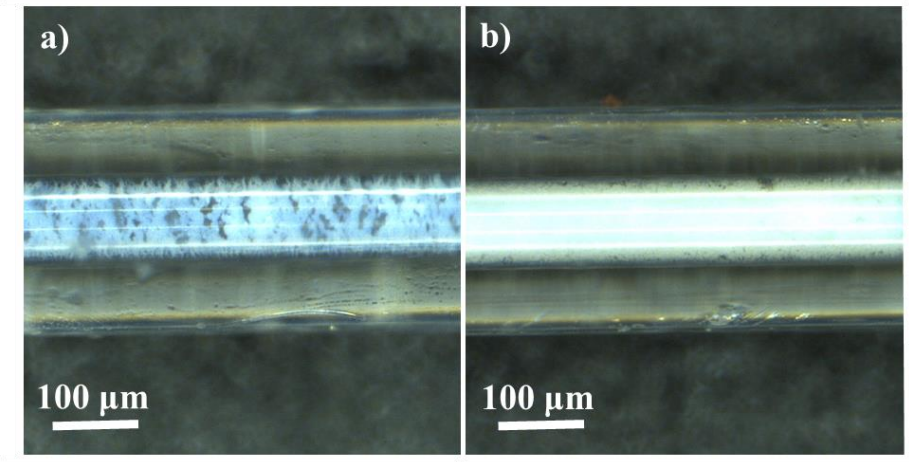

Figure 8.5. Microscope images of the different filled capillaries prepared in this study: a) Cap. P25/F-127 and b) Cap. P25.

The photocatalytic activity of the capillaries (Cap. P25/F-127 and Cap. P25) prepared in this Chapter and the same active phase used in a conventional reactor, were evaluated for comparison purposes. Fig. 8.6 includes the comparison in propene conversion for samples Cap. P25/F-127, Cap. P25 and P25 in a conventional reactor configuration. As already shown and discussed previously, the P25 in a conventional reactor presents the best value of propene conversion in absolute terms with respect to P25 incorporated inside the microcapillaries (Cap. P25 and Cap. P25/F-127). However, the conversion for the conventional reactor with respect to the capillary with comparable pressure drops is less than five times higher in spite of the fact that the residence time is more than 30 times higher. Interestingly, if we compare the CO_2 production rate per mole of P25 (Fig. 8.6), the Cap. P25/F-127 sample presents a significantly larger value than the other samples, being seven times higher (0.0685 moles CO_2/(moles P25·s)) than for the conventional reactor (0.0096 moles CO_2/(moles P25·s)). Comparing only the microcapillaries, it is observed that the CO_2 production rate per mole of P25 in the Cap. P25/F-127 sample is approximately double (0.0685 moles CO_2/(moles P25·s)) that of the Cap. P25 sample (0.0305 moles CO_2/(moles P25·s)), even though the residence time is lower when the surfactant is used.

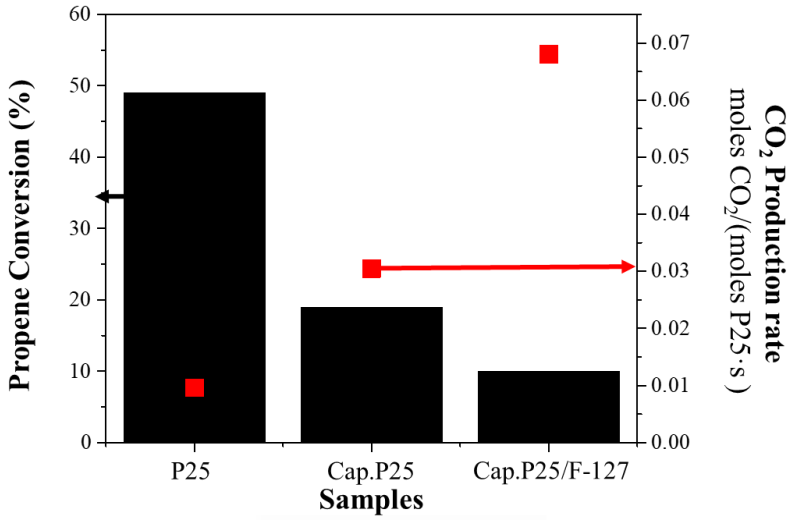

Figure 8.6. Comparison of propene conversion and CO_2 production rates for P25 incorporated in a conventional reactor (P25), P25 incorporated in a microcapillary (Cap. P25) and P25 with surfactant incorporated in a microcapillary (Cap. P25/F-127).

Considering the results obtained in this Chapter in terms of characterization of the microcapillaries and their performance in the photocatalytic oxidation of propene at low concentrations, the most promising outlook seems to be the following: (1) we have established two different strategies for filling microcapillaries using a suspension of benchmark P25: one with ethanol and P25 alone and another with the same reagents but using a surfactant with the aim of creating porosity among the particles of P25; (2) both microcapillaries (Cap. P25 and Cap. P25/F-127) present an improvement of the photoactivity per mole of photocatalyst probably due to an improved mass transfer; (3) the microcapillary with a porous packed bed presents a significant improvement in the photocatalytic activity per mole of P25 and a low pressure drop with respect to the microcapillary filled only with P25, making this capillary (Cap. P25/F-127) interesting for the elimination of VOCs in the gas phase.

Our results clearly show that it is possible to fill a microcapillary with the benchmark P25 photocatalyst in a packed bed configuration by a simple and cost-effective method. The prepared capillary microreactors display a remarkable photocatalytic activity with respect to the benchmark P25 in a conventional reactor. This approach can open the door to implementing microreactors with a photocatalyst inside (microphotoreactors) with high performance for the elimination of VOCs at low concentration with low pressure drops.

8.4. Conclusions

This Chapter presents an easy methodology to immobilize a benchmark photocatalyst (P25) inside a capillary microreactor (Fused silica capillary with UV transparent coating), using a packed bed configuration without previous treatment, by using a dispersion of the sample (P25) in EtOH. This procedure has been modified using a non-ionic surfactant (F-127) in solution in order to create porosity inside the packed bed inside the microreactor. In both cases the microreactors present a remarkable improved photocatalytic activity per mole of active phase (P25) with respect to the benchmark P25 disposed in the conventional reactor. Moreover, the microcapillary with some porosity among the P25 particles presents the best photocatalytic performance expressed per mole of active phase (P25) and a pressure drop comparable to the conventional reactor used with a thin P25 bed. This approach opens possibilities of applying this microtechnology with photocatalysts to the abatement of VOCs at low concentration in gas phase by overcoming one of its greatest drawbacks, which is the pressure drop across the reactor.

8.5. Referencias

[1] A. Šalić, A. Tušek, B. Zelić, J. Appl. Biomed. 10 (2012) 137-153.
[2] E.V. Rebrov, A. Berenguer-Murcia, H.E. Skelton, B.F.G. Johnson, A.E.H. Wheatley, J.C. Schouten, Lab Chip. 9 (2009) 503-506.
[3] K.S. Elvira, X.C. Solvas, R.C.R. Wootton, A.J. de Mello, Nat. Chem. 5 (2013) 905-915.
[4] P. Watts, C. Wiles, Chem. Commun. 5 (2007) 443-467.
[5] J.C. Colmenares, R.S. Varma, V. Nair, Chem. Soc. Rev. 2 (2017) 6675-6686.
[6] A. Tanimu, S. Jaenicke, K. Alhooshani, Chem. Eng. J. 327 (2017) 792-8210.
[7] X. Yao, Y. Zhang, L. Du, J. Liu, J. Yao, Renew. Sustain. Energy Rev. 47 (2015) 519-539.
[8] M. Oelgemöller, O. Shvydkiv, Molecules 16 (2011) 7522-7550.
[9] I. Azzouz, Y.G. Habba, M. Capochichi-Gnambodoe, F. Marty, J. Vial, Y. Leprince-Wang, T. Bourouina, Microsyst. Nanoeng. 4 (2018) 17093.
[10] G. Kolb, V. Hessel, Chem. Eng. J. 98 (2004) 1-38.
[11] Y. Matsushita, N. Ohba, S. Kumada, K. Sakeda, T. Suzuki, T. Ichimura, Chem. Eng. J. 135 (2008) 303-308.
[12] M. Krivec, K. Žagar, L. Suhadolnik, M. Čeh, G. Drazic, ACS Appl. Mater. Interfaces. 5 (2013) 9088-9094.
[13] M. Krivec, A. Pohar, B. Likozar, G. Drazic, AIChE Journal. 61, (2015) 572-581.
[14] C. Shen, Y.J. Wang, J.H. Xu, G.S. Luo, Chem. Eng. J. 277 (2015) 48-55.
[15] L. Suhadolnik, A. Pohar, B. Likozar, M. Čeh, Chem. Eng. J. 303 (2016) 292-301.
[16] L. Suhadolnik, A. Pohar, U. Novak, B. Likozar, A. Mihelič, M. Čeh, J. Ind. Eng. Chem.72, (2019) 178-188.
[17] R. Munirathinam, J. Huskens, W. Verboom, Adv. Synth. Catal. 357 (2015) 1093-1123.
[18] I. Miguel-García, M. Navlani-García, J. García-Aguilar, Á. Berenguer-Murcia, D. Lozano-Castelló, D. Cazorla-Amorós, Chem. Eng. J. 275 (2015) 71-78.
[19] M.A. Lillo-Ródenas, N. Bouazza, A. Berenguer-Murcia, J.J. Linares-Salinas, P. Soto, A. Linares-Solano, Appl. Catal. B Environ. 71 (2007) 298-309.
[20] Y. Huang, S.S.H. Ho, R. Niu, L. Xu, Y. Lu, J. Cao, S. Lee, Molecules. 21 (2016) 56.

Chapter 9

Photooxidation of Propene Using Photo-Microfluidic Chip Reactors

In this Chapter, we have presented a photo-microreactor illuminated with a low power LED light as a highly efficient system to achieve the total oxidation of propene using a TiO_2 photocatalyst. This abatement system (photo-microreactor) consists of an immobilized benchmark photocatalyst (TiO_2, P25) inside a commercial glass microchannel chip (UV transparent microfluidic chips, internal volume of 9.5 μl) using a packed-bed configuration without any previous treatment. The P25 inside the microreactor shows a nearly homogenous filling of the particles resulting in a low pressure drop throughout the system. In terms of propene abatement (Catalytic activity), the P25 inside the commercial microreactor reaches total propene conversion (100 %) under flow conditions at low concentrations (100 ppmv) due to shorter diffusion distances, large surface-to-volume ratios, efficient heat transfer, and improved light penetration inside the microchannel. Moreover, the prepared microreactor uses a low consumption power source (LED), low residence time and presents a relatively low pressure drop making this device (P25 inside a commercial microreactor) very interesting for the abatement of volatile organic compounds at low concentration for example at indoor ambients due to its small size (45 × 15 mm).

9.1. Introduction

Nowadays, the interest of the community scientific in the study and the use of photomicroreactors in heterogeneous phocatalysis is growing due to the advantages presented in Chapter 8 "Photooxidation of Propene Using Capillary Microreactors with TiO_2 Fillings". However, in this technology the efficiency is still limited due to the low production volume capability, high pressure drops in the system, mass transfer limitations, photon transfer limitations, recombination of photo-excited electrons and holes and the material of the microreactor can be degraded when it is used in some applications [1-4].

The scientific community has performed several studies exploring different microrreactors with the aim of improving these devices in different configurations for photocatalysis such as in water purification, photochemistry and bioparticle deactivation [1,5-8]. The different designs of microreactors existing nowadays can be classified in four configurations [1]: i) the micro-capillary reactor, ii) the single-microchannel reactor, iii) the multi-microchannel reactor and iv) the planar microreactor, as shown in Fig. 9.1.

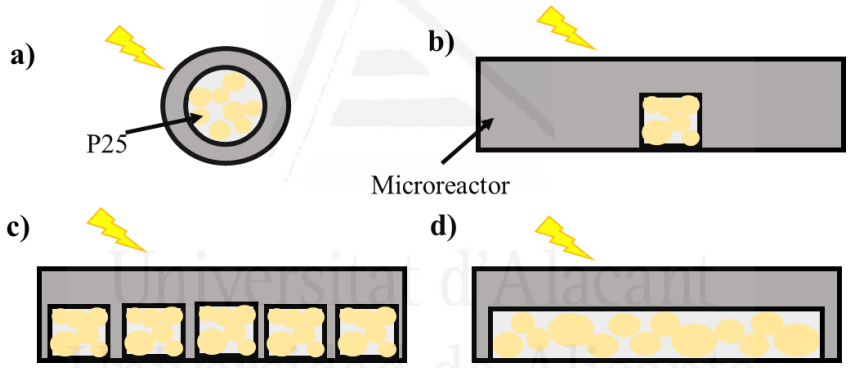

Figure 9.1. Typical configurations of microfluidic reactors for photocatalytic applications (cross section views): a) micro-capillary reactor, b) single-microchannel reactor, c) the multi-microchannel reactor and d) the planar microreactor [1].

In this Thesis, we have focused on the study of the abatement of propene in gas phase using a microreactor since propene is a representative example of low molecular weight VOCs, as described in Chapters 1, 3, 4 and 5. Moreover, in Chapter 8 "Photooxidation of Propene Using Capillary Microreactors with TiO_2 Fillings" we studied and described a system based in a micro-capillary reactor configuration incorporating P25 in a packed-bed configuration with low pressure drop and low propene flow. This device presents a great catalytic activity per mole of P25 but the overall conversion of propene was low. Although the work presented in Chapter 8 is interesting from a fundamental point of view, there are some studies that use microfluidic chip reactors with single-microchannel and multi-microchannel reactor

configurations, where these devices present high catalytic activity in different reactions [1,9,10].

In this sense, Gorges et al presented a photocatalytic microreactor (multi-microchannel reactor configuration) with immobilized titanium dioxide coated in the walls as photocatalyst and illuminated by UV light for the degradation of the model substance 4-chlorophenol. The illuminated specific surface of the microstructured reactor surpasses that for conventional photocatalytic reactors by a factor between 4-400 [11]. Kobayashi et al developed an efficient microchannel reactor where conducted hydrogenation reactions that proceeded smoothly to afford the desired products quantitatively within 2 minutes for a variety of substrates [12]. Takei et al showed a titania-modified microchannel chip (TMC) that provides an efficient photocatalytic synthesis of L-pipecolinic acid from L-lysine. The conversion rate in this microreactor was 70 times larger than in a cuvette reactor with almost the same selectivity and enantiomeric excess [13]. Nakamura et al presented photocatalytic microchips (single-microchannel reactor configuration) for organic syntheses. They showed a few organic syntheses of the reduction of nitro and aldehyde aromatics and the oxidation of alcohol aromatics, and the yields for the reduction and oxidation reached >90% and >70%, respectively [14]. Castedo et al. studied the effect of temperature on the gas-phase photocatalytic H_2 generation using microreactors (multi-microchannel reactor configuration) and Au/TiO_2 photocatalyst under UVA and sunlight irradiation [15]. The results of the different devices showed that these systems present a potential to allow their application to photocatalytic synthesis as well as photodegradation, although in these cases the reactions are usually performed in liquid phase and using a wall coated configuration [16-18].

With this in mind, in this Chapter a photo-microfluidic chip reactor with single-microchannel reactor and packed-bed configuration using TiO_2 (P25) as the active phase, was used in order to reach the total photo-oxidation of propene, using a LED lamp to irradiate the photo-microreactor. This device represents a significant enhancement of the net photocatalytic activity (represented as CO_2 production rate) compared to the photoactivity of the same active material in a plug-flow reactor or the P25 incorporated in microcapillary reactor, previously described in Chapter 3 "Photooxidation of Propene with TiO_2 Photocatalyst" and Chapter 8 "Photooxidation of propene using capillary microreactors with TiO_2 fillings", in the abatement of propene at low concentrations in the gas phase using a low lamp output power, respectively. This photo-microfluidic chip reactor with P25 opens up the possibility for its use in small places (for example indoor air treatment) with great propene abatement performance using a microreactor with small size, 45 x 15 mm (Fig. 9.2).

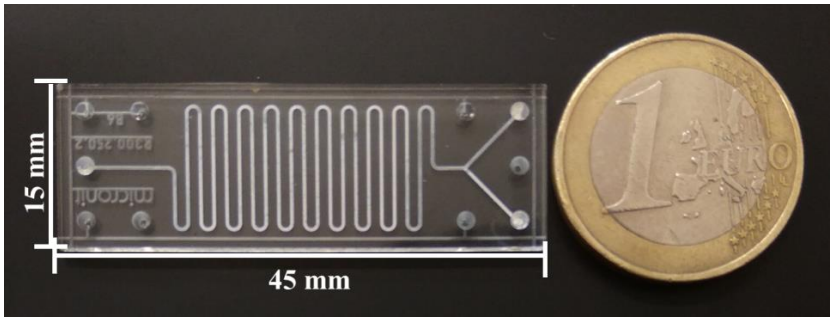

Figure 9.2. Picture of the microfluidic chip reactor with a size of 45 x 15 mm used in this Chapter and a 1€ coin with a diameter of 23 mm.

9.2. Materials and Methods

9.2.1. Materials

UV light transparent microfluidic chips (Borosilicate glass) with a length of channel of 250 mm and an internal volume of 9.5 μL (Micronit Microtechnologies) were used as microreactors. A fluidic Connect PRO Chip Holder (Micronit Microtechnologies) was used for supporting the standard 45 mm x 15 mm micro-etched glass plates to incorporate the TiO_2 and to perform the catalytic test. A LED light LED ENGIN (LZ4-04UV00) with a maximum radiation peak at 365 nm and a maximum output power of 2.4 W was used to carry out the catalytic tests. A DC regulated power supply from Promax (FAC-662B) was used to control the output power of the LED light to perform the propene photooxidation tests.

The reagents used in this Chapter were commercial titanium dioxide (P25, Evonik), absolute ethanol (EtOH, 99.8%, Fisher Scientific), Pluronic F-127 (F-127, Sigma-Aldrich) and deionized water. All reagents were used as received, without any further purification.

9.2.2. Incorporation of P25 Inside the Microfluidic Chip

The incorporation of a benchmark TiO_2 sample (P25) without any treatment inside the microfluidic chip was carried out by introducing a dispersion of P25 in EtOH in the presence of a surfactant (F-127). The surfactant was used with the aim of creating porosity among the P25 particles inside the microreactor, as described and showed in Chapter 8 "Photooxidation of propene using capillary microreactors with TiO_2 fillings". The system was prepared as follows, this preparation being an adaptation of the methodology described in Chapter 8: 20 mg of F-127 (16% wt. with respect to the mass of P25) were dissolved in 600 mg of EtOH (solution A). Then, 111 mg of the titanium oxide (P25) were weighed and dispersed in solution A. This dispersion was stirred vigorously for 30 min. The dispersion was injected into the microreactor (45mm x 15mm microfluidic chips, Micronit) supported in a fluidic Connect PRO Chip Holder using a 1 mL syringe. The filled microreactor was sealed and left to set at room temperature for 4h. The sealed microreactor was then annealed

at 60 ºC for 24 h. After annealing, the microreactor was opened and dried overnight at 120 ºC. The filled microreactor was calcined at 350 °C for 6 h with a heating rate of 1 °C/min in order to remove the surfactant F-127 and generate the porosity among the particles of P25 inside the microreactor. This sample was labelled Microreact-P25.

9.2.3. Sample Characterization

Optical microscopy was employed for the characterization of the commercial TiO_2 (P25) filling inside the microreactor using a Leica microscope (EZ4 HD). A high sensitivity balance (Mettler Toledo, AX205 DeltaRange) with a weight resolution of 0.01 mg was used for precisely knowing the mass (mg) of P25 incorporated inside the microreactor from the difference in weight before and after filling the microreactor. It must be noted that the use of a surfactant and the preparation of a stable dispersion (using P25/EtOH mixtures) are two key parameters in order to successfully and reproducibly prepare the loaded microreactors, as it was shown in Chapter 8. The former is important to avoid compact photocatalyst beds which results in high pressure drops and the latter is key to obtain reproducible results.

9.2.4. Catalytic Tests

The photocatalytic performance of the P25 incorporated in the microfluidic chips (microreactor) or in a conventional reactor [19], prepared for comparison purposes, was studied using two different experimental systems designed in our laboratory, as was described in Chapter 2 “Experimental Techniques”.

For the measurement of the catalytic activity in the abatement of propene using P25 incorporated inside the microreactor, the device was assembled in a Fluidic Connect PRO Chip Holder as shown in Fig. 9.3. With the aim of studying the possible effect of the better illumination efficiency in the microreactor configuration, the LED light (LED ENGIN, 2.4 W, 365 nm) was connected to a DC regulated power supply (Promax, FAC-662B) to control the output power of the LED light, as shown in Table 9.1, using the LED manufacturer instructions. A factor to be taken into account in photocatalysis is that the irradiance (radiation power) depends on the distance from the LED to the photocatalyst as described by the Inverse-square law. In this Chapter, the radiant flux calculated in Table 9.1 can be used as the irradiance in the microreactor configuration used due to the proximity between the light source and the reactor (1cm). In this sense, it is important to highlight the relevance of the illumination already described in Chapter 4 “Photooxidation of Propene with P25 Encapsulated in Silica” and Chapter 8 “Photooxidation of Propene Using Capillary Microreactors with TiO_2 Fillings”. The experimental system designed for the conventional reactor, described in Chapter 3 “Photooxidation of Propene with TiO_2 Photocatalyst”, consists of a vertical quartz reactor where the photocatalyst bed (0.1g) is placed in a packed-bed configuration on quartz wool without any special immobilization protocol involved. The total reactor height is 50 mm and the catalytic bed is placed in a section of the reactor with 20 mm of diameter. This system uses a

commercial UV lamp (Philips) with a power of 1 W with its radiation peak appearing at 365 nm [19]. This lamp is used for the conventional reactor and the irradiation used in this configuration is also unaffected due to the proximity between the light source and the reactor (1 cm). The void volume of the photocatalyst bed in the microreactor was calculated using the bulk density of P25 and the value obtained was 96%. In the conventional reactor since the photocatalyst bed occupied a small fraction of the quartz reactor and its height could not be measured reliably, the void volume was not calculated albeit its value would be much higher than that in the microreactor.

Table 9.1. Voltage and intensity used in the LED light to obtain a given radiant flux (irradiance) of the LED using the manufacturer instructions.

Voltage (V)	Intensity (mA)	Radiant flux (W/cm^2)
12.5	8	0.11
13	66	0.39
13.2	108	0.53
13.4	162	0.66
13.6	217	0.81
13.8	315	1.05

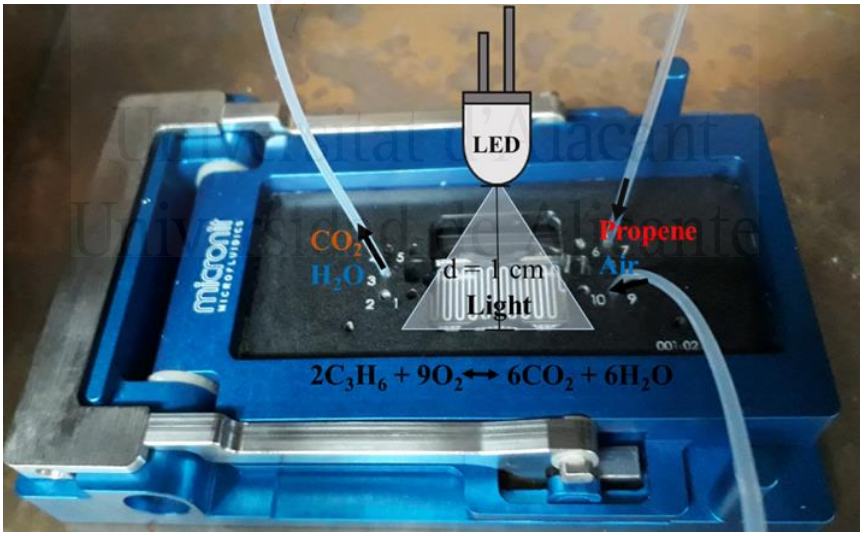

Figure 9.3. Illustration of the experimental set up used for photocatalytic oxidation of VOCs.

The microreactor with P25 prepared in this Chapter (Microreact-P25) was used for the total oxidation of propene at low concentrations (100 ppmv in air) at room temperature (25 ºC). The calibrated gas cylinder was supplied by Carburos Metálicos, S.A. The propene-containing stream contained 100 ppmv of propene diluted in synthetic air and without the addition of any humidity. The flow rate of the propene-

containing stream was set at 8 (STP) mL/min and the mass of active phase (P25) inside the microreactor used in this study was 1.18 mg. In this Chapter, we also studied the performance of the P25 in a conventional reactor described preciously in Chapter 3 "Photooxidation of Propene with TiO_2 Photocatalyst". The flow rate of the propene-containing stream was 30 (STP) mL/min and the mass of P25 was 110 mg. Table 9.2 summarizes the experimental conditions used in both reactors.

Table 9.2. Reactor length and volume, mass of P25 inside the microreactors and the conventional reactor, flow rate of propene, residence time used in the photooxidation experiments and registered pressure drop.

Sample	Microreact-P25	P25 in conventional reactor
Reactor length (mm)	250	50
Reactor Volume (mL)	0.095	15.7
Mass of P25 (mg)	1.18	110
Propene flow (mL/min)	8	30
Residence time (mg·min/mL)	0.149	3.66
Pressure Drop (bar)	0.60	0

The propene-containing stream was passed through the microreactor or the conventional reactor containing the photocatalyst. The outlet was injected into a GC chromatograph (6890N Agilent,) equipped with a CTR-I column (Alltech) operating at 75 ºC. GC chromatography permits to follow the evolution of the concentration of propene in the outlet gas. Propene conversion was calculated using the expression described in Chapter 8 (eq. 8.1). Moreover, the CO_2 production rate was calculated per mole of P25, taken as the active phase, using the expression described before in Chapter 8 (eq. 8.2) (with the aim to normalize the results with the amount of P25). The mass balances were checked in all reactions to corroborate that CO_2 was the only reaction product, thus corroborating the selectivity of the photocatalytic process.

Additionally, blank tests were performed under the same experimental conditions as the catalytic tests but in the absence of the TiO_2 photocatalysts. No catalytic activity was detected in any of the two reactor configurations.

9.3. Results and Discussion

9.3.1. Characterization of the Active Phase (P25) inside of the Microreactor

The overview of the P25 filling inside the microfluidic chip (microreactor) is showed in Figs. 9.4 a)-d). Figs. 9.4 a)-b) show a good packing and immobilization of the active phase (P25) inside the microreactor observing a film of P25 on the walls of the microreactor in comparison with the empty microreactor (Fig. 9.4 c)). Fig. 9.4 d) presents an almost complete filling of the particles inside the microreactor of 300 μm in channel diameter. However, it is also possible to observe some empty spaces in the microreactor.The almost complete homogenous filling achieved and the use of a template (surfactant, Pluronic F-127), results in a low pressure drop (0.60 bar) for the microreactor with P25 (Microreact-P25) when passing the flow of propene (8 mL/min), showing that the reactor is not blocked (Table 9.2). This result is interesting from an applied point of view since these systems frequently suffer either of high pressure drops or complete blockage due to the compactness of the catalyst bed as was showed in Chapter 8 and in the literature [20]. Moreover in this study we also analyzed the SEM images of P25 particles in powder form (Fig. 9.4 e) and f)). These SEM images show a heterogeneous particle distribution and a high degree of interparticle space, which may favour low pressure drops throughout the reactor.

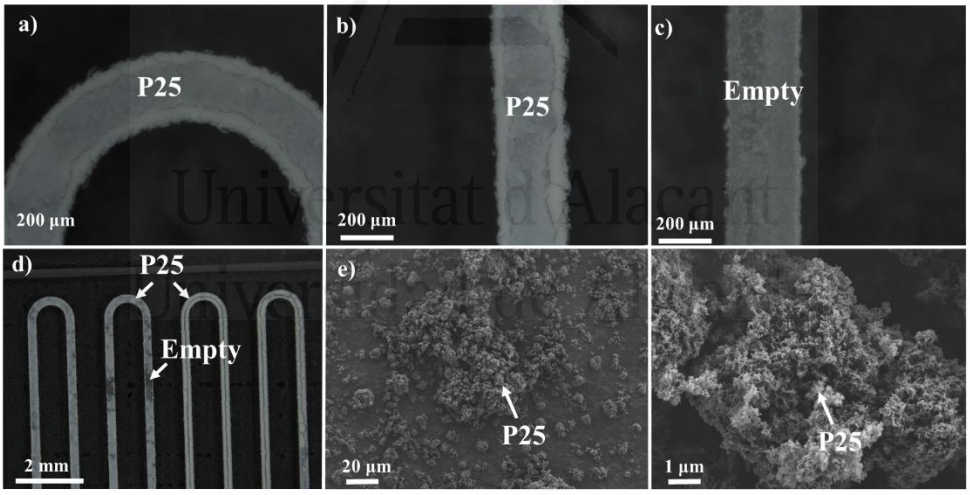

Figure 9.4. Microscope images of the microreactor prepared in this Chapter: (a, b, d) Microreactor with catalyst (Microreact-P25) at different scale. Figure 9.4 c) Microreactor without catalyst. Figure 9.4 e, f) SEM images of the P25 in powder form studied in this Chapter at different scale.

9.3.2. Effect of the UV-LED Irradiance upon the TiO_2 Active Phase inside a Microreactor in the Photocatalytic Oxidation of Propene.

The effect of the LED output power in the photo-microreactor (Microreact-P25) in the propene photooxidation (LED irradiance) is shown in Fig. 9.5. The microreactor without active phase (P25) does not present any propene conversion even when setting the maximum incident radiation power on the sample at 2.4 W/cm^2. However, the sample Microreact-P25 that contained the catalytic phase (P25, 1.18 mg) showed some conversion (7%) even at low LED incident radiation power (0.1 W/cm^2). The small propene conversion under these conditions is due to the very low LED output. When the LED incident radiation power was increased, a high propene conversion was observed, reaching a total propene conversion (100%) at 0.53 W/cm^2 of LED output power. This result is very interesting because it is indicative of the good light penetration through the catalyst with a low LED power yielding a total abatement of propene in the gas stream as observed in Chapters 4, 8 and in the literature [21,22].

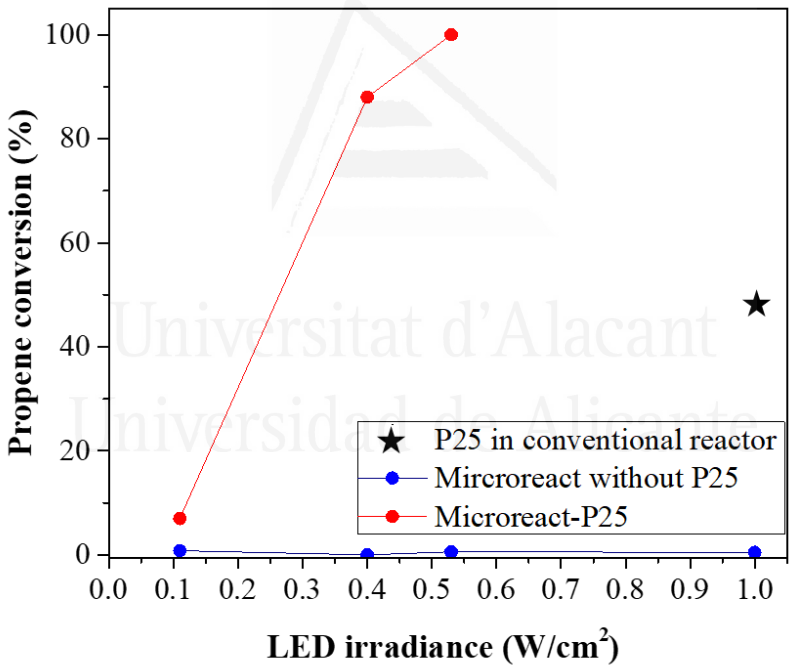

Figure 9.5. Photocatalytic response of the microreactor with P25 (Microreact-P25) at different UV-LED incident radiation power during the oxidation of propene at low concentration. The photocatalytic response of P25 in a conventional reactor is shown for comparison purposes. The conditions of both catalytic tests are shown in Table 9.2.

In addition, the effect of incident radiation power on the P25 inside the microreactor with respect to the P25 sample incorporated in a conventional reactor was compared (Fig. 9.5 and Table 9.2). The Microreact-P25 presents a total propene conversion (100 %) when a flow of 8 mL/min of propene/air is passed through the

sample (Microreact-P25) with a low LED power density (0.5 W/cm^2) as shown in Fig. 9.5. However, the sample P25 incorporated in a conventional reactor presents a 49 % of propene conversion when a stream of 30 mL/min of propene/air was passed through the conventional reactor with a power density of 1 W/cm^2. In this sense we observed that the P25 incorporated in a microrreactor presents a higher propene conversion with respect to P25 in a convectional reactor using a low power density and a small mass of catalyst. Moreover, the sample Microreact-P25 presents a significantly higher CO_2 production rate (moles CO_2/(s·moles P25)) with respect to the same photocatalyst in a convectional reactor. This value of CO_2 production rate is around 40 times higher in the microreactor (Table 9.3). This fact indicates a substantial improvement in the activity of P25 inside the microreactor due to a better illumination of the photocatalyst, an improved mixing efficiency under turbulent regime and a good contact between the catalyst and the gas due to the reduced size of the microreactor channel. In this Chapter the amount of photocatalyst per unit of surface area of the photoreactor was also studied. The amount of P25 per unit of surface area is over one order of magnitude higher for the sample Microreact-P25 compared to the conventional reactor (0.0049 mg/mm^2 and 0.0001 mg/mm^2, respectively). This parameter indicates that a high amount of P25 in the sample Microreact-P25 is exposed on the surface of the microreactor, therefore a higher quantity of P25 is illuminated. In this Chapter we have also obtained the quantum efficiency of the P25 incorporated in both systems for comparison purposes [23]. The sample Microreact-P25 (0.5W of power) presents a 20 % of apparent quantum efficiency (QE) and the same P25 photocatalyst in a conventional reactor (1W of power) has a QE of 16%. These values indicate that P25 inside the microreactor presents a better apparent QE with respect to the same material in a conventional reactor. However, these values are not very representative since in this study we used a UV polychromatic lamp. This light can generate misleading results as mentioned by Bolton et al in their study [24]. Moreover this result did not take into account the catalyst mass and it was considered that all the irradiated light is absorbed by the catalyst. These considerations make the results unreliable as described by Herrmann [23].

Moreover, for comparison purposes, the catalytic properties of the P25 inside the microfluidic chips (Micronit) presented in this Chapter, were compared with the activity catalytic of the same active phase inside a capillary (Cap.P25), previously described in Chapter 8, as showed in Table 9.3. Sample Microreact-P25 presents a total propene conversion (100 %) and a CO_2 production rate of 0.399 moles CO_2/(s·moles P25) when a flow of 8 mL/min of propene/air is passed through the sample (Microreact-P25) with a relatively low LED power density (0.5 W/cm^2) containing only 1.1 mg of catalyst inside the microchips as showed in Table 9.3. These figures of catalytic activity and propene conversion are significantly higher than for sample Cap. P25. This sample (Cap. P25) presents only a 10 % of propene conversion and a CO_2 production rate of 0.069 moles CO_2/(s·moles P25), being this

figure already higher than the same active phase (P25) working in a conventional reactor but much lower than that for the microfluidic chip reactor. In the case of Cap. P25, a stream of 1 mL/min of propene/air was passed through the capillary reactor using a power density of 1 W/cm^2 for the LED light. In the case of the capillary, only 0.1 mg of the catalyst were placed inside the microreactor as shown in Table 9.3. Another important characteristic of the commercial microfluidic chips presented in this Chapater (Micronit) with respect to capillaries is the higher diameter (250 μm) of the channel where the active phase is incorporated with respect to capillaries (100 μm). This characteristic allows the microfluidic chips (the microreactor presented in this Chapter) to be filled with more active phase (P25) and be able to work with larger flows than the capillaries (previously described in Chapter 8).

Table 9.3. Comparison of P25 incorporated in different microreactors (microfluidic chips and capillary) and the P25 in a conventional reactor

Sample	Microreact-P25	P25 in conventional reactor	Cap. P25
Mass of P25 (mg)	1.18	110	0.1
Propene flow (mL/min)	8	30	1
Residence time (mg·min/mL)	0.148	3.66	0.103
Pressure Drop (bar)	0.6	0	0.5
Propene conversion (%)	100	49	10
CO_2 production rate (moles CO_2/(s·moles P25))	0.399	0.0097	0.069

These results show that sample Microreact-P25, under the conditions of analysis in this Chapter, has a higher propene conversion and catalytic activity than the same catalyst in a convectional reactor and capillary reactor as shown Table 9.3. It must be remarked that the incorporation of the active phase is easy and straightforward in the case of the microfluidic chip reactor compared to the capillary probably due to its higher diameter.

9.3.3. Effect of Residence Time in the Propene Conversion in the Microreactor Loaded with P25

Different flows of propene with the same LED output power (1 W) were passed through the sample (Microreact-P25) maintaining the same mass of catalyst (1.18 mg) in all cases in order to study the effect of the residence time in this configuration (Table 9.4). Propene conversion decreases with decreasing the residence time due to a lower contact time between reagents and the catalyst surface, which agrees with previous studies described in the literature [25,26]. Moreover, this system was blocked (propene did not pass through sample Microreact-P25) with a propene flow over 24 mL/min due to the small diameter of the microreactor. Concerning the CO_2 production rate, this parameter increased with decreasing residence time, what can be related to the increase in pressure.

Table 9.4. Influence of the residence time in the microreact-P25 in terms of pressure drop, propene conversion and CO_2 production rate.

Sample	Microreact-P25	Microreact-P25	Microreact-P25	Microreact-P25	Microreact-P25
Mass of P25 (mg)	1.18	1.18	1.18	1.18	1.18
Propene flow (mL/min)	5	8	10	15	20
Residence time (mg·min/mL)	0.236	0.148	0.118	0.079	0.059
Pressure Drop (bar)	0.40	0.60	0.75	1.00	1.25
Propene conversion (%)	100	100	99	77	61
CO_2 production rate (molesCO_2/(s·moles P25))	0.249	0.399	0.498	0.560	0.589

The effect of residence time in a microreactor and a conventional reactor configuration with P25 in propene conversion are compared in Table 9.5. Although the residence time of the conventional reactor (3.33 (mg·min)/mL) is higher than that of the microreactor (0.148 (mg·min)/mL), the propene conversion in the microreactor configuration (microreact-P25 in Table 9.5) is 100% and the CO_2 production rate (moles CO_2/(s·moles P25)) is around 40 times higher, which cannot be explained with the higher pressure drop of the microreactor. The remarkable results are a consequence of the advantages of using a microreactor configuration (large surface-to-volume ratio and higher mixing efficiency, among others) and, specially an improved illumination of the active phase (P25) as mentioned in Chapter 4 and in the

literature [25]. It must be noted that concerning the mixing regime, both reactors should be comparable since both of them are made up of packed beds of small P25 nanoparticles. Under these conditions the flow of gas through the bed itself can be considered a turbulent flow regime, and thus mixing would be provided by turbulence. If the microreactor would have been prepared by wash-coating, a layer of the photocatalyst would have been deposited and thus laminar flow might be expected, but as we have shown in this Chapter (see Fig. 9.4), the photocatalyst is deposited as a porous filling. Thus, the better performance of the sample Microreact-P25 can be attributed, among other causes, to the improved mixing efficiency in the microchannel. Since, the length of the pack-bed microreactor channel (250 mm) is higher than the length of the pack-bed in the convectional reactor (50 mm), the contact of the propene with the active phase in the microreactor device is favored.

Table 9.5. Comparison of the operation conditions (residence time, power density and pressure drop) and catalytic activity (propene conversion and CO_2 production rate) of both configurations (microreactor and conventional reactor).

Sample	Microreact-P25	P25 in conventional reactor
Residence time (mg·min/mL)	0.148	3.66
Power density (W/mg·cm^2)	93	3
Propene conversion (%)	100	49
CO_2 production rate (moles CO_2/(s·moles P25))	0.399	0.0096
Pressure Drop (bar)	0.60	0

9.3.4. Evaluation of the Catalyst Stability of the P25 Incorporated in a Packed-Bed Microfluidic Chip Reactor Configuration

As in any heterogeneous catalytic system, cycling and stability tests are necessary to prove the interest of the catalyst from an application point of view. In the case of VOCs removal the photocatalyst can be deactivated due to the formation of physisorbed products and/or the catalyst may be removed from the reactor during operation. The catalytic activity of P25 inside the microreactor was studied for 24 hours at two different LED output power (0.4 W and 1 W) as shown in Fig. 9.6. The performance of the P25 inside the microreactor when irradiated with 0.4 W/cm^2 was partially stable for the first 6 h. Nevertheless, after 24h the propene conversion

dropped by 8%. In the case of the sample irradiated with an output power density of 1 W/cm^2 the catalyst is stable for 24 h because the irradiated light is sufficient to completely oxidize the propene that passed through the Microreact-P25 throughout the duration of stability test. Moreover, under these conditions the total propene conversion was achieved after 5 min and the CO_2 concentration is constant throughout the experimental run. This is evidenced by the fact that 300 ppm of CO_2 was detected in the reactor outlet due to the total oxidation of propene once the quasi-steady state was reached.

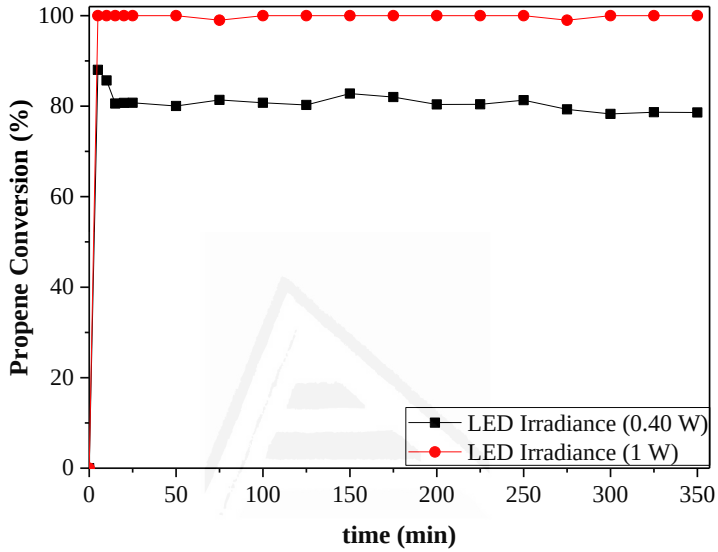

Figure 9.6. Stability of the catalyst (Microreact-P25) under continuous operation at different LED output power density (0.4 W/cm^2 and 1 W/cm^2) in the total oxidation of propene.

Another test for the catalyst stability was performed by multiple consecutive on/off light cycle experiments at different light output power densities (0.4 W/cm^2 and 1 W/cm^2), as showed in Fig. 9.7. The performance of the sample did not show a noticeable change in the propene conversion value at the end of each cycle in both cases (0.4 W/cm^2 and 1 W/cm^2). Moreover, the mass balances were checked in all reactions to corroborate that CO_2 was the only reaction product. The mass (mg) of P25 incorporated in the microreactor did not change after the stability tests. The good results in the stability test and the high abatement capability of propene, make this Microreact-P25 system very interesting for its application in the removal of this type of contaminants in indoor atmospheres.

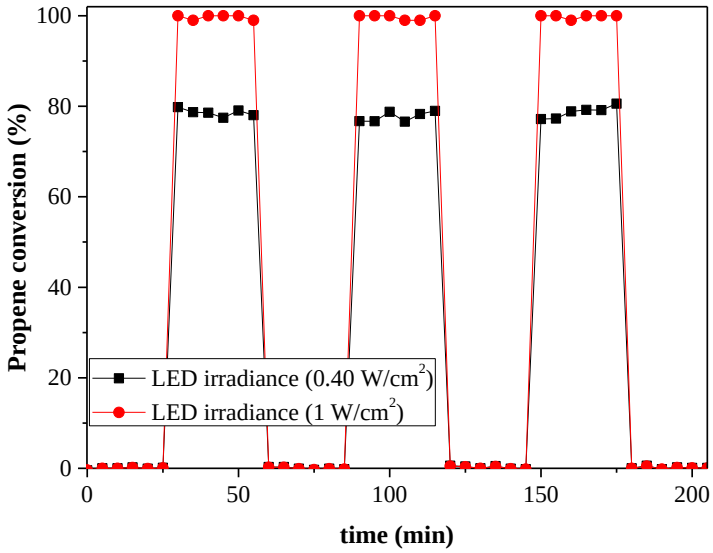

Figure 9.7. Stability of the catalyst (Microreact-P25) in cyclic operation: On-Off transient experiments at different LED output power density (0.4 W/cm^2 and 1 W/cm^2) in the oxidation total of propene.

9.4. Conclusions

In this Chapter, we have presented a photo-microfluidic chip reactor illuminated with LED which represents a highly efficient system to achieve total photocatalytic propene oxidation at low concentration, consisting on commercial TiO_2 incorporated in a commercial microreactor through a simple and straightforward experimental method. This system can totally mineralize the propene contained in an air stream at low concentrations using a few milligrams (1.18 mg) of catalyst (TiO_2, P25) inside the microreactor using a UV-LED light (0.55 W/cm^2) and low residence time (0.14 mg·min/mL), with excellent performance in terms catalytic activity (CO_2 production rate) compared to the same catalyst in a conventional reactor and in a microcapillary reactor. Moreover, the P25 inside of the microfluidic chip reactor presents a high stability under continuous and cyclic operation in the propene photooxidation under LED illumination conditions (0.4 W and 1W), which are significantly more cost-effective than conventional Hg or Xe lamps, commonly used for experiments performed under UV light. The results obtained in this Chapter make this system (P25 inside a microreactor) highly interesting for environmental applications in gas phase. Moreover, this technology could be considered a proof-of-concept for using microreactors in environmental applications as for example the use of this system for indoor air purification due to its small size and high activity. Nevertheless, the development of catalysts able to operate under solar/visible light irradiation would be necessary. The low amount of catalyst used in the microreactors is also an important factor since this improves the cost-efficiency of this technology, even if microchannel reactors are not cheap at present.

9.5. Referencias

[1] N. Wang, X. Zhang, Y. Wang, W. Yu, H. L.W. Chan, Lab. Chip. 14 (2014) 1074-1082.

[2] M. Yew, Y. Ren, K.S. Koh, C. Sun, C. Snape, Global Challenges. 3 (2019) 1800060

[3] J. P. McMullen, K. F. Jensen, Annu. Rev. Anal. Chem. 3 (2010) 19-42.

[4] K. Ren, J. Zhou, H. Wu, Acc. Chem. Res. 46, (2013) 2396-2406.

[5] S.S Ahsan, A. Gumus, D. Erickson, Lab Chip, 13 (2013) 409-414.

[6] J.R. Adleman, D.A. Boyd, D.G. Goodwin, D. Psaltis, Nano Lett. 9 (2009) 4417-4423.

[7] A. Manz, N. Graber, H. M. Widmer, Sens. Actuators, B. 1 (1990) 244-248.

[8] M.I.H. Ansari, S. Hassan, A. Qurashi, F.A. Khanday, Biosens. Bioelectron. 85 (2016) 247-260.

[9] K.S. Elvira, X.C. Solvas, R.C. Wootton, A.J. Mello, Nat. Chem. 5 (2013) 905-915.

[10] X. Yao, Y. Zhang, L. Du, J. Liu, J. Yao, Renew. Sustain. Energy Rev. 47 (2015) 519-539

[11] R. Gorges, S. Meyer, G. Kreisel, J. Photochem. Photobiol. A Chem. 167 (2004) 95-99.

[12] J. Kobayashi, Y. Mori, K. Okamoto, R. Akiyama, M. Ueno, T. Kitamori, S. Kobayashi, Science. 304 (2004) 1305-1308.

[13] G. Takei, T. Kitamori, H.B. Kim, Catal. Comm. 6 (2005) 357-360.

[14] A. Nakamura, K. Yoshida, S. Kuwahara, K. Katayama, J. Photochem. Photobiol. A Chem. 323 (2016) 35-40.

[15] A. Castedo, A. Casanovas, I. Angurell, L. Soler, J. Llorca, Fuel 222 (2018) 327-333.

[16] M. Krivec, K. Žagar, L. Suhadolnik, M. Čeh, G. Drazic, ACS Appl. Mater. Interfaces. 5 (2013) 9088-9094.

[17] A. Tanimu, S. Jaenicke, K. Alhooshani, Chem. Eng. J. 327 (2017) 792-821

[18] A.N. Wang, X.M. Zhang, B.L. Chen, W.Z. Song, N.Y. Chan, H.L.W. Chan, Lab Chip, 12 (2012) 3983-3990.

[19] M.Á. Lillo-Ródenas, N. Bouazza, Á. Berenguer-Murcia, J.J. Linares-Salinas, P. Soto, A. Linares-Solano, Appl. Catal. B Environ. 71 (2007) 298-309.

[20] R. Munirathinam, J. Huskens, W. Verboom, Adv. Synth. Catal. 357 (2015) 1093-1123

[21] C.J. Bueno-Alejo, J.L. Hueso, R. Mallada, I. Julian, J. Santamaria, Chem. Eng. J. 358 (2019) 1363-1370.

[22] M. Oelgemöller, O. Shvydkiv, Molecules. 16 (2011) 7522-7550

[23] J. M. Herrmann, J. Photochem. Photobiol. A Chem. 216 (2010) 85-93.

[24] J. R. Bolton, I. Mayor-Smith, K. G. Linden, J. Photochem. Photobiol. A Chem. 91 (2015)1252-1262.

[25] F. Khodadadian, M.W. de Boer, A. Poursaeidesfahani, J.R. van Ommen, A.I. Stankiewicz, R. Lakerveld, Chem. Eng. J. 333 (2018) 456-466.

[26] J. Jeong, K. Sekiguchi, W. Lee, K. Sakamoto, J. Photochem. Photobiol. A Chem. 169 (2005) 279-287.

Chapter 10

General Conclusions
Conclusiones Generales

In this PhD Thesis we have studied the design and preparation of materials based on titanium oxide and titanosilicates for their application in several catalytic reactions. The general conclusions of the different studies performed in this PhD Thesis are outlined in several sections for a clearer presentation.

❖ Photooxidation of propene with TiO_2 based photocatalyst:

✓ A synthesis strategy for TiO_2 with hierarchical porosity has been developed through the modification of a reported synthesis.

✓ TiO_2 samples calcined at 250 and 500 ºC have a high photocatalytic activity for propene photooxidation. Their performance is similar, and even slightly higher, to P25 (commercial TiO_2).

✓ A facile encapsulation of P25 (TiO_2) in different silica materials (spherical silica with hierarchical porosity, mesoporous silica and precipitated silica) was performed by the modification of an established methodology.

✓ The increase in the loading of P25 causes a modification in the morphology and porosity of the composite affecting the photocatalytic activity in the Silica/TiO_2 composites.

✓ The choice of a correct porous network for the silica matrix is crucial to obtain composites with high catalytic activity per mole of P25.

✓ An easy preparation method of TiO_2-MWCNT has been developed. The incorporation of MWCNT in the TiO_2 synthesis improves the properties of the final composite material in terms of better absorption of Visible light and lower e^--h^+ recombination rate.

✓ Longer sonication times or using a more powerful ultrasound source in the dispersion of the MWCNT generates a better dispersion of the carbon material and higher active surface area and oxygen species on the MWCNT. These factors determine a good interaction between the titanium species and the carbon material during the synthesis, what improves the photocatalytic activity of the composite.

❖ Propylene epoxidation with Ni-$TiSiO_2$ catalyst:

✓ Ni-based titano-silicate catalysts (transition metal catalyst) can be used for gas-phase catalytic epoxidation of propylene.

✓ The best catalysts based in transition metal (0.5% and 1% Ni/Ti-SiO_2) show a conversion of propylene of about 6 %, a selectivity over 85 % and a PO formation rate of 112 g PO/(kg_{cat}·h). These values are very interesting because they are similar to the best catalysts described in the literature (Au-based Ti-SiO_2).

✓ The preliminary study done using DFT calculations show that the interaction between Ni and Ti phases is very important to produce the active sites for epoxidation, which are responsible for the formation of the hydroperoxide-species intermediate.

❖ Hydrogen production from ammonia borane with Cu/TiO_2-MWCNT photocatalyst:

✓ The support presents a great importance in the catalytic activity of the active phase (Cu nanoparticles) observing that the presence of MWCNT improves the catalytic activity in the AB dehydrogenation reaction under Visible light irradiation due to the electron scavenging properties of this carbon material.

✓ The catalytic activity of Cu/TiO_2-MWCNT photocatalyst depends on the Cu content and the sample with lower copper loading displayed better catalytic activity than those catalysts with higher copper loadings (2 and 5 wt.%).

✓ The most interesting sample (Cu1%/TiO_2-MWCNT) presents high cyclability (3 cycles).

❖ Photooxidation of propene with comercial TiO_2 incorporated in microreactors:

✓ An easy methodology to immobilize a benchmark photocatalyst (P25) inside a capillary microreactor, using a packed bed configuration without previous treatment, by using a dispersion of the sample (P25) and a surfactant (Pluronic, F-127) in EtOH, was performed.

✓ The P25 incorporated inside the capillary microreactor presents an improved photocatalytic activity per mole of active phase (P25) with respect to the benchmark P25 placed in a conventional reactor.

✓ The microcapillary with some porosity among the P25 particles presents the best photocatalytic performance expressed per mole of active phase (P25) and a pressure drop comparable to the conventional reactor used with a thin P25 bed.

✓ A photo-microfluidic chip reactor illuminated with LED has been prepared as a highly efficient system to achieve total photocatalytic propene oxidation at low concentration, consisting on commercial TiO_2 incorporated in a commercial microreactor through a simple and straightforward experimental method.

✓ The photo-microfluidic chip reactor can totally mineralize propene using a low amount (1.18 mg) of catalyst (TiO_2, P25) inside the microreactor using a UV-LED light (0.55 W/cm^2) with excellent performance in terms catalytic activity (CO_2 production rate) compared to the same catalyst in a conventional reactor and in a microcapillary reactor.

✓ The P25 inside of the microfluidic chip reactor presents a high stability under continuous and cyclic operation in propene photooxidation under LED illumination conditions.

En esta Tesis Doctoral se ha estudiado el diseño y preparación de materiales basados en óxido de titanio y titanosilicatos para su aplicación en varias reacciones catalíticas. Las conclusiones generales de los estudios realizados en esta Tesis Doctoral se presentan en diferentes secciones para una mejor comprensión.

❖ Fotooxidación de propeno con fotocatalizadores basados en TiO_2:

- ✓ Se ha desarrollado una metodología para sintetizar TiO_2 con porosidad jerárquica a través de la modificación de una síntesis publicada en la bibliografía.

- ✓ La muestras de TiO_2 calcinadas a 250 y 500 ºC presentan una elevada actividad fotocatalítica para la oxidación de propeno. Su actividad catalítica es similar e incluso superior a la P25 (TiO_2 comercial).

- ✓ Se ha realizado una fácil encapsulación de P25 (TiO_2) en materiales de sílice con distinta porosidad (sílice esférica con porosidad jerárquica, sílice mesoporosa y sílice precipitada) mediante la modificación de una metodología establecida.

- ✓ El incremento de la cantidad de P25 provoca la modificación en la morfología y porosidad de la sílice, afectando a la actividad fotocatalítica de los materiales compuestos Sílice/TiO_2.

- ✓ La elección de la red porosa de la sílice es crucial para obtener materiales compuestos con elevada actividad fotocatalítica por mol de P25.

- ✓ Se ha desarrollado una metodología sencilla para la preparación de materiales compuestos TiO_2-MWCNT. La incorporación de MWCNT en la síntesis de TiO_2 mejora las propiedades del material compuesto final en términos de una mejor absorción de luz visible y baja velocidad de recombinación de pares e^--h^+.

- ✓ Mayores tiempos de tratamiento de ultrasonidos o el uso de un tratamiento de ultrasonidos más intenso en la dispersión de MWCNT genera una mejor dispersión del material de carbón y además genera una mayor área superfícial activa y grupos oxigenados en los MWCNT. Estos factores determinan una mejor interacción entre las especies de titantio y el material de carbón durante la síntesis, lo que mejora la actividad fotocatalítica del material compuesto final.

❖ Epoxidación de propileno con catalizadores Ni-$TiSiO_2$:

✓ Los catalizadores basados en Ni soportados sobre un titanosilicato (catalizadores basados en metales no-nobles) pueden ser usados para la reacción catalítica de epoxidación de propieleno en fase gaseosa.

✓ Los mejores catalizadores basados en metales de transición (0.5% y 1% Ni/Ti-SiO_2) muestran una conversión de propileno de 6 %, una selectividad de 85 % y una velocidad de formación de epóxido de propileno de 112 g OP/(kg_{cat}·h). Estos resultados son muy interesantes porque son similares a los mejores catalizadores descritos en la literatura (catalizadores de Ti-SiO_2 basados en Au).

✓ Los estudios preliminares realizados usando cálculos DFT muestran que la interacción entre las fases de Ni y Ti es muy importante para producir los sitios activos para la epoxidación, los cuales son responsables de la formación de especies hidroperóxido.

❖ Producción de hidrógeno a partir de amino borano mediante el fotocatalizador Cu/TiO_2-MWCNT:

✓ El soporte presenta una gran importancia en la actividad catalítica de la fase activa (nanopartículas de Cu), observándose que la presencia de nanotubos de carbono de pared múltiple mejora la descomposición del amino borano bajo la irradiación de luz visible

✓ La actividad catalítica del fotocatalízador Cu/TiO_2-MWCNT depende del contenido de Cu. Se observó que la muestra que presenta una menor carga de Cu presenta una mejor actividad catalítica.

✓ La muestra Cu1%/TiO_2-MWCNT presenta una alta ciclabilidad (3 ciclos).

❖ Fotooxidación de propeno con TiO_2 comercial incorporado en microrreactores:

✓ Se ha desarrollado una metodología sencilla para inmovilizar el fotocatalizador de referencia P25 en el interior de microcapilares, usando una configuración de lecho empaquetado sin tratamiento previo, mediante el uso de una dispersión de la muestra (P25) y surfactante (Pluronic, F-127) en EtOH.

✓ El catalizador incorporado en un microrreactor (capilar) presenta un incremento en la fotoactividad por mol de la fase activa (P25) con respecto a la misma fase incorporada en un reactor convencional.

✓ El microcapilar con cierta porosidad entre las partículas de P25 presenta un valor de actividad fotacatalítica expresado por moles de fase activa (P25) elevado; además, presenta una baja caída de presión comparable a las medidas en un reactor convencional con un lecho empaquetado delgado de partículas de P25.

✓ Se ha preparado un reactor de chip para microfluídica con P25 e iluminado con LEDs, el cual representa un sistema con una elevada eficiencia para lograr la fotooxidación total de propeno a bajas concentraciones.

✓ El reactor de chip para microfluídica con P25 puede oxidar totalmente el propeno con poca cantidad de catalizador (1,18 mg), usando una luz UV-LED (0,55 W/cm^2), con una excelente respuesta en términos de actividad catalítica (velocidad de producción de CO_2), en comparación con el mismo catalizador en un reactor convencional y un microreactor en forma de capilar.

✓ La P25 incorporada en un reactor de chip para microfluídica presenta una alta estabilidad en condiciones de operación continua y cíclica en la fotoxidación de propeno bajo iluminación con LEDs.